FLOW ACCELERATED ORGANIC COATING DEGRADATION

A Dissertation
Submitted to the Graduate Faculty
of the
North Dakota State University
of Agriculture and Applied Science

By

Qixin Zhou

In Partial Fulfillment
for the Degree of
DOCTOR OF PHILOSOPHY

Major Department:
Mechanical Engineering

March 2014

Fargo, North Dakota

North Dakota State University
Graduate School

Title

Flow Accelerated Organic Coating Degradation

By

Qixin Zhou

The Supervisory Committee certifies that this ***disquisition*** complies with North Dakota State University's regulations and meets the accepted standards for the degree of

DOCTOR OF PHILOSOPHY

SUPERVISORY COMMITTEE:

Dr. Yechun Wang
Chair

Dr. Chad Ulven

Dr. Xiangfa Wu

Dr. Gordon P. Bierwagen

Approved:

4/11/2014
Date

Dr. Alan R. Kallmeyer
Department Chair

ABSTRACT

Applying organic coatings is a common and the most cost effective way to protect metallic objects and structures from corrosion. Water entry into coating-metal interface is usually the main cause for the deterioration of organic coatings, which leads to coating delamination and underfilm corrosion. Recently, flowing fluids over sample surface have received attention due to their capability to accelerate material degradation. A plethora of works has focused on the flow induced metal corrosion, while few studies have investigated the flow accelerated organic coating degradation. Flowing fluids above coating surface affect corrosion by enhancing the water transport and abrading the surface due to fluid shear. Hence, it is of great importance to understand the influence of flowing fluids on the degradation of corrosion protective organic coatings.

In this study, a pigmented marine coating and several clear coatings were exposed to the laminar flow and stationary immersion. The laminar flow was pressure driven and confined in a flow channel. A 3.5 wt% sodium chloride solution and pure water was employed as the working fluid with a variety of flow rates. The corrosion protective properties of organic coatings were monitored inline by Electrochemical Impedance Spectroscopy (EIS) measurement. Equivalent circuit models were employed to interpret the EIS spectra. The time evolution of coating resistance and capacitance obtained from the model was studied to demonstrate the coating degradation. Thickness, gloss, and other topography characterizations were conducted to facilitate the assessment of the corrosion. The working fluids were characterized by Fourier Transform Infrared Spectrometer (FTIR) and conductivity measurement.

The influence of flow rate, fluid shear, fluid composition, and other effects in the coating degradation were investigated. We conclude that flowing fluid on the coating surface accelerates the transport of water, oxygen, and ions into the coating, as well as promotes the migration of coating materials from the coating into the working fluid, where coatings experience more severe deterioration in their barrier property under flowing conditions. Pure water has shown to be a much more aggressive working fluid than electrolyte solutions. The flowing fluid over the coating surface could be used as an effective acceleration method.

ACKNOWLEDGMENTS

It is my pleasure to take this opportunity to thank all the people who helped me during my study and research at North Dakota State University.

I would like to express my great appreciation to Dr. Yechun Wang, my dissertation committee chair, for her guidance, patience, kindness, and motivation. Without her persistent help and support this dissertation would not have been possible.

I would like to acknowledge my committee members, Dr. Gordon P. Bierwagen, Dr. Xiangfa Wu, and Dr. Chad A. Ulven. I would also like to give my great appreciation to Dr. Dennis E. Tallman. Their valuable and insight questions and suggestions have driven me to understand my research deeply.

I am pleased to thank Dohn Lee and Dr. Dean C. Webster for their gracious supply of coatings, Dr. Guodong Liu for gracious supply of deionized water, and Dr. Wenfang Sun for providing the usage of rotary evaporator.

I am also thankful to the professors who tutored me in classes, the department staff who assisted me in many aspects of my study and research, and my fellow students and friends who helped, entertained, and enlightened me.

My hearty thanks give to my dearest parents, Changfu Zhou and Ping Dong, who have been supporting me no matter where I am. My grateful appreciation also goes to my husband, Xiaofeng Qu, who is always my strong supporter anytime.

My graduate study and dissertation research was supported by the Four-year Presidential Doctoral Graduate Fellowship of North Dakota State University and One-year Teaching Assistantship from Mechanical Engineering Department. This work was supported by NDSU Advance FORWARD Program sponsored by NSF HRD-0811239.

DEDICATION

This dissertation is dedicated to my parents, Changfu Zhou and Ping Dong, my husband, Xiaofeng Qu, and my grandmother, Yulan Cai, who bring love, joy, and meaning to my life.

TABLE OF CONTENTS

LIST OF TABLES

LIST OF FIGURES

CHAPTER 1. INTRODUCTION

1.1. Background

Coatings can be described by their appearance, such as clear, pigmented, metallic, or glossy. They can also be classified by their function, like corrosion protective, abrasion protective, skid resistance, and decorative or photosensitive [1]. Coatings can be distinguished as organic or inorganic, although there is an overlap between these two categories. For example, many coatings consist of inorganic pigment particles that are dispersed in an organic matrix (the binder). Our study focuses on corrosion protective organic coatings.

The annual cost related to corrosion and corrosion prevention is significant. According to the National Association of Corrosion Engineers (NACE), the total direct cost of corrosion in the U.S. is approximately 3.1% of GDP [2]. Recent examination by NACE shows that corrosion costs in the U.S. approached $1 trillion dollars in 2013 [3]. Beyond the economic costs, corrosion can lead to technological delays, structural failures, and dramatic damage to humans and the environment [4]. Protection from corrosion is one of the primary performance properties of organic coatings. Using organic coatings is the most common and cost effective approach to protect metallic objects and structures from corrosion [5]. The function of protection from corrosion can be performed via an electrochemical mechanism and/or a barrier mechanism. The electrochemical mechanism inhibits corrosive reactions by adding anticorrosive pigments in a metal. It also performs by the passivation of metal forming stable and adhesive layers on the metal surface. Moreover, organic coatings can generate barriers between the substrate and the

environment. This barrier can reduce the transportation of oxygen, water, and ions to the coating metal interface [6].

1.2. Field and Laboratorial Tests for Organic Coating Characterization

Lifetime prediction of organic coatings plays an essential role in coating industry. Ranking or indication of coating performance and estimation when to replace the paints are required to demonstrate the competition ability of coatings in the market.

1.2.1. Field Testing

Field testing referred to as simulated-service testing, is the most reliable evaluation method. The testing is important for material selection, predicting the probable service life of a product or structure, and evaluating new commercial coatings and formula. The test specimens or structural components are exposed to outdoor environment which is representative for the general service situation. The duration of field testing normally requires several months or years. Some atmospheric tests of metals, for example, zinc-coated steel, have been conducted for more than 30 years.

The field testing includes the exposure to the atmosphere, water, and the geographical environment with special conditions or bacteriological factors. According to ISO 12944 “Coating and varnishes ― Corrosion protection of steel structures by protection coating systems” [7], it defines immersion, splash zone, and atmospheric as three major environment for coatings under exposure. Details on the classification of different exposure environment could refer to Fig.2 of the Refs [4]. Also, the category of corrosivity and environment impact factors on anticorrosive coatings are summarized in Table 1 of the Refs [4].

1.2.2. Acceleration Test Methods

Organic coatings are often designed to have a service lifetime of more than 50 years. Although outdoor field testing is reliable, it is so time consuming. Therefore, acceleration test methods are needed to evaluate the long-term performance of a coating within a limited time.

The goal of acceleration tests is to impose a repeatable and measurable set of stresses to a coating, which is similar but greater than the stresses the coating faces in field use. These excess stresses ideally cause the system to fail in a shorter time, but the failure mechanism reserves the same as in the normal conditions [8, 9]. Acceleration tests enable to study and rank the performance of new coatings as well as to predict the lifetime of coatings with no prior field use or without complete field testing.

Various acceleration tests are conducted by prolonged exposure to light, temperature, oxygen, moisture and condensation, mechanical stress, and environmental pollutants [10-13]. Different laboratorial studies focus on one aging factor or a combination of them in order to better understand coatings' degradation mechanisms and ultimately find a better way to predict coatings' lifetime. Existing acceleration test methods for organic coatings include salt fog chambers, QUV test, thermal cycling test, cyclic wet-dry test, and etc. Details of the acceleration test methods could refer to Table 2 of the Refs. [14].

Radiation (ultraviolet, x-rays or other energetic particles) can lead to ionization, resulting in the breaking of polymeric chains, for example, carbon-carbon bonds can be ruptured by ultraviolet (UV) radiation [15]. Damages in organic coatings by UV radiation could be discoloration, surface embrittlement, cracking, and loss of strength [16-20]. One

study mentioned that UV radiation brought the generation of porosity and hydrophilic regions in the clear and pigmented coatings [21].

Temperature affects organic coatings by inducing thermal stresses in the system and by changing the mechanical properties of the viscoelastic coatings. Coating degradation attributes to the creation of conductive pathways in the coatings as cracks filling with electrolyte and local delamination. The increasing transport processes can enhance the coating degradation process since it increases the propagation of defects and promotes the diffusion process within the coating matrix [22, 23].

Mechanical stress also influences the long term performance of organic coatings and it is probably conducive to synergistic effects with other aging parameters [24-26]. Fedrizzi's group studied the aging of organic coatings after deformation and found out that the more the coatings were deformed, the more they were damaged in the aging process [27, 28]. The degradation of coil coatings was accelerated by inducing mechanical stress since the uniaxial stain created defects at the vicinity of pigments; as a result, water uptake was enhanced [29].

Some laboratorial acceleration tests for organic coatings may alter the failure mechanism or still require a long exposure time. Therefore, a more efficient acceleration test method which preserves the coating failure mechanism as well as accelerates its degradation is needed for rapid service lifetime prediction of organic coatings.

1.3. Flow Induced Corrosion

1.3.1. Classification of Flow Induced Corrosion

Flow induced corrosion occurs in a wide variety of industry environments, such as vehicles, pipes, heat exchangers, chemical reactors, and offshore and marine facilities.

Flow induced corrosion is complicated, since flow velocity, flow pattern, solid particles, liquid droplets, and gas bubbles all contribute to corrosion process.

Investigations on flow induced corrosion have been developed since the 1950s, from single phase pipe flow to multiphase flow with slurries and bubbles. A number of mechanisms have been studied to describe the conjoint action of flow and corrosion. Heitz classified four types of flow induced corrosion: mass transport controlled corrosion, phase transport controlled corrosion, erosion corrosion, and cavitation corrosion [30]. Each is schematically represented in Figure 1.1.

Mass transport controlled corrosion is generally uniform and its rate determining step is the convective diffusion. Phase transport controlled corrosion is generally observed in crude oil streams. The phase transport is a rate determining step since the corrosive phase is contained in a multiphase fluid. Erosion corrosion is specified by a combination of flow induced mechanical forces and electrochemical processes. Erosion corrosion involves a multiphase flow, which can generate shear stress and pressure. The shear stress and pressure is caused by a high velocity flow and a severe attack of solid particles to a surface. Generally, erosion corrosion can be characterized by an appearance of grooves, waves, rounded holes, shallow pits, horseshoes, or other local phenomena related to the flow direction [31]. Cavitation corrosion is caused by the formation and collapse of vapor bubbles in a liquid against a surface. It occurs in hydraulic turbines, pump impellers, and ship propellers. It also occurs on surfaces in contact with high velocity liquids that are subject to changed pressures.

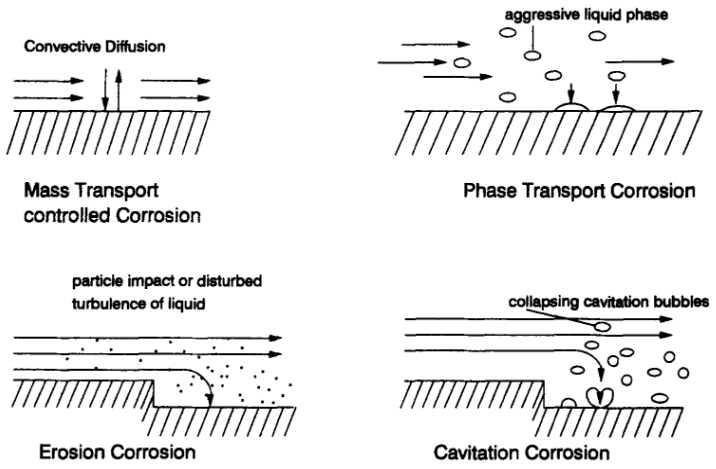

Figure 1.1. Four main mechanisms of flow induced corrosion [30].

1.3.2. Effect of Flow Velocity

In general, flow velocity plays a critical role in flow induced corrosion. Flow velocity affects corrosion in two ways: by the wall shear stress and through a mass transfer process [32]. For wall shear stress, there is a viscous sub-layer next to the surface when a fluid comes into contact with a metal surface. The thickness of this sub-layer decreases if the flow velocity increases. Consequently, the wall shear stress increases. The way flow velocity changes a viscous sub-layer depends on many factors: viscosity of the fluid, geometry and roughness of the surface, and temperature of the environment. When the mass transport of reactants occurs at a surface, a flowing fluid will influence the concentration gradient of reactants, which, in turn, influences the corrosion rate.

When a flow velocity is high, the flow tends to remove the oxidation film and salt deposits on a metal surface [4]. In addition, this high velocity can increase the mass transfer process of corrosive species: oxygen, carbon dioxide, and corrosive ions. As a result, more metal is exposed to corrosive media and corrodes faster. One study found that a higher mass loss rate was observed for AISI 1020 and SS316L metals when the

flow velocity was increased, which was due to the increased kinetic energy of the flowing fluid [33]. Another experiment investigated the erosion corrosion behavior of TiN coated α-Ti alloy in silica slurry by jet-in-slit rig [34]. At the low slurry velocity, a TiN coating deposited on the alloy substrate, thus presenting good erosion corrosion resistance. When the slurry velocity was increased, the protective effect of the coating layer was reduced due to perforating, cracking, and fragmenting on the TiN coating, eventually, the coatings were damaged and exhibited poor erosion corrosion resistance.

Whereas increasing flow velocity generally increases corrosion rates, it also has some beneficial effects. High velocity can eliminate local accumulation of aggressive agents on a metal surface; thus, this high velocity flow can avoid pitting and crevice corrosion. Stable pitting was evident during a laminar flow regime where the velocity was smaller than its critical velocity, but the growth of stable pits was impeded when the flow was above the critical velocity [32]. A critical velocity can be identified, above which the austenitic stainless steels undergo less pitting, and an approximate critical velocity is 1.5 m/s in the study [32]. High velocity fluid has sufficient kinetic energy so that it can penetrate through the sub-layer to the metal surface; thus, the growth of metastable pitting is disturbed by the high velocity fluid. Another study found that, in an erosion corrosion condition, water that circulated at a velocity below the critical velocity was the main cause of the failure of the tubular heat exchanger [35]. Since the low velocity flow cannot wash away salt deposits in pipes, the accumulation of deposits may reduce the diameter and eventually block tubes.

The effects of flow velocity on erosion corrosion are studied in order to understand the mechanisms of flow induced corrosion. The erosion corrosion regime is

defined by the rate ratio of corrosion to erosion: K_c / K_e. K_c and K_e satisfy the relationship of $K_{ec} = K_c + K_e$, where K_{ec} is the total erosion corrosion rate which can be measured experimentally, and K_c is the total corrosion rate which can be calculated by Faraday's law. Therefore, the total erosion rate, K_e, can be calculated mathematically. A well-established erosion corrosion regime is defined as follows: If $K_c / K_e < 0.1$, the erosion dominates; if $0.1 \leq K_c / K_e < 1$, it is erosion corrosion; if $1 \leq K_c / K_e < 10$, it is corrosion erosion; and if $K_c / K_e \geq 10$, corrosion dominates [36-40]. Stack's group investigated the mapping mechanism of the erosion corrosion process of metals by combining the effects of slurry, velocity, and applied potentials [37].

1.3.3. Effect of Flow Pattern

The system of flowing fluid is complex since it involves different flow patterns. The intensity of interaction between flowing media and solid walls depends on the number of fluid phases and the velocity in each phase. The flow pattern that is easiest to describe is the undisturbed, developed single phase flow. Other flow patterns become difficult to describe in a hydrodynamic way, such as two phase flow (liquid in liquid, gas in liquid, and solid in liquid) and multiphase flow in horizontal, inclined, or vertical flow systems [41]. Different flow patterns have different flow velocities, velocity gradients, boundary layers, and other flow properties. These factors can influence mass and momentum transfer process, which, in turn, affect flow induced corrosion.

Studies have been investigated the influence of flow pattern in the corrosion behavior of different materials. Swirl flow was found to result in a higher rate of diffusion controlled corrosion than axial flow for a given velocity in pipes [42]. The corrosion rate of carbon steel was proportional to slug turbulence, which is characterized

as a Froude number, under multiphase slug flow [43]. The corrosion of steel caused by carbon dioxide was increased by slug flow in a vertical upward direction [44]. The characteristics of the slug flow, like the changed shear stress, normal stress, and mass transfer near the wall, significantly affected the carbon dioxide corrosion process [44]. The corrosion inhibitor behavior of large pipelines under multiphase flow was studied using electrochemical impedance spectroscopy [45-47]. The increase of the corrosion rate and reduction of inhibitors' performance was due to higher turbulence and higher frequency of bubble impact on the metal surface.

Different substrate geometries contribute to different flow regimes which influence the mass transfer process. The diffusion controlled corrosion rate was determined by the geometry of the bottom of agitated vessel. A conical bottom suffered less corrosion than a flat bottom for a given set of conditions [48]. An aluminum alloy was damaged by erosion corrosion in a two phase jet flow [49]. The relative velocities of steam to droplets depended on the length of the straight portion of the nozzle outlet. At every flow rate, a long straight portion caused the formation of large droplets with large velocity. As a result, the mass loss was increased with an increase in the length of the straight portion.

1.3.4. Effect of Fluid Composition

The penetration of water into a metal-coating interface is usually a main cause for the degradation and the loss of corrosion protective function of organic coatings, which can eventually lead to coating delamination and underfilm corrosion. The water in the interface can bring the loss of adhesion and formation of a separate water phase at the interface. The water will cause the anodic and cathodic zones to be contacted and formed

an electrochemical cell. Also, water in coatings can generate osmotic pressure due to the presence of soluble impurities with a self-amplifying effect, and the osmotic pressure could recall further water uptake. In addition, water penetration can cover the paths through the coating which will accelerate the corrosion process, since these paths are preferential accessed for solvates ions [50].

Numerous studies have been published on the durability of organic coatings by using salt solution such as NaCl solution as the working fluid [51-57]. Also, the evaluations of water uptake into organic coatings often adopt salt solutions as the test medium. Salt solutions are highly conductive and have a very low resistance to the transport of ions. For example, the resistivity of a NaCl solution (1M) is 11.6 Ω·cm at 20 ˚C [31]. So the resistance of the ionic conducting path between the anode and the cathode is lower, which is preferential for a corrosion cell.

In addition to NaCl solutions, corrosion studies for metallic materials adopt pure water (e.g. deionized or distilled water) as the working fluid. Hodgkiess and Mantzavinos studied the corrosion of copper nickel alloys in distilled water at 20–80 ˚C with and without injecting carbon dioxide [58]. They also investigated the corrosion of condenser tube materials in distilled water [59]. Lu et al. evaluated the stress cracking corrosion of stainless steel in pure water at different temperatures [60, 61]. Alentejano et al. studied the localized corrosion inhibition of stainless steel in deaerated pure water in the presence and absence of chloride ions [62]. Lytle's group investigated copper pitting corrosion in a drinking water distribution system [63].

Therefore, it is of great importance to study the influence of fluid composition in the degradation of organic coatings. It is valuable to use pure water which could simplify

the water uptake, since the penetration of salt solution may involve the ion diffusion which may influence the water uptake. On the other hand, the ions concentration of working fluid could affect the degradation of organic coatings, which calls for extensive investigations.

1.4. Flow Induced Organic Coating Degradation

Many studied have investigated flow induced corrosion for bare metals; however, the influence of flow induced organic coating degradation has received less attention. Some studies have investigated erosion corrosion behavior of thermal sprayed coatings, but these coatings are hard coatings and out of the scope of organic coatings [64-67]. Flow induced organic coating degradation involves the fluid-wall interactions, which include mass transfer, heat transfer, fluctuating shear stress parallel to the surface, fluctuating energy density perpendicular to the surface, particle impact, and gas bubbles collapsing near the wall [41]. These fluid-wall interactions are difficult to describe in a hydrodynamic way for a coating-metal system.

Traditionally, researchers have investigated the degradation of organic coatings immersed in stationary solutions, e.g. Refs. [50, 56, 68]. Recently, more attention has been paid to investigations of coatings in flowing solutions. Initially, Jeffcoate and Bierwagen reported that flowing electrolytes have a marked effect on the performance of coating systems [69]. Wei, Zhang, and Ke studied the degradation of epoxy powder coating under flowing and static immersion conditions in a 3% NaCl solution; they used a rotating cylinder apparatus to generate the flowing field [70]. Thu, Bierwagen, and Touzain reported the degradation behavior of three different organic coatings under laminar flow [6]. In general, these earlier studies did not correlate the coating degradation

to the flow rate. To our knowledge, the work which related varying flow rates to the degradation of organic coating was first conducted by Wang and Bierwagen [57]. They concluded that barrier properties of the organic coating decreased exponentially with the increasing flow rate of a 3.5 wt% NaCl solution. They also proposed that the flowing electrolyte solution could be used in acceleration tests for the service lifetime prediction of organic coatings.

1.5. Objectives

Our goal is to understand the degradation mechanism of coatings under flow induced corrosion which is believed to be an efficient acceleration test. It fails coatings in a shorter time without altering the degradation mechanism. Flowing fluids are employed as the acceleration media, and the degradation process can be monitored by organic coating's electrochemical property as well as its topography. In order to understand the mechanism of flow induced organic coating degradation, we aim to investigate the following aspects:

- The influence of flow rate
- The influence of fluid shear
- The influence of working fluid
- The influence of flowing mode: recirculated and non-recirculated
- The influence of fluid composition: NaCl concentration
- Water and ion diffusion processes
- Coating materials release process
- Numerical simulations on convective diffusion process

The influence of flowing fluid on organic coating degradation is discussed in Chapter 2 for marine coating and Chapter 3 for clear coating. The simulation on convective diffusion of NaCl into organic coatings is presented in Chapter 4. The influence of fluid compositions on organic coating degradation is discussed in Chapter 5. Other influencing factors for coating degradation are reported and summarized in Chapter 6. Another research project which simulated the Scanning Electrochemical Microscopy (SECM) approach curves for heterogeneous metal surfaces is also included in Chapter 7. All major findings of the study on flow accelerated degradation of organic coatings are summarized in Chapter 8. The recommendation for future work is presented in Chapter 9.

The study on the flow accelerated degradation of corrosion protective organic coatings has resulted in three publications: The influence of different flow rates on marine coating degradation has been published in Corrosion Science [71]; the influence of different flow compositions on clear coating degradation has been published in Progress in Organic Coatings [72]; the third one focuses on the topography characterizations on coating surface when flow accelerated the degradation [73]. The other research on the simulation of SECM approach curves for heterogeneous metal surface has been published in Journal of the Electrochemical Society [74]. The study on the effects of fluid shear on clear coating degradation will be submitted for publication in the near future. In addition, the major findings of our study have been presented in national and international meetings including AIChE, ASME, NACE, and ND EPSCoR conference.

1.6. References

[1] Z.W.J. Wicks, F.N. Jones, S.P. Pappas, D.A. Wicks, Organic Coatings, 3rd ed., John Wiley & Sons, Inc., Hoboken, New Jersey, 2007.

[2] C.T. Laboratories, Corrosion costs and preventive strategies in the united states, *http://www.nace.org/content.cfm?parentid=1011&currentID=1045*, (1998).

[3] Cost of corrosion to exceed $1 trillion in the United States in 2013, *http://www.g2mtlabs.com/2011/06/nace-cost-of-corrosion-study-update/*.

[4] P.A. Sorensen, S. Kiil, K. Dam-Johansen, C.E. Weinell, Anticorrosive coatings: a review, *Journal of Coatings Technology and Research*, **6** (2009) 135-176.

[5] G.P. Bierwagen, Reflections on corrosion control by organic coatings, *Progress in Organic Coatings*, **28** (1996) 43-48.

[6] Q.L. Thu, G.P. Bierwagen, S. Touzain, EIS and ENM measurements for three different organic coatings on aluminum, *Progress in Organic Coatings*, **42** (2001) 179-187.

[7] ISO 12944, *International Standards Organization, Geneve*, (1998).

[8] G.P. Bierwagen, L. He, J. Li, L. Ellingson, D.E. Tallman, Studies of a new accelerated evaluation method for coating corrosion resistance - thermal cycling testing, *Progress in Organic Coatings*, **39** (2000) 67-78.

[9] G.P. Bierwagen, D.E. Tallman, J. Li, L. He, C.S. Jeffcoate, EIS studies of coated metals in accelerated exposure, *Progress in Organic Coatings*, **46** (2003) 149-158.

[10] T. Yuzawa, C. Watanabe, S. Tsuge, N. Shimane, H. Imai, Application of a pyrolysis-GC/MS system incorporating with micro-UV irradiation to rapid

evaluation of the weatherability of acrylic coating paints for house exterior walls, *Polymer Degradation and Stability*, **96** (2011) 91-96.

[11] O. Haillant, D. Dumbleton, A. Zielnik, An Arrhenius approach to estimating organic photovoltaic module weathering acceleration factors, *Solar Energy Materials and Solar Cells*, **95** (2011) 1889-1895.

[12] O. Guseva, S. Brunner, P. Richner, Service life prediction for aircraft coatings, *Polymer Degradation and Stability*, **82** (2003) 1-13.

[13] B.W. Johnson, R. McIntyre, Analysis of test methods for UV durability predictions of polymer coatings, *Progress in Organic Coatings*, **27** (1996) 95-106.

[14] F.X. Perrin, C. Merlatti, E. Aragon, A. Margaillan, Degradation study of polymer coating: Improvement in coating weatherability testing and coating failure prediction, *Progress in Organic Coatings*, **64** (2009) 466-473.

[15] M.A. Meyers, K.K. Chawla, Mechanical Behavior of Materials, 2nd ed., Cambridge University Press, 2009.

[16] J.H. Park, G.D. Lee, H. Ooshige, A. Nishikata, T. Tsuru, Monitoring of water uptake in organic coatings under cyclic wet–dry condition, *Corrosion Science*, **45** (2003) 1881-1894.

[17] B.S. Skerry, C.H. Simpson, Accelerated test method for assessing corrosion and weathering of paints for atmospheric corrosion control, *Corrosion*, **49** (1993) 663.

[18] F.X. Perrin, M. Irigoyen, E. Aragon, J.L. Vernet, Evaluation of accelerated weathering tests for three paint systems: a comparative study of their aging behaviour, *Polymer Degradation and Stability*, **72** (2001) 115-124.

[19] S. Brunner, P. Richner, U. Müller, O. Guseva, Accelerated weathering device for service life prediction for organic coatings, *Polymer Testing*, **24** (2005) 25-31.

[20] J. Mallégol, M. Poelman, M.G. Olivier, Influence of UV weathering on corrosion resistance of prepainted steel, *Progress in Organic Coatings*, **61** (2008) 126-135.

[21] M.G. Penon, S.J. Picken, M. Wübbenhorst, J. van Turnhout, Water sorption in UV degraded clear and pigmented epoxy coatings assessed by dielectric sorption analysis, *Polymer Degradation and Stability*, **92** (2007) 1247-1254.

[22] A. Miszczyk, K. Darowicki, Effect of environmental temperature variations on protective properties of organic coatings, *Progress in Organic Coatings*, **46** (2003) 49-54.

[23] S. Touzain, Q.L. Thu, G. Bonnet, Evaluation of thick organic coatings degradation in seawater using cathodic protection and thermally accelerated tests, *Progress in Organic Coatings*, **52** (2005) 311-319.

[24] N. Fredj, S. Cohendoz, X. Feaugas, S. Touzain, Effect of mechanical stress on kinetics of degradation of marine coatings, *Progress in Organic Coatings*, **63** (2008) 316-322.

[25] N. Fredj, S. Cohendoz, X. Feaugas, S. Touzain, Some consequences of saline solution immersion on mechanical behavior of two marine epoxy-based coatings, *Progress in Organic Coatings*, **69** (2010) 82-91.

[26] N. Fredj, S. Cohendoz, X. Feaugas, S. Touzain, Ageing of marine coating in natural and artificial seawater under mechanical stresses, *Progress in Organic Coatings*, **74** (2012) 391-399.

[27] F. Deflorian, L. Fedrizzi, S. Rossi, Effects of mechanical deformation on the protection properties of coil coating products, *Corrosion Science*, **42** (2000) 1283-1301.

[28] A. Bergo, L. Fedrizzi, Thermal aging of painted galvanized steel after mechanical deformation, *Progress in Organic Coatings*, **52** (2005) 328-338.

[29] A.C. Bastos, A.M.P. Simões, Effect of uniaxial strain on the protective properties of coil-coatings, *Progress in Organic Coatings*, **46** (2003) 220-227.

[30] E. Heitz, Mechanistically based prevention strategies of flow-induced corrosion, *Electrochimica Acta*, **41** (1996) 503-509.

[31] J.R. Davis, Corrosion Understanding the Basics, ASM International, Materials Park Ohio, 2000.

[32] J.A. Wharton, R.J.K. Wood, Influence of flow conditions on the corrosion of AISI 304L stainless steel, *Wear*, **256** (2004) 525-536.

[33] S.S. Rajahram, T.J. Harvey, R.J.K. Wood, Erosion-corrosion resistance of engineering materials in various test conditions, *Wear*, **267** (2009) 244-254.

[34] J. Tu, The effect of TiN coating on erosion-corrosion resistance of α-Ti alloy in saline slurry, *Corrosion Science*, **42** (2000) 147-163.

[35] K. Ranjbar, Effect of flow induced corrosion and erosion on failure of a tubular heat exchanger, *Materials & Design*, **31** (2010) 613-619.

[36] M.M. Stack, N. Corlett, S. Turgoose, Some thoughts on modelling the effects of oxygen and particle concentration on the erosion–corrosion of steels in aqueous slurries, *Wear*, **255** (2003) 225-236.

[37] M.M. Stack, T.M. Abd El Badia, Mapping erosion-corrosion of WC/Co-Cr based composite coatings: Particle velocity and applied potential effects, *Surface and Coatings Technology*, **201** (2006) 1335-1347.

[38] Y.P. Purandare, M.M. Stack, P.E. Hovsepian, Velocity effects on erosion-corrosion of CrN/NbN "superlattice" PVD coatings, *Surface and Coatings Technology*, **201** (2006) 361-370.

[39] M.M. Stack, T.M. Abd El-Badia, Some comments on mapping the combined effects of slurry concentration, impact velocity and electrochemical potential on the erosion–corrosion of WC/Co–Cr coatings, *Wear*, **264** (2008) 826-837.

[40] R. Malka, S. Nešić, D.A. Gulino, Erosion–corrosion and synergistic effects in disturbed liquid-particle flow, *Wear*, **262** (2007) 791-799.

[41] R.A. Cottis, L.L. Shreir, Shreir's Corrosion, Elsevier, Amsterdam, London, 2010.

[42] A.S. Shehata, S.A. Nosier, G.H. Sedahmed, The role of mass transfer in the flow-induced corrosion of equipments employing decaying swirl flow, *Chemical Engineering and Processing*, **41** (2002) 659-666.

[43] J. Villarreal, D. Laverde, C. Fuentes, Carbon-steel corrosion in multiphase slug flow and CO_2, *Corrosion Science*, **48** (2006) 2363-2379.

[44] D. Zheng, D. Che, Y. Liu, Experimental investigation on gas-liquid two-phase slug flow enhanced carbon dioxide corrosion in vertical upward pipeline, *Corrosion Science*, **50** (2008) 3005-3020.

[45] Y. Chen, T. Hong, M. Gopal, W.P. Jepson, EIS studies of a corrosion inhibitor behavior under multiphase flow conditions, *Corrosion Science*, **42** (2000) 979-990.

[46] Y. Chen, W.P. Jepson, EIS measurement for corrosion monitoring under multiphase flow conditions, *Electrochimica Acta*, **44** (1999) 4453-4464.

[47] T. Hong, Y.H. Sun, W.P. Jepson, Study on corrosion inhibitor in large pipelines under multiphase flow using EIS, *Corrosion Science*, **44** (2002) 101-112.

[48] Y.M. El-Shazly, R.R. Zahran, H.A. Farag, G.H. Sedahmed, Mass transfer in relation to flow induced corrosion of the bottom of cylindrical agitated vessels, *Chemical Engineering and Processing: Process Intensification*, **43** (2004) 745-751.

[49] H. Nanjo, Y. Kurata, N. Sanada, K. Miyauchi, R. Ohshima, K. Koike, Erosion-corrosion damage of aluminum alloy in a high-speed, high-temperature, two-phase flow, *Wear*, **186-187, Part 2** (1995) 573-578.

[50] M. Del Grosso Destreri, J. Vogelsang, L. Fedrizzi, F. Deflorian, Water up-take evaluation of new waterborne and high solid epoxy coatings. Part II: electrochemical impedance spectroscopy, *Progress in Organic Coatings*, **37** (1999) 69-81.

[51] N. Fredj, S. Cohendoz, S. Mallarino, X. Feaugas, S. Touzain, Evidencing antagonist effects of water uptake and leaching processes in marine organic coatings by gravimetry and EIS, *Progress in Organic Coatings*, **67** (2010) 287-295.

[52] R.C. Barik, J.A. Wharton, R.J.K. Wood, K.R. Stokes, Electro-mechanical interactions during erosion–corrosion, *Wear*, **267** (2009) 1900-1908.

[53] H. Marchebois, S. Touzain, S. Joiret, J. Bernard, C. Savall, Zinc-rich powder coatings corrosion in sea water: influence of conductive pigments, *Progress in Organic Coatings*, **45** (2002) 415-421.

[54] A.S.L. Castela, A.M. Simões, M.G.S. Ferreira, E.I.S. evaluation of attached and free polymer films, *Progress in Organic Coatings*, **38** (2000) 1-7.

[55] F. Deflorian, S. Rossi, M. Fedel, Organic coatings degradation: Comparison between natural and artificial weathering, *Corrosion Science*, **50** (2008) 2360-2366.

[56] V. Barranco, S. Feliu, EIS study of the corrosion behaviour of zinc-based coatings on steel in quiescent 3% NaCl solution. Part 1: directly exposed coatings, *Corrosion Science*, **46** (2004) 2203-2220.

[57] Y. Wang, G.P. Bierwagen, A new acceleration factor for the testing of corrosion protective coating: flow-induced coating degradation, *Journal of Coatings Technology and Research*, **6** (2009) 429-436.

[58] T. Hodgkiess, D. Mantzavinos, Corrosion of copper-nickel alloys in pure water, *Desalination*, **126** (1999) 129-137.

[59] D. Mantzavinos, T. Hodgkiess, S.L.C. Lai, Corrosion of condenser tube materials in distilled water, *Desalination*, **138** (2001) 365-370.

[60] Z. Lu, T. Shoji, Y. Takeda, Y. Ito, A. Kai, S. Yamazaki, Transient and steady state crack growth kinetics for stress corrosion cracking of a cold worked 316L stainless steel in oxygenated pure water at different temperatures, *Corrosion Science*, **50** (2008) 561-575.

[61] Z. Lu, T. Shoji, T. Dan, Y. Qiu, T. Yonezawa, The effect of roll-processing orientation on stress corrosion cracking of warm-rolled 304L stainless steel in oxygenated and deoxygenated high temperature pure water, *Corrosion Science*, **52** (2010) 2547-2555.

[62] C.R. Alentejano, I.V. Aoki, Localized corrosion inhibition of 304 stainless steel in pure water by oxyanions tungstate and molybdate, *Electrochimica Acta*, **49** (2004) 2779-2785.

[63] D.A. Lytle, M.N. Nadagouda, A comprehensive investigation of copper pitting corrosion in a drinking water distribution system, *Corrosion Science*, **52** (2010) 1927-1938.

[64] H.Y. Al-Fadhli, J. Stokes, M.S.J. Hashmi, B.S. Yilbas, The erosion–corrosion behaviour of high velocity oxy-fuel (HVOF) thermally sprayed inconel-625 coatings on different metallic surfaces, *Surface and Coatings Technology*, **200** (2006) 5782-5788.

[65] V.A.D. Souza, A. Neville, Corrosion and synergy in a WCCoCr HVOF thermal spray coating—understanding their role in erosion–corrosion degradation, *Wear*, **259** (2005) 171-180.

[66] S. Shrestha, T. Hodgkiess, A. Neville, Erosion–corrosion behaviour of high-velocity oxy-fuel Ni–Cr–Mo–Si–B coatings under high-velocity seawater jet impingement, *Wear*, **259** (2005) 208-218.

[67] D. Toma, W. Brandl, G. Marginean, Wear and corrosion behaviour of thermally sprayed cermet coatings, *Surface and Coatings Technology*, **138** (2001) 149-158.

[68] F. Rezaei, F. Sharif, A.A. Sarabi, S.M. Kasiriha, M. Rahmaniam, E. Akbarinezhad, Evaluating water transport through high solid polyurethane coating using the EIS method, *Journal of Coatings Technology and Research*, **7** (2010) 209-217.

[69] C.S. Jeffcoate, G.P. Bierwagen, Electrochemical comparison of coating performance in flowing vs. stationary electrolyte, in: G.P. Bierwagen (Ed.) American Chemical Society Symposium Series, American Chemical Society, Washington, DC, 1998, pp. 151-160.

[70] Y. Wei, L. Zhang, W. Ke, Comparison of the degradation behaviour of fusion-bonded epoxy powder coating systems under flowing and static immersion, *Corrosion Science*, **48** (2006) 1449-1461.

[71] Q. Zhou, Y. Wang, G.P. Bierwagen, Influence of the composition of working fluids on flow-accelerated organic coating degradation: Deionized water versus electrolyte solution, *Corrosion Science*, **55** (2012) 97-106.

[72] Q. Zhou, Y. Wang, Comparisons of clear coating degradation in NaCl solution and pure water, *Progress in Organic Coatings*, **76** (2013) 1674-1682.

[73] Q. Zhou, Y. Wang, F. Azarmi, A topography characterization of organic coatings degradation under flowing deionized water, *Journal of Materials Science and Engineering A*, **1** (2011) 599-606.

[74] Q. Zhou, Y. Wang, D.E. Tallman, M.B. Jensen, Simulation of SECM approach curves for heterogeneous metal surfaces, *Journal of the Electrochemical Society*, **159** (2012) H644-H649.

CHAPTER 2. FLOW ACCELERATED DEGRADATION OF MARINE COATINGS: THE EFFECT OF FLOW RATE

2.1. Introduction

Organic coatings perform two primary functions: protection and decoration [1]. Applying organic coatings is the most common and usually the most cost effective approach to protect metallic objects and structures against corrosion [2]. Organic coatings act as barriers providing resistance to the transportation of oxygen, water, and ions to the coating metal interface, and hence limiting corrosion [3].

Flow induced corrosion is complicated, since flow velocity, flow pattern, solid particles, and impact angles all contribute to the corrosion process [4-11]. Heitz classified four types of mechanisms to describe the conjoint action of flow and corrosion [12]. They are mass transport controlled corrosion, phase transport controlled corrosion, erosion corrosion, and cavitation corrosion. Many researches are focused on studying erosion corrosion regimes so as to reveal the internal mechanism of the flowing corrosion, e.g. Refs. [8, 11, 13-17]. A plethora of studies has been conducted for flow induced un-coated metal corrosion, e.g. Refs. [5-10, 13-15], while the influence of flow over organic coatings has received less attention.

Traditionally, investigations on the degradation of organic coatings are performed for coatings immersed in stationary solutions, e.g. Refs. [18-20]. Recently, more attention has been paid on flowing solution over the organic coatings [3, 21, 22]. However, the flow rate is not correlated with the coating degradation in the afore-mentioned studies. To our knowledge, the only work which related varying flow rates with the degradation of organic coatings was conducted by Wang and Bierwagen [23]. They concluded that

barrier properties of the coating decreased exponentially with the increasing flow rate of a 3.5 wt% NaCl solution and proposed that the flowing electrolyte solution could be used in acceleration tests for the service lifetime prediction of organic coatings.

The goal of the study in this chapter is to improve the understanding of the performance of organic coating under different flow rates, since recent work has proved that flow conditions accelerate coating degradation [21, 23]. Deionized (DI) water has been used as the working fluid in this study. Electrochemical impedance spectroscopy (EIS) measurement was utilized as the main approach to characterize the coating degradation. EIS has been considered as a valuable and powerful tool to assess the degradation of organic coatings, e.g. Refs [19, 20, 23-25]. EIS has long been used to predict the service lifetime of corrosion protective coatings, rank the coatings systems, and measure the water uptake in coatings. EIS data are also assimilated to develop meaningful models to analyze the physical behavior of the coating degradation. Thus, equivalent circuit modeling was developed to interpret the EIS spectra. In addition, the topological changes of the coating surface were characterized as the degradation was accelerated by flowing fluid.

2.2. Materials and Methods

2.2.1. Coatings and Sample Preparation

The organic coatings used in this study were Korabor Aluminum Primer RP140 and Korethan Topcoat UT6581 (graciously supplied by KCC Corporation). The primer was a chlorinated rubber based coating with aluminum flake pigment. The topcoat was a polyurethane resin based finish coat.

Q-panel standard steel panels (S-36 from Q-Panel Lab Products) were cut into 76 × 76 mm and used as the metal substrate. The panels were then pretreated by abrasion with 320 and 600 grit sand paper, and then cleaned with acetone and hexane before coatings were applied. The liquid paints were applied by air spraying and cured in room temperature for 24 h. All the coating samples were allowed to completely dry for several days at the room temperature before testing.

2.2.2. Experimental Setup and EIS Measurement

A flow channel was adopted from the study conducted by Dr. Wang and Dr. Bierwagen [23] as shown in Figure 2.1. The picture of the flow channel and EIS setups in the experiment is shown in Figure 2.2. The flow channel was constructed with plastic sheets. Coated panels were adhered to the upper and lower channel walls. The platinum meshes were embedded through the plastic plate to the upper channel wall acting either as counter or reference electrode. The working fluid (DI water) was pumped from the fluid reservoir to the test section, which was the gap between the two panels facing each other, and then recycled to the reservoir. The flow rate was maintained by a rotameter at 3.683 and 5.233 cm^3/s, respectively. The temperature was controlled at 25 ˚C by a water bath and a temperature controlling system. The flowing and temperature controlling systems are shown in Figure 2.3.

The three-electrode setup was employed for EIS measurements in this study. For coatings immersed in flowing fluids, the electrochemical cell was composed of a steel panel acting as the working electrode, a pair of platinum meshes, on the left and right sides of the test panel, acting as the counter electrode, and another platinum electrode, near the flow outlet, acting as the reference electrode. EIS measurements were performed

using the Reference 600 Potentiostat and Electrochemical Multiplexer ECM8 by Gamry Instruments, as shown in Figure 2.4. The scanning frequency range was from 10^{-2} to 10^{5} Hz with 10 points per decade using 15 mV AC perturbation coupled with the open circuit potential. EIS measurements were carried out every day during the immersed period. All the measurements were performed at the room temperature. The experiments of the same flow rate repeated by at least four coating samples to avoid adulterations due to pores or local defects.

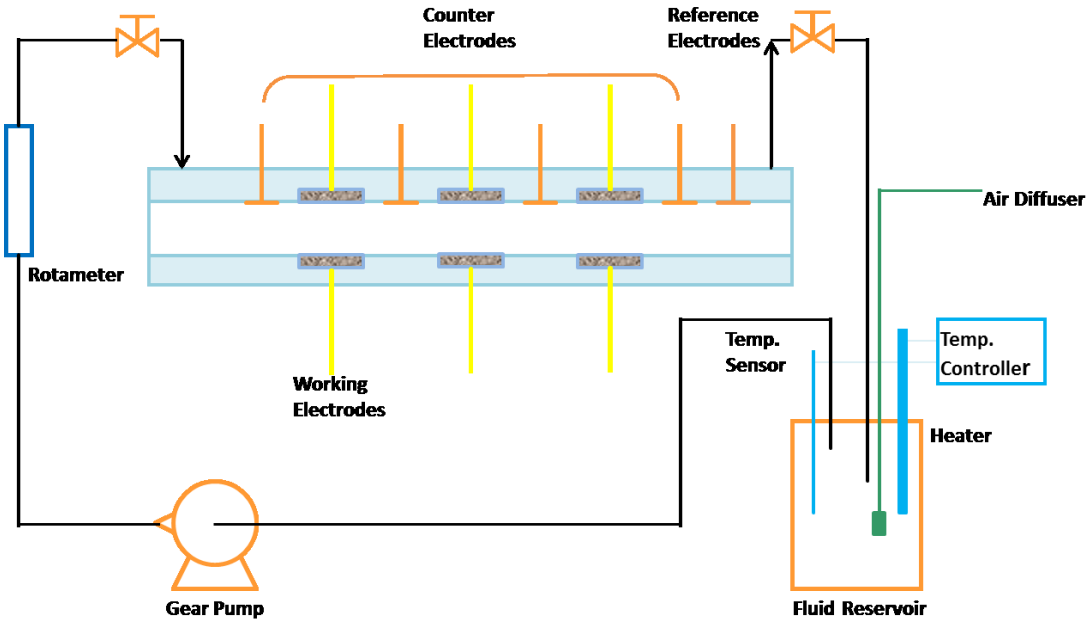

Figure 2.1. Schematic diagram of the circulating flow [23].

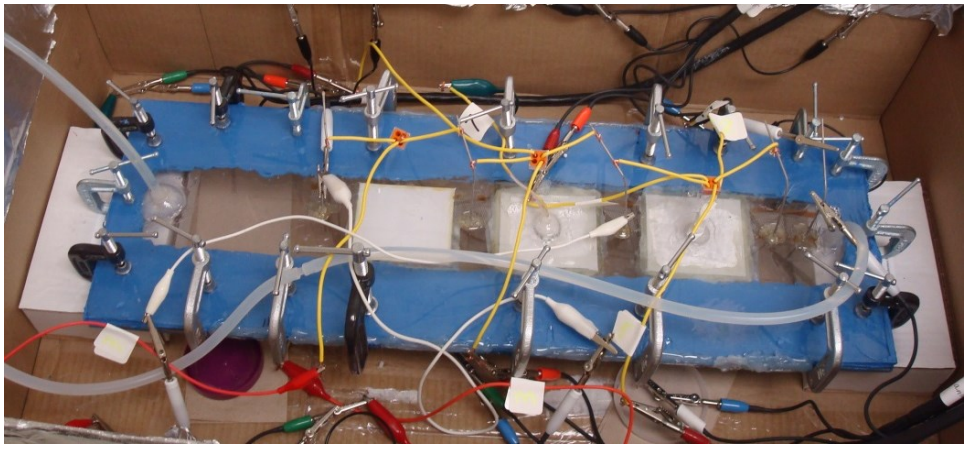

Figure 2.2. A picture of the circulating flow channel and EIS setups.

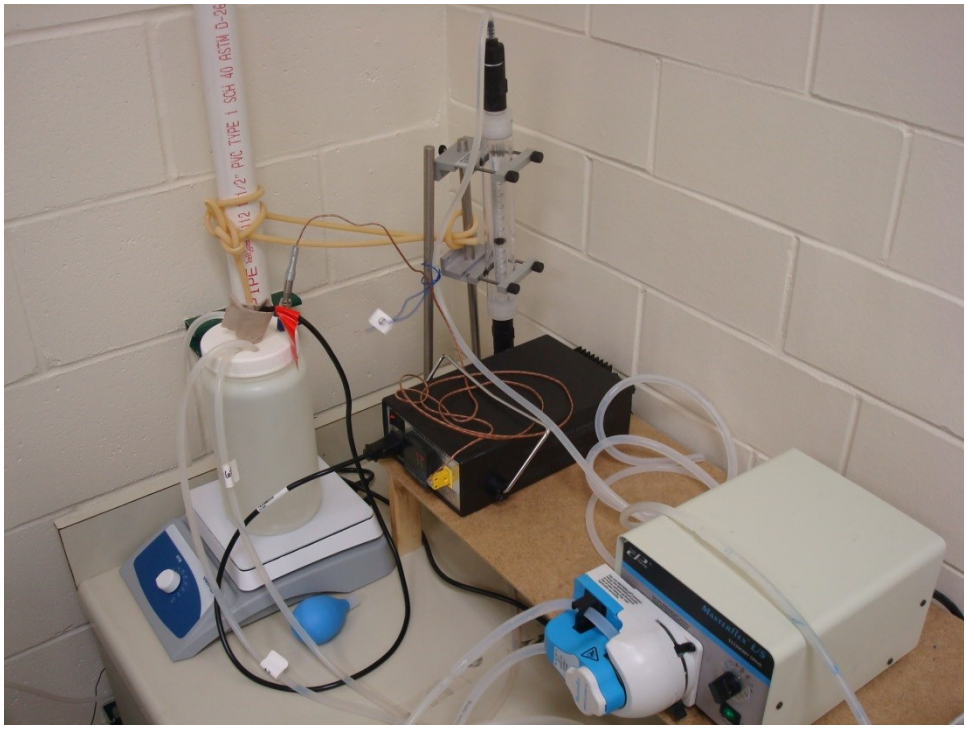

Figure 2.3. Pumps, flow meter, and temperature controlling systems for the flowing immersion tests.

Figure 2.4. Potentiostat, Electrochemical Multiplexer, and software for EIS measurement.

The stationary immersion tests were also conducted in order to compare with flowing immersions to demonstrate the influence of flowing fluids on the degradation of organic coatings. A traditional three electrode stationary setup was an O-ring glass electrochemical cell as shown in Figure 2.5 and Figure 2.6. The 3 cm diameter O-ring glass tube with silicon joint was clamped onto the test panel. The testing area of each coating sample is 7.07 cm^2. A cardboard was placed on the rear side of the panel to insulate the substrate from the clamp. A saturated calomel electrode was employed as the reference electrode; the steel panel and a platinum mesh were worked as the working and counter electrode, respectively.

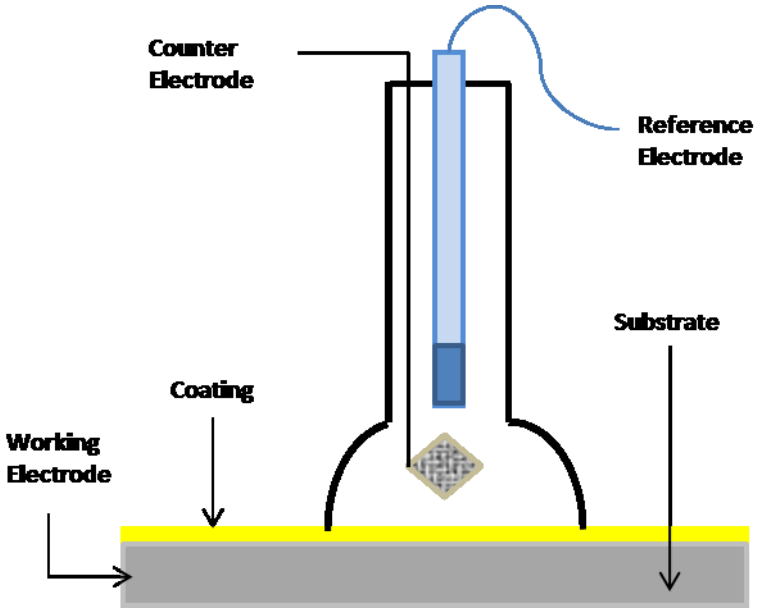

Figure 2.5. Schematic diagram of EIS cell under stationary immersion [2, 19].

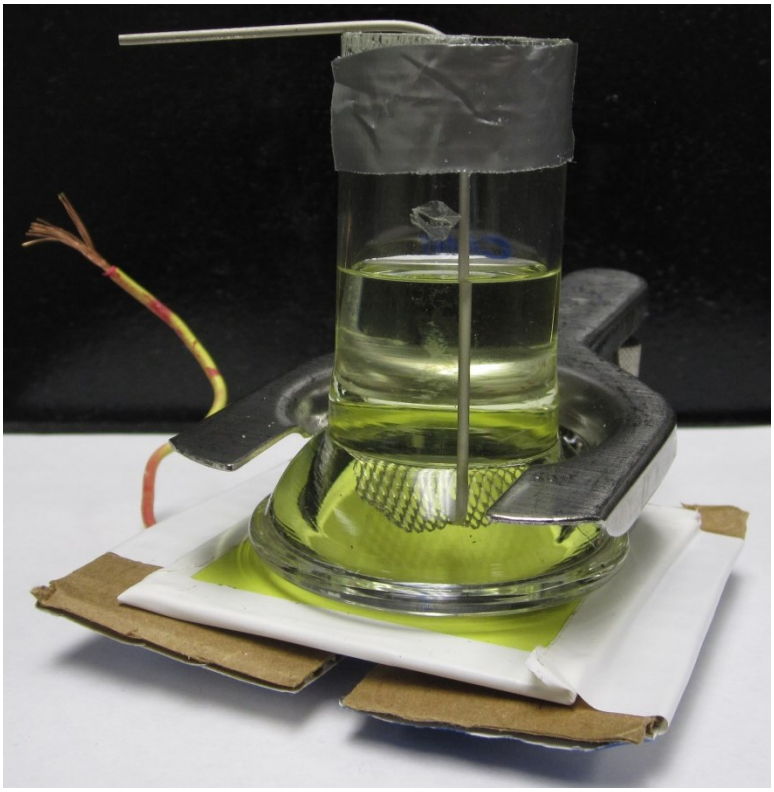

Figure 2.6. A picture of the stationary immersion and EIS setups.

2.2.3. Topography Characterization

Coating thickness and gloss were measured using an Elcometer coating thickness gauge and a NovoTrio statistical glossmeter before and after the immersion, respectively. The average thickness of dry coatings is 48 ± 5 μm in the experiment. An Axiovent 40 MAT (Focus Precision Instrument) was used for optical microscopy test. All images were collected over a magnification of 10× and 20×, depending on the features present on a given sample. The Atomic Force Microscope (AFM) observation was performed using a Nanoscope IIIa (Digital Instruments). All images were obtained in air and collected over a range of scan sizes, which were 100, 50, and 5 μm images each time. The optical microscopy and AFM can closely examine the topography of the coating samples. We focus on the visualization and discussion of the topographical changes of the coating occurred during the degradation.

2.3. Results and Discussion

2.3.1. EIS Results

To characterize the barrier properties of organic coatings, EIS data were collected for coating samples immersed in flowing and stationary DI water. Since all coating samples behave similarly under the same experimental condition, we present results for one representative sample for each flow rate. As shown in Figure 2.7 (a) for stationary immersion, the impedance modulus |Z| is plotted as a function of the frequency in EIS tests as well as the immersion time. Similar figures for samples immersed in flowing DI water at flow rates of Q=3.683 cm^3/s and Q=5.233 cm^3/s are presented in Figure 2.7 (b) and (c), respectively.

For all flow rates, the impedance modulus decreased with the immersion time, showing a loss of protective properties of the coatings. Due to the good quality of the coating samples which have no pinholes or air bubbles, the decrease of impedance modulus mainly indicated water uptake into the coating layer. The non-linear behavior of the impedance modulus at higher frequencies could be the response of DI water contributing to EIS spectra, since the solution resistance may affect the Bode plot of EIS. Cottis and Turgoose mentioned in Chapter 4 of the book "Electrochemical Impedance and Noise" [26] that if the solution resistance is very small the impedance modulus linearly decreases as the frequency increases at high frequencies of the Bode plot; however, if the solution resistance is large and not negligible (e.g. DI water), non-linear behavior is observed at high frequencies. (Please refer to Fig. 4.3 on page 37 of the Refs. [26]).

We also measured the electrochemical impedance of DI water itself by EIS method using a three-electrode cell. Platinum meshes were used as working and counter electrode. A saturated calomel electrode was used as the reference electrode and placed in the middle between the working and the counter electrode. The range of the measured impedance modulus was from 10^3 to 10^5 Ω. Hence the DI water is believed to have a high resistance which is not negligible [27]. In the afore-mentioned measurement, the modulus is found to be independent on the frequency at mid-to-high frequencies. In addition, the non-linear behavior at high frequencies of EIS spectra is also observed in literature for other working fluids, e.g. Refs [3, 28, 29].

The change of phase angle as a function of frequency for coating samples immersed under different flow rates are shown in Figure 2.8. The magnitude of phase

angle decreases at low frequencies as the immersion time increases. The decrease of the phase angle indicates the barrier property of the coating is reduced since water absorption leads to the development of penetrating paths within the coating.

The impedance modulus at low frequency serves as a strong indicator of the corrosion resistance of coating samples [30]. To illustrate the change in the coating's barrier property over time, a plot of the relative low-frequency (0.01 Hz) impedance modulus as a function of time is shown in Figure 2.9. The relative low-frequency impedance modulus is obtained by normalizing the low-frequency impedance modulus with the modulus at initial immersion. The decrease of relative low-frequency impedance modulus is substantial at the early stage of immersion followed by a relatively slower decrease. The decrease is more pronounced for flowing DI water than stationary immersion. Moreover, higher flow rates of the DI water further accelerates the decrease of the low-frequency impedance modulus. The high decrease rate reveals the flowing fluid enhances the water permeation into the coating metal interface, thus the process of organic coating degradation is accelerated by the flowing fluids. Similar behavior of the barrier properties (reflected via low-frequency impedance modulus) of the coatings was reported by Wang and Bierwagen for coating samples immersed in NaCl solution with a variety of flow rates [23].

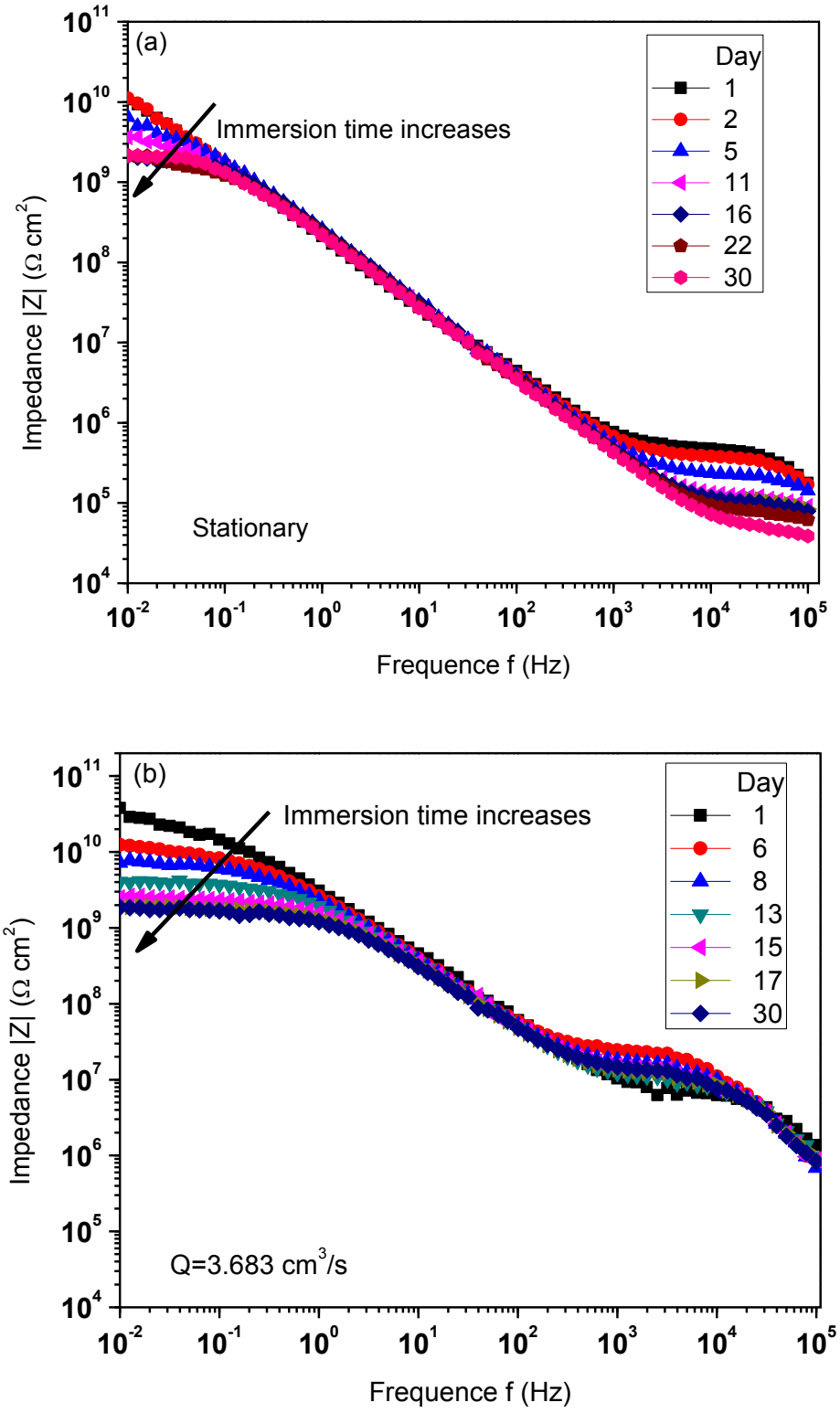

Figure 2.7. Impedance modulus as a function of frequency for coating samples immersed in DI water with flow rates (a) Q=0 (stationary), (b) Q=3.683 cm^3/s, and (c) Q=5.233 cm^3/s.

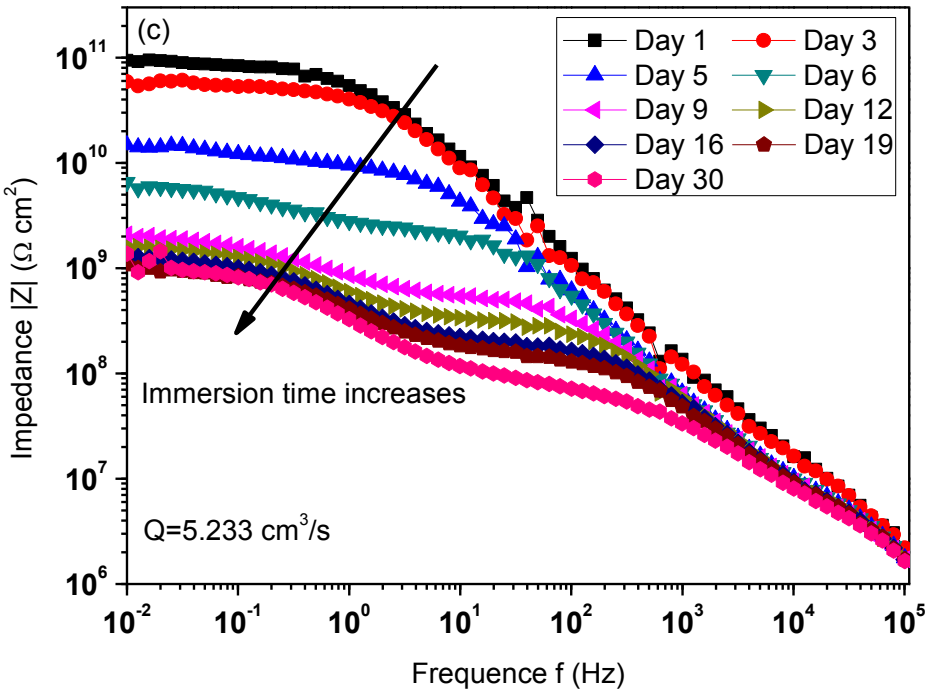

Figure 2.7. Impedance modulus as a function of frequency for coating samples immersed in DI water with flow rates (a) Q=0 (stationary), (b) Q=3.683 cm^3/s, and (c) Q=5.233 cm^3/s, (continued).

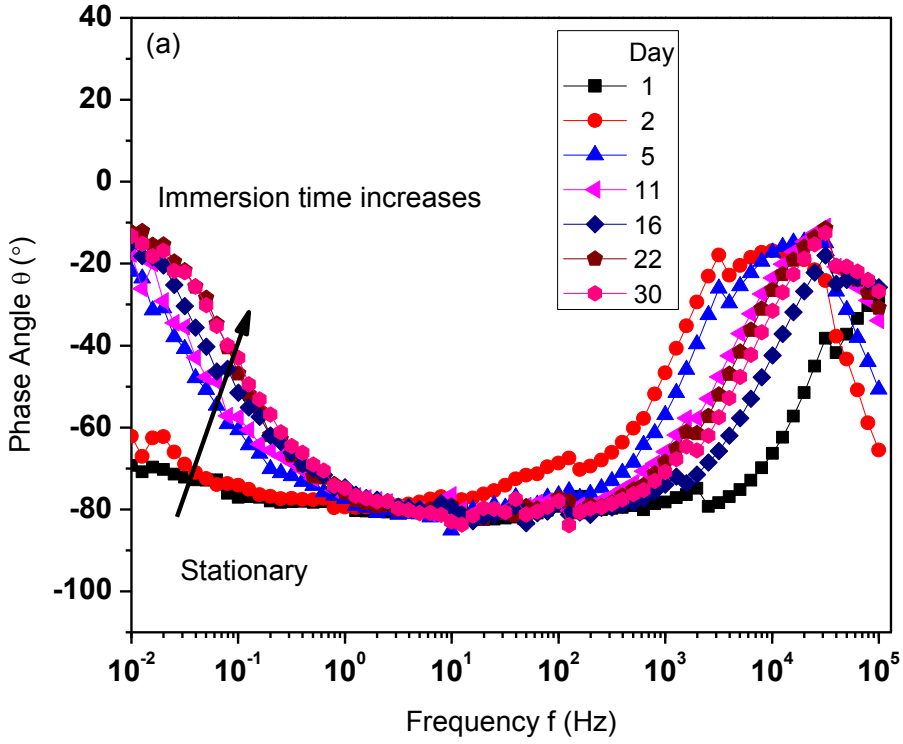

Figure 2.8. Phase angle as a function of frequency for coating samples immersed in DI water with flow rates (a) Q=0 (stationary), (b) Q=3.683 cm^3/s, and (c) Q=5.233 cm^3/s.

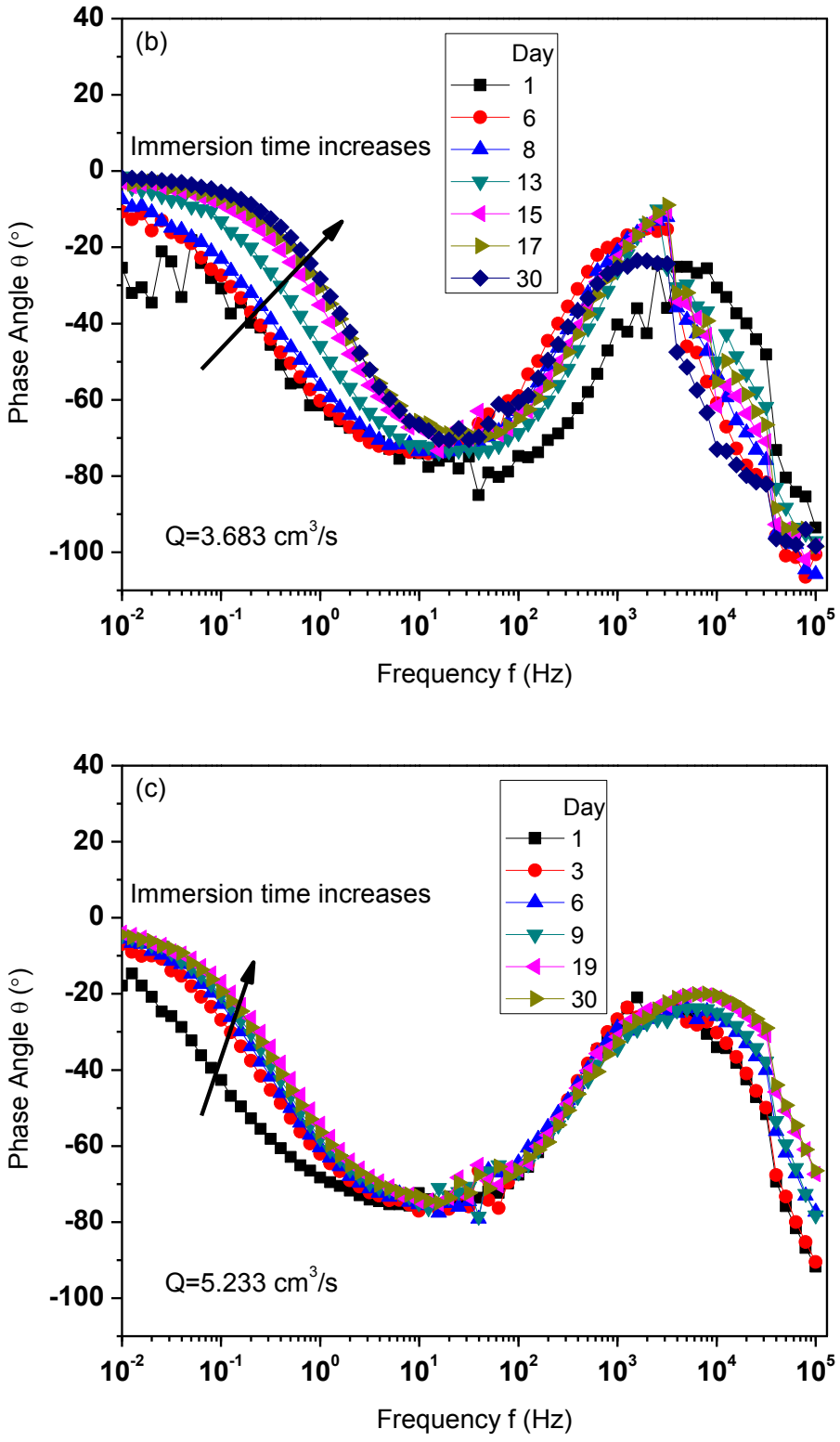

Figure 2.8. Phase angle as a function of frequency for coating samples immersed in DI water with flow rates (a) Q=0 (stationary), (b) Q=3.683 cm^3/s, and (c) Q=5.233 cm^3/s, (continued).

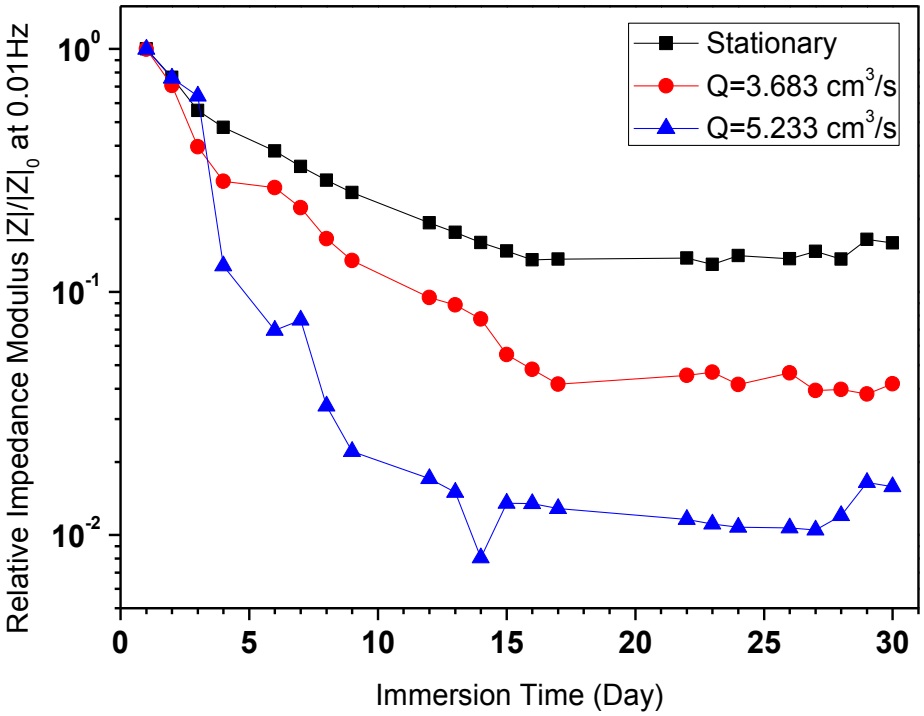

Figure 2.9. Relative impedance modulus as a function of immersion time for coating samples immersed in DI water with flow rates Q=0 (stationary), 3.683, and 5.233 cm^3/s.

2.3.2. Equivalent Circuit Modeling

An equivalent circuit model as shown in Figure 2.10 has been used to analyze the physical behavior of coatings as they are degrading. In this study, software Zview was employed to fit model elements (i.e. solution resistance R_s, coating film resistance R_c, and constant phase element CPE) with the EIS spectra [31]. A constant phase element (CPE) is used in the circuit to take into consideration the non-ideal capacitance behavior of the coating. Mathematically, a CPE impedance (Z_{CPE}) is given by [8],

$$Z_{CPE} = \frac{(j\omega)^{-\alpha}}{Y} \qquad (2\text{-}1)$$

where ω is the angular frequency; Y and α are constants, which stand for the coating capacitance and the exponent of the constant phase element, respectively. Generally, 0 <

$\alpha < 1$; when $\alpha = 1$ and $Y = C$, the CPE behaves like an ideal capacitor with capacitance C; when $\alpha = 0$, a resistance is represented. In this model, CPE element (represented for coating capacitance) is in parallel with the coating resistance (R_c). The solution resistance (R_s) is also included to consider the contribution of DI water to the overall impedance. The coating capacitance (C_c) can be calculated using the following expression:

$$C_c = Y^{1/\alpha}\left(\frac{1}{R_s} + \frac{1}{R_c}\right)^{(\alpha-1)/\alpha} \qquad (2\text{-}2)$$

where Y, α, R_s, and R_c are modeling elements for the equivalent circuit presented in Figure 2.10.

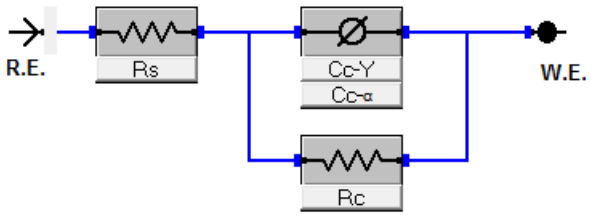

Figure 2.10. Equivalent circuit model used for the impedance analysis of coating samples immersed in DI water. R_s is solution resistance; C_c is coating capacitance; R_c is coating resistance [31].

Figure 2.11 shows the relative values of the coating capacitance (C_c), the CPE phase element (α), and the coating resistance (R_c) as a function of immersion time under flowing and stationary DI water immersion. The relative values were obtained by normalizing the element values with those at the initial immersion. The values for impedance modulus |Z|, C_c, α, and R_c at the initial immersion are listed in Table 2.1. In coating study, it is impossible to perform different acceleration tests on the same sample. Hence, in sample preparations we tried to spray the coating substrate in exactly the same

approach at the same time to ensure those samples to have approximately very similar properties. In this work, we have chosen to analyze a group of samples with the closet initial conditions. Thus, the initial values for individual parameters in different immersion tests are at the same order of magnitude with slight deviations from each other (as shown in Table 2.1).

We observe an exponential increase of the coating capacitance (C_c) for the larger flow rate; while for the stationary and lower flow rate immersion C_c increases slowly and gradually approaches to a plateau. The constant phase element exponent (α) decreases during the immersion, more with the decrease for larger flow rates. The decrease in α implies the organic coating has no longer exhibited as an ideal capacitor after 30 days of flowing immersion [8, 20]. For example, the absolute value of α dropped from 0.9238 to 0.3838 for coatings immersed in the flowing DI water with flow rate of Q=5.233 cm^3/s. The coating resistance (R_c) shows a rapid decrease initially and then maintains relatively constant during the immersion period for all cases. A larger flow rate caused a more substantial decrease for R_c.

Table 2.1. Initial values of parameters for coating samples immersed in DI water.

Parameters	**Stationary**	**Q=3.683 cm^3/s**	**Q=5.233 cm^3/s**
$\|Z\|$ ($\Omega\ cm^2$)	1.56×10^{10}	3.80×10^{10}	8.44×10^{10}
C_c (F/cm^2)	2.86×10^{-9}	3.14×10^{-9}	5.73×10^{-9}
α	0.9458	0.9128	0.9238
R_c ($\Omega\ cm^2$)	1.09×10^{9}	1.86×10^{9}	5.46×10^{9}

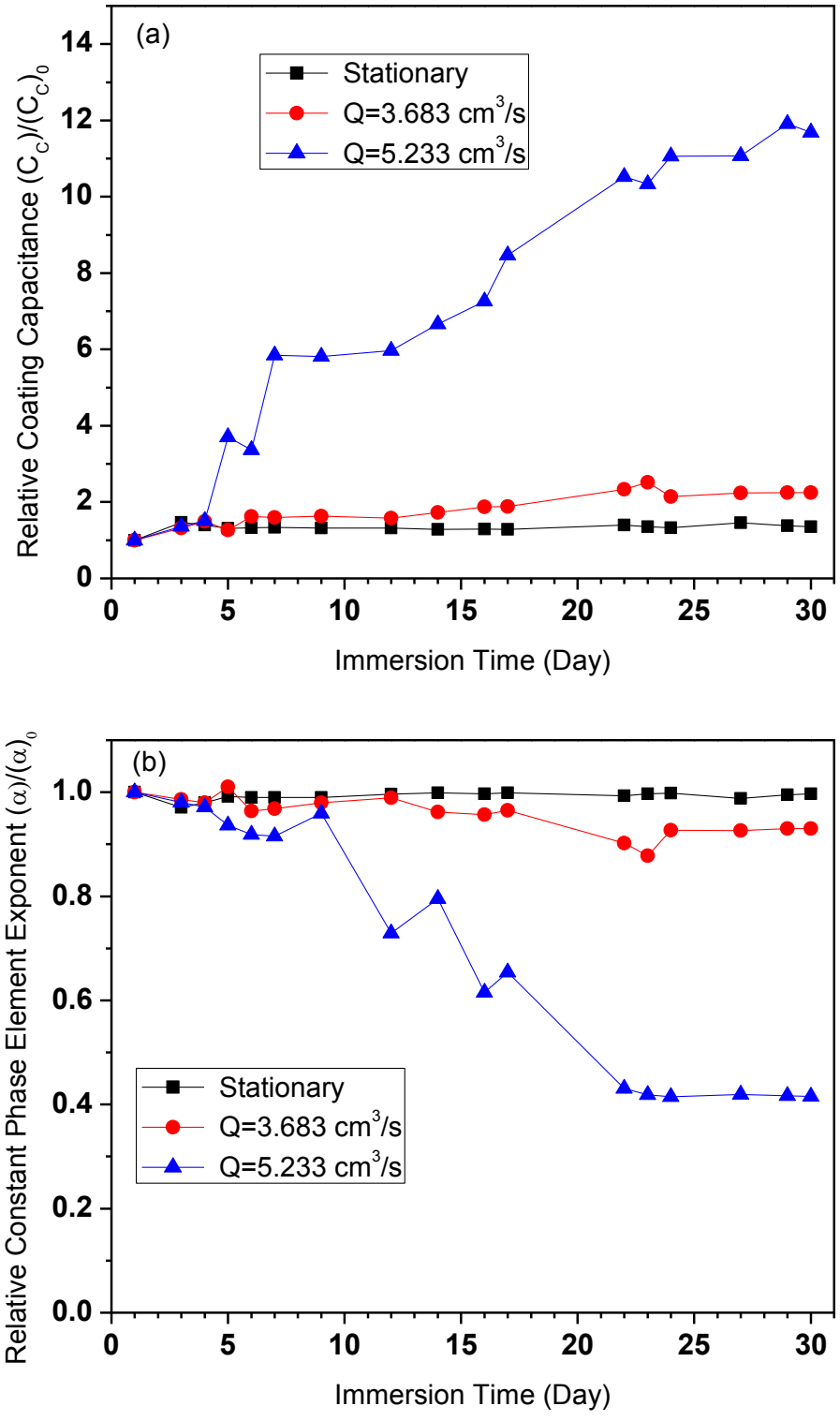

Figure 2.11. Equivalent circuit model elements as a function of immersion time for coating samples immersed in DI water with flow rates Q=0 (stationary), 3.683, and 5.233 cm^3/s. (a) Coating capacitance (C_c), (b) CPE element exponent (α), and (c) Coating resistance (R_c).

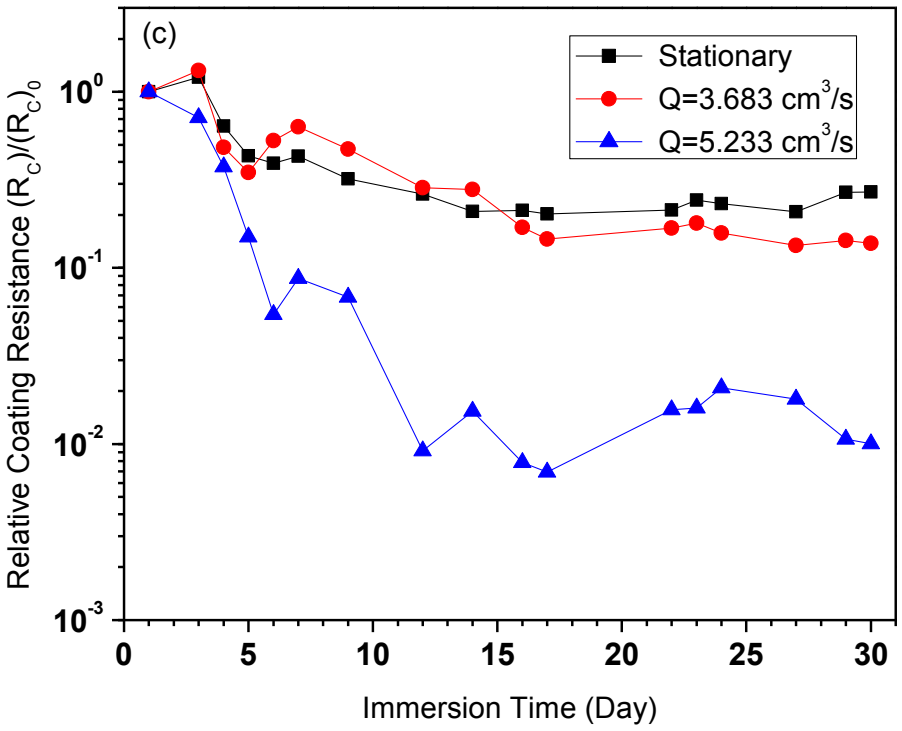

Figure 2.11. Equivalent circuit model elements as a function of immersion time for coating samples immersed in DI water with flow rates Q=0 (stationary), 3.683, and 5.233 cm^3/s. (a) Coating capacitance (C_c), (b) CPE element exponent (α), and (c) Coating resistance (R_c), (continued).

The increase of coating capacitance and decrease of resistance during immersion implies coating degradation occurs. An ideal capacitance behavior is obtained for excellent coatings [3]. When a substrate is exposed to an aggressive environment, development for a resistive behavior is employed to indicate that the degradation has occurred [3]. The capacitance evolution is usually related to the penetration of water, oxygen, and ions into the coating, and generally, its value is expected to increase with the immersion time. Water permeation results in the increase of the relative permittivity of the entire coating system and attenuation of the barrier property of organic coatings. The

behavior of the equivalent circuit elements in Figure 2.11 shows that the coatings immersed in DI water flowing with a higher flow rate tends to experience more severe penetration of water, fluid shear abrasion, and attenuation of coatings barrier properties. The results are qualitatively in agreement with the findings by Wang and Bierwagen [23] although a different working fluid was employed.

2.3.3. Topography Results

The change of the thickness of the organic coatings immersed in DI water is shown in Figure 2.12. The coating thickness increased significantly after immersion in the flowing DI water, while it maintained almost the same in stationary immersion. This is because blisters (which can be seen by naked eyes) generated on the coating surface after the immersion in flowing DI water. However, there was no obvious blistering on the coating surface after stationary immersion. It indicated that the flowing fluid caused more substantial surface changes on the coating.

The gloss of the coating surface was evaluated to quantify the roughness on the coating surface before and after immersion in DI water. Gloss reflects the smoothness of the surface. A mirror-like surface has a high gloss value, while a rough surface shows a lower one. The values obtained from the glossmeter indicate the percentage of the light reflection on the coating surface with respect to that on a black glass standard at three different grazing angles: 20˚, 60˚, and 85˚. The gloss measurements of the coatings are listed in Table 2.2. For all three grazing angles, the gloss values were reduced after the immersion which implied that the surface became rougher due to blistering. The decrease in the gloss value is much more pronounced for coatings immersed in the flowing DI water. It demonstrates that more blistering has taken place for those coating samples.

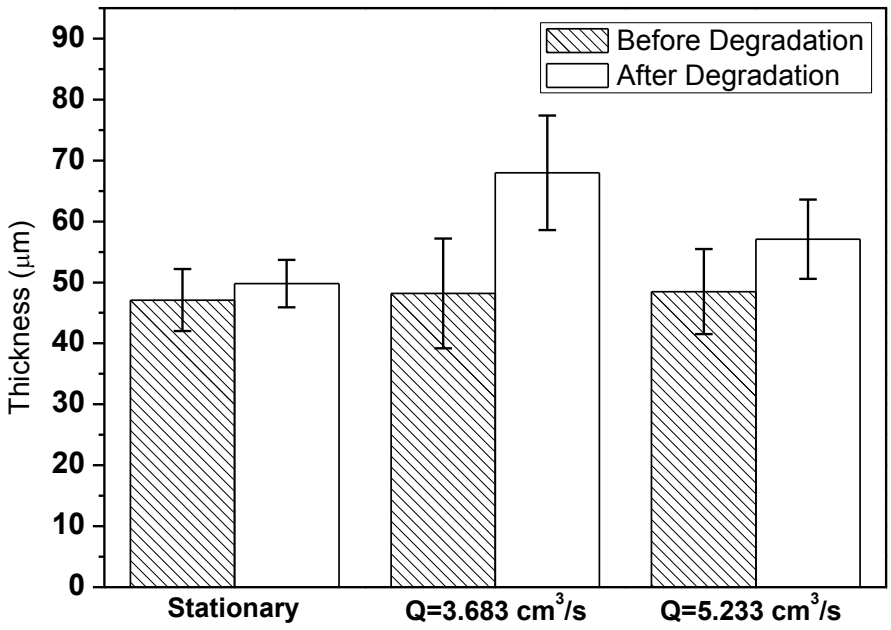

Figure 2.12. Thickness of coatings samples immersed in DI water with flow rates Q=0 (stationary), 3.683, and 5.233 cm^3/s.

Table 2.2. Gloss measurements for coating samples immersed in DI water with flow rates Q=0 (stationary), 3.683, and 5.233 cm^3/s.

Immersion	**Before Immersion**			**After Immersion**		
Condition	**20˚**	**60˚**	**85˚**	**20˚**	**60˚**	**85˚**
Stationary	11.9 ± 1.7	43.0 ± 2.8	45.9 ± 2.9	9.7 ± 1.0	37.6 ± 1.2	42.0 ± 2.6
Q=3.683 cm^3/s	19.3 ± 4.7	45.9 ± 8.4	29.1 ± 7.5	5.4 ± 3.5	18.5 ± 9.3	13.2 ± 7.1
Q=5.233 cm^3/s	18.5 ± 5.3	57.3 ± 4.9	55.4 ± 4.5	8.3 ± 0.9	30.4 ± 0.8	35.7 ± 3.8

The optical microscopy images of the coating surface are presented in Figure 2.13 for the coating before and after immersion in DI water. The surface was smooth before immersion. Under stationary immersion, DI water contributed little to modify the coating surface. However, after the immersion in flowing DI water, spherical protuberances

appeared on the coating surface. These protuberances could be the blisters connecting with each other. These images can verify the gloss measurement results that flowing condition contributed more to increase the surface roughness. The blistering also resulted in the increasing coating thickness as well as the decreasing gloss.

The topography change measured by AFM was in good agreement with the optical microscopy. As shown in Figure 2.14 (a), the surface was flat before immersion with a small number of tips and holes. After 30 days immersion in the flowing DI water, blisters formed on the coating surface, as shown in Figure 2.14 (b). The left and right corners of this image are out of the AFM measurement range due to the large height. It indicated that blistering on the coating surface was rather severe under the flowing condition. After 30 days immersion in the stationary DI water, there are some protuberances on the coating surface, as shown in Figure 2.14 (c). The AFM device was equipped with topographic analysis software capable of measuring both values of square roughness (RMS) and average roughness (Ra). These roughness values were all obtained from 100 μm images of the coating surface before and after the immersion, and the average values are listed in Table 2.3. It is clear that the roughness of the coating surface has increased after the degradation. Flowing condition contributed more to increase the surface roughness due to blistering.

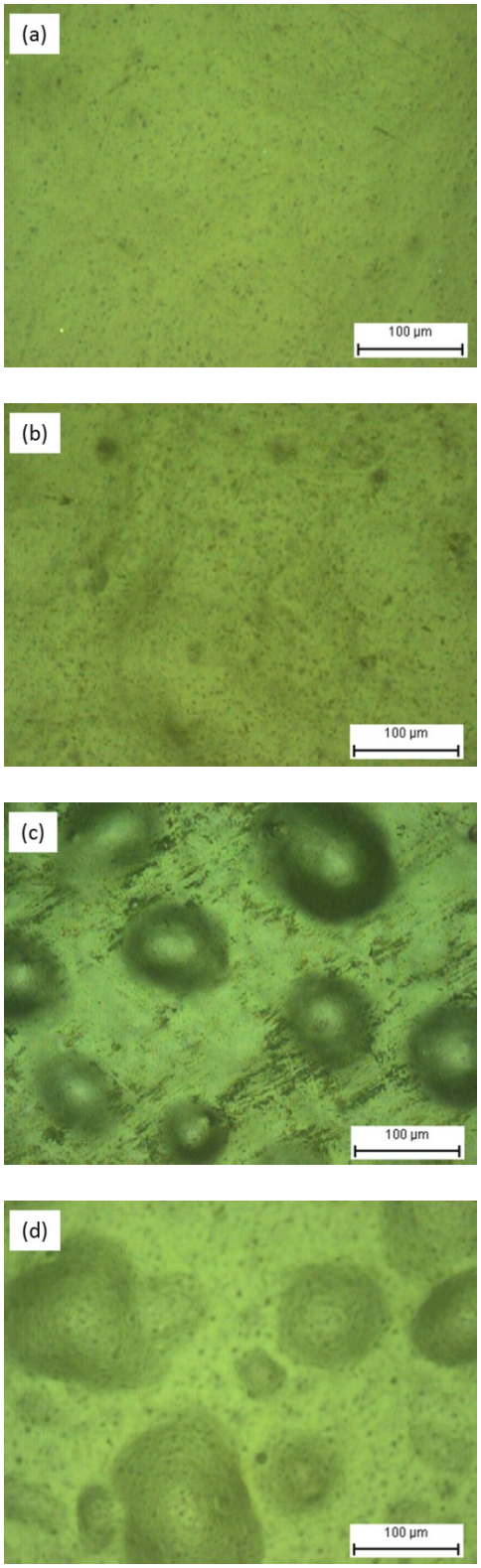

Figure 2.13. Optical microscopy images of the coating surface before and after DI water immersion. (a) Before immersion, (b) after stationary immersion, (c) after immersion of flow rate Q=3.683 cm^3/s, and (d) after immersion of flow rate Q=5.233 cm^3/s.

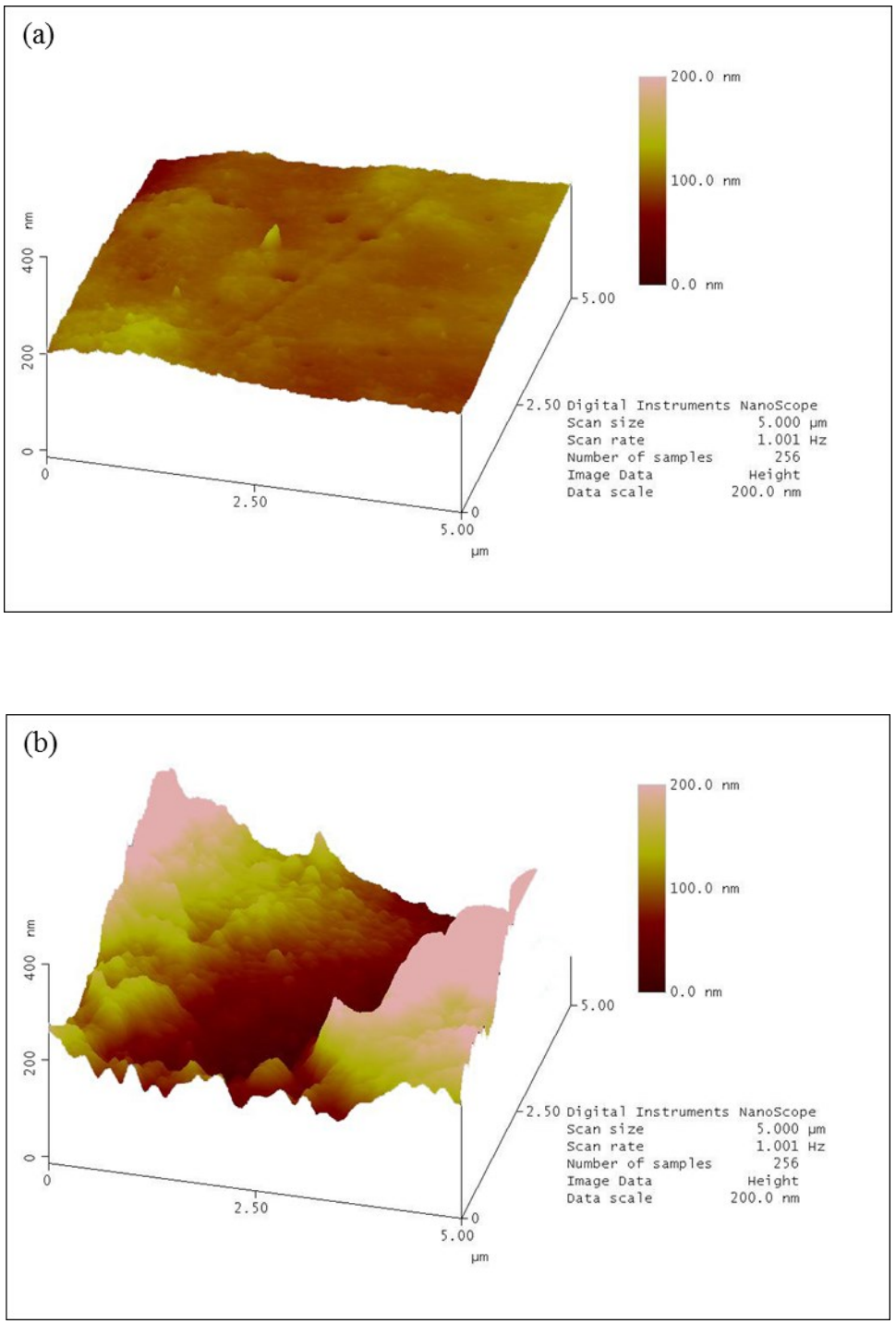

Figure 2.14. AFM images for the coating surface topography before and after degradation. (a) Before degradation, (b) after degradation with flow rate Q=3.683 cm^3/s, and (c) after degradation under DI water stationary immersion.

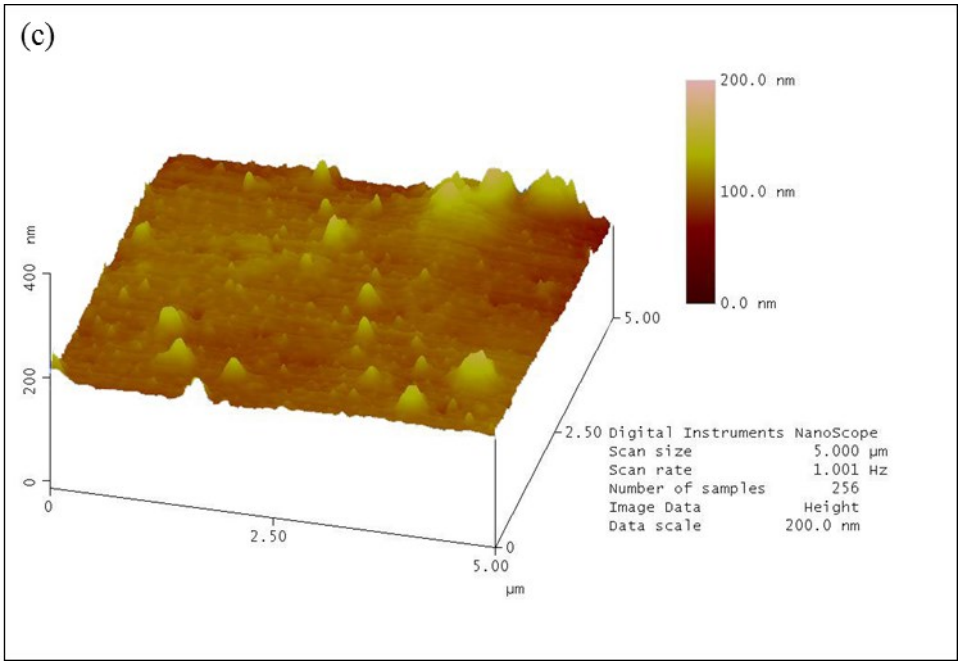

Figure 2.14. AFM images for the coating surface topography before and after degradation. (a) Before degradation, (b) after degradation with flow rate Q=3.683 cm^3/s, and (c) after degradation under DI water stationary immersion, (continued).

Table 2.3. Roughness of coating samples before degradation and after degradation in DI water with flow rates Q=0 (stationary), 3.683, and 5.233 cm^3/s.

Parameters	**Before Degradation**	**After Degradation**		
(nm)		**Stationary**	**Q=3.683 cm^3/s**	**Q=5.233 cm^3/s**
RMS	118.15	124.52	147.58	209.98
Ra	92.26	96.67	102.61	156.24

Blistering is a common phenomenon in coating degradation representing the initial physical change due to the alternating environment [32]. The formation of blistering is usually the first visible indication of insufficient protection by organic coating against corrosion [33]. Blistering may be caused by the permeation of water to coating metal interface due to osmotic pressure [34]. Our study shows that the flowing

fluid over the coating surface promoted blistering to a more severe level. We believe that soluble species (e.g. polar plasticizers and/or the non-cured polymer chain) may be diffusing out of the coating as water and ions percolate into the coating since mass loss of the coating and conductivity changes of the solution during the coating immersion has been reported in literature [35, 36]. Blistering promoted by flowing fluid may be explained by the fact that flowing DI water helps to maintain a large concentration difference of soluble species released from coatings between the coating layers and the bulk solution by constantly refreshing the fluid on the coating surface. Hence the osmotic pressure is maintained throughout the immersion which promotes the generation of blisters. On the contrary, for coatings in the stationary immersion, the ion concentration difference decreases due to the diffusion so that the osmotic effect diminishes as equilibrium is achieved. However, other factors may also influence the blistering of coatings in flowing DI water, such as the fluid shear exerted on the coating surface.

2.4. Conclusions

The study in this chapter evaluated via EIS the electrochemical behavior of the organic coating immersed in DI water with flow rate Q=0, 3.683, and 5.233 cm^3/s. The influence of flow rate on the coating degradation was demonstrated by the results of EIS measurement, equivalent circuit modeling, and topography of the coating surface.

The impedance spectra of coatings decreased with the immersion time and the decrease was more substantial for flowing fluid at higher flow rate disregard of the fluid type, which revealed flowing fluid accelerated the water penetration into the coating layer. Equivalent circuit modeling of the EIS data showed higher coating capacitance and lower coating resistance under flowing immersion. The topography of the coating surface

changed more substantially for higher flow rate due to its enhancement of blister formation. Thus flowing fluids bring much greater deterioration to the coatings than the corresponding stationary condition. And this deterioration is more aggressive under higher flow rate. Therefore, we conclude that the flowing DI water degrades the barrier properties of organic coatings more substantially. And the flowing fluid over the coating surface could be used as an effective acceleration method.

2.5. References

[1] G.P. Bierwagen, The science of durability of organic coatings: a foreword, *Progress in Organic Coatings*, **15** (1987) 179-195.

[2] G.P. Bierwagen, Reflections on corrosion control by organic coatings, *Progress in Organic Coatings*, **28** (1996) 43-48.

[3] Q.L. Thu, G.P. Bierwagen, S. Touzain, EIS and ENM measurements for three different organic coatings on aluminum, *Progress in Organic Coatings*, **42** (2001) 179-187.

[4] X. Jiang, Y. Zheng, W. Ke, Effect of flow velocity and entrained sand on inhibition performances of two inhibitors for CO_2 corrosion of N80 steel in 3% NaCl solution, *Corrosion Science*, **47** (2005) 2636-2658.

[5] A.S. Shehata, S.A. Nosier, G.H. Sedahmed, The role of mass transfer in the flow-induced corrosion of equipments employing decaying swirl flow, *Chemical Engineering and Processing*, **41** (2002) 659-666.

[6] J.A. Wharton, R.J.K. Wood, Influence of flow conditions on the corrosion of AISI 304L stainless steel, *Wear*, **256** (2004) 525-536.

[7] J. Villarreal, D. Laverde, C. Fuentes, Carbon-steel corrosion in multiphase slug flow and CO_2, *Corrosion Science*, **48** (2006) 2363-2379.

[8] L. Niu, Y. Cheng, Synergistic effects of fluid flow and sand particles on erosoin-corrosion of aluminum in ethylene glycol-water solutions, *Wear*, **265** (2008) 367-374.

[9] D. Zheng, D. Che, Y. Liu, Experimental investigation on gas-liquid two-phase slug flow enhanced carbon dioxide corrosion in vertical upward pipeline, *Corrosion Science*, **50** (2008) 3005-3020.

[10] L. Xu, Y. Cheng, Effect of fluid hydrodynamics on flow-assisted corrosion of aluminum alloy in ethylene glycol-water solution studied by a microelectrode technique, *Corrosion Science*, **51** (2009) 2330-2335.

[11] Y.P. Purandare, M.M. Stack, P.E. Hovsepian, Velocity effects on erosion-corrosion of CrN/NbN "superlattice" PVD coatings, *Surface and Coatings Technology*, **201** (2006) 361-370.

[12] E. Heitz, Mechanistically based prevention strategies of flow-induced corrosion, *Electrochimica Acta*, **41** (1996) 503-509.

[13] K. Ranjbar, Effect of flow induced corrosion and erosion on failure of a tubular heat exchanger, *Materials & Design*, **31** (2010) 613-619.

[14] J. Tu, The effect of TiN coating on erosion-corrosion resistance of α-Ti alloy in saline slurry, *Corrosion Science*, **42** (2000) 147-163.

[15] S.S. Rajahram, T.J. Harvey, R.J.K. Wood, Erosion-corrosion resistance of engineering materials in various test conditions, *Wear*, **267** (2009) 244-254.

[16] M. Bjordal, E. Bardal, T. Rogne, T.G. Eggen, Erosion and corrosion properties of WC coatings and duplex stainless steel in sand-containing synthetic sea water, *Wear*, **186-187** (1995) 508-514.

[17] M.M. Stack, T.M. Abd El Badia, Mapping erosion-corrosion of WC/Co-Cr based composite coatings: Particle velocity and applied potential effects, *Surface and Coatings Technology*, **201** (2006) 1335-1347.

[18] V. Barranco, S. Feliu, EIS study of the corrosion behaviour of zinc-based coatings on steel in quiescent 3% NaCl solution. Part 1: directly exposed coatings, *Corrosion Science*, **46** (2004) 2203-2220.

[19] F. Rezaei, F. Sharif, A.A. Sarabi, S.M. Kasiriha, M. Rahmaniam, E. Akbarinezhad, Evaluating water transport through high solid polyurethane coating using the EIS method, *Journal of Coatings Technology and Research*, **7** (2010) 209-217.

[20] M. Del Grosso Destreri, J. Vogelsang, L. Fedrizzi, F. Deflorian, Water up-take evaluation of new waterborne and high solid epoxy coatings. Part II: electrochemical impedance spectroscopy, *Progress in Organic Coatings*, **37** (1999) 69-81.

[21] C.S. Jeffcoate, G.P. Bierwagen, Electrochemical comparison of coating performance in flowing vs. stationary electrolyte, in: G.P. Bierwagen (Ed.) American Chemical Society Symposium Series, American Chemical Society, Washington, DC, 1998, pp. 151-160.

[22] Y. Wei, L. Zhang, W. Ke, Comparison of the degradation behaviour of fusion-bonded epoxy powder coating systems under flowing and static immersion, *Corrosion Science*, **48** (2006) 1449-1461.

[23] Y. Wang, G.P. Bierwagen, A new acceleration factor for the testing of corrosion protective coating: flow-induced coating degradation, *Journal of Coatings Technology and Research*, **6** (2009) 429-436.

[24] L. Liu, Y. Li, C. Zeng, F. Wang, Electrochemical impedance spectroscopy (EIS) studies of the corrosion of pure Fe and Cr at 600 °C under solid NaCl deposit in water vapor, *Electrochimica Acta*, **51** (2006) 4736-4743.

[25] B.R. Hinderliter, S.G. Croll, D.E. Tallman, Q. Su, G.P. Bierwagen, Interpretation of EIS data from accelerated exposure of coated metals based on modeling of coating physical properties, *Electrochimica Acta*, **51** (2006) 4505-4515.

[26] R. Cottis, S. Turgoose, Electrochemical Impedance and Noise, NACE International, Houston, 1999.

[27] J.R. Davis, Corrosion Understanding the Basics, ASM International, Materials Park Ohio, 2000.

[28] H. Hu, N. Li, J. Cheng, L. Chen, Corrosion behavior of chromium-free dacromet coating in seawater, *Journal of Alloys and Compounds*, **472** (2009) 219-224.

[29] F. Wong, R.G. Buchheit, Utilizing the structural memory effect of layered double hydroxides for sensing water uptake in organic coatings, *Progress in Organic Coatings*, **51** (2004) 91-102.

[30] G.P. Bierwagen, L. He, J. Li, L. Ellingson, D.E. Tallman, Studies of a new accelerated evaluation method for coating corrosion resistance - thermal cycling testing, *Progress in Organic Coatings*, **39** (2000) 67-78.

[31] V.F. Lvovich, Impedance spectroscopy application to electrochemical and dielectric phenomena, John Wiley & Sons, Hoboken, New Jersey, 2012.

[32] X. Yang, D.E. Tallman, G.P. Bierwagen, S.G. Croll, S. Rohlik, Blistering and degradation of polyurethane coatings under different accelerated weathering tests, *Polymer Degradation and Stability*, **77** (2002) 103-109.

[33] W. Funke, Blistering of paint films and filiform corrosion, *Progress in Organic Coatings*, **9** (1981) 29-46.

[34] J.H. Park, G.D. Lee, H. Ooshige, A. Nishikata, T. Tsuru, Monitoring of water uptake in organic coatings under cyclic wet–dry condition, *Corrosion Science*, **45** (2003) 1881-1894.

[35] A.S.L. Castela, A.M. Simões, M.G.S. Ferreira, E.I.S. evaluation of attached and free polymer films, *Progress in Organic Coatings*, **38** (2000) 1-7.

[36] N. Fredj, S. Cohendoz, S. Mallarino, X. Feaugas, S. Touzain, Evidencing antagonist effects of water uptake and leaching processes in marine organic coatings by gravimetry and EIS, *Progress in Organic Coatings*, **67** (2010) 287-295.

CHAPTER 3. FLOW ACCELERATED DEGRADATION OF CLEAR COATINGS: THE EFFECT OF FLUID SHEAR

3.1. Introduction

Various acceleration tests have been conducted by prolonged exposure to light, temperature, oxygen, moisture and condensation, mechanical stress, and environmental pollutants [1-4]. Different laboratorial studies focus on one aging factor or a combination of them in order to better understand coating degradation mechanisms and ultimately find a better way to predict the service lifetime of coatings. The sunlight, particularly UV radiation, is often adopted to accelerate coating degradation. Coatings may become loss of gloss, discoloration, chalking, and embrittlement after UV exposure. Hu et al. [5] exposed an acrylic polyurethane coating in a fluorescent UV/condensation on the condition of UV (λ=340 nm) radiation at 60 ˚C for 8 h followed by water condensation at 50 ˚C for 4 h. The yellow index and low frequency impedance showed greater coating degradation caused by UV exposure. In the study by Touzain et al. [6], the degradation of two thick organic coatings (300 μm) was accelerated by exposing to a high temperature (45 ˚C) and thermal cycles (25–85 ˚C). The high temperature enhanced diffusion processes within the coating film, increased water absorption and chain mobility, and accelerated the coating degradation. Guermazi et al. [7] studied the mechanical property of a pipe coating used for marine applications by immersing samples in synthetic sea water at different temperatures. The coating properties measured by its elastic modulus and tensile strength decrease as the temperature increases. The degradation of three coil coatings was investigated under wet conditions and different thermal treatments at different temperatures, cyclically or continuously [8, 9]. The thermal cycling produced

much greater damage to the coating system than the exposure to a constant temperature. Studies have shown that QUV chambers, salt spray exposure, or Prohesion tests can also deliver accelerated weathering which combines the influences of UV, temperature, thermal, pH, and etc. [10-12]. In addition to those afore-mentioned well-known factors, the influence of mechanical stress on coating degradation was studied. The marine epoxy coatings were evaluated under tensile, compressed, and unstressed mode [13-15]. The tensile strain brought a reorganization of polymer chains that modify the water ingress into the coating; as a result, the mechanical stress in the visco-elastic domain accelerated the coating degradation.

Recently, more attention has been paid to the coating degradation in flowing solutions. It is believed that fluid flow over organic coatings could be considered as an acceleration factor for coating degradation [16-20]. However, due to the limited number of studies on organic coating degradation in flowing environment, the degradation mechanism is still not completely understood. In this study, we focus on the influence of fluid shear on the degradation of organic coatings as well as the correspondent change in the composition of the working fluid. Some studies have reported the influence of fluid shear on flow induced metal corrosion. For example, Hussain et al. evaluated the duplex stainless steel in flowing artificial seawater with sand particles by a jet impingement apparatus [21]. The high shear stress caused the oxide film thickness of the stainless steel to decrease considerably in the high turbulence region. Barker et al. found that high shear stress promoted the preferential weld corrosion of pipeline steel [22]. The efficiency of the corrosion inhibitor for the carbon steel was also found to decrease by increasing the fluid shear [23].

The aim of the study in this chapter is to improve the understanding on flow accelerated organic coating degradation, with a focus on the influence of the fluid shear. We hypothesize that in addition to the accelerated diffusion of ions into the coating [18-20], the fluid flow on the coating surface promotes the migration of coating material from inside the coating into the working fluid and the coating thickness is also reduced due to fluid shear. As described in section 3.2, measurements of the Fourier Transform Infrared Spectrometer (FTIR) and solution conductivity were carried out for the working fluid after the immersion. Coating thickness was also measured. The degradation of the organic coating was characterized in line by electrochemical impedance spectroscopy (EIS) measurements. The EIS spectra were interpreted by suitable equivalent circuit models. The time evolution of coating resistance and coating capacitance was analyzed for different fluid shear. Results are analyzed in section 3.3 followed by conclusions in section 3.4.

3.2. Materials and Methods

3.2.1. Coatings and Sample Preparation

An epoxy based clear coating was chosen for evaluation, which has been widely used as a base coat in marine coatings [24-28]. We purposefully chose an epoxy coating instead of a pigmented marine coating since the composition of the epoxy coating is known, which provides convenience for the analysis of the working fluid composition if the coating material is released into the fluid. The epoxy coating was composed of EPON Resin 828 (Hexion Specialty Chemicals) as the base component, and EPIKURE 3164 as curing agent (AHEW 256, Hexion Specialty Chemicals). The weight ratio of curing agent

to EPON Resin 828 is 1.36. The coating sample preparation procedure is the same as described in Chapter 2.

3.2.2. Experimental Setup and EIS Measurement

In this study, an epoxy coating was exposed to laminar flow as well as stationary immersion. The laminar flow was pressure driven and confined in a flow channel. The flow channel was modified based on our previous study [18, 19] as shown in Figure 3.1. The channel was milled from a thick plastic sheet (Figure 3.1 a); the top channel wall (Figure 3.1 b) was glued to the base to complete the flow channel (Figure 3.1 c). Coating samples were attached to the inserting moduli as shown in Figure 3.1 (d) which can be inserted into the flow channel (Figure 3.1 c). Platinum meshes were attached on the top channel acting either as counter or reference electrodes. The channel's cross sectional area is 6.46 cm^2. The schematic of the experimental setup is shown in Figure 3.2. The picture of the flow channel and EIS setups in the experiment is shown in Figure 3.3. The working fluid, 3.5 wt% NaCl solution, was pumped from the fluid reservoir to the flow channel, and then recycled back to the reservoir. In our experiments, the flow rate was maintained at 0, 2.233, 3.683, and 5.233 cm^3/s, corresponding to mean flow velocities of 0, 0.346, 0.570, and 0.810 cm/s, respectively. The temperature was controlled at 25˚C by a water bath and a temperature controlling system, same as in Chapter 2.

The electrochemical cell for EIS measurement and EIS testing conditions are the same as described in Chapter 2. The experiments of the same flow rate were repeated using at least four coating samples.

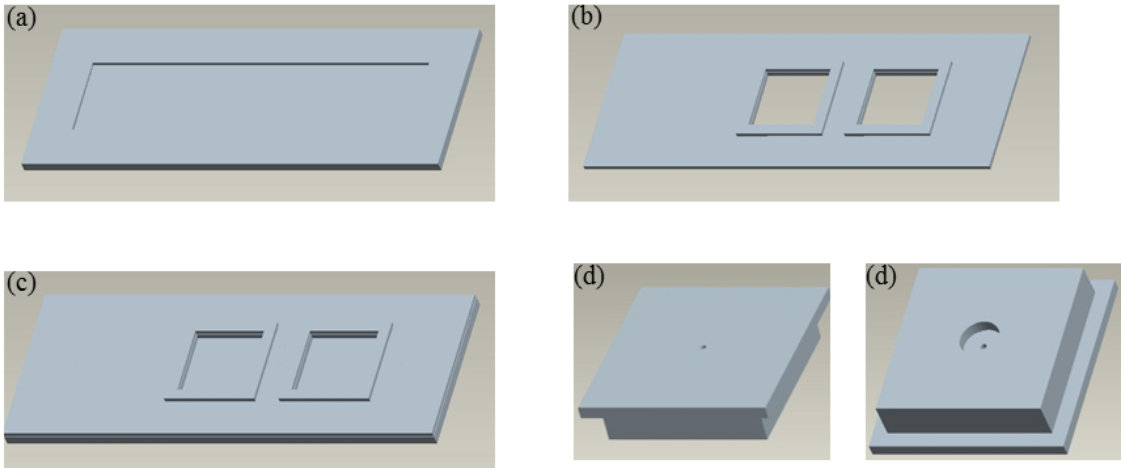

Figure 3.1. Schematic diagram of flow channel, (a) base, (b) top, (c) the whole channel, and (d) inserting modulus.

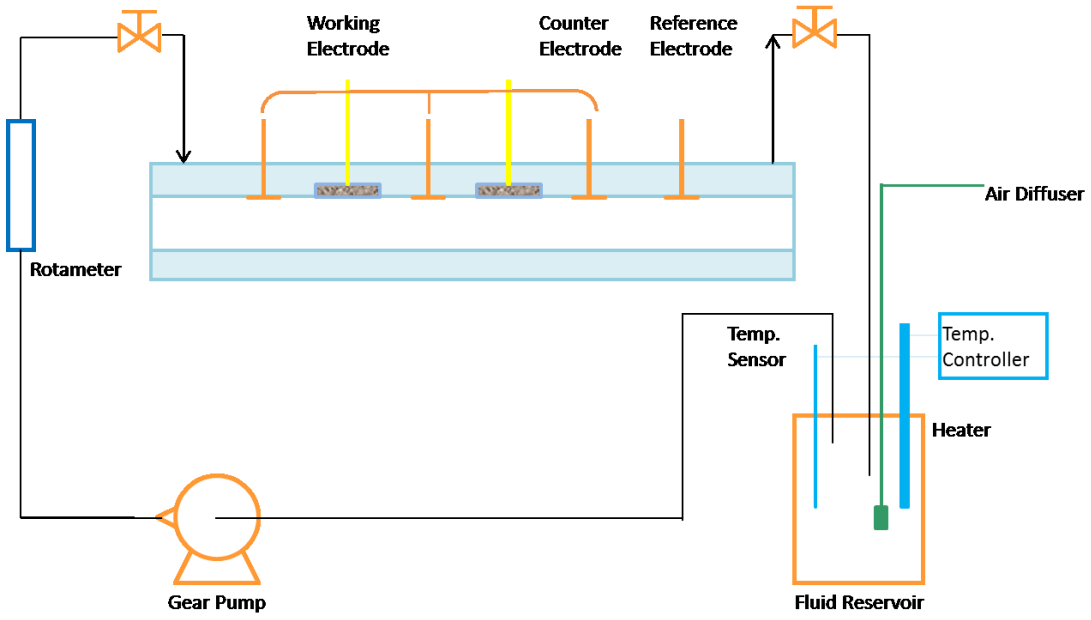

Figure 3.2. Schematic diagram of recirculating flow.

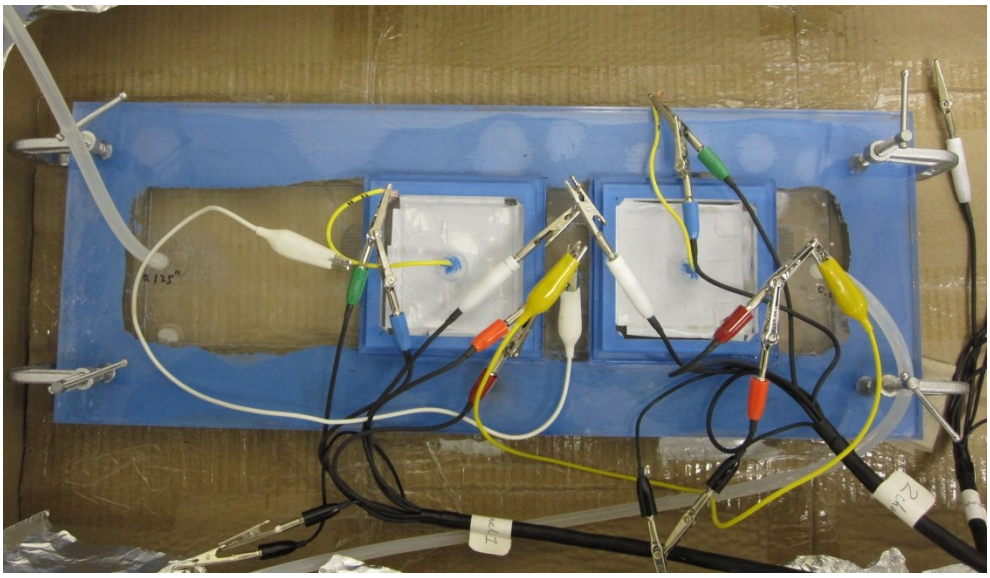

Figure 3.3. A picture of the circulating flow channel and EIS setups.

3.2.3. Thickness and FTIR Measurements

Thickness of coating samples was measured using an Elcometer 415 coating thickness gauge before and after immersion. Conductivity of working fluid was measured by ORION 4 STAR pH-Conductivity Portable (Thermo Scientific) in order to monitor properties of immersed solution during coating immersion. The samples from the working fluid after immersion were also analyzed by FTIR (Thermo Scientific Nicolet 8700). In order to obtain a good response of FTIR, the working fluid was extracted by HPLC grade methylene chloride as a solvent. The extracted liquid was concentrated by vacuum distillation in a rotary evaporator before the FTIR measurement. The FTIR spectrum was subtracted by the absorption of methylene chloride to get rid of the disturbance of the solvent. Each spectrum was achieved by performing 32 scans between 4000 cm^{-1} and 400 cm^{-1} with a resolution of 4 cm^{-1}.

3.3. Results and Discussion

3.3.1. FTIR Results

After immersion until coating fails, the working fluid (3.5 wt% NaCl solution) was characterized by FTIR measurement. The FTIR spectra are shown in Figure 3.4 for working fluid under different flow rates. The results show that the organic components in the working fluid should be hydrocarbons since the major absorption peaks appear near 3000 cm^{-1} and the range near 1460 and 1375 cm^{-1}, which accounts for C-H. The organic materials could also be epoxides since there are several small absorption peaks in the range from 1500 cm^{-1} to 1000 cm^{-1}. Table 3.1 summarized the FTIR peaks and the corresponding assignments. However, the height of the peaks cannot reflect the amount of the organic materials in the solution based on the FTIR spectra. We performed FTIR measurements for the working fluid after the stationary immersion of the samples. No substantial absorption peaks are found. Hence the curve for the stationary immersion is not included in Figure 3.4.

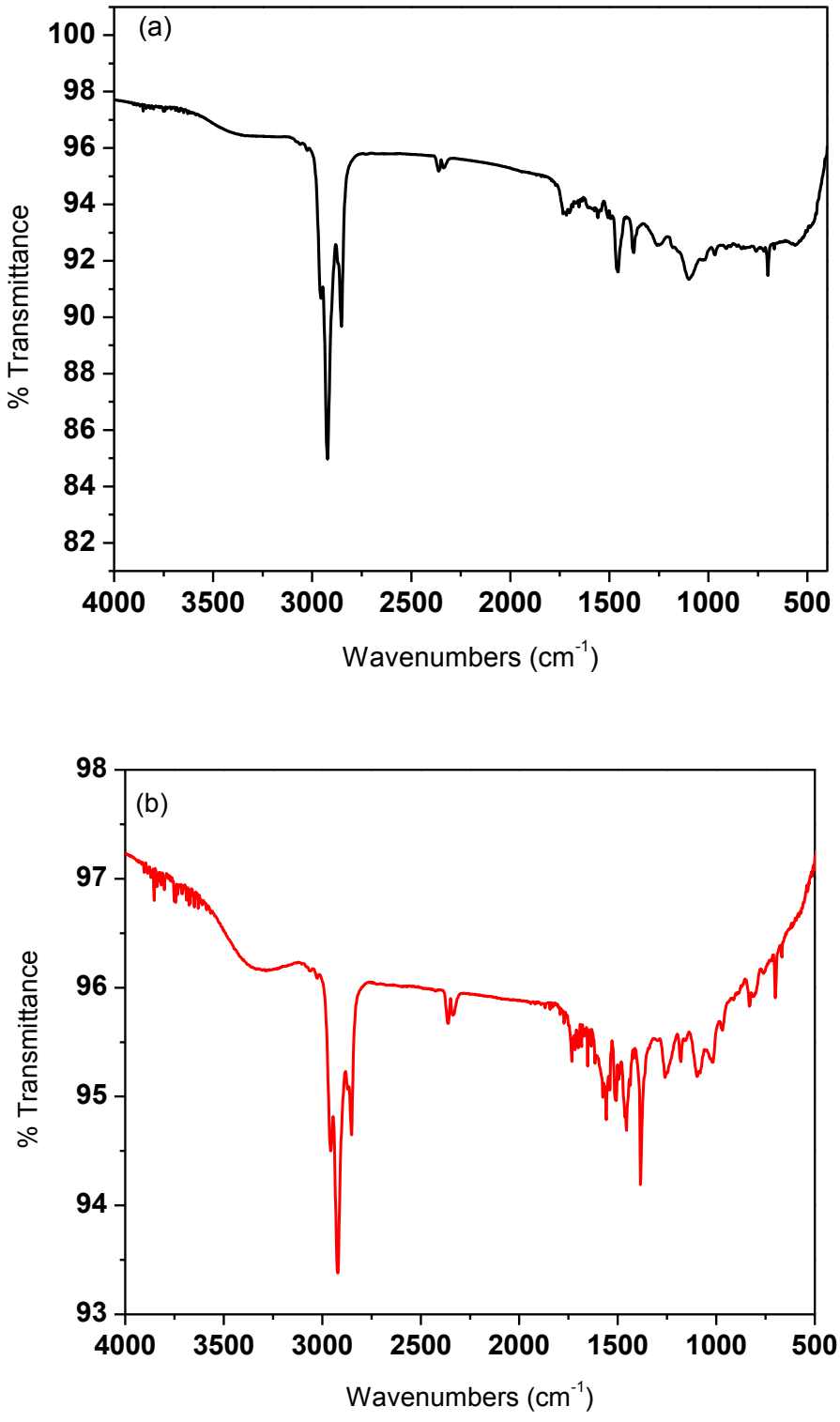

Figure 3.4. FTIR spectra of the working fluid after coating degradation for flow rates (a) Q=2.233 cm^3/s, (b) Q=3.683 cm^3/s, and (c) Q=5.233 cm^3/s.

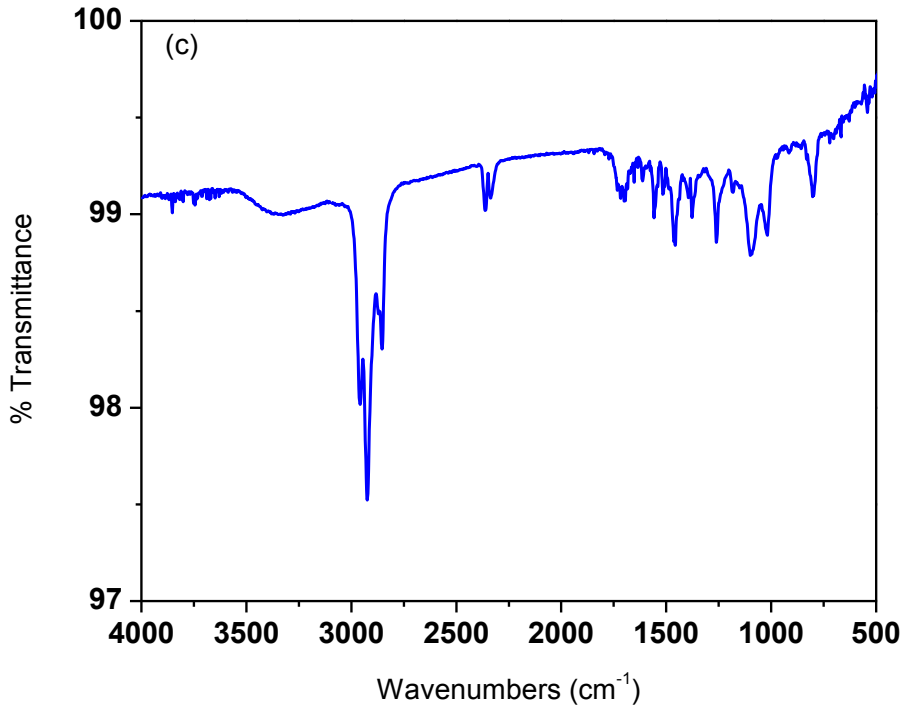

Figure 3.4. FTIR spectra of the working fluid after coating degradation for flow rates (a) Q=2.233 cm^3/s, (b) Q=3.683 cm^3/s, and (c) Q=5.233 cm^3/s, (continued).

The components of the epoxy coating, EPON Resin 828 and curing agent, were also characterized by FTIR measurements as shown in Figure 3.5. According to the Safety Data Sheets (SDS), the EPON Resin 828 is an undiluted clear difunctional bisphenol A/epichlorohydrin derived liquid epoxy resin; the curing agent 3164 is a proprietary oligomeric polyamine, with the major composition as alicyclic aliphatic polyamine, alkyletheramine, and alkylphenol. The FTIR peaks and their corresponding assignments are also listed in Table 3.1. By comparing the FTIR spectra between the working fluid and the epoxy coating, we believe that the presence of the hydrocarbons in the working fluid comes from the components of the epoxy coating for flowing conditions. However, no such conclusion can be made for samples immersed in

stationary working fluid. Hence, we believe that the fluid flow above the coating surface accelerated the transport of unreacted C-H groups from the coating to the solution.

The epoxy coating is on the degradation and flowing fluid brings the degraded products into the surrounding solutions as a result of the shear stress. The flow shear stress trends to continuously remove corrosion products or coating materials into the solutions; as a result, flowing fluid will refresh the coating surface and expose more coating materials to the aggressive environment and ultimately it will accelerate the coating degradation. High fluid velocity will increase the flow shear stress so as to increase the corrosion rate [23]. One study evaluated the degradation of photocatalytic coatings under a water flow [29]. The solution (NaCl solution or/and humic acids) was circulated parallel to the coating's surface; in the meanwhile, UV radiation was imposed to the immersed coatings. It reported that coating materials (TiO_2 nanoparticles) were released into the solution by the effect of water flow and UV exposure.

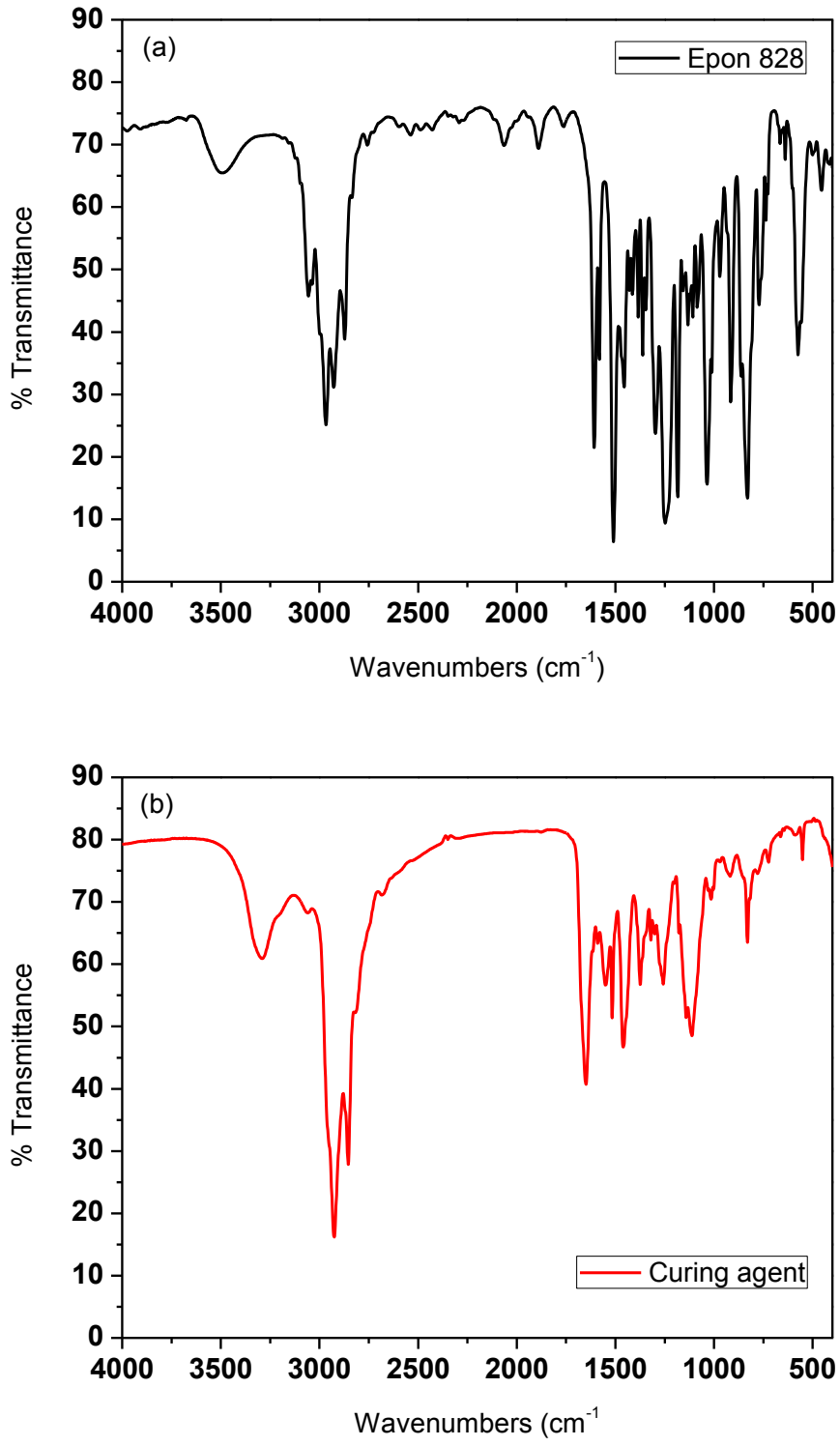

Figure 3.5. FTIR spectra of two components of the epoxy coating. Epon Resin 828 is the base component and EPIKURE 3164 is the curing agent.

Table 3.1. Assignment of the FTIR peaks.

Peak Positions (cm^{-1})					**Assignment [30]**
Q=2.233 cm^3/s	**Q=3.683 cm^3/s**	**Q=5.233 cm^3/s**	**Epon 828**	**Curing Agent**	
				3290	Secondary amines N-H stretch (3500-3300) cm^{-1}
			3055		Aromatic rings C-H strerch (3050-3010) cm^{-1}
2955	2957	2958	2966		Methyl group C-H asymmetric streth ~2962 cm^{-1} (2960±10) cm^{-1}
2923	2921	2924	2927	2925	Methylene group C-H asymmetric stretch ~2926 cm^{-1} (2926±5) cm^{-1}
			2872		Methyl group C-H symmetric stretch ~2872 cm^{-1} (2872±10) cm^{-1}
2852	2851	2853		2854	Methylene group C-H symmetric stretch ~2853 cm^{-1} (2853±5) cm^{-1}
			1607	1649	Aromatic C=C stretch
			1581	1549	(1600, 1585, 1500, 1450) cm^{-1}
			1510	1516	Secondary amines N-H bending
			1455	1460	(1650-1550) cm^{-1}
1456	1456	1457			Methylene group $–CH_2$ scissoring ~1465 cm^{-1} (1465±20) cm^{-1}
					Methyl group $–CH_3$ asymmetric bending ~1450 cm^{-1} (1450±20) cm^{-1}
1377	1384	1377	1384	1374	Methyl group $-CH_3$ symmetric bending ~1375 cm^{-1} (1375±5) cm^{-1}
			1297		Epoxides small-ring stretch
			1247		(1280-1230) cm^{-1}
			1184		Ethers C-O stretch
			1035		(1300-1000) cm^{-1}
1098	1096	1098		1257	C-N stretch (1350-1000) cm^{-1}
				1111	Ethers C-O-C asymmetric stretch ~1120 cm^{-1}
			915		Epoxides small-ring asymmetric stretch (950-815) cm^{-1}
			830		Epoxides small-ring symmetric
			772		stretch (880-750) cm^{-1}
					1,4-Disubstituted rings (850-800) cm^{-1}
				830	1,4-Disubstituted rings (850-800) cm^{-1}
					Out-of-plane N-H bending 800 cm^{-1}

3.3.2. Solution Conductivity

FTIR measurements provide evidence that unreacted C-H groups are released into solution (i.e. working fluid) under flowing conditions. Nevertheless, it cannot quantitatively relate the amount of coating "debris" with the flow rates. Hence, we monitored the conductivity of the working fluid throughout the immersion of the samples. The initial conductivity values of 3.5 wt% NaCl solution for coating immersion under different flow rates are summarized in Table 3.2, including the blank NaCl solution (without coating samples immersed). As shown in Figure 3.6, the increase rate of the fluid conductivity is plotted as a function of immersion time for experiments with different flow rates. The increase rate of conductivity is defined using the expression:

$$\text{Conductivity Increase Rate} = (k_t - k_0)/k_0 \qquad (3\text{-}1)$$

where k_t is the conductivity of solution at time t; k_0 is the initial conductivity. We observe that the conductivity increases substantially under flowing conditions while it maintains almost the same value in stationary immersion. Higher flow rates are found to achieve a higher increase rate. The conductivity of the 3.5 wt% NaCl solution (blank solution) was also measured during its exposure to the air, but it showed no noticeable increase for the same length of the exposure time.

Table 3.2. Initial conductivity of 3.5 wt% NaCl solution.

Parameters	**Blank (NaCl solution)**	**Q=0 (Stationary)**	**Q=2.233 cm^3/s**	**Q=3.683 cm^3/s**	**Q=5.233 cm^3/s**
Initial Conductivity (mS/cm)	57.5 ± 0.1	57.4 ± 0.2	57.3 ± 0.2	57.3 ± 0.2	56.9 ± 0.3

According to the SDS, EPON Resin 828 has a negligible solubility and curing agent 3164 has a partial solubility in the water; so we prepared two mixtures for which we mixed a small amount of liquid EPON Resin 828 into a 3.5 wt% NaCl solution and the same for the curing agent. In order to mix EPON Resin 828 and the curing agent with the NaCl solution as much as possible, each of the mixtures was continuously stirred for five days, and the conductivity of the mixture was monitored during the stirring. It was found that the conductivity increased from 58.0 mS/cm to 66.6 mS/cm for EPON 828 mixture (an increase rate of 0.148), and from 58.6 mS/cm to 67.8 mS/cm for the curing agent mixture (an increase rate of 0.157). Based on this phenomenon as well as the behavior of the blank solution mentioned above, we believe that, after coating degradation during immersion, the increased conductivity of the working fluid comes from the contribution of both components of the epoxy. Fredj et al. also reported the conductivity of the aging solutions increased when two epoxy coatings were immersed for 6 months [31]. They inferred that the increased conductivity was due to the ionic species releasing into the solution. Therefore, both the FTIR spectrum and the increase of the conductivity of the working fluid verify the leaching of organic materials from the coating into the surrounding fluid.

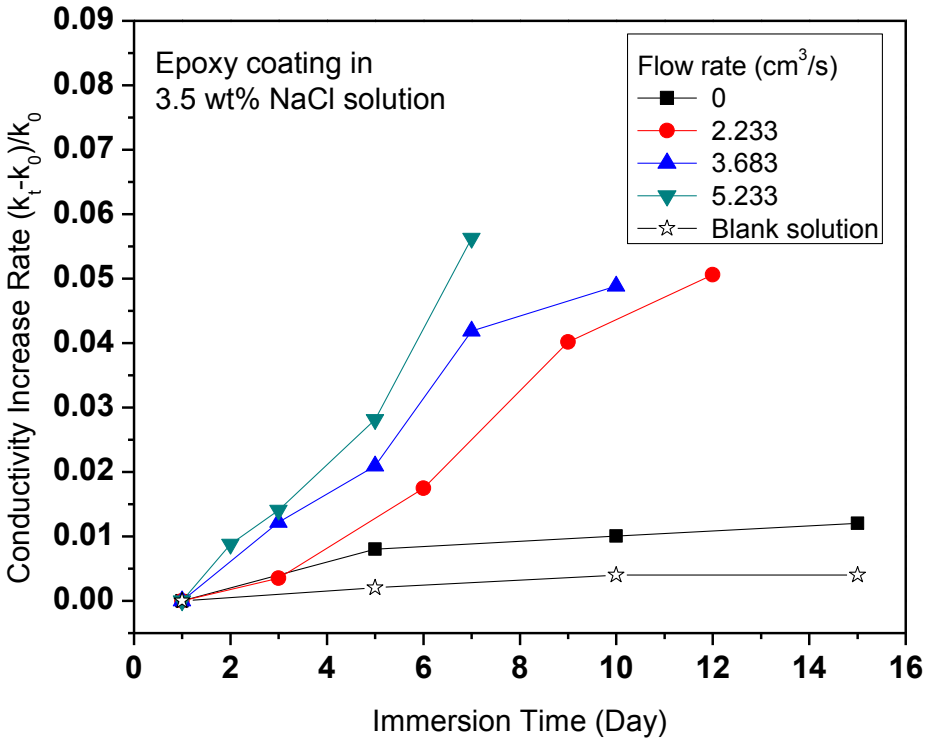

Figure 3.6. Conductivity increase rate of immersed solution as a function of immersion time for coating samples immersed in 3.5 wt% NaCl solution with flow rates Q=0 (stationary), 2.233, 3.683, and 5.233 cm^3/s, as well as the blank solution.

3.3.3. Coating Thickness

The thickness of epoxy coating was measured before and after immersion. As shown in Figure 3.7, under the stationary immersion, the thickness of epoxy coating increased due to the swelling of coating film as a result of water uptake. Under flowing conditions, we observed less but still discernable increase in the coating thickness. For higher flow rates (e.g. Q=5.233 cm^3/s), however, the coating thickness decreased after immersion. We thus believe that the change of coating thickness under flowing conditions may result from the combined effects of swelling and fluid shear which wears off materials from the coating. At small flow rates, the swelling of the coating contributes

more substantially in the thickness change. As the flow rate increases, the fluid shear dominates the combined effects; as a result, coating thickness decreases as shown in Figure 3.8. To quantitatively separate these two effects, Figure 3.9 shows the change in coating thickness due to fluid shear as a function of the flow rate. We assume the coating samples swell the same percentage based on its initial thickness during immersion; and we take the swelling rate of the coating under stationary immersion as a reference (10.59% of the thickness increase). Hence, under the swelling influence alone, the average coating thickness is calculated to be 34.39, 36.72, and 34.84 μm for samples immersed in working fluid with flow rates of 2.233, 3.683, 5.233 cm^3/s, respectively. Thus, the difference between the calculated thickness and the measured thickness for coatings after immersion is believed to result from the fluid shear. The fluid shear stress is calculated for each flow rate in the experiments. NaCl solution, as a typical Newtonian fluid, leads to a linear relation between the flow rate and the wall shear stress.

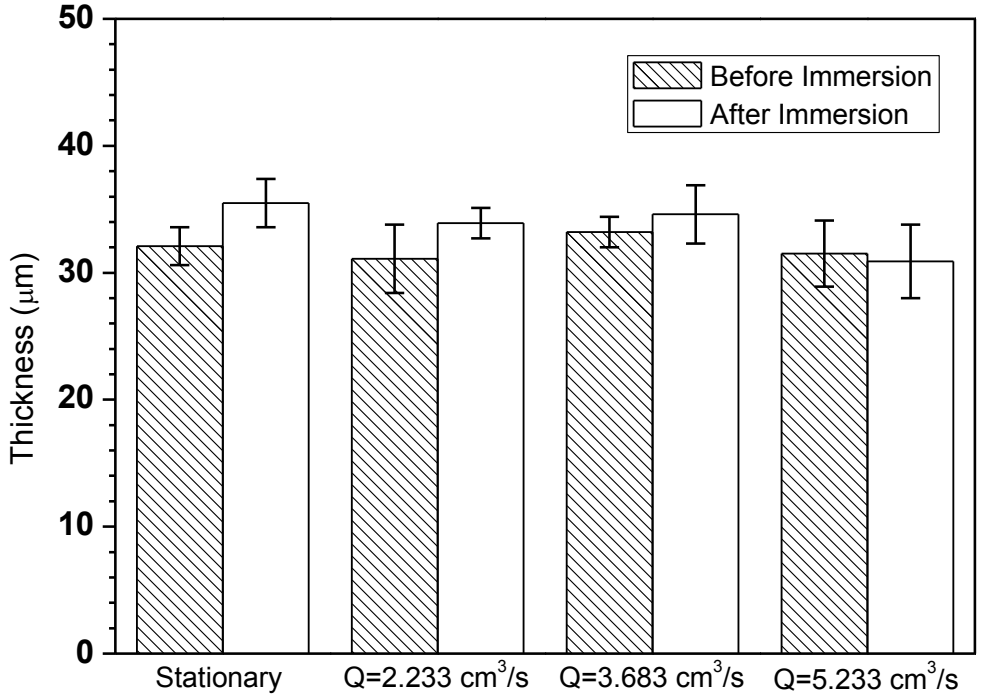

Figure 3.7. Thickness of coating samples immersed in 3.5 wt% NaCl solution with flow rates Q=0 (stationary), 2.233, 3.683, and 5.233 cm^3/s.

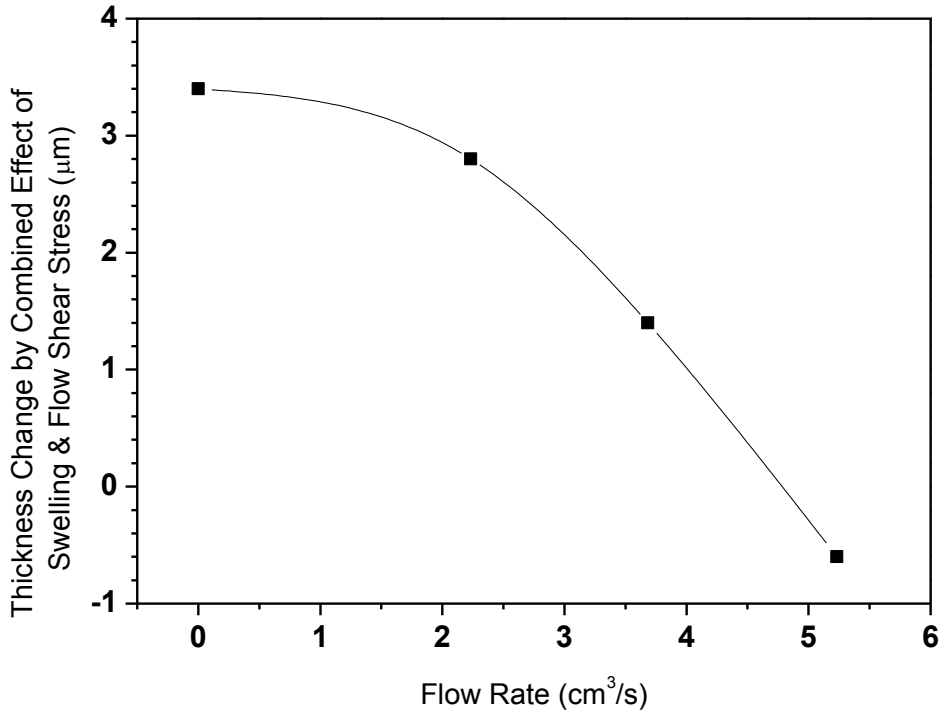

Figure 3.8. Thickness change as a function of flow rates for coating samples immersed in 3.5 wt% NaCl solution.

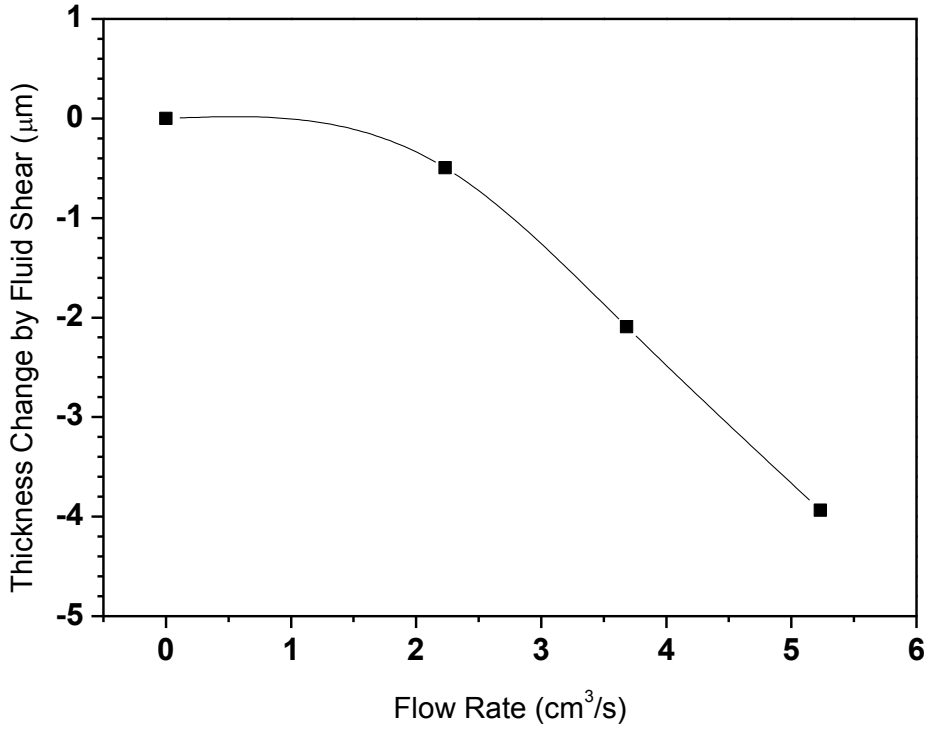

Figure 3.9. Thickness change due to fluid shear as a function of the flow rate for coating samples immersed in 3.5 wt% NaCl solution.

Due to the large aspect ratio of the width (10.16 cm) and the depth (0.636 cm) of the flow channel, the fluid shear calculation could be simplified into a two-dimensional problem. The schematic is shown in Figure 3.10. The laminar flow moves in the *x* direction parallel to the coating surface, and there is no velocity in the *y* direction. In this case the continuity becomes $\frac{\partial u}{\partial x} = 0$. For a steady flow $\frac{\partial u}{\partial t} = 0$, the Navier-Stokes equations could be reduced to

$$0 = -\frac{\partial p}{\partial x} + \mu(\frac{\partial^2 u}{\partial y^2}) \tag{3-2}$$

Equation 3-2 can be integrated to give Equation 3-3 with the boundary conditions: $u = 0$ when $y = \pm h$, where *h* is half of the channel depth

$$u = \left(\frac{\partial p}{\partial x}\right)\frac{(y^2 - h^2)}{2\mu} \tag{3-3}$$

The volumetric flow rate, q, passing between the channel walls is obtained as

$$q = -\frac{2}{3}\left(\frac{\partial p}{\partial x}\right)\frac{h^3}{\mu} \tag{3-4}$$

Substituting Equation 3-4 into Equation 3-3 gives

$$u = -\frac{3}{4}\frac{q(y^2 - h^2)}{h^3} \tag{3-5}$$

The shear stress is defined from the relationship

$$\tau = -\mu\frac{du}{dy} \tag{3-6}$$

Put Equation 3-5 into Equation 3-6, the shear stress becomes

$$\tau = \frac{3}{2}\frac{\mu q y}{h^3} \tag{3-7}$$

When $y = h$, the shear stress at the coating surface becomes

$$\tau = \frac{3}{2}\frac{\mu q}{h^2} \tag{3-8}$$

The width (the dimension in z direction) of the flow channel is 10.16 cm, and the flow rates in this study are 2.233, 3.683, 5.233 cm^3/s; thus, the corresponding two dimensional flow rate q are 0.2198, 0.3625, 0.5151 cm^2/s. The half depth of the flow channel, h, is 0.318 cm, and μ=10^{-3} $N{\cdot}s/m^2$ for the NaCl solution; therefore, according to Equation 3-8, the shear stress acting on the coating surface are 3.26×10^{-3}, 5.38×10^{-3}, 7.64×10^{-3} pa, respectively. The shear stress linearly increases with the flow rate.

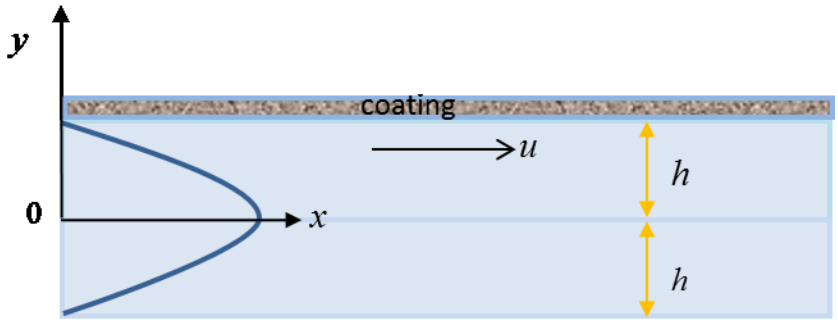

Figure 3.10. Schematic of flow geometry domain.

3.3.4. EIS Results and Equivalent Circuit Modeling

Both the FTIR and thickness measurements confirm the release of coating materials into the working fluid. We then proceed to investigate the change in coating's barrier property using EIS, which reflects the internal composition of the coatings. Since all coating samples behave similarly under the same experimental condition unless defects exist prior to experiments, we present results for one representative sample for each flow rate. As shown in Figure 3.11 for epoxy coating immersed in a 3.5 wt% NaCl solution with a flow rate of Q=2.233 cm^3/s, the impedance modulus is plotted as a function of the frequency applied in EIS tests as well as immersion time. We observe that the low frequency impedance modulus decreases from the order of magnitude of 10^6 to 10^4 as the immersion time increases. This indicates the deterioration of the barrier property of organic coatings. Since all clear coatings show similar behavior for EIS spectra under different flow rates, the Bode plot of coating sample immersed in the flow rate of Q=2.233 cm^3/s is chosen to demonstrate the coating's degradation process.

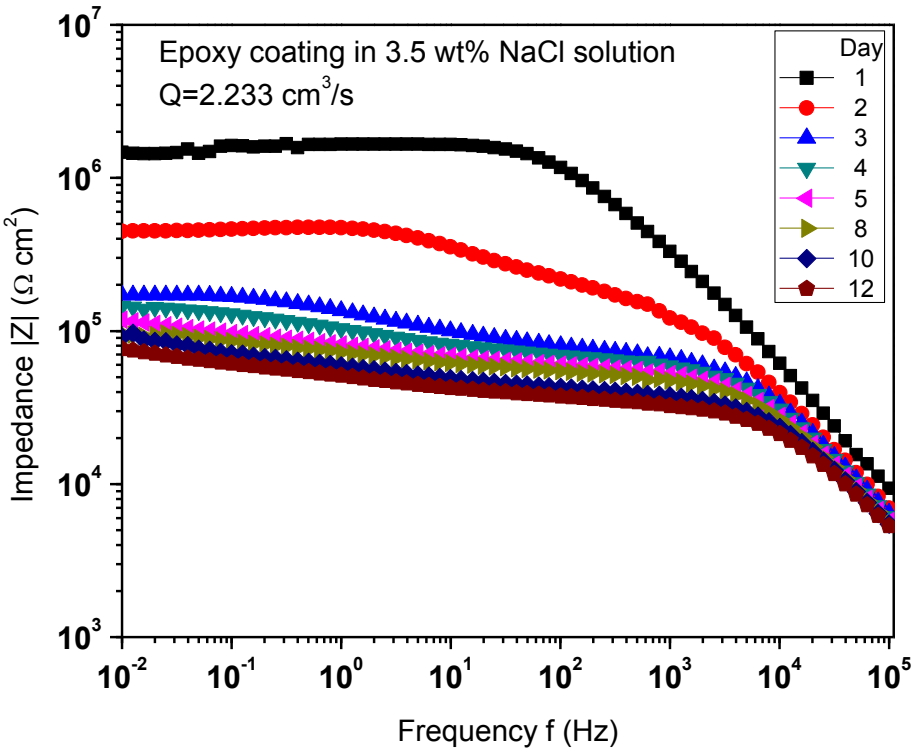

Figure 3.11. Impedance modulus as a function of frequency for epoxy coating immersed in 3.5 wt% NaCl solution with flow rates Q=2.233 cm^3/s.

To illustrate the effect of flow rate on the barrier property of the coating during immersion, the impedance modulus of EIS spectra at low frequency was studied representing the corrosion resistance of coating samples [17, 32, 33]. A plot of the relative impedance modulus at low-frequency (0.01 Hz) as a function of immersion time is shown in Figure 3.12 for different flow rates. The relative low-frequency impedance modulus is obtained by normalizing the low-frequency impedance modulus with the modulus at the initial immersion. The low-frequency (0.01 Hz) values for representative coating samples in different flow rates at initial immersion are listed in Table 3.3. The table shows that the initial impedance values are at the same order of magnitude for epoxy coating immersed in NaCl solution with different flow rates.

We observe from Figure 3.12 that the relative low-frequency (0.01 Hz) impedance modulus decreases with the increase of the immersion time, and the decrease rate is substantial at the early state of immersion followed by a relatively slower decrease. Higher flow rates accelerate the decrease of the low-frequency impedance modulus, which reveals that the flowing fluid accelerates coating degradation by enhancing the water percolation and ions diffusion into the coating metal interface. Similar behavior of coating's barrier properties was also reported for pigmented marine coating samples immersed in NaCl solution and pure water with a variety of flow rates [18, 19].

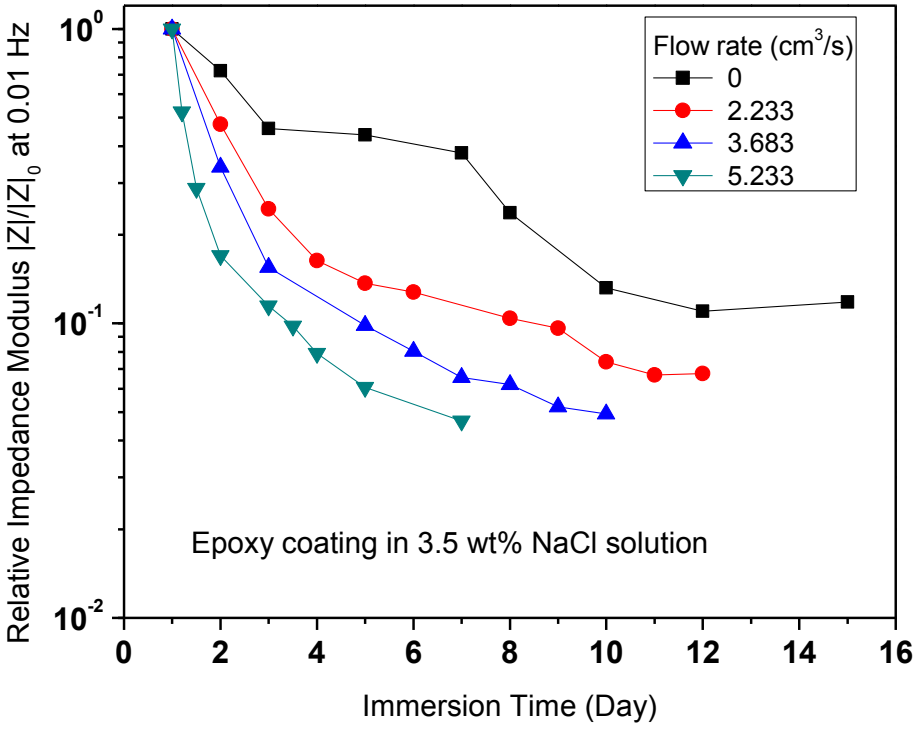

Figure 3.12. Relative impedance modulus as a function of immersion time for coating samples immersed in 3.5 wt% NaCl solution with flow rates Q=0 (stationary), 2.233, 3.683, and 5.233 cm^3/s.

Table 3.3. Initial values of parameters for coating samples immersed in flowing 3.5 wt% NaCl solution.

Parameters	**Q=0 (Stationary)**	**Q=2.233 cm^3/s**	**Q=3.683 cm^3/s**	**Q=5.233 cm^3/s**
$\|Z\|_{0.01Hz}$ (Ω cm^2)	2.46×10^6	8.80×10^5	1.47×10^6	1.12×10^6
R_{po} (Ω cm^2)	4.31×10^5	4.12×10^5	1.13×10^6	9.15×10^5
C_c (F/cm^2)	1.11×10^{-10}	1.14×10^{-10}	1.07×10^{-10}	1.20×10^{-10}

An equivalent circuit model is employed to interpret EIS data and analyze the physical behavior of coatings as they are degrading. The model used for degraded coating is shown in Figure 3.13 [34-38]. R_s is solution resistance; R_{po} is pore resistance; R_{ct} is charge transfer resistance; C_c and C_{dl} are constant phase element (CPE), which is used to simulate the non-ideal capacitance behavior. The impedance of a CPE is given mathematically by

$$Z_{CPE} = \frac{(j\omega)^{-\alpha}}{Y} \tag{3-9}$$

where ω is the angular frequency; α is a dimensionless parameter; Y is a parameter with dimensions $\Omega^{-1} \cdot s^{\alpha}$ representative for constant phase element. In this study, we denote C_c for coating capacitance and C_{dl} for double layer capacitance. Analysis of EIS spectra is performed using Echem Analyst software by Gamry Instruments. More explanations for the model and the fitting agreement with experimental data have been described in detail in our previous study [39]. Similar equivalent circuit models are also found to simulate the degradation behavior of organic coatings in existing publications [34-38].

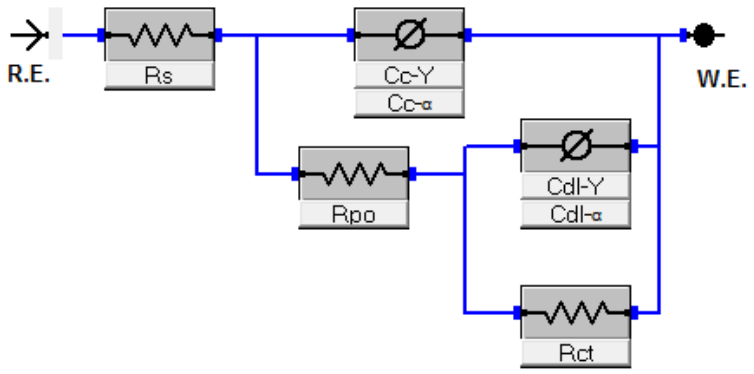

Figure 3.13. Equivalent circuit model used for the impedance analysis of coating samples immersed in 3.5 wt% NaCl solution under different flow rates. R_s is solution resistance; C_c is coating capacitance; R_{po} is pore resistance; C_{dl} is double layer capacitance; R_{ct} is charge transfer resistance.

In order to demonstrate the influence of flow rate on the coating's degradation, we choose to analyze the relative values of the modeling elements in the afore-mentioned equivalent circuit model. The relative values are obtained by normalizing the element values with those at initial immersion. The values of model elements at initial immersion under different flow rates are listed in Table 3.3. Figure 3.14 shows the time revolution of relative pore resistance under different flow rates. The coating resistance, presented by the pore resistance in the equivalent circuit model, is an important parameter in the assessment of coating performance; its magnitude at a given time indicates the state of degradation [40]. We observe from Figure 3.14 that the flowing fluid plays a critical role on reducing the coating's resistance. For example, the decrease of the relative pore resistance under the flow rate of Q=5.233 cm^3/s is much substantial than that in the stationary immersion (flow rate Q=0 cm^3/s). The more prominent decrease of pore resistance implies that ion diffusion is enhanced by higher flow rates. The faster decrease in the pore resistance may reflect a higher rate in coating degradation.

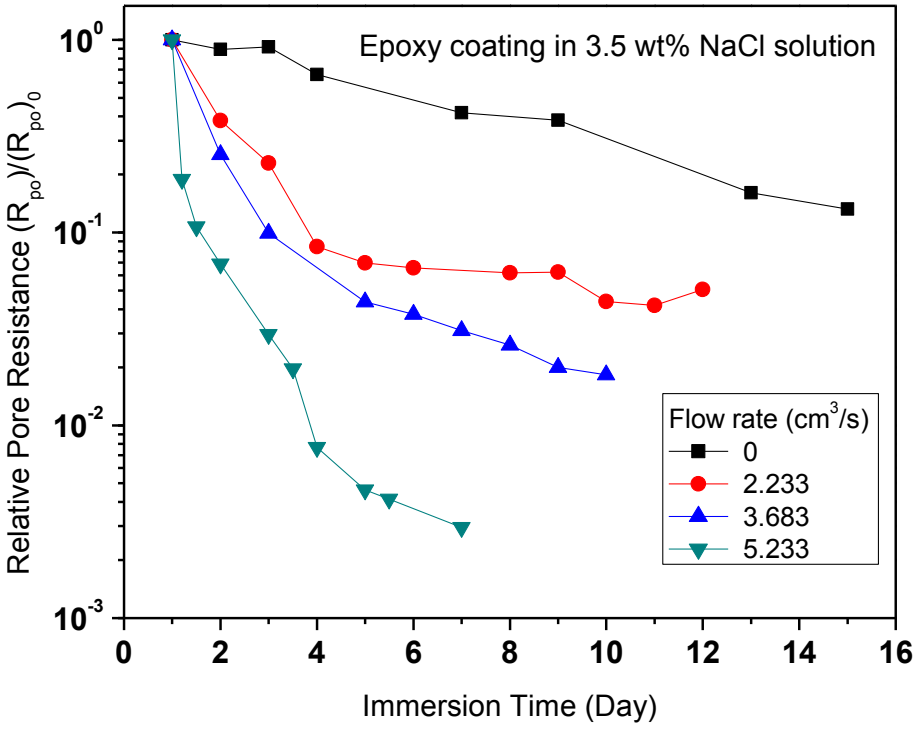

Figure 3.14. Relative pore resistance as a function of immersion time for coating samples immersed in 3.5 wt% NaCl solution with flow rates Q=0 (stationary), 2.233, 3.683, and 5.233 cm^3/s.

The coating capacitance (C_c) can be calculated using the following expression [15, 41-43]:

$$C_c = Y^{1/\alpha}\left(\frac{1}{R_s}+\frac{1}{R_{po}}\right)^{(\alpha-1)/\alpha} \tag{3-10}$$

where Y, α, R_s, and R_{po} are modeling elements for the equivalent circuit presented earlier in Figure 3.13. The time evolution of relative coating capacitance is shown in Figure 3.15 to demonstrate the influence of flow rate on the water uptake into organic coatings. The initial values of coating capacitance under different flow rates are also listed in Table 3.3. We observe an exponential increase of the coating capacitance under immersion in the

larger flow rate; while for stationary and lower flow rate immersion, coating capacitance increases slowly and gradually approaches to a plateau. The increase in coating capacitance is due to the release of unreacted materials, water uptake, the diffusion of oxygen, and ions into coatings; and obviously, higher flow rates accelerate those transport phenomena. Overall, the decrease in coating resistance and increase in coating capacitance indicates that the coating experiences more severe penetration of water and ions, as well as attenuation of coating's barrier property under immersion with a higher flow rate. The results are qualitatively in agreement with previous findings [18, 19].

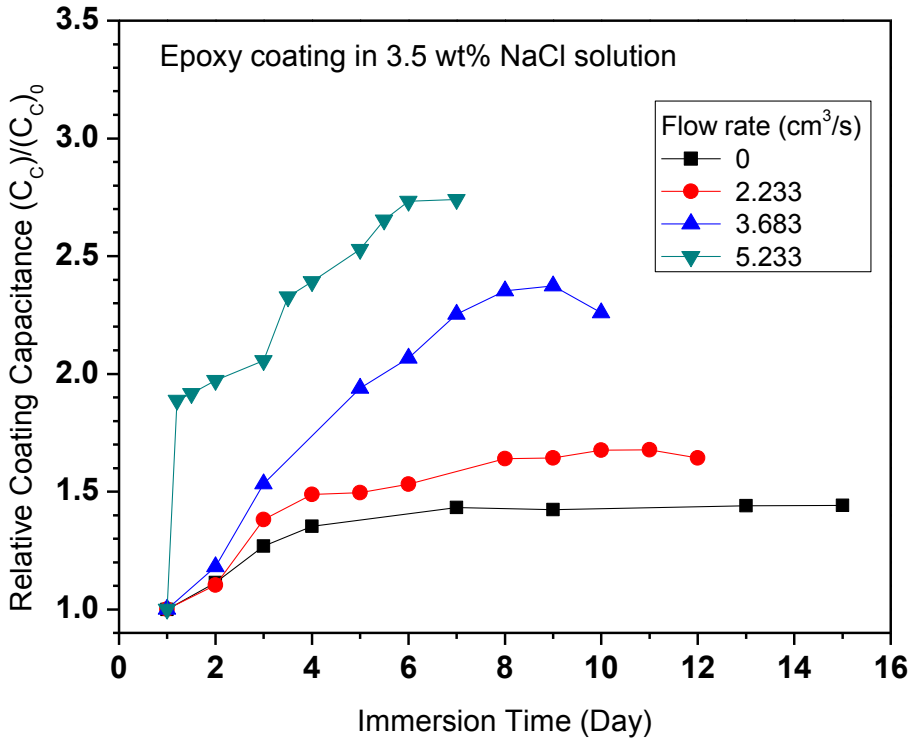

Figure 3.15. Relative coating capacitance as a function of immersion time for coating samples immersed in 3.5 wt% NaCl solution with flow rates Q=0 (stationary), 2.233, 3.683, and 5.233 cm^3/s.

We then studied coating's permittivity to investigate the change of coating's internal property after immersion in flowing fluid. The coating's relative permittivity can be calculated using the following equation:

$$\varepsilon_R = \frac{C_c \cdot d}{A \cdot \varepsilon_0} \tag{3-11}$$

where ε_R is relative permittivity; C_c is coating capacitance, F; d is coating thickness, μm; A is coating area, cm^2; and ε_0 is the vacuum permittivity, $\varepsilon_0 = 8.854 \times 10^{-12}$ F/m. We observe from Figure 3.16 that the relative permittivity of the coating increases after immersion and a higher flow rate results in a larger increase rate. The evolution of coating's permittivity demonstrates that flowing fluid not only wears coating's surface by fluid shear, it also influences its overall internal property, contributed from polymer networking or curing.

To clearly demonstrate the effect of flow accelerated on coating degradation, the time the coating needed to failure is plotted as a function of different flow rates, as shown in Figure 3.17. The coating's failure time is defined as the day when the low-frequency impedance modulus monitored by EIS decreases dramatically and after that it tends to be constant, or the day when the decrease of the low-frequency impedance modulus changes slowly. Also, at the failure time, the low frequency impedance modulus at 0.01 Hz drops to $4 \times 10^4 \sim 8 \times 10^4$ Ω cm^2 for coating samples immersed in different flowing conditions. We usually observed some corrosion spots on the coating surface when it failed. It is obvious that flow accelerates the coating degradation and the coating tends to fail earlier at higher flow rates.

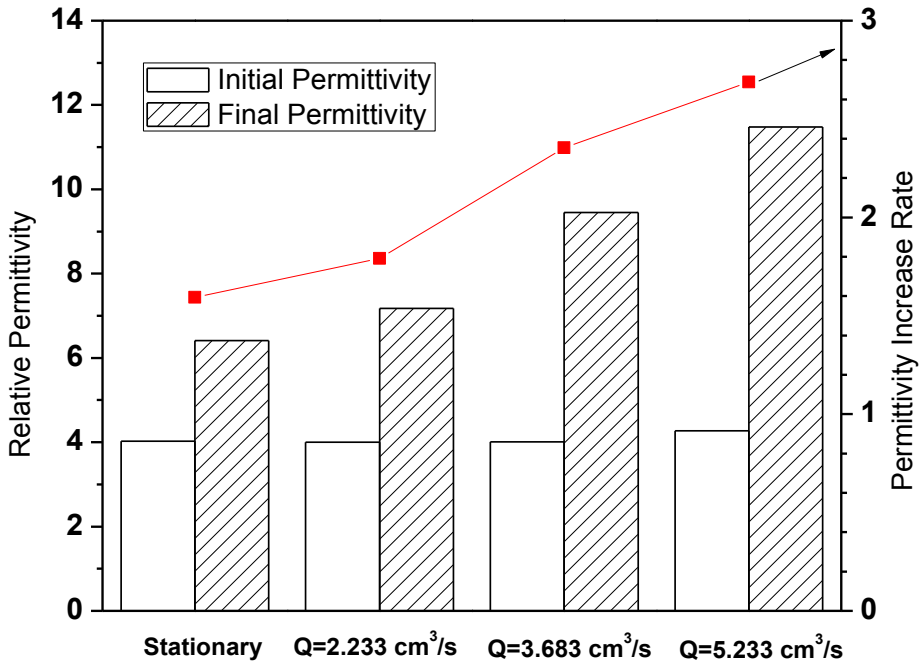

Figure 3.16. Relative permittivity and permittivity increase rate as a function of flow rate for coating samples immersed in 3.5 wt% NaCl solution.

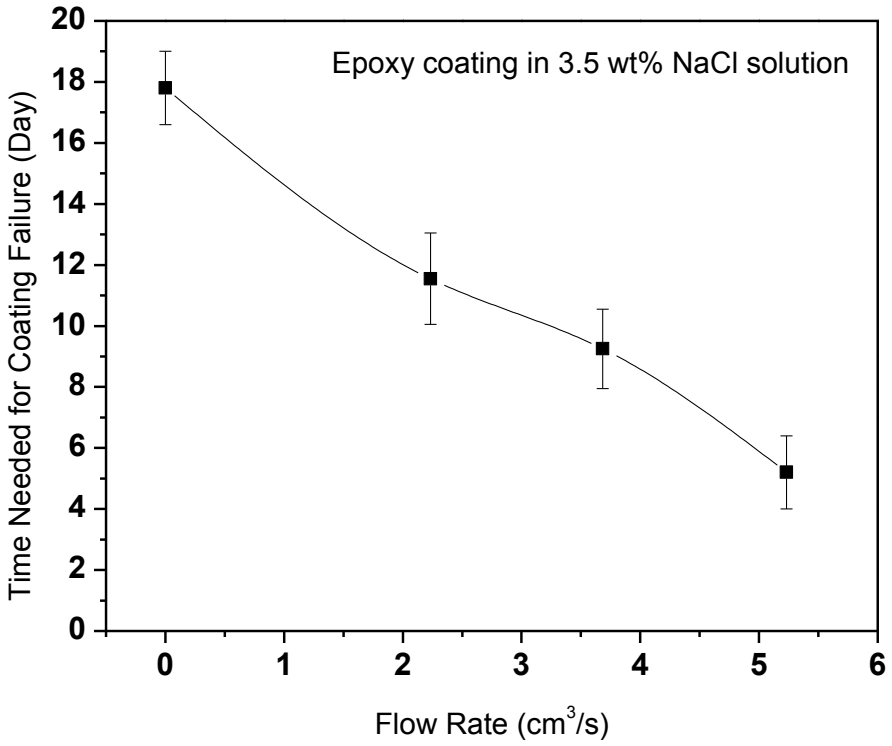

Figure 3.17. The time needed for coating failure as a function of flow rate for coating samples immersed in 3.5 wt% NaCl solution.

3.4. Conclusions

The study in this chapter evaluated the flow accelerated organic coating degradation with a focus on the influence of fluid shear. By monitoring the composition change of the working fluid, we believe that the organic materials released from the coating into surrounding fluid under flowing conditions, demonstrated by the FTIR spectrum and the increased conductivity. The change of coating thickness presented the combined effects of the swelling and the fluid shear, and the fluid shear decreased the coating thickness under higher flow rates. EIS and equivalent circuit models were also studied to investigate the change in coating's barrier property. Higher flow rates accelerated the decrease in coating resistance and the increase in coating capacitance, since the higher flow rates accelerated the release of unreacted materials, water uptake, and the diffusion of oxygen and ions into coatings. The evolution of coating's permittivity demonstrates that flowing fluid not only wears coating's surface by fluid shear, it also influences its internal property. Overall, we conclude that flowing fluid on the coating surface promotes the migration of coating materials from inside the coating into the working fluid, as well as accelerates the transport of water and ions into the coating, where coatings experience more severe deterioration in its barrier property under flowing conditions.

3.5. References

[1] T. Yuzawa, C. Watanabe, S. Tsuge, N. Shimane, H. Imai, Application of a pyrolysis-GC/MS system incorporating with micro-UV irradiation to rapid evaluation of the weatherability of acrylic coating paints for house exterior walls, *Polymer Degradation and Stability*, **96** (2011) 91-96.

[2] O. Haillant, D. Dumbleton, A. Zielnik, An Arrhenius approach to estimating organic photovoltaic module weathering acceleration factors, *Solar Energy Materials and Solar Cells*, **95** (2011) 1889-1895.

[3] O. Guseva, S. Brunner, P. Richner, Service life prediction for aircraft coatings, *Polymer Degradation and Stability*, **82** (2003) 1-13.

[4] B.W. Johnson, R. McIntyre, Analysis of test methods for UV durability predictions of polymer coatings, *Progress in Organic Coatings*, **27** (1996) 95-106.

[5] J. Hu, X. Li, J. Gao, Q. Zhao, Ageing behavior of acrylic polyurethane varnish coating in artificial weathering environments, *Progress in Organic Coatings*, **65** (2009) 504-509.

[6] S. Touzain, Q.L. Thu, G. Bonnet, Evaluation of thick organic coatings degradation in seawater using cathodic protection and thermally accelerated tests, *Progress in Organic Coatings*, **52** (2005) 311-319.

[7] N. Guermazi, K. Elleuch, H.F. Ayedi, The effect of time and aging temperature on structural and mechanical properties of pipeline coating, *Materials & Design*, **30** (2009) 2006-2010.

[8] L. Fedrizzi, A. Bergo, F. Deflorian, L. Valentinelli, Assessment of protective properties of organic coatings by thermal cycling, *Progress in Organic Coatings*, **48** (2003) 271-280.

[9] F. Deflorian, L. Fedrizzi, S. Rossi, Effects of mechanical deformation on the protection properties of coil coating products, *Corrosion Science*, **42** (2000) 1283-1301.

[10] X. Yang, C. Vang, D.E. Tallman, G.P. Bierwagen, S.G. Croll, S. Rohlik, Weathering degradation of a polyurethane coating, *Polymer Degradation and Stability*, **74** (2001) 341-351.

[11] X. Yang, J. Li, S.G. Croll, D.E. Tallman, G.P. Bierwagen, Degradation of low gloss polyurethane aircraft coatings under UV and prohesion alternating exposures, *Polymer Degradation and Stability*, **80** (2003) 51-58.

[12] R.J. Varley, E.K. Simmonds, J.E. Seebergh, D.H. Berry, Investigation of factors impacting the in-service degradation of aerospace coatings, *Progress in Organic Coatings*, **74** (2012) 679-686.

[13] N. Fredj, S. Cohendoz, X. Feaugas, S. Touzain, Effect of mechanical stress on kinetics of degradation of marine coatings, *Progress in Organic Coatings*, **63** (2008) 316-322.

[14] N. Fredj, S. Cohendoz, X. Feaugas, S. Touzain, Effect of mechanical stresses on marine organic coating ageing approached by EIS measurements, *Progress in Organic Coatings*, **72** (2011) 260-268.

[15] N. Fredj, S. Cohendoz, X. Feaugas, S. Touzain, Ageing of marine coating in natural and artificial seawater under mechanical stresses, *Progress in Organic Coatings*, **74** (2012) 391-399.

[16] C.S. Jeffcoate, G.P. Bierwagen, Electrochemical comparison of coating performance in flowing vs. stationary electrolyte, in: G.P. Bierwagen (Ed.) American Chemical Society Symposium Series, American Chemical Society, Washington, DC, 1998, pp. 151-160.

[17] Q.L. Thu, G.P. Bierwagen, S. Touzain, EIS and ENM measurements for three different organic coatings on aluminum, *Progress in Organic Coatings*, **42** (2001) 179-187.

[18] Y. Wang, G.P. Bierwagen, A new acceleration factor for the testing of corrosion protective coating: flow-induced coating degradation, *Journal of Coatings Technology and Research*, **6** (2009) 429-436.

[19] Q. Zhou, Y. Wang, G.P. Bierwagen, Influence of the composition of working fluids on flow-accelerated organic coating degradation: Deionized water versus electrolyte solution, *Corrosion Science*, **55** (2012) 97-106.

[20] Y. Wei, L. Zhang, W. Ke, Comparison of the degradation behaviour of fusion-bonded epoxy powder coating systems under flowing and static immersion, *Corrosion Science*, **48** (2006) 1449-1461.

[21] E.A.M. Hussain, M.J. Robinson, Erosion–corrosion of 2205 duplex stainless steel in flowing seawater containing sand particles, *Corrosion Science*, **49** (2007) 1737-1754.

[22] R. Barker, X. Hu, A. Neville, The influence of high shear and sand impingement on preferential weld corrosion of carbon steel pipework in CO_2-saturated environments, *Tribology International*, **68** (2013) 17-25.

[23] O.O. Ige, R. Barker, X. Hu, L.E. Umoru, A. Neville, Assessing the influence of shear stress and particle impingement on inhibitor efficiency through the application of in-situ electrochemistry in a CO_2-saturated environment, *Wear*, **304** (2013) 49-59.

[24] N. Fredj, S. Cohendoz, X. Feaugas, S. Touzain, Some consequences of saline solution immersion on mechanical behavior of two marine epoxy-based coatings, *Progress in Organic Coatings*, **69** (2010) 82-91.

[25] J.R. Svendsen, G.M. Kontogeorgis, S. Kiil, C.E. Weinell, M. Grønlund, Adhesion between coating layers based on epoxy and silicone, *Journal of Colloid and Interface Science*, **316** (2007) 678-686.

[26] S.S. Pathak, A. Sharma, A.S. Khanna, Value addition to waterborne polyurethane resin by silicone modification for developing high performance coating on aluminum alloy, *Progress in Organic Coatings*, **65** (2009) 206-216.

[27] D.P. Schmidt, B.A. Shaw, E. Sikora, W.W. Shaw, L.H. Laliberte, Corrosion protection assessment of sacrificial coating systems as a function of exposure time in a marine environment, *Progress in Organic Coatings*, **57** (2006) 352-364.

[28] A. Husain, O. Al-Shamah, A. Abduljaleel, Investigation of marine environmental related deterioration of coal tar epoxy paint on tubular steel pilings, *Desalination*, **166** (2004) 295-304.

[29] J. Olabarrieta, S. Zorita, I. Peña, N. Rioja, O. Monzón, P. Benguria, L. Scifo, Aging of photocatalytic coatings under a water flow: Long run performance and TiO_2 nanoparticles release, *Applied Catalysis B: Environmental*, **123–124** (2012) 182-192.

[30] D.L. Pavia, G.M. Lampman, G.S. Kriz, Introduction to spectroscopy: a guide for students of organic chemistry, Brooks/Cole, 2001.

[31] N. Fredj, S. Cohendoz, S. Mallarino, X. Feaugas, S. Touzain, Evidencing antagonist effects of water uptake and leaching processes in marine organic

coatings by gravimetry and EIS, *Progress in Organic Coatings*, **67** (2010) 287-295.

[32] B.R. Hinderliter, K. Allahar, G.P. Bierwagen, D.E. Tallman, S.G. Croll, Water sorption and diffusional properties of a cured epoxy resin measured using alternating ionic liquids/aqueous electrolytes in electrochemical impedance spectroscopy, *Journal of Coatings Technology and Research*, **5** (2008) 431-438.

[33] G.P. Bierwagen, L. He, J. Li, L. Ellingson, D.E. Tallman, Studies of a new accelerated evaluation method for coating corrosion resistance - thermal cycling testing, *Progress in Organic Coatings*, **39** (2000) 67-78.

[34] V.F. Lvovich, Impedance spectroscopy application to electrochemical and dielectric phenomena, John Wiley & Sons, Hoboken, New Jersey, 2012.

[35] P.L. Bonora, F. Deflorian, L. Fedrizzi, Electrochemical impedance spectroscopy as a tool for investigating underpaint corrosion, *Electrochimica Acta*, **41** (1996) 1073-1082.

[36] C. Corfias, N. Pebere, C. Lacabanne, Characterization of a thin protective coating on galvanized steel by electrochemical impedance spectroscopy and a thermostimulated current method, *Corrosion Science*, **41** (1999) 1539-1555.

[37] Y. González-García, S. González, R.M. Souto, Electrochemical and structural properties of a polyurethane coating on steel substrates for corrosion protection, *Corrosion Science*, **49** (2007) 3514-3526.

[38] J. Zhang, J. Hu, J. Zhang, C. Cao, Studies of water transport behavior and impedance models of epoxy-coated metals in NaCl solution by EIS, *Progress in Organic Coatings*, **51** (2004) 145-151.

[39] Q. Zhou, Y. Wang, Comparisons of clear coating degradation in NaCl solution and pure water, *Progress in Organic Coatings*, **76** (2013) 1674-1682.

[40] M. Del Grosso Destreri, J. Vogelsang, L. Fedrizzi, F. Deflorian, Water up-take evaluation of new waterborne and high solid epoxy coatings. Part II: electrochemical impedance spectroscopy, *Progress in Organic Coatings*, **37** (1999) 69-81.

[41] G.J. Brug, A.L.G. van den Eeden, M. Sluyters-Rehbach, J.H. Sluyters, The analysis of electrode impedances complicated by the presence of a constant phase element, *Journal of Electroanalytical Chemistry and Interfacial Electrochemistry*, **176** (1984) 275-295.

[42] M.E. Orazem, B. Tribollet, Electrochemical Impedance Spectroscopy, John Wiley & Sons, Inc., Hoboken, New Jersey, 2008.

[43] F. Wong, R.G. Buchheit, Utilizing the structural memory effect of layered double hydroxides for sensing water uptake in organic coatings, *Progress in Organic Coatings*, **51** (2004) 91-102.

CHAPTER 4. SIMULATION ON CONVECTIVE DIFFUSION OF NACL INTO ORGANIC COATINGS

4.1. Introduction

In order to study the coating degradation mechanism, we are interested in finding out which factors dominate the flow accelerated degradation of corrosion protective organic coatings. We are curious about whether the convective diffusion of aggressive species, like NaCl ions, could influence the electrochemical property of organic coatings. Since it is difficult to obtain the concentration distribution of ions in the coating by experimental approach, we employ numerical methods to simulate the ions convective diffusion.

The simulation in this chapter will present the concentration distribution of soluble species (i.e. NaCl ions) in the coating under different flow velocities. Based on this simulation, we will understand the effect of flow velocity on the convective diffusion, and also we will investigate whether the diffusion of ions is the dominant factor to affect the coating's performance under flowing conditions.

4.2. Numerical Model Setup

4.2.1. Assumptions

The rectangular flow channel that we designed and employed provides a two-dimension Hele-Shaw flow as shown in Figure 4.1. The flow is assumed to be fully developed steady flow. The flow is only in x direction, no velocity in y or z direction. The fluid is a 3.5 wt% NaCl solution which behaves like an incompressible Newtonian fluid. Since the water diffusion into coatings is much faster than the diffusion of NaCl ions, we assume the coating has already been saturated with water before NaCl diffusion. The

diffusion coefficient of water into epoxy coating is in the order of magnitude of 10^{-13} m^2/s [1-3], while the diffusion coefficient is in the order of magnitude of 10^{-15} m^2/s for NaCl ions diffusing into epoxy coatings [4-6].

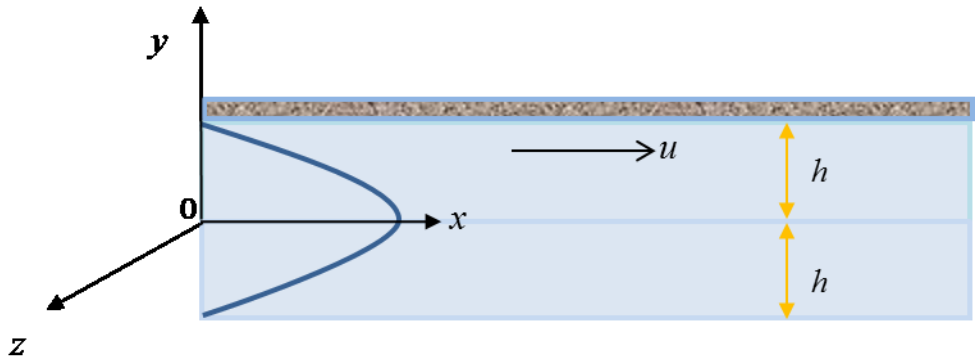

Figure 4.1. Simulation domain and geometrical parameters of the flow.

4.2.2. Governing Equations

The convective diffusion equations are employed to control the diffusion process of NaCl ions from bulk solution to the coating matrix. The general convective diffusion equation is shown in Equation 4-1.

$$D\left(\frac{\partial^2 c}{\partial x^2}+\frac{\partial^2 c}{\partial y^2}\right)-u_x\frac{\partial c}{\partial x}-\frac{\partial c}{\partial T'}=0 \qquad (4\text{-}1)$$

where D is the diffusion coefficient, m^2/s; c is the concentration of diffused species, mol/L; u_x is the velocity in x direction, m/s; T' is the diffusion time, s.

In our study, the simulation domain is split into two parts: the bulk flow domain and the coating matrix domain. We conduct the dimensionless study, so all the parameters in Equation 4-2 and 4-3 are nondimensionalized.

The governing equation for bulk flow domain is:

$$\left(\frac{\partial^2 C}{\partial x^2}+\frac{\partial^2 C}{\partial y^2}\right)-Pe\cdot U_x\frac{\partial C}{\partial x}-\frac{\partial C}{\partial t}=0 \tag{4-2}$$

where Peclet number $P_e = h\cdot\frac{U_m}{D_{ib}}$; $D_{ib} = 1.26\times10^{-9}\ m^2/s$, which is the diffusion coefficient of NaCl ions in water [7].

C is the concentration of NaCl ions, which is scaled with the concentration of NaCl solution.

U_x is the velocity component in the *x* direction of the Hele-Shaw flow. The velocity scale is the maximum velocity U_m at the centerline of the channel.

h is the half of the channel thickness, which is the size scale.

t is the diffusion time, scaled with h^2/D_{ib}.

The governing equation for coating matrix domain is:

$$\lambda\left(\frac{\partial^2 C}{\partial x^2}+\frac{\partial^2 C}{\partial y^2}\right)-\frac{\partial C}{\partial t}=0 \tag{4-3}$$

where $\lambda = D_{ic}/D_{ib}$; $D_{ic} = 1.23\times10^{-15}\ m^2/s$, which is the diffusion coefficient of NaCl ions in the epoxy coating [2, 5]. Other parameters are defined the same as in Equation 4-2.

4.2.3. Initial and Boundary Conditions

We use finite difference method to solve the partial differential governing equations, thus we need the initial and boundary conditions. For bulk flow domain, at the initial time, the flow channel is full of the 3.5 wt% NaCl solution, which is used as the concentration scale, as listed in Table 4.1; while for the coating matrix domain, because there is no NaCl ion in the coating at the very beginning, its concentration should be 0, as listed in Table 4.2.

As for the boundary conditions, for the bulk domain, at the flow inlet (where *x* = 0), the concentration of NaCl should equal to the 3.5 wt% NaCl solution ($C = 1$); at the

flow outlet and in the centerline of the flow channel, the gradient of the concentration should be zero, because no ions accumulate at these boundaries. In the meanwhile, there is no accumulation of ions in the boundary of coating's domain, so its concentration gradient should be zero. The initial and boundary conditions for bulk flow domain and coating matrix domain are listed in Table 4.1 and Table 4.2, respectively. L is the length of the coating sample; δ is the thickness of the coating sample.

Table 4.1. The initial and boundary conditions for bulk flow domain.

$t = 0$	$C = 1$		I.C.
$t \geq 1$	$x = 0$	$C = 1$	B.C.1
	$x = L/h$	$\frac{\partial C}{\partial x} = 0$	B.C.2
	$y = 0$	$\frac{\partial C}{\partial y} = 0$	B.C.3

Table 4.2. The initial and boundary conditions for coating matrix domain.

$t = 0$	$C = 0$		I.C.
$t \geq 1$	$x = 0$	$\frac{\partial C}{\partial x} = 0$	B.C.1
	$x = L/h$	$\frac{\partial C}{\partial x} = 0$	B.C.2
	$y = (h + \delta)/h$	$\frac{\partial C}{\partial y} = 0$	B.C.3

The convergence tests are also conducted as shown in Figure 4.2 to demonstrate the relatively error of the finite difference simulation. The node of 2500 creates an error of 1.08% with respect to the results obtained using the maximum number of nodes allowed by our computer configuration. The node of 2500 is chosen for the simulation since it represents the best compromise between computational accuracy and computation time.

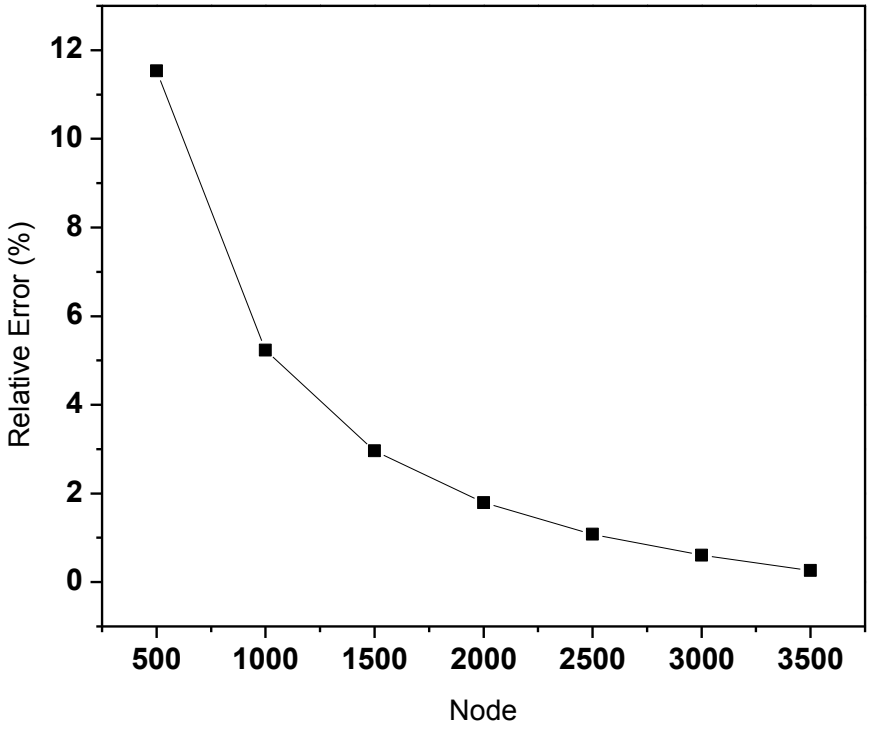

Figure 4.2. Relative error as a function of node in convergence tests.

4.3. Results and Discussion

4.3.1. Concentration Distribution of NaCl Ions in Coating's Domain

In Chapter 3, the epoxy coating was immersed in the 3.5 wt% NaCl solution under three flow rates, which are 2.233, 3.683, and 5.233 cm^3/s, respectively. In this

Chapter, we aim to model the NaCl diffusion into the epoxy coating under the three flow rates used in the experiments.

In order to transform flow rates to the corresponding flow velocities, we need to conduct the following calculations. As described in Chapter 3, the velocity profile should be in the relationship

$$u = -\frac{3}{4} \cdot q \cdot \frac{(y^2 - h^2)}{h^3} \tag{4-4}$$

where q is volumetric rate of flow passing between the channel walls, cm^2/s; h is the half of the channel thickness, h = 0.318 cm. The maximum velocity occurs in the centerline of flow channel ($y = 0$), so the expression of the maximum velocity becomes

$$u_{max} = \frac{3}{4} \cdot \frac{q}{h} \tag{4-5}$$

The width (the dimension in *z* direction) of the flow channel is 10.16 cm, so the corresponding q is 0.2198, 0.3625, and 0.5151 cm^2/s in two dimensions. Therefore, the maximum velocity is 0.0052, 0.0085, and 0.0121 m/s, respectively.

We use MATLAB to conduct the finite difference simulation on the convective diffusion of NaCl into coatings. We obtain the distribution of NaCl ions in the coating as a function of the diffusion time. We choose to plot the NaCl distribution on a particular time under the three flow velocities as shown from Figure 4.3 to Figure 4.5. The *x* axial is the length of the coating sample, scaled with h; the *y* axial is the thickness of the coating sample, also scaled with h; the color presents the dimensionless NaCl concentration in the coating domain. The colorful figures (Figure 4.3 to Figure 4.5) demonstrate that near the flow inlet and the flowing solution, the concentration of NaCl ions in the coating is very high presented by the dark red color; while far away from the flow inlet and near the

top layer of the coating, the concentration of NaCl ions is relatively low presented by the dark blue color. Between the two regions, it shows a distribution of the concentrations presented by a gradual change of the color. So the simulated results of the distribution of NaCl ions agree with the actual physical behavior of the convective diffusion.

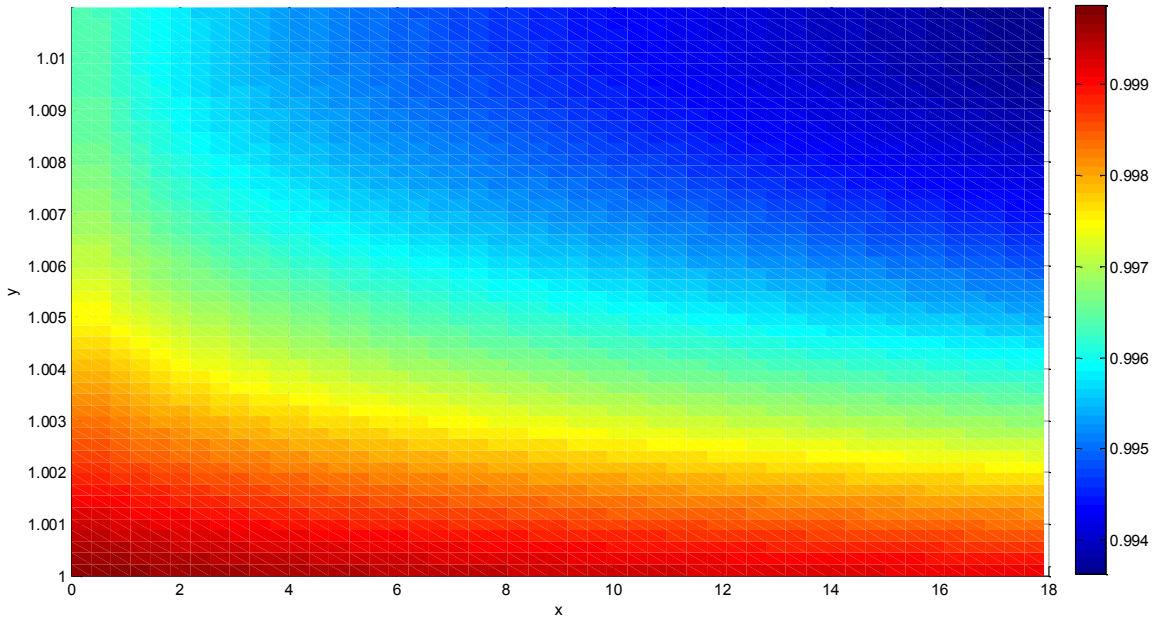

Figure 4.3. NaCl ions distribution in the coating domain; $T' = 20$ d, $U_{max} = 0.0052$ m/s.

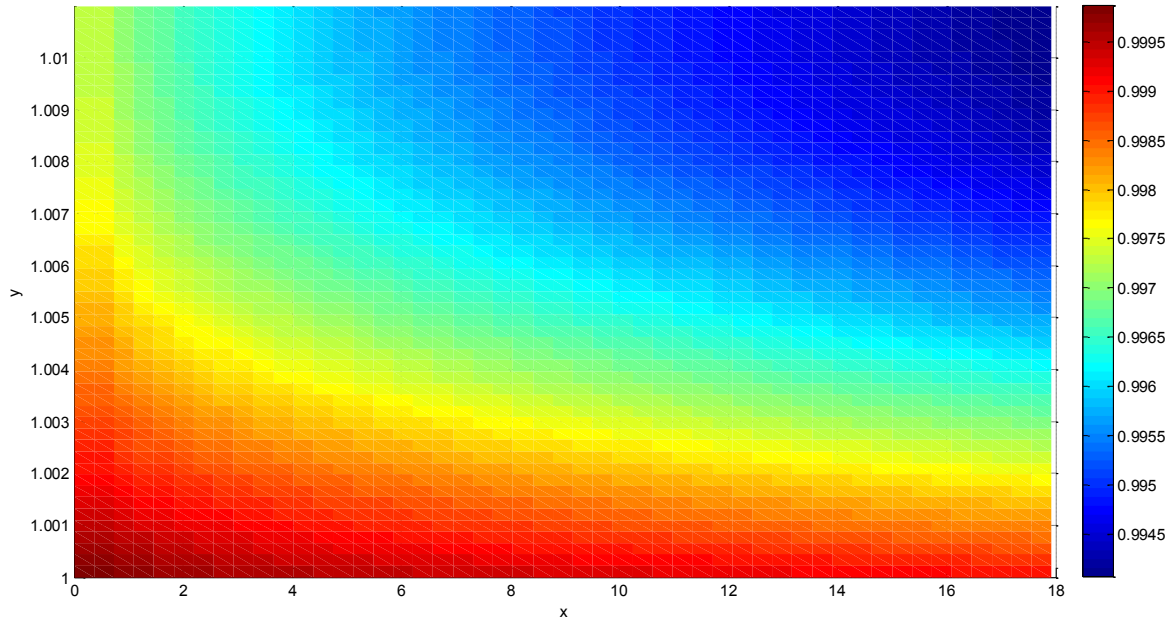

Figure 4.4. NaCl ions distribution in the coating domain; $T' = 20$ d, $U_{max} = 0.0085$ m/s.

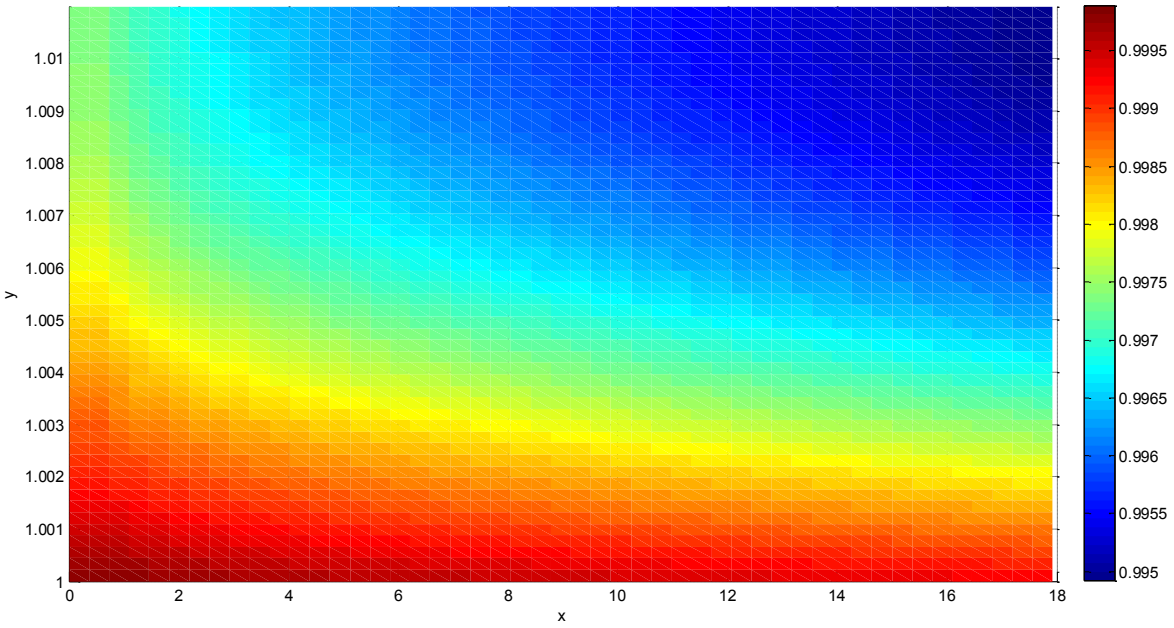

Figure 4.5. NaCl ions distribution in the coating domain; $T' = 20$ d, $U_{max} = 0.0121$ m/s.

4.3.2. Effect of Flow Velocity on NaCl Diffusion

Figure 4.3 shows the 2D plot of NaCl ions concentration in the coating domain. We integrate the concentration distribution in the coating domain, and then divide by the domain area, so we obtain the average concentration in the coating domain. We calculate the average NaCl concentration on different diffusion periods. In order to demonstrate the effect of flow velocity on NaCl diffusion, we compare the average NaCl concentration with different flow velocities as a function of the diffusion time, as shown in Figure 4.6. It is obvious that the average NaCl concentration increases as the increase of the diffusion time under three flow velocities. But the average NaCl concentration does not demonstrate significant difference among different flow velocities. So it indicates that the effect of the flow velocity is not the dominant factor in the diffusion of NaCl ions into the coating matrix.

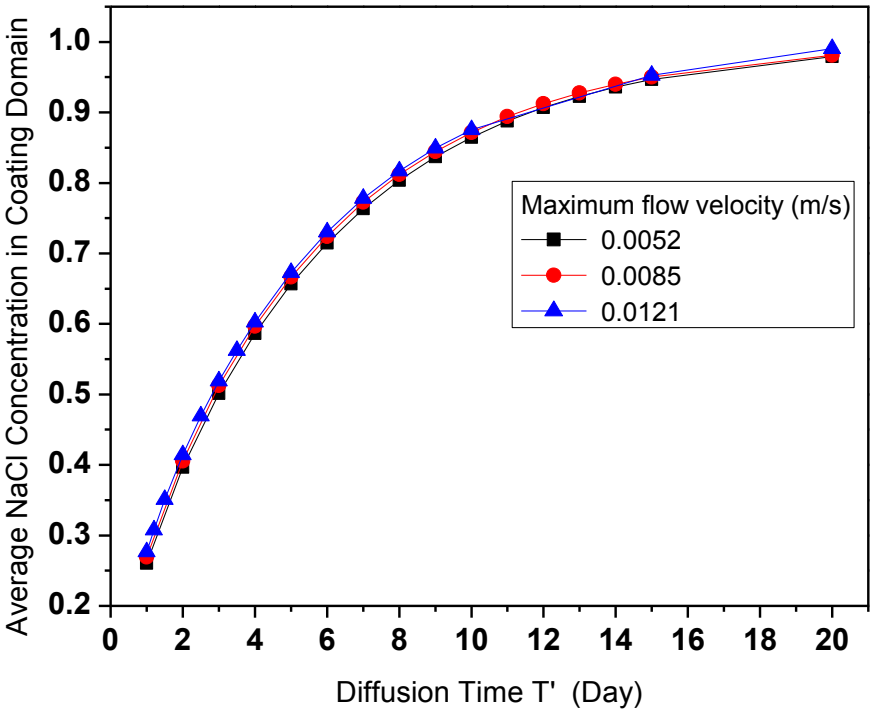

Figure 4.6. Average NaCl concentration in coating domain as a function of diffusion time under the maximum flow velocity of 0.0052, 0.0085, and 0.0121 m/s, respectively.

4.3.3. Simulated Coating's Impedance Modulus

In order to demonstrate the influence of the diffused NaCl ions on the coating's electrochemical property, we try to generate a relation between the NaCl concentration in the coating and the corresponding coating's impedance modulus.

Based on the NaCl concentration in the coating, the permittivity and conductivity of NaCl could be obtained from Equation 4-6 [8] and Equation 4-7 [9], respectively:

$$\varepsilon_s = \varepsilon_{sw} \cdot (1.0 - 3.742 \times 10^{-4} \cdot T \cdot c + 0.034 \cdot c^2 - 0.178 \cdot c + 1.515 \times 10^{-4} \cdot T - 4.929 \times 10^{-6} \cdot T^2) \quad (4\text{-}6)$$

where ε_s is the relative permittivity of NaCl solution with different concentrations; ε_{sw} is the relative permittivity of water at 25 ˚C, $\varepsilon_{sw} = 78.54$; T is the temperature of 25 ˚C; c is the concentration of NaCl, mol/L.

$$\sigma = B1 + B2 \cdot c$$
$$B1 = 0.086374 + 0.030606 \cdot T - 0.0004121 \cdot T^2 \quad (4\text{-}7)$$
$$B2 = 0.077454 + 0.001687 \cdot T + 0.00001937 \cdot T^2$$

where T is the temperature of 25 ˚C; c is the NaCl concentration, wt‰.

The evaluated coating system comprises the coating matrix, the diffused NaCl ions, and the water which is saturated in the coating before NaCl diffusion. Therefore, the system's effective permittivity and conductivity should be calculated by combining these elements based on Maxwell-Garnet equations as shown in Equation 4-8 and Equation 4-9 [10].

$$\varepsilon_{eff} = \varepsilon_p \frac{2\varepsilon_p + \varepsilon_s + 2VF(\varepsilon_s - \varepsilon_p)}{2\varepsilon_p + \varepsilon_s - VF(\varepsilon_s - \varepsilon_p)} \quad (4\text{-}8)$$

where ε_{eff} is the relative effective permittivity of the coating system; ε_p is the relative permittivity of the epoxy coating itself, $\varepsilon_p = 9$ [10]; ε_s is the relative permittivity of NaCl solution, which could be obtained from Equation 4-6; VF is the water volume fraction in the coating matrix; $VF = 8.8\%$ is chosen for the calculation, which comes from the experimental estimation.

$$\sigma_{eff} = \sigma_p \frac{2\sigma_p + \sigma_s + 2VF(\sigma_s - \sigma_p)}{2\sigma_p + \sigma_s - VF(\sigma_s - \sigma_p)} \tag{4-9}$$

where σ_{eff} is the effective conductivity of the coating system; σ_p is the conductivity of the epoxy coating itself, $\sigma_p = 1.45 \times 10^{-14}\ S/m$ [10]; σ_s is the conductivity of NaCl solution, which could be obtained from Equation 4-7; VF is defined the same as in Equation 4-8.

The capacitance of the evaluated coating system can be calculated in the following relation:

$$C = \frac{\varepsilon_0 \cdot \varepsilon_{eff} \cdot A}{d} \tag{4-10}$$

where ε_0 is the vacuum permittivity, $\varepsilon_0 = 8.854 \times 10^{-12}\ F/m$; ε_{eff} is the relative effective permittivity of the system, which could be obtained from Equation 4-8; A is the area of the coating surface, $A = 3.249 \times 10^{-3}\ m^2$ for the experimental sample; d is the thickness of the coating film, $d = 3.5 \times 10^{-5}\ m$.

The resistance of the evaluated coating system can be calculated from

$$R = \frac{d}{A \cdot \sigma_{eff}} \tag{4-11}$$

where σ_{eff} is the effective conductivity of the coating system, which could be obtained from Equation 4-9; A and d are defined the same as in Equation 4-10.

Therefore, by combing coating capacitance (Equation 4-10) and coating resistance (Equation 4-11), the impedance modulus could be obtained from Equation 4-12 [10],

$$\log(|Z|) = \log(R) - 0.5 \cdot \log[1 + (\omega \mathcal{C} R)^2] \quad (4\text{-}12)$$

where |Z| is the impedance modulus of the coating system, Ω; $\mathcal{C}$ is the coating system's capacitance, F, from Equation 4-10; R is the coating system's resistance, Ω, from Equation 4-11; ω is the angular frequency.

Above-mentioned calculation procedures could be summarized in the flow chart as shown in Figure 4.7. We calculate the impedance modulus as a function of the angular frequency from 10^{-2} Hz to 10^{5} Hz, which is the same as the testing frequencies by electrochemical impedance spectroscopy (EIS) measurement. We also calculate the impedance modulus on different diffusion periods under different flow velocities. We compare the impedance modulus on the first day and the final day to demonstrate the influence of diffused NaCl ions on the overall impedance modulus, as shown in Figure 4.8, for three different flow velocities. It is obvious that the impedance modulus is almost overlapped between the first day and the final day under the same flow velocity. It indicates that the diffused NaCl ions themselves have little effect on the coating's impedance modulus based on the simulated results. The convective diffusion of aggressive species (NaCl ions in this study) alone is not the dominant factor in changing the coating's electrochemical property.

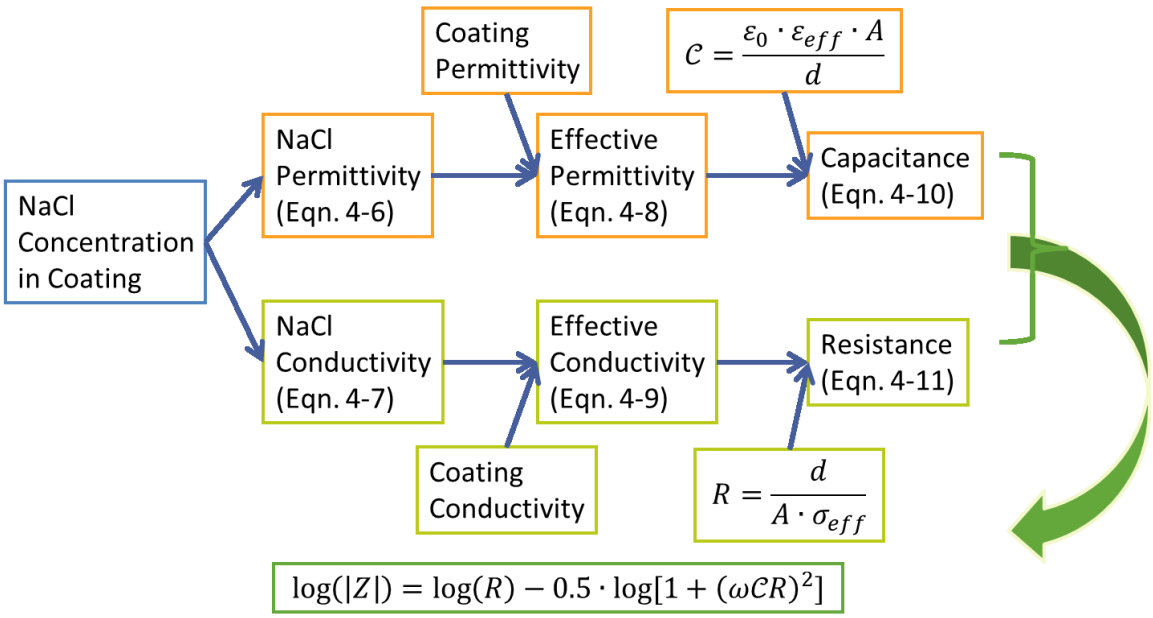

Figure 4.7. Calculation procedures for coating's impedance modulus based on the NaCl concentration in the coating matrix.

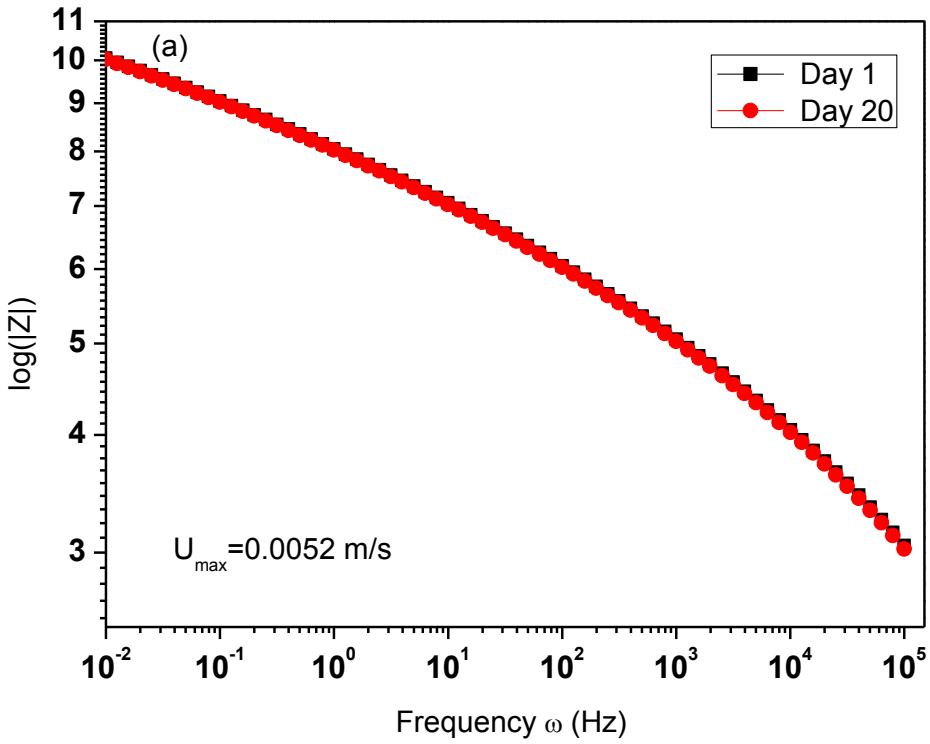

Figure 4.8. Simulated impedance modulus as a function of frequency and diffusion time for coatings under three flow velocities, (a) Umax = 0.0052 m/s, (b) Umax = 0.0085 m/s, (c) Umax = 0.0121 m/s.

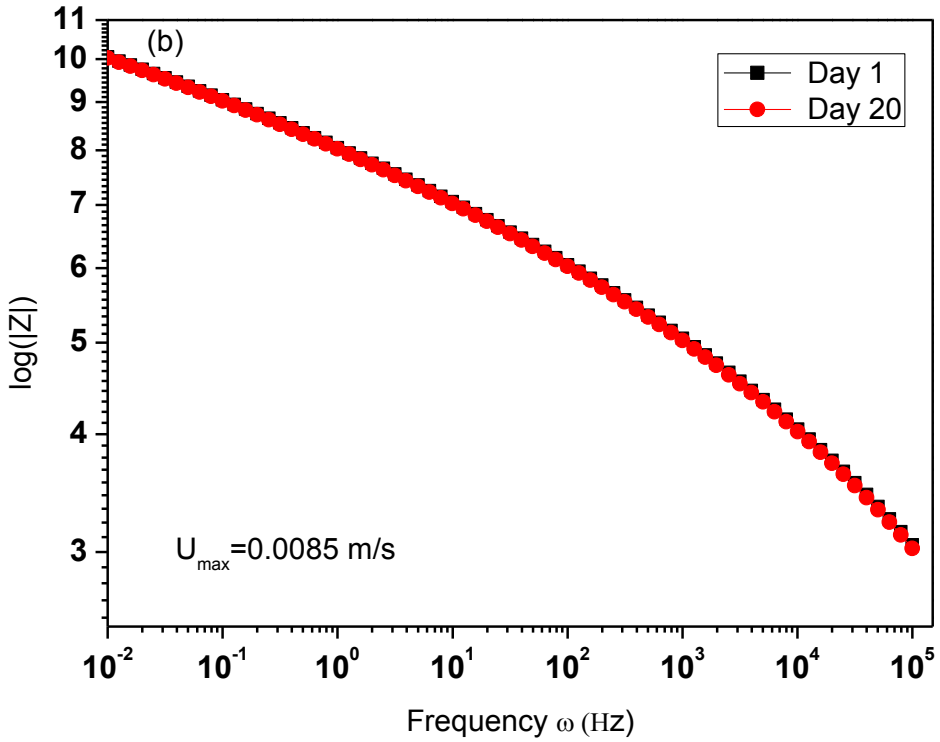

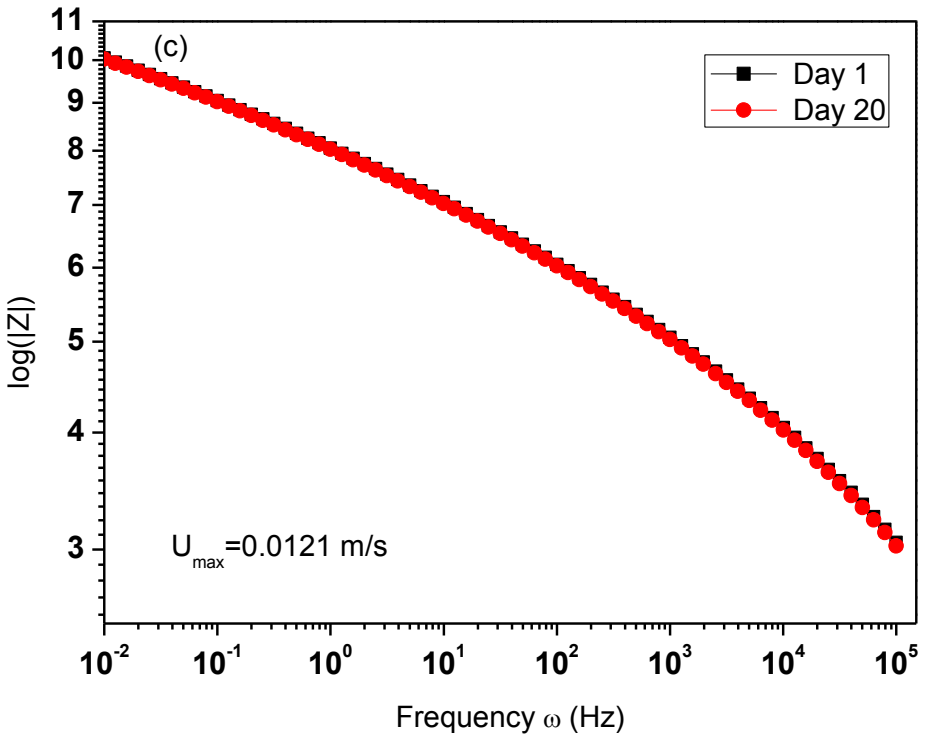

Figure 4.8. Simulated impedance modulus as a function of frequency and diffusion time for coatings under three flow velocities, (a) Umax = 0.0052 m/s, (b) Umax = 0.0085 m/s, (c) Umax = 0.0121 m/s, (continued).

4.4. Conclusions

The study in this chapter simulated the convective diffusion process of NaCl ions into the epoxy coating. The finite difference model successfully simulated the diffusion process by using MATLAB. The concentration distribution as well as the average concentration in the coating domain could be obtained directly from the simulation. By comparing the average concentration in the coating under different flow velocities, it is obvious that flow velocity has no significant effect on the diffusion of NaCl ions at the same diffusion period. Moreover, by relating the concentration of NaCl in the coating and coating's impedance modulus, it is clear that the convective diffusion of NaCl ions alone is not the dominant factor in influencing coating's electrochemical property.

4.5. References

[1] S. Zhang, S. Li, X. Luo, W. Zhou, Mechanism of the significant improvement in corrosion protection by lowering water sorption of the coating, *Corrosion Science*, **42** (2000) 2037-2041.

[2] J. Hu, J. Zhang, C. Cao, Determination of water uptake and diffusion of Cl^- ion in epoxy primer on aluminum alloys in NaCl solution by electrochemical impedance spectroscopy, *Progress in Organic Coatings*, **46** (2003) 273-279.

[3] M.M. Wind, H.J.W. Lenderink, A capacitance study of pseudo-fickian diffusion in glassy polymer coatings, *Progress in Organic Coatings*, **28** (1996) 239-250.

[4] J. Zhang, J. Hu, J. Zhang, C. Cao, Studies of impedance models and water transport behaviors of polypropylene coated metals in NaCl solution, *Progress in Organic Coatings*, **49** (2004) 293-301.

[5] N. Fredj, S. Cohendoz, S. Mallarino, X. Feaugas, S. Touzain, Evidencing antagonist effects of water uptake and leaching processes in marine organic coatings by gravimetry and EIS, *Progress in Organic Coatings*, **67** (2010) 287-295.

[6] F. Galliano, D. Landolt, Evaluation of corrosion protection properties of additives for waterborne epoxy coatings on steel, *Progress in Organic Coatings*, **44** (2002) 217-225.

[7] T. Chen, G. Zhang, Transmission process of chemical engineering, Chemical Industry Press, Beijing, China, 2004.

[8] A. Peyman, C. Gabriel, E.H. Grant, Complex permittivity of sodium chloride solutions at microwave frequencies, *Bioelectromagnetics*, **28** (2007) 264-274.

[9] W. Ellison, A. Balana, G. Delbos, K. Lamkaouchi, L. Eymard, C. Guillou, C. Prigent, New permittivity measurements of seawater, *Radio Science*, **33** (1998) 639-648.

[10] O.A. Stafford, B.R. Hinderliter, S.G. Croll, Electrochemical impedance spectroscopy response of water uptake in organic coatings by finite element methods, *Electrochimica Acta*, **52** (2006) 1339-1348.

CHAPTER 5. EFFECTS OF THE WORKING FLUID ON ORGANIC COATING DEGRADATION: NACL SOLUTION VERSUS PURE WATER

5.1. Introduction

Various studies have investigated the degradation behavior of organic coatings. Electrolytes like NaCl solution are most often adopted for corrosion studies, e.g. Refs. [1-6]. In addition to NaCl solutions, the influence of pure water (e.g. deionized or distilled water) on the corrosion of metallic materials has been investigated [7-10]. Frequently, pure water was used in gravimetric methods to study water diffusion in free-standing films, e.g. Refs. [11-13]. Taylor and Moongkhamklang investigated the initial water entry into epoxy coatings using distilled water and NaCl solutions as working fluids [14]. Their usage of distilled water had validated the autofluorescence properties of epoxy coatings, which served as a foundation for the employment of fluorescence microscopy in their study. They observed a higher density of fluorescence sites on coatings exposed to distilled water than samples exposed to electrolyte solutions. However, this study only provided information for initial water entry and did not focus on the time-dependent degradation behavior of the coatings. An FTIR/ATR method was employed to investigate the non-Fickian sorption and desorption of pure water and electrolyte solution into epoxy coatings [15]. Water diffusion coefficients were obtained in that study but the long-term coating degradation was discounted. Different from existing works, this study focuses on the influence of working fluids on the long-term deterioration of coatings in terms of its corrosion protective functions, or barrier properties, as a result of coating degradation and

water uptake. It is the first time that the influence of pure water as working fluid was compared with that of NaCl solution for the afore-mentioned purpose and scope.

It is of great fundamental importance to study the influence of different working fluids on the degradation of organic coatings. The coating degradation could be influenced by water uptake and ion diffusion determined by both the working fluid and the coating barrier properties. For example, study has shown that the cathodic delamination rate of a polyester coating on mild steel was greatly influenced by the diffusion of anions; as a result, the delamination rate in KCl solution is higher than that in KBr solution [16]. Once the aggressive species, like water, oxygen, and ions, have percolated through organic coatings to the coating-metal interface, degradation is considered to take place. Cathodic electrochemical reaction then takes place by consuming water and oxygen. Meanwhile, the metal substrate is corroded as a result of anodic reaction. Also, the coating will delaminate from the substrate and small "pockets" which contain corrosion products will be generated in the coating-metal interface [16, 17]. Due to the oxygen involved in the cathodic reaction, the corrosion process can be influenced by the concentration of dissolved oxygen which percolates to the coating-metal interface [18-21]. As a result, the oxygen concentration in the working fluid may be one of the important influencing factors for the corrosion process. The concentration of dissolved oxygen in pure water is higher than that in NaCl solutions under same conditions. For example, pure water contains 9.1 mg/L dissolved oxygen at 20˚C under 101.1 kPa, while sea water with a salinity of 35 has 7.2 mg/L dissolved oxygen under the same condition [22]. Hence it is compelling to evaluate the coating degradation by using

pure water as the working fluid in which the oxygen concentration is different from that in NaCl solutions.

The aim of the study in this chapter is to improve the understanding of barrier properties of organic coatings by differentiating the influences of pure water and NaCl solution on the degradation and water uptake behavior of coatings. This chapter will first compare the influence of the two different working fluids on coating degradation as characterized in line by electrochemical impedance spectroscopy (EIS) measurements. The EIS method has been found to be the major, standard, and adequate investigation tool to evaluate organic coatings. It has been employed in our previous study on coating degradation in flowing fluids including pure water [23]. The EIS spectra will then be interpreted by suitable equivalent circuit models. We then present the time evolution of coating resistance, capacitance, and the water volume fraction of the coatings. The time dependent behaviors of the afore-mentioned properties of the coatings immersed in pure water will then be discussed by comparing with those for coatings in NaCl solution.

5.2. Materials and Methods

5.2.1. Coatings and Sample Preparation

The commercially available polyurethane and epoxy based clear coatings were chosen for evaluation. These coatings have been widely used as base coat in marine coatings [24-28]. We purposefully chose different coatings, or, similar coatings with different curing agents and/or processing methods, to increase the diversity of the coating samples and to generalize our conclusions. A polyurethane coating, denoted as P, was composed of 67.4 wt% acrylic polyol (Joncryl 906, BASF), 15.0 wt% polyisocyanates (DESMODURN 3200, Bayer Material Science), 17.0 wt% tertiary butyl acetate (TBA,

ASHLAND), and 0.6 wt% dibutyltin dilaurate (DBTD, Sigma-Aldrich), in addition to one drop of polyether modified polydimethylsiloxane (BYK-300, Chemie). Coating P was formulated by mixing all components well before application. The epoxy resin, EPON 828, was crosslinked with three different amine curing agents with different AHEW numbers to generate three types of epoxy/amine coatings. The epoxy coating, denoted as E1, was formulated by base component, 63.5 wt% epoxy resin (EPON Resin 828, Miller-Stephenson), 30.3 wt% modified mannich based curing agent (EPI-CURE Curing agent 3251, AHEW 350–390, Resolution Performance Products), and 6.2 wt% xylene. Another epoxy coating, denoted as E2, was composed of 73.3 wt% epoxy resin (EPON Resin 828, Miller-Stephenson) as the base component, 20.3 wt% cycloaliphatic amine (Amicure PACM, AHEW 54.2, Air Products) as the epoxy curing agent, and 6.4 wt% xylene. The third epoxy coating, denoted as E3, was composed of EPON Resin 828 (Hexion Specialty Chemicals) as the base component, and EPIKURE 3164 as curing agent (AHEW 256, Hexion Specialty Chemicals). The weight ratio of curing agent to EPON Resin 828 is 1.36. All four coatings that we used were clear coatings with no pigments, so their barrier property against water uptake is provided by the polymer network only; in this way, the ingress behavior of water into these coatings may be comparable. We used the same marine coating as described in Chapter 2.

Q-panel standard steel panels (S-36 from Q-Panel Lab Products) were used as the metal substrate. Before painting, the panels were pretreated by abrasion with 320 and 600 grit sand paper, and then cleaned with acetone and hexane. The coatings of P, E1, and E2 were applied by the draw-down method and cured at 80 ˚C for 0.5 h. The epoxy coating E3 was applied by air spraying and cured at room temperature for 24 h. All the coating

samples were allowed to completely dry for several days at the room temperature before testing. The sample preparation for marine coating is described in Chapter 2.

5.2.2. Experimental Setup and EIS Measurement

The working fluids adopted in this study for coatings immersion were pure water and 3.5 wt% NaCl solution. The 3.5 wt% NaCl solution was prepared using the same pure water. The pH and conductivity value of the pure water and 3.5 wt% NaCl solution was measured as shown in Table 5.1. The fluid samples for pH and conductivity tests were open to the air at the room temperature, which was under the same condition as the immersion test. The pH and conductivity values were observed to be constant for blank solutions (without coating immersion), when the property of working fluids was monitored during the experiment. The conductivity value for the pure water employed in this study was measured about 167.5 μs/cm, which is larger than the reported value for highly purified water such as deionized or distilled water [7, 29, 30], but it is still smaller than that of the 3.5 wt% NaCl solution by orders of magnitude. In the current work, we are not interested in studying the coating degradation in highly purified water, since its properties, especially the ion concentration is almost impossible to maintain during coating immersion due to the exposure to the coating sample and the air.

The traditional three-electrode EIS setup was employed for evaluating clear coating degradation, as shown in Figure 2.5 in Chapter 2. Three samples of each coating system were tested for pure water or NaCl solution immersion. For marine coating degradation in flowing fluids, the experimental setup and EIS measurement was also the same as described in Chapter 2. The EIS measurement conditions, coating thickness, and gloss measurement are described in Chapter 2.

Table 5.1. Property for 3.5 wt% NaCl solution and pure water.

Working Fluid	pH	Conductivity
3.5 wt% NaCl	6.70 ± 0.1	57.5 ± 0.1 ms/cm
Pure Water	7.58 ± 0.2	167.5 ± 14.3 μs/cm

5.3. Results and Discussion

5.3.1. EIS Results

Since all samples of each coating system behaved similarly under the same experimental condition, we present results for one representative sample for each coating system. As shown in Figure 5.1 (a) for coating P immersed in the 3.5 wt% NaCl solution, the impedance modulus is plotted as a function of the frequency applied in EIS tests as well as immersion time. A similar figure for pure water immersion is shown in Figure 5.1 (b). For both working fluids, the low frequency impedance modulus decreases with the increase of the immersion time. The decrease rate of the impedance modulus is more significant at the initial immersion, followed by a relatively slower decrease. This behavior demonstrates that barrier property of organic coatings is deteriorated by long-term (15 days in our experiments) immersion in working fluids, and eventually, the coating loses its protective property. Since all the clear coatings show similar EIS spectra, the Bode plot of coating P is chosen to present the coating's degradation process.

The impedance modulus of EIS spectra at low frequency serves as a strong indicator of the corrosion resistance of coating samples [31, 32]. To illustrate the change in the coating's barrier property during immersion, a plot of the relative impedance modulus at low-frequency (0.01 Hz) as a function of time is shown in Figure 5.2 for all

samples of four types of clear coatings. The relative low-frequency impedance modulus is obtained by normalizing the low-frequency impedance modulus with the modulus at the initial immersion. The low-frequency (0.01 Hz) values for representative samples of each type of coating system at the initial immersion are listed in Table 5.2. The table shows that the initial impedance values are at the same order of magnitude for the same coating system immersed in two different working fluids.

We observe from Figure 5.2 that the universal trend among all coating samples is that the relative impedance modulus shows a faster decrease in the first few days, and then it maintains a relative slow decrease rate during immersion. This phenomenon is the same for both 3.5 wt% NaCl and pure water immersion. However, the relative impedance modulus decreases more substantially for coatings immersed in pure water, as indicates that these coatings are more sensitive to pure water than the NaCl solution.

We are interested in comparing the trend of relative impedance modulus of coating samples immersed in pure water with that in 3.5 wt% NaCl solution. Although the impedance of pure water contributes to the original EIS data, relative impedance values can discount the influence of the absolute magnitudes in order to demonstrate well the changes taking place over time. Moreover, the property of pure water throughout this study is almost constant and its impedance ($10^3 – 10^4$ Ω) is much smaller than that of the coating system, so the variations of the measured impedance modulus are believed to represent the changes in coating's barrier property.

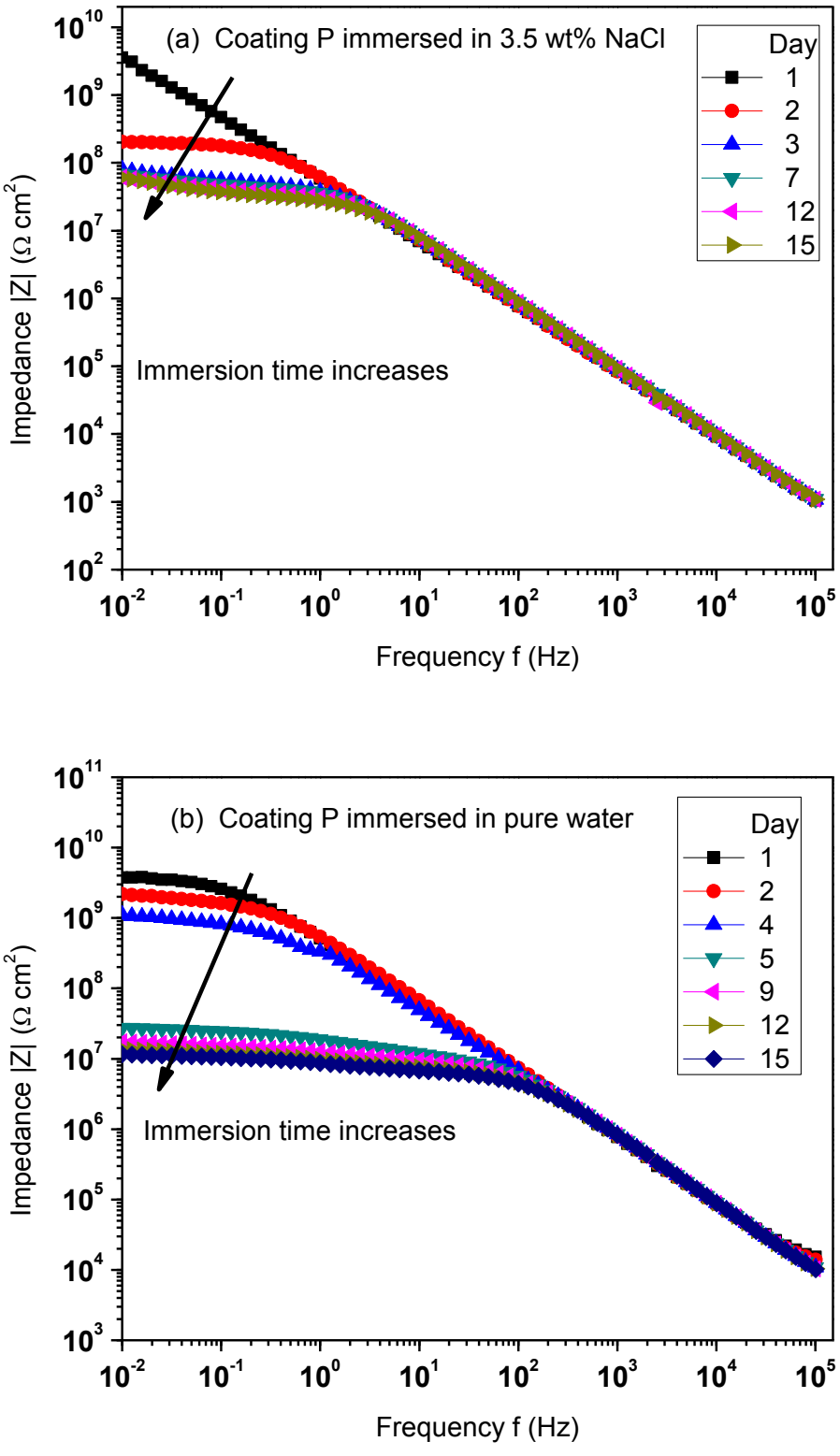

Figure 5.1. Impedance modulus as a function of frequency for coating P immersed in (a) 3.5 wt% NaCl solution and (b) pure water.

Table 5.2. Initial impedance at 0.01 Hz for coating samples immersed in 3.5 wt% NaCl solution and pure water.

Coating	3.5 wt% NaCl (Ω)	Pure Water (Ω)
P	5.05×10^8	5.32×10^8
E1	5.24×10^6	6.01×10^6
E2	8.16×10^9	1.91×10^{10}
E3	1.31×10^6	4.68×10^6

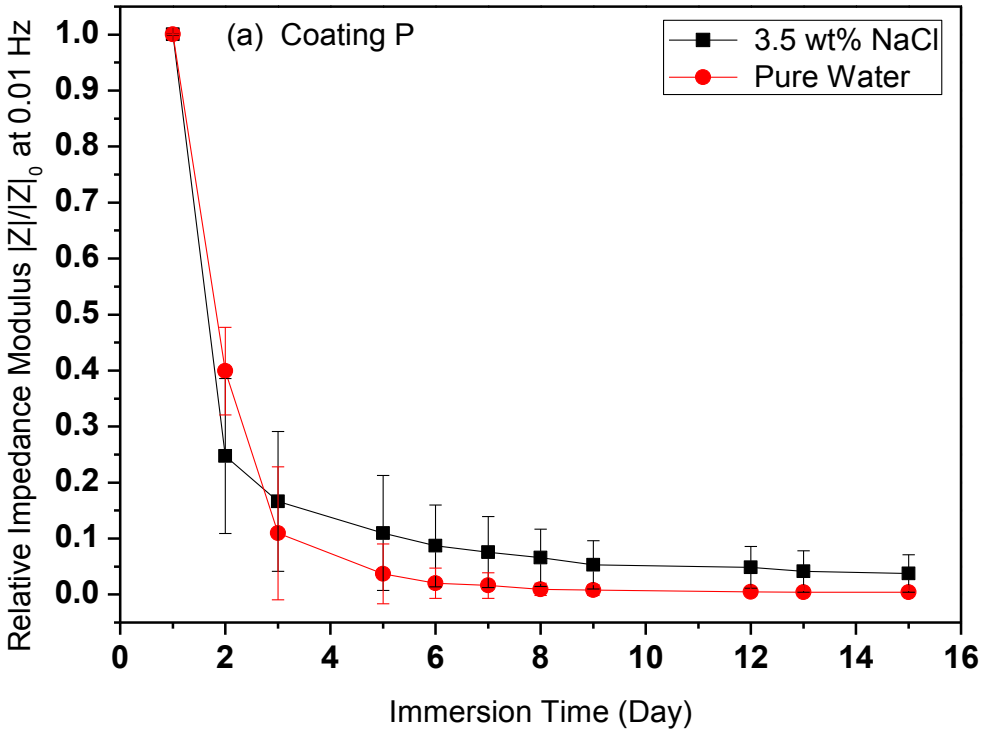

Figure 5.2. Relative impedance modulus as a function of immersion time for coating samples of (a) P, (b) E1, (c) E2, (d) E3 immersed in 3.5 wt% NaCl solution and pure water.

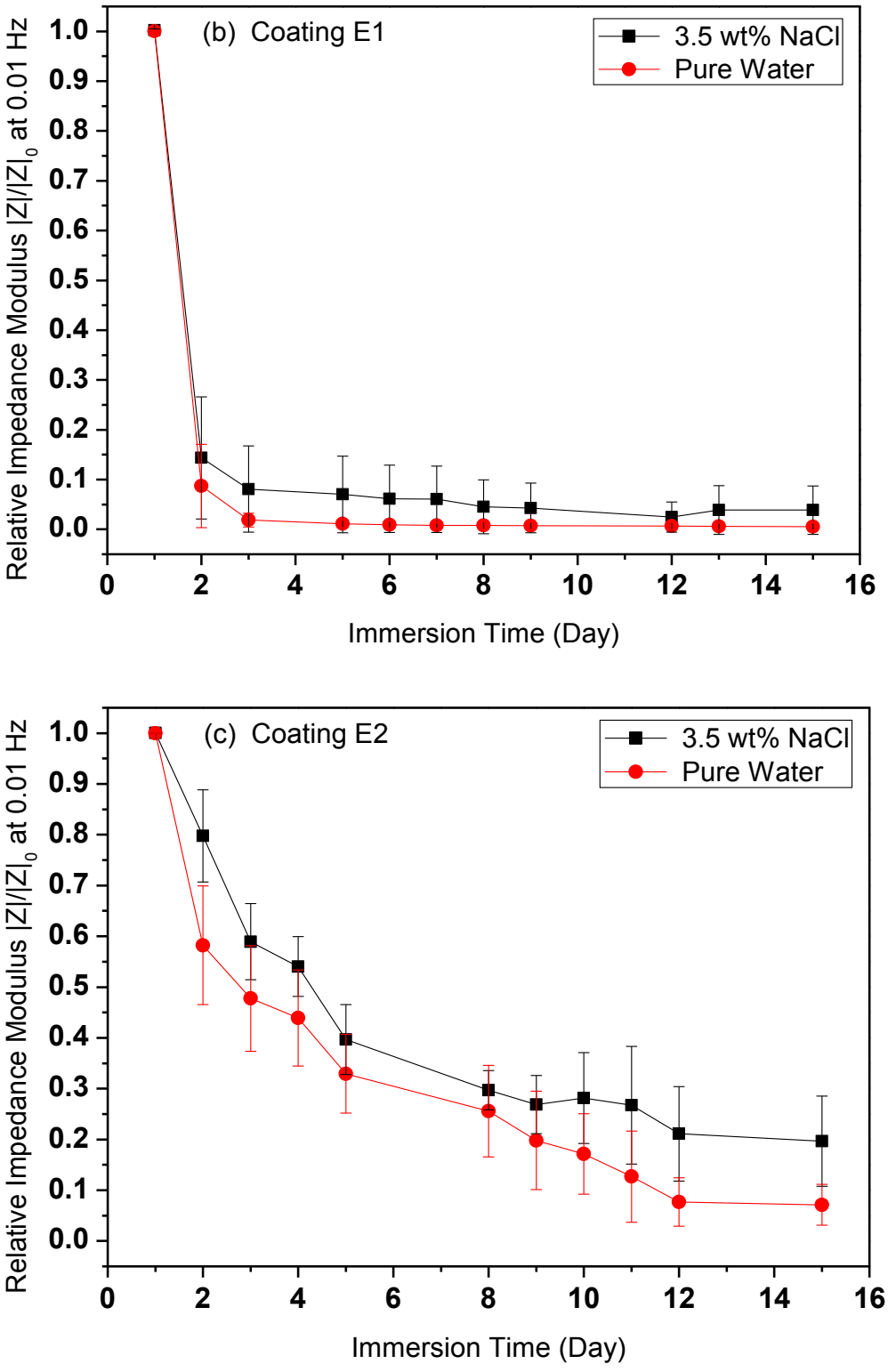

Figure 5.2. Relative impedance modulus as a function of immersion time for coating samples of (a) P, (b) E1, (c) E2, (d) E3 immersed in 3.5 wt% NaCl solution and pure water, (continued).

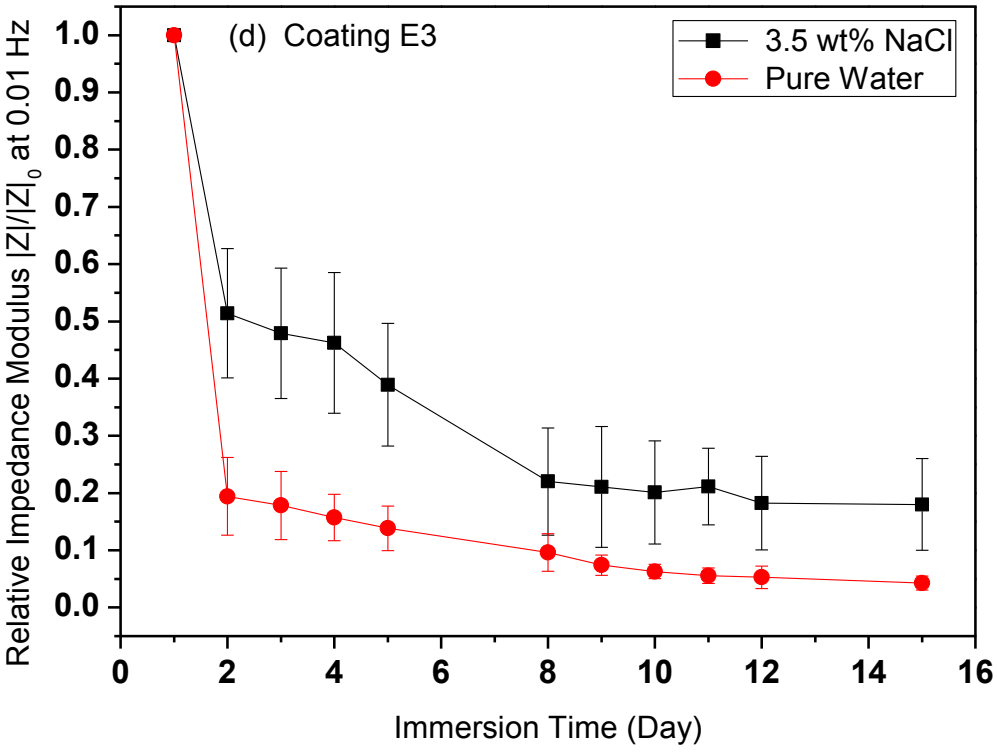

Figure 5.2. Relative impedance modulus as a function of immersion time for coating samples of (a) P, (b) E1, (c) E2, (d) E3 immersed in 3.5 wt% NaCl solution and pure water, (continued).

5.3.2. Equivalent Circuit Modeling

Equivalent circuit models are employed to interpret EIS data and provide a physical explanation for the evaluated phenomenon. The most commonly used model for degraded coating is shown in Figure 5.3 (a) [33, 34]. This model considers the degradation of coatings with time since water percolates into the organic coating while a new liquid-metal interface is formed beneath the coating. R_s is solution resistance; C_c is coating capacitance; R_{po} is pore resistance, which is the resistance for ions transport within the coating; C_{dl} is double layer capacitance, which is formed as ions from the solution are attracted to the electrode surface; R_{ct} is charge transfer resistance, which

describes the situation where kinetically controlled electrochemical reactions take place at the electrode. When the water percolates into the coating, we may assume that the coating has delaminated within a small area, where a pocket has formed underneath the coating with the working fluid. Thus, the interface between the pocket of working fluid and the metal substrate may be modeled as a double layer capacitance in parallel with a charge transfer resistance.

When we refer to the Nyquist plot (complex plane plot) of the EIS data, we observe the depressed semicircles for all samples, which indicate that capacitors in real EIS experiments do not behave ideally. As a result, we need to consider a constant phase element (CPE), which is used to simulate the non-ideal capacitance behavior. Therefore, we employed a second degraded coating model by modifying ideal capacitance with CPE, as shown in Figure 5.3 (b) [33-37]. The impedance of a CPE is given mathematically by

$$Z_{CPE} = \frac{(j\omega)^{-\alpha}}{Y} \tag{5-1}$$

where ω is the angular frequency; α is a dimensionless parameter; Y is a parameter with dimensions $\Omega^{-1}\cdot s^{\alpha}$ representative for constant phase element. Generally, $0 < \alpha < 1$; when $\alpha = 1$ and $Y = C$, the CPE behaves like an ideal capacitor with capacitance C; when $\alpha = 0$, a resistance is represented. Similar equivalent circuit models are also found to simulate the degradation behavior of organic coatings in existing publications [33-37].

Analysis of EIS spectra is performed using Echem Analyst software by Gamry Instruments. By comparing two degraded coating models, Model 2 presents a better agreement to the experimental data, with a smaller value of the fitting goodness, which is the weighted sum of squares of error between the model and the data. Coating P immersed in NaCl solution and pure water are shown as fitting examples for both models

in Figure 5.4. The fitting results for each coating system are presented in Figure 5.5. The goodness of fitting is summarized in Table 5.3, comparing with the Kramers Kronig transform [38].

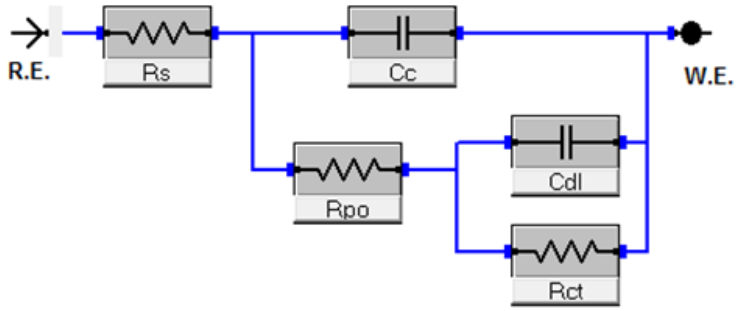

(a) Degraded Coating Model 1

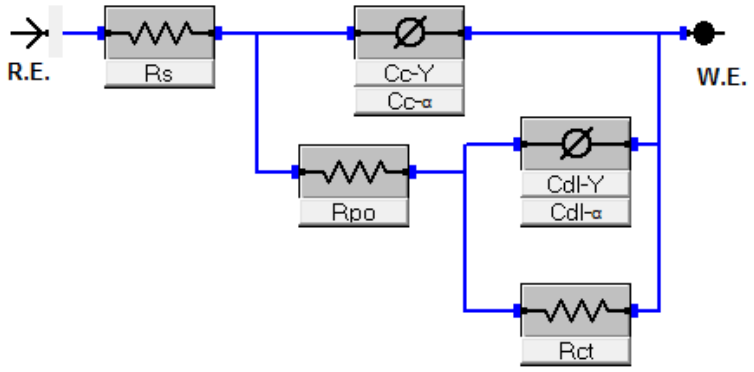

(b) Degraded Coating Model 2

Figure 5.3. Equivalent circuit model used for the impedance analysis of coating samples immersed in 3.5 wt% NaCl solution and pure water. R_s is solution resistance; C_c is coating capacitance; R_{po} is pore resistance; C_{dl} is double layer capacitance; R_{ct} is charge transfer resistance.

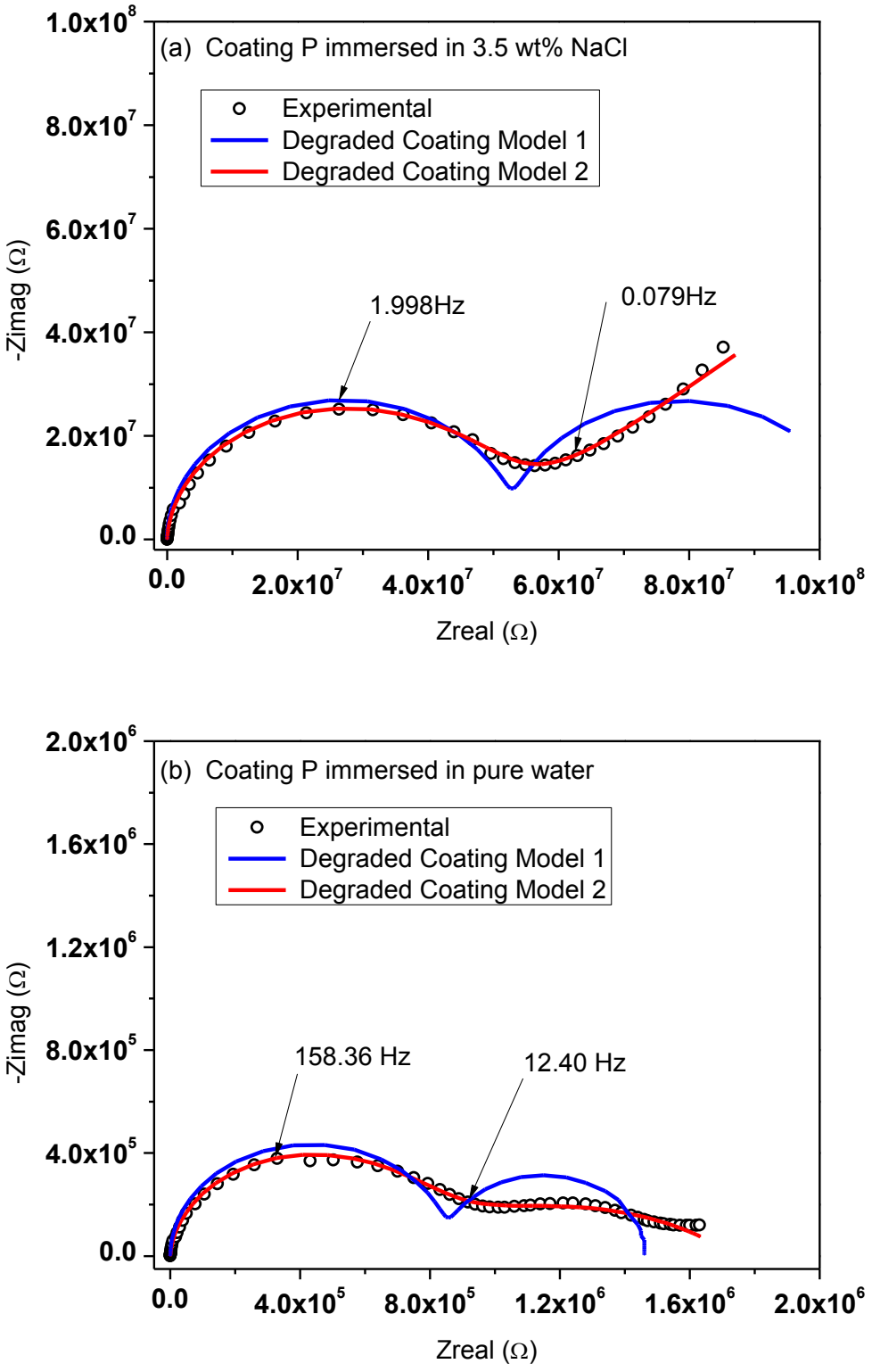

Figure 5.4. The Nyquist plots for experimental data and fitting results by different models for coating P immersed in (a) 3.5 wt% NaCl solution on Day 8 and (b) pure water on Day 15.

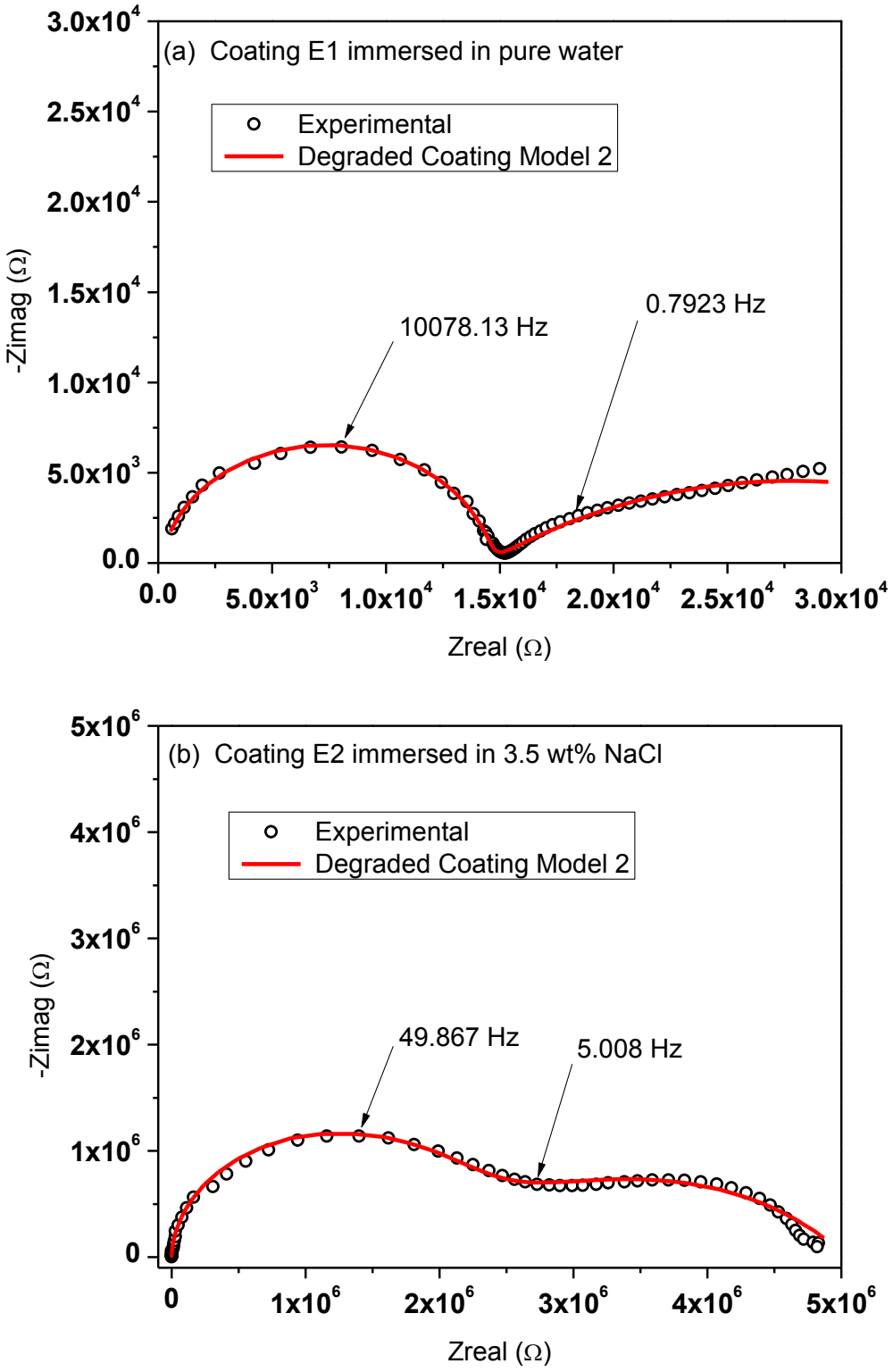

Figure 5.5. The Nyquist plots for experimental data and fitting results by degraded coating model 2. (a) Coating E1 immersed in pure water on Day 7; (b) coating E2 immersed in 3.5 wt% NaCl on Day 3; (c) coating E3 immersed in 3.5 wt% NaCl on Day 2.

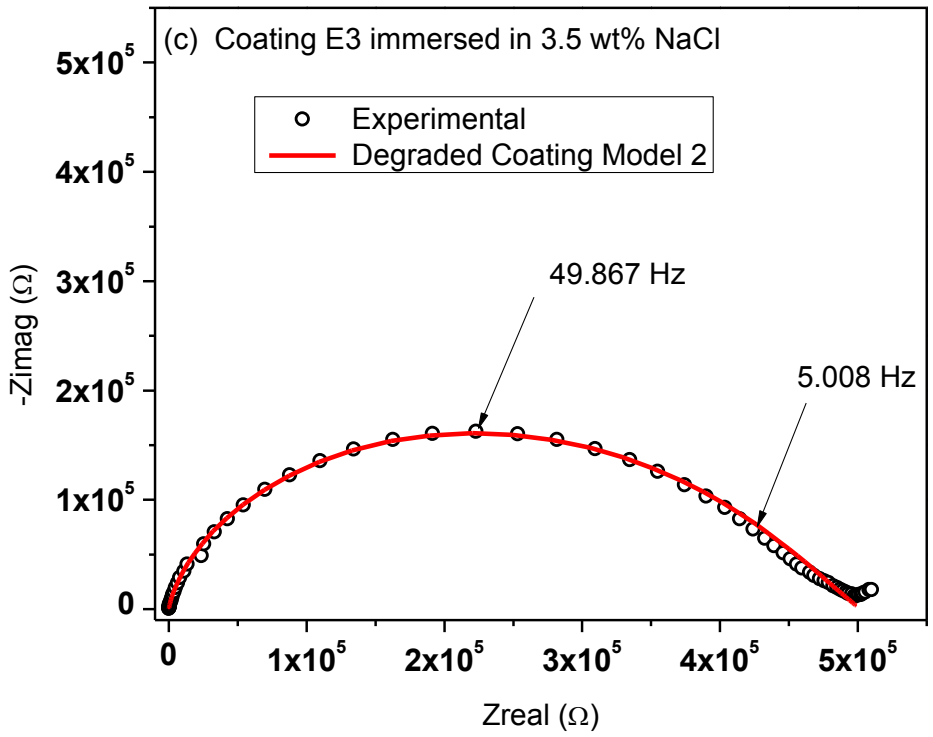

Figure 5.5. The Nyquist plots for experimental data and fitting results by degraded coating model 2. (a) Coating E1 immersed in pure water on Day 7; (b) coating E2 immersed in 3.5 wt% NaCl on Day 3; (c) coating E3 immersed in 3.5 wt% NaCl on Day 2, (continued).

Table 5.3. Goodness of fit for different coating systems.

Coating	Working Fluid	Immersion Time	Model 2	Kramers Kroning
P	NaCl solution	Day 8	1.31×10^{-3}	9.68×10^{-4}
	Pure water	Day 15	6.80×10^{-4}	4.81×10^{-4}
E1	NaCl solution	Day 15	7.84×10^{-4}	1.04×10^{-4}
	Pure water	Day 7	4.16×10^{-4}	1.53×10^{-4}
E2	NaCl solution	Day 3	1.28×10^{-3}	7.54×10^{-4}
	Pure water	Day 15	3.43×10^{-3}	2.59×10^{-3}
E3	NaCl solution	Day 2	5.22×10^{-4}	1.98×10^{-4}
	Pure water	Day 3	7.55×10^{-4}	4.38×10^{-5}

5.3.3. Coating Resistance and Capacitance

In order to compare the transient behavior of different samples of the same coating immersed in 3.5 wt% NaCl and pure water, we choose to analyze the relative values of the modeling elements in the afore-mentioned equivalent circuit model (degraded coating model 2). The relative values are obtained by normalizing the element values with those at initial immersion. The values of model elements at initial immersion are listed in Table 5.4. Figure 5.6 shows the relative pore resistance of Coating P, E1, E2, and E3 as a function of immersion time under 3.5 wt% NaCl solution and pure water immersion. The relative values of the pore resistance decreases as the immersion time increases for all tested coatings, especially in the first few days; this trend is similar to the evolution of relative impedance modulus as shown in Figure 5.2. The coating resistance,

presented by the pore resistance in the equivalent circuit model, is an important parameter in the assessment of coating performances; its magnitude at a given time indicates the state of degradation [39]. Coatings with high resistance will be expected to perform better than those with low resistance. The decrease in the pore resistance values of the coating samples shows the deteriorating barrier property of the coatings in both NaCl solution and pure water. We also observe that the pore resistance of the coatings immersed in pure water decreases more substantially than that in the NaCl solution. While smaller values of the pore resistance implies faster ion diffusion in the coatings, the faster decrease in the pore resistance may reflect a higher rate in coating degradation, which was observed for samples immersed in pure water.

Table 5.4. Initial values of model elements for coating samples employed to plot Figures 5.6. and 5.7.

Coating	**Working Fluid**	**R_{po} (Ω)**	**C_c (F)**
P	NaCl solution	6.66×10^{7}	9.30×10^{-10}
	Pure water	6.89×10^{7}	9.20×10^{-10}
E1	NaCl solution	9.52×10^{4}	5.42×10^{-10}
	Pure water	8.40×10^{4}	5.58×10^{-10}
E2	NaCl solution	4.97×10^{8}	7.67×10^{-10}
	Pure water	1.62×10^{9}	6.90×10^{-10}
E3	NaCl solution	1.12×10^{6}	1.61×10^{-9}
	Pure water	1.05×10^{6}	1.43×10^{-9}

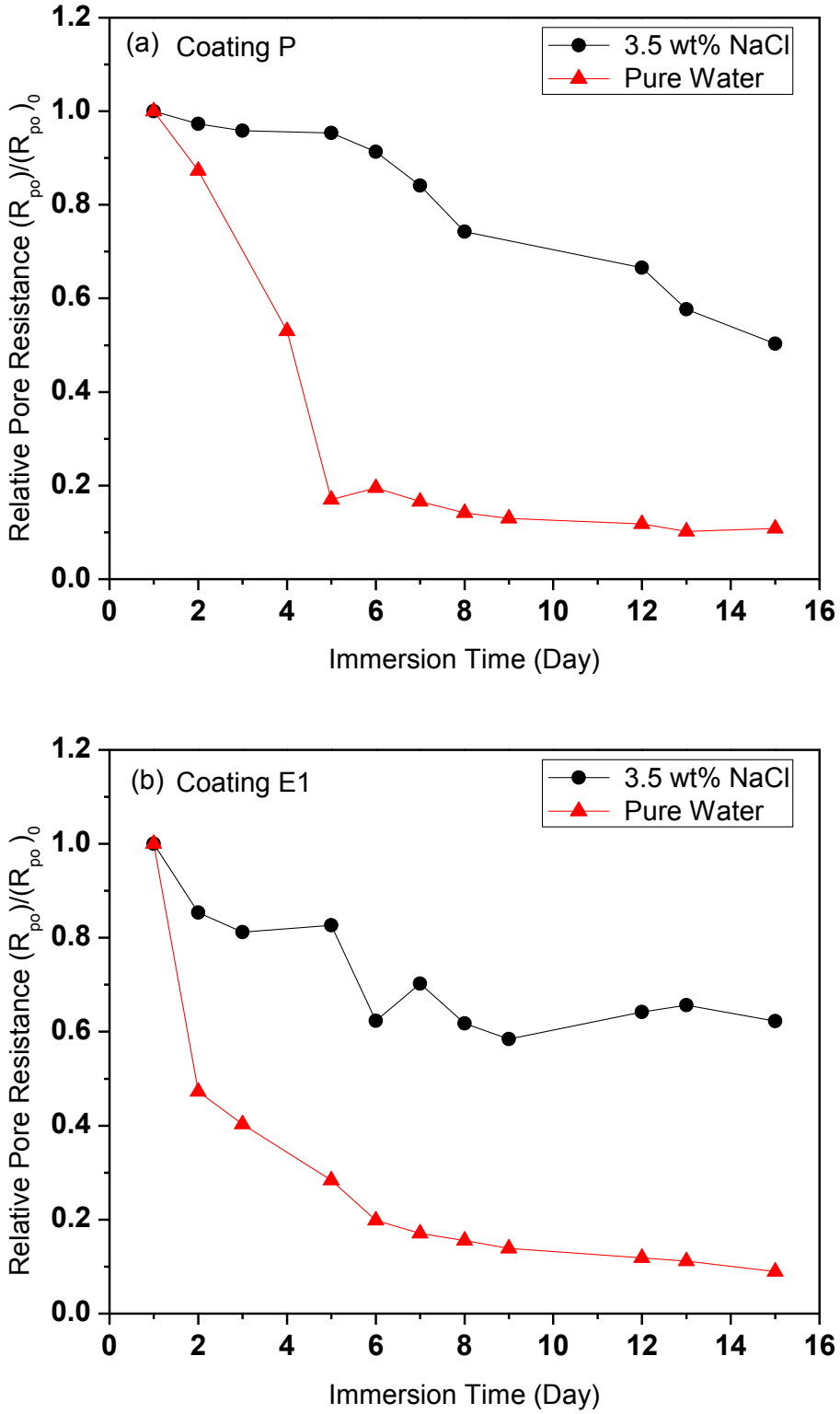

Figure 5.6. Relative pore resistance as a function of immersion time for coating samples immersed in 3.5 wt% NaCl solution and pure water. (a) Coating P; (b) coating E1; (c) coating E2; (d) coating E3.

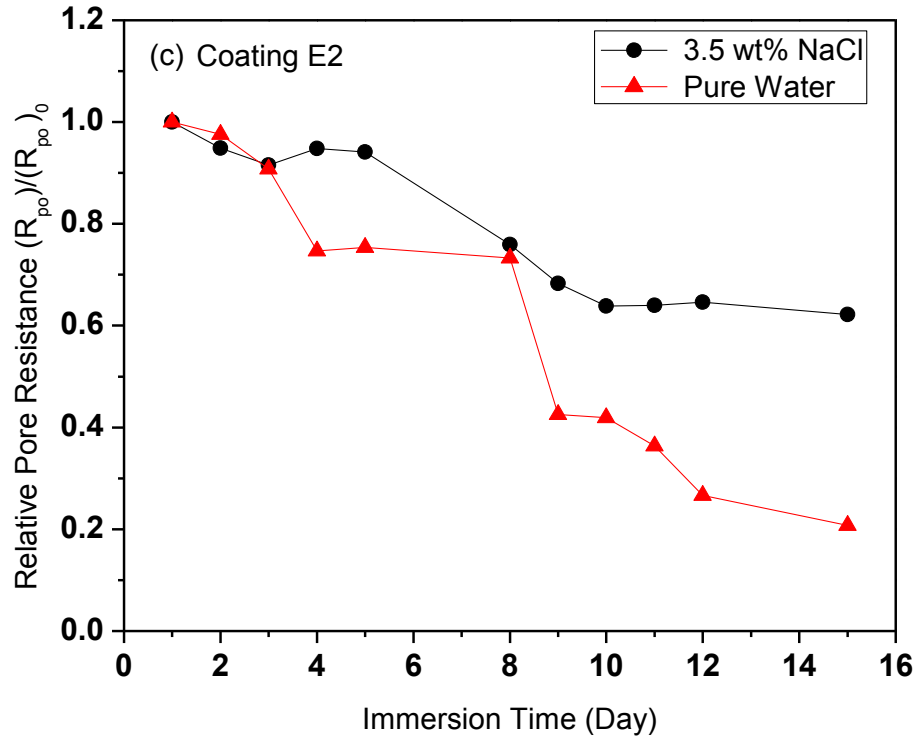

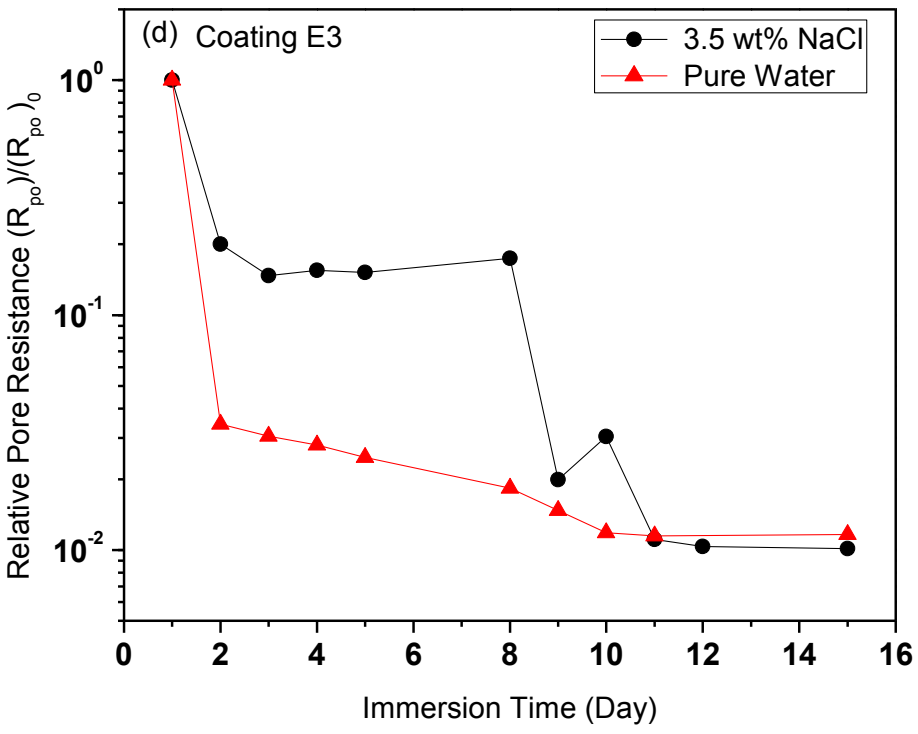

Figure 5.6. Relative pore resistance as a function of immersion time for coating samples immersed in 3.5 wt% NaCl solution and pure water. (a) Coating P; (b) coating E1; (c) coating E2; (d) coating E3, (continued).

The coating capacitance (C_c) can be calculated using the following expression [17, 38, 40, 41]:

$$C_c = Y^{1/\alpha}\left(\frac{1}{R_s} + \frac{1}{R_{po}}\right)^{(\alpha-1)/\alpha} \quad (5\text{-}2)$$

where Y, α, R_s, and R_{po} are modeling elements for the equivalent circuit presented earlier in Figure 5.3 (b). The time evolution of coating capacitance (C_c) for four coatings immersed in the two working fluids is shown in Figure 5.7. The relative coating capacitance increases substantially with immersion time for all coating samples immersed in the NaCl solution and pure water during initial immersion of the first few days (which depend on different coatings materials and application procedures). Afterwards, the capacitance becomes almost independent on the immersion time. The increase in coating capacitance is due to the uptake of water, oxygen, and ions when the coating is exposed to an aggressive environment. Since the relative permittivity of water (80.4 at 20˚C) is much higher than that of organic coatings (usually between 2 and 8), the water uptake brings an increase of the apparent permittivity of the entire coating system, which leads to the increase of the coating capacitance. The rapid increase of coating capacitance in the initial period suggests that water is percolated into coatings, and the slower increase or steady value of coating capacitance demonstrates that the water uptake has reached saturation. We also observe that the increase in coating capacitance is greater in the pure water and different coating systems present similar absorption process.

We calculate the water volume fraction based on the Brasher and Kingsbury (BK) equation [42]. The BK relation is the most frequently used equation to estimate the water content in a coating matrix:

$$\emptyset = \frac{\log(C_t/C_0)}{\log\varepsilon_w} \tag{5-3}$$

where $\emptyset$ is the water volume fraction in the coating; C_t is the coating capacitance at time t; C_0 is the initial coating capacitance; ε_w is the relative permittivity of working fluid. For the calculation in this chapter, we adopt $\varepsilon_w = 80.4$ as the relative permittivity of pure water at 20˚C, while we choose $\varepsilon_w = 74.0$ for the 3.5 wt% NaCl solution at 20˚C [43]. The BK relation could be used for the pure water in this study, since the conductivity value of the pure water (as shown in Table 5.1) in this study is larger than the minimum conductivity value (2.0×10^{-5} $(\Omega\cdot cm)^{-1}$) for BK equation, which meets the assumption of the BK equation, although the BK method cannot be used for coatings immersed in distilled water which has too low a conductivity.

The water volume fraction in coating P, E1, E2, and E3 immersed in 3.5 wt% NaCl and pure water is shown in Figure 5.7. The water volume fraction has a similar trend with its related coating capacitance. We observe from Figure 5.7 that the increase in the water volume fraction is faster for coatings immersed in pure water than that of 3.5 wt% NaCl solution. We also found that coatings are able to absorb more water when they are immersed in pure water, as shown in Table 5.5 for the saturated water volume fraction of different coatings in two working fluids. The higher values for the water volume fraction at saturation for coatings in pure water may also imply a more deteriorated barrier property of coatings for pure water immersion, which is indicated by the more substantial drop in impedance modulus, as shown in Figure 5.2.

We also conducted a single frequency test at 10 kHz, which has been widely employed to monitor the variation of coating capacitance as water uptake into the coatings [11, 19, 44]. The coating capacitance can be calculated:

$$C_c = \frac{1}{2\pi f |Z| \sin\theta} \quad (5\text{-}4)$$

where f is the frequency of the imposed AC voltage; |Z| is impedance modulus; and θ is the phase angle. The water volume fraction can then be calculated based on the capacitance using a similar approach presented earlier. Coating E3 is taken as an example to present the time evolution of coating capacitance and water volume fraction derived from single frequency tests, as shown in Figure 5.8. The overall trend of coating capacitance is similar to that obtained by equivalent circuit modeling. The saturated water volume fraction is 5.13% and 6.74% for coating E3 immersed in the NaCl solution and pure water, respectively. The results confirm that coatings contain more water after immersion in pure water than in the NaCl solution as mentioned previously in Table 5.5.

The faster increase of coating capacitance or water volume fraction for coatings immersed in pure water may be resulted from the faster water diffusion process. The water diffusion coefficient in organic coatings is in the order of magnitude of 10^{-9} cm^2s^{-1} [13, 45, 46], while the value is in the order of magnitude of 10^{-10} cm^2s^{-1} for NaCl solution diffusing into organic coatings [44, 47, 48]. For example, study has reported the diffusion coefficient of NaCl solution in two epoxy based coatings (one is a self-priming, two-component, epoxy-polyamide/amine paint; the other is a solvent-free, two component, polyamine cured epoxy paint) to be 1×10^{-10} and 7×10^{-10} cm^2s^{-1} at room temperature, respectively [48]. One explanation for the slower diffusion of NaCl solution is the smaller diffusion coefficient of Cl^- ion in organic coatings; for example, the diffusivity of Cl^- ion through epoxy coating on aluminum alloy substrate was reported to be 4.68×10^{-12} cm^2s^{-1} [45]. And the diffusion of Cl^- may influence the water uptake. The other explanation is that a higher salt concentration in the immersing solution slows down the water diffusion

through the coating, which presents a larger induction time [16]. The reduced diffusion in the coating could be reflected by the reduced activity of the water due to the presence of ions in the solution [16]. A conventional fluorescence microscopy method had been employed to investigate the mode of ions and water diffusion through an epoxy coating as described in Ref. [14]. The number of sites for water entering epoxy coatings was quantified for coatings immersed in pure water and salt solutions. The site density was found to increase with decreasing ionic concentration or increasing water activity [14]. Therefore, ions in the working fluid and their different diffusion properties may influence the water uptake so as to influence the coating degradation.

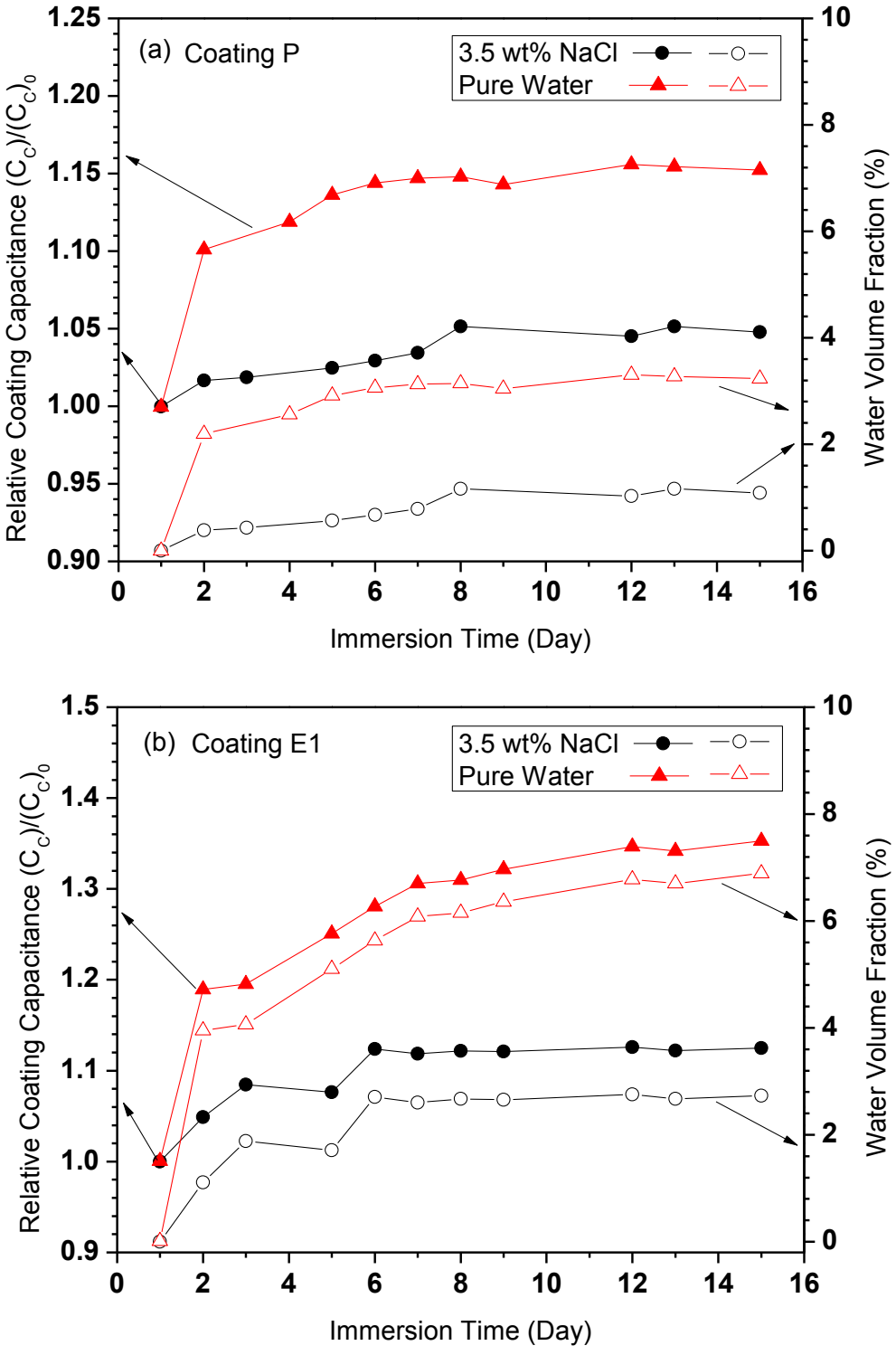

Figure 5.7. Relative coating capacitance and water volume fraction as a function of immersion time for coating samples immersed in 3.5 wt% NaCl solution and pure water. (a) Coating P; (b) coating E1; (c) coating E2; (d) coating E3. The solid symbols are for the relative coating capacitance while the hollow symbols are for the water volume fraction.

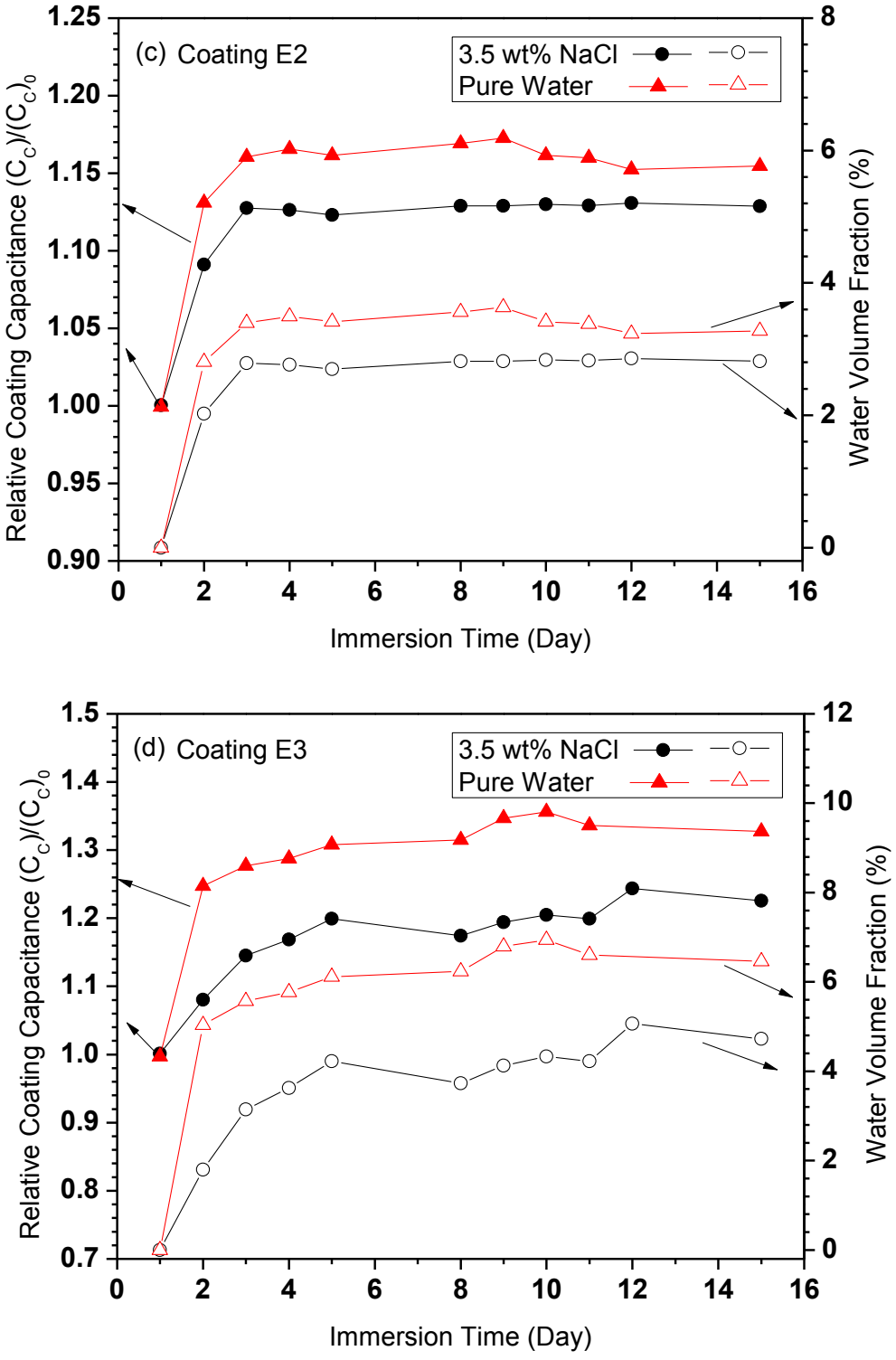

Figure 5.7. Relative coating capacitance and water volume fraction as a function of immersion time for coating samples immersed in 3.5 wt% NaCl solution and pure water. (a) Coating P; (b) coating E1; (c) coating E2; (d) coating E3. The solid symbols are for the relative coating capacitance while the hollow symbols are for the water volume fraction, (continued).

Table 5.5. Saturated water volume fraction in different coating systems.

Coating	Working Fluid	Saturated Water Volume Fraction ($\emptyset_s$, %)
P	NaCl solution	1.11
	Pure water	3.07
E1	NaCl solution	2.69
	Pure water	6.37
E2	NaCl solution	2.80
	Pure water	3.42
E3	NaCl solution	4.35
	Pure water	6.31

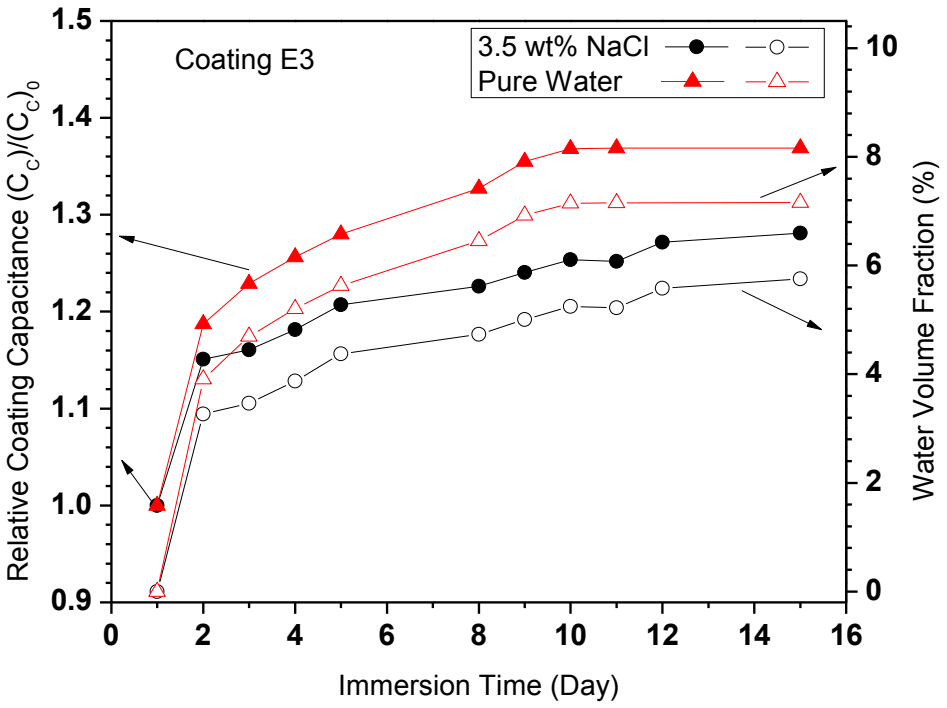

Figure 5.8. Relative coating capacitance and water volume fraction as a function of immersion time for coating E3 immersed in 3.5 wt% NaCl solution and pure water, measured by single frequency tests. The solid symbols are for the relative coating capacitance while the hollow symbols are for the water volume fraction.

We also monitor the thickness and topography of organic coatings immersed both in the 3.5 wt% NaCl solution and the pure water. The thickness of all organic coating samples almost remains the same before and after immersion as shown in Figure 5.9, although the working fluids are different. Little modification has taken place on the coating's surface since negligible changes in gloss values are found as shown in Table 5.6. Therefore, we believe that under stationary immersion of the coatings, the EIS data mainly reflects the water percolation into the coatings and the coating degradation. The changes in coating thickness and topology can be neglected.

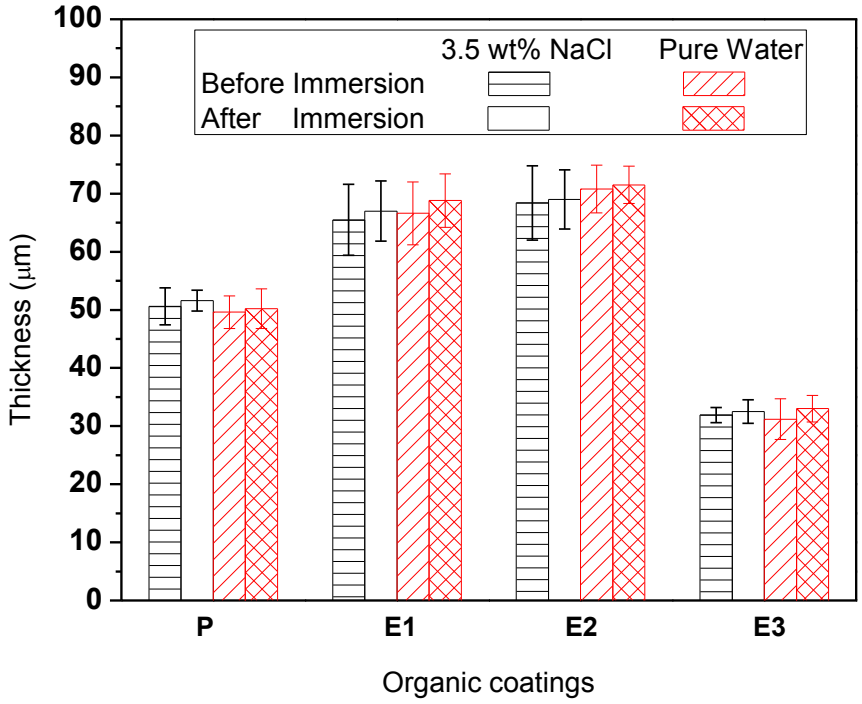

Figure 5.9. Thickness of coating samples immersed in 3.5 wt% NaCl solution and pure water.

Table 5.6. Gloss measurements for coating samples immersed in 3.5 wt% NaCl solution and pure water.

Coating	3.5 wt% NaCl Solution						Pure Water					
	Before Immersion			After Immersion			Before Immersion			After Immersion		
	20°	60°	85°	20°	60°	85°	20°	60°	85°	20°	60°	85°
P	90.7 ±1.27	98.5 ±1.37	88.6 ±1.40	90.3 ±2.80	97.5 ±1.87	81.0 ±3.47	87.7 ±1.70	99.0 ±1.57	79.8 ±1.37	86.8 ±2.10	98.1 ±1.30	74.4 ±2.53
E1	102.5 ±1.75	105.7 ±1.45	87.2 ±1.20	99.7 ±0.70	103.4 ±1.50	85.1 ±3.65	101.3 ±1.60	105.0 ±1.40	94.5 ±1.05	95.4 ±0.80	102.0 ±1.15	90.8 ±2.25
E2	106.5 ±1.67	108.2 ±1.03	89.7 ±5.40	102.1 ±2.10	106.1 ±0.35	87.1 ±3.50	109.8 ±1.07	109.4 ±1.67	97.5 ±5.73	105.1 ±1.85	106.4 ±0.85	94.3 ±3.40
E3	91.8 ±2.37	100.7 ±1.23	98.3 ±3.13	85.2 ±2.10	95.7 ±2.90	95.2 ±2.90	93.6 ±2.83	101.2 ±1.17	103.3 ±2.13	88.3 ±1.95	98.7 ±2.45	97.8 ±3.30

5.3.4. Comparisons of Marine Coating Degradation in Flowing NaCl Solution and Pure Water

In order to compare the influence of different working fluids, the relative low-frequency impedance modulus of coatings immersed in pure water is compared with that in a 3.5 wt% NaCl solution. The initial values of parameters for marine coating samples are listed in Table 5.7. Comparison results are presented in Figure 5.10 for three different flow rates. For all cases, coating immersed in NaCl solution show more abrupt decrease in its impedance modulus at initial immersion (up to 5-7 days) while the long-term decrease is more substantial for coatings immersed in pure water. We observe that for a

30-day immersion period the decrease in the barrier property of coating is more substantially accelerated by flowing pure water than the NaCl solution.

The equivalent circuit model used in the marine coating study is the same as that in Chapter 2. The initial values of modeling elements are also listed in Table 5.7. As shown in Figure 5.11, the relative coating capacitance of coating samples immersed in pure water shows greater increase over the entire immersion time that that in the NaCl solution for all flow rates (Q = 0, 3.683, 5.233 cm^3/s). The existence of chloride ion in coating layers may lower the relative permittivity of the percolating fluid in the coating [43]. This may explain in part the fact that the coating capacitance shows higher values in pure water. We believe NaCl solution may exist in the coating layers due to the percolation of water and the diffusion of ions into the coating [19, 49-52], although the concentration may not be exactly 3.5 wt%. The energy dispersive X-ray (EDX) and X-ray photoelectron spectroscopy (XPS) test have been used to confirm the presence of chloride element on the interface of the coating and substrate due to the diffusion of Cl^- from the solution [49, 50].

Figure 5.12 shows the transient behavior of the relative values of coating resistance for coatings immersed in pure water as well as those in the NaCl solution. The decrease in coating resistance is more substantial for coatings in pure water immersion, especially for higher flow rates. Pure water incurs a more substantial decrease in coating resistance (R_c); greater difference in R_c between the pure water and 3.5 wt% NaCl occurs for higher flow rates. The advantage of using relative values is that it demonstrates well the changes taking place over time and discounts the influence of the absolute values for different coating samples in different working fluids. Hence, we are able to conclude that

the increase of coating capacitance is more pronounced in flowing conditions. We also notice that the difference in the evolution of relative coating capacitance between the two working fluids is more prominent for higher flow rates. The barrier properties of the organic coatings are reduced earlier and rather severe by the flowing pure water immersion.

The behavior of physical elements (C_c and R_c) in the equivalent circuit model shows that pure water deteriorates the barrier properties of organic coatings more aggressively than 3.5 wt% NaCl solution. This would imply that the pure water is interacting spontaneously with coating components. The fact that the flowing pure water accelerates more aggressively the coating degradation may be explained by the large difference between the concentration of water soluble substances released from the coating located in coating layers and that in the refreshing pure water over the coating surface.

Table 5.7. Initial values of parameters for marine coating samples immersed in 3.5 wt% NaCl solution and pure water employed to plot Figures 5.10- 5.12.

Para meters	**3.5 wt% NaCl Solution**			**Pure Water**		
	Q=0 cm^3/s	**Q=3.683 cm^3/s**	**Q=5.233 cm^3/s**	**Q=0 cm^3/s**	**Q=3.683 cm^3/s**	**Q=5.233 cm^3/s**
$\|Z\|$ (Ω cm^2)	1.18×10^{10}	1.57×10^{10}	2.64×10^{10}	1.56×10^{10}	3.80×10^{10}	8.44×10^{10}
C_c (F/cm^2)	1.34×10^{-9}	3.24×10^{-9}	5.81×10^{-9}	2.86×10^{-9}	3.14×10^{-9}	5.73×10^{-9}
R_c (Ω cm^2)	1.12×10^{9}	1.23×10^{9}	2.01×10^{9}	1.09×10^{9}	1.86×10^{9}	5.46×10^{9}

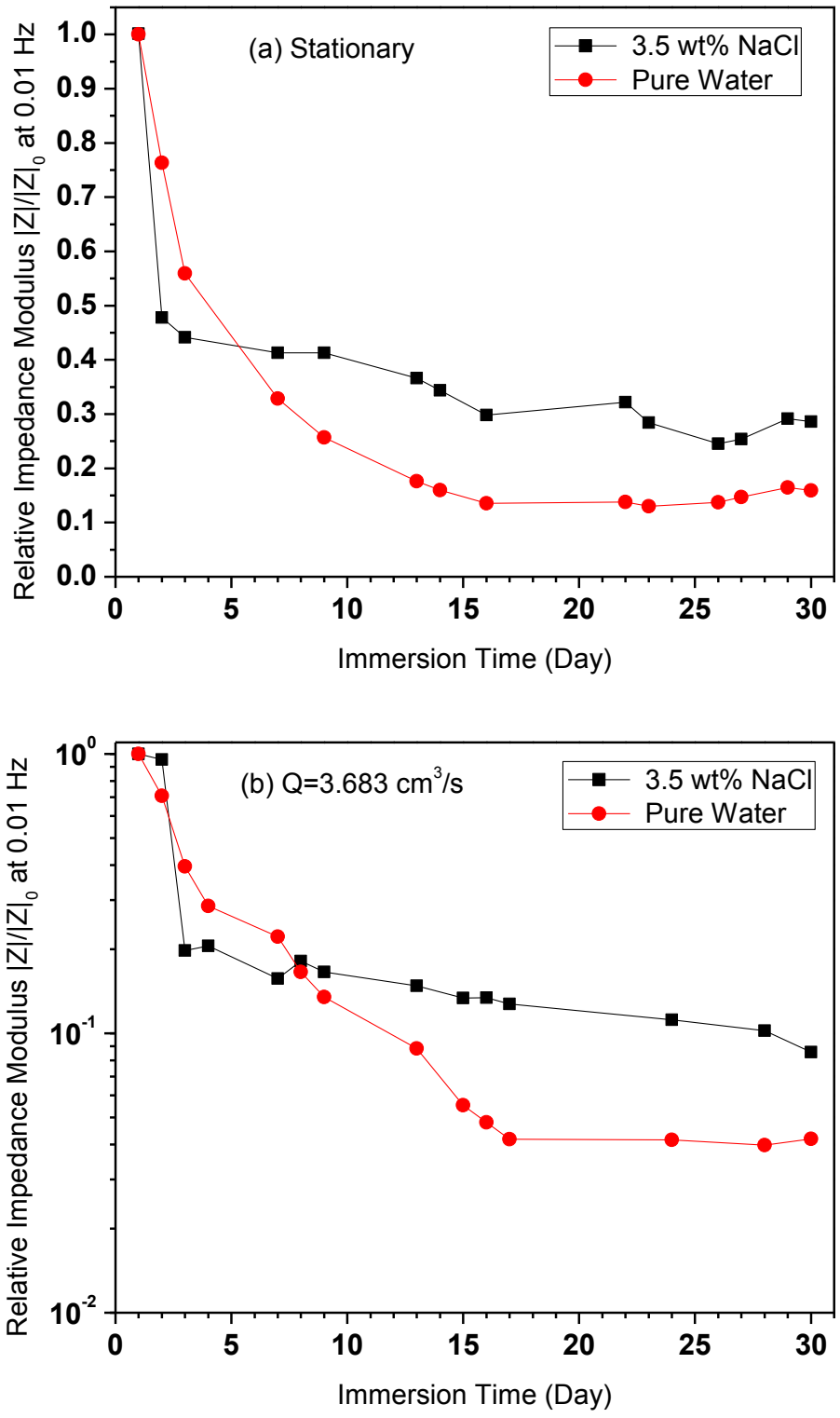

Figure 5.10. Relative impedance modulus as a function of immersion time for marine coating samples immersed in 3.5 wt% NaCl solution and pure water for flow rates (a) Q=0 (stationary), (b) Q=3.683, and (c) Q=5.233 cm^3/s.

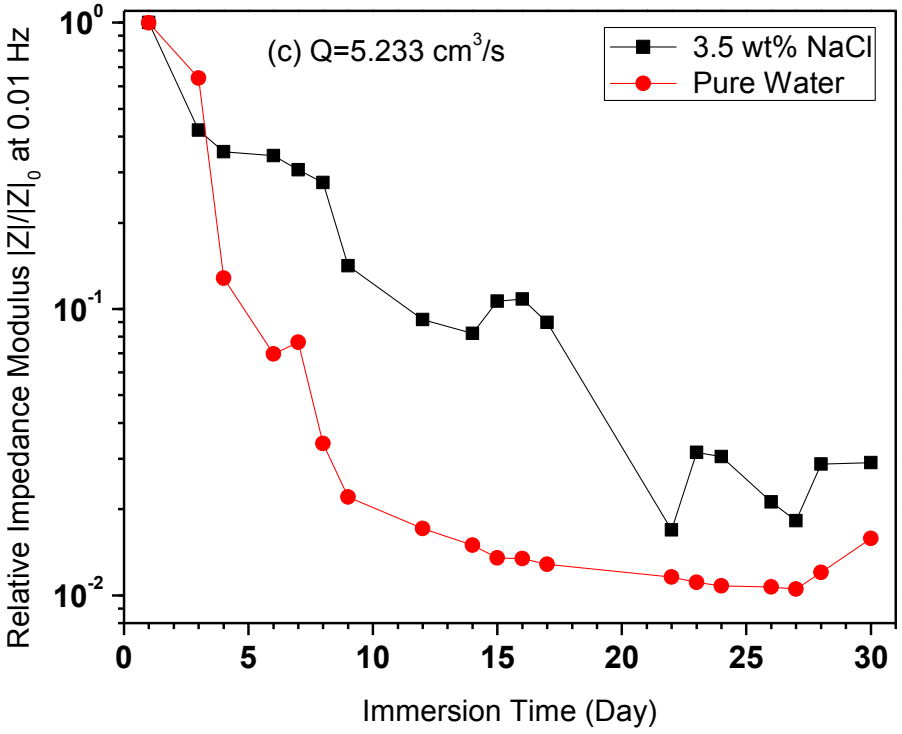

Figure 5.10. Relative impedance modulus as a function of immersion time for marine coating samples immersed in 3.5 wt% NaCl solution and pure water for flow rates (a) Q=0 (stationary), (b) Q=3.683, and (c) Q=5.233 cm^3/s, (continued).

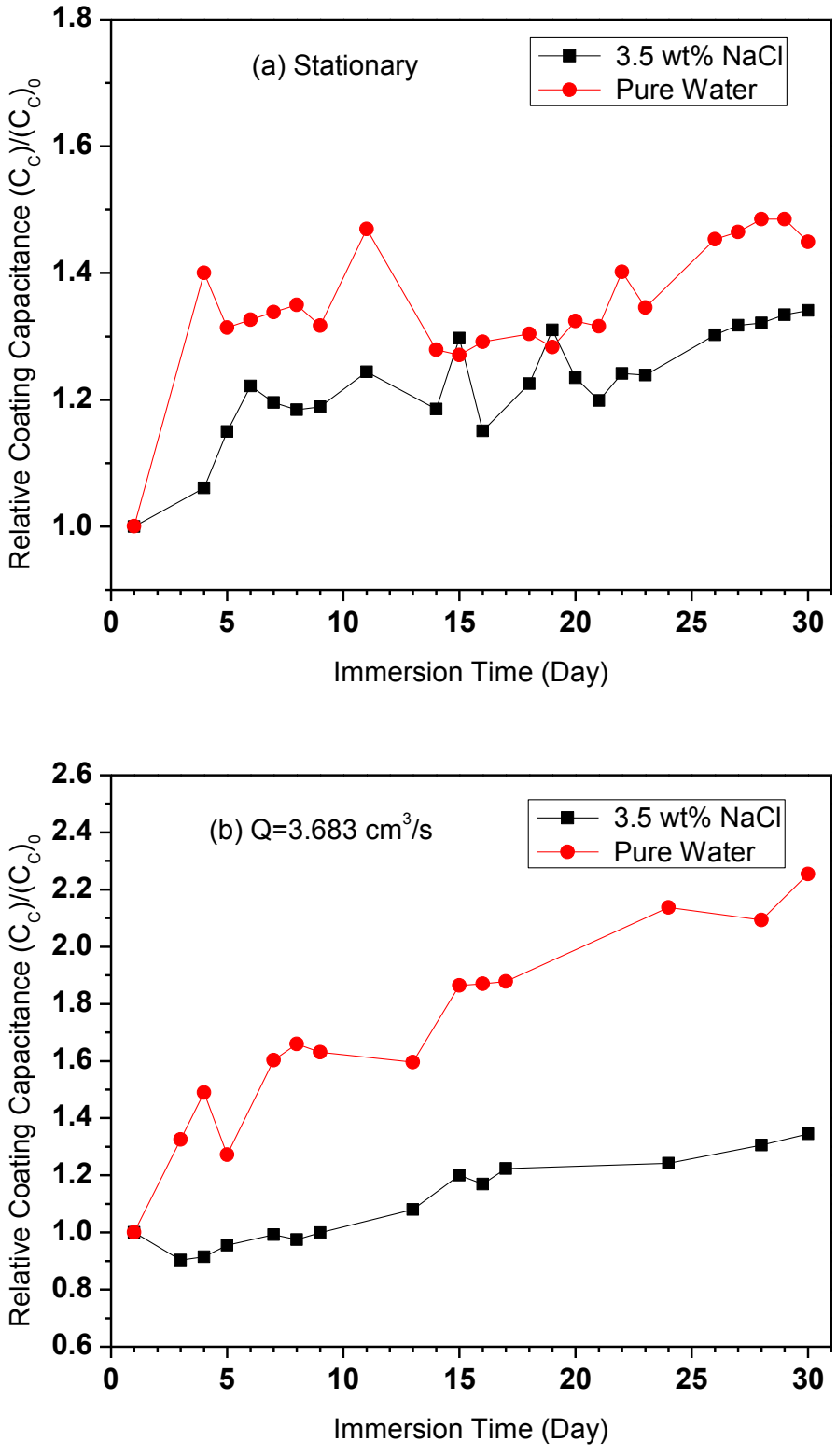

Figure 5.11. Relative coating capacitance C_c as a function of immersion time for marine coating samples immersed in 3.5 wt% NaCl solution and pure water for flow rates (a) Q=0 (stationary), (b) Q=3.683, and (c) Q=5.233 cm^3/s.

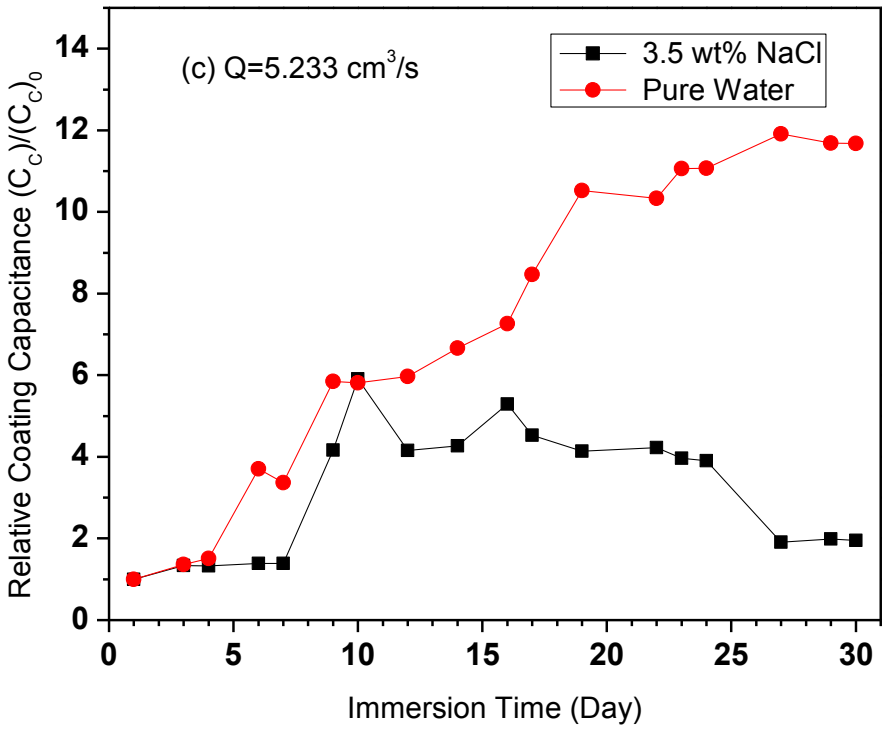

Figure 5.11. Relative coating capacitance C_c as a function of immersion time for marine coating samples immersed in 3.5 wt% NaCl solution and pure water for flow rates (a) Q=0 (stationary), (b) Q=3.683, and (c) Q=5.233 cm^3/s, (continued).

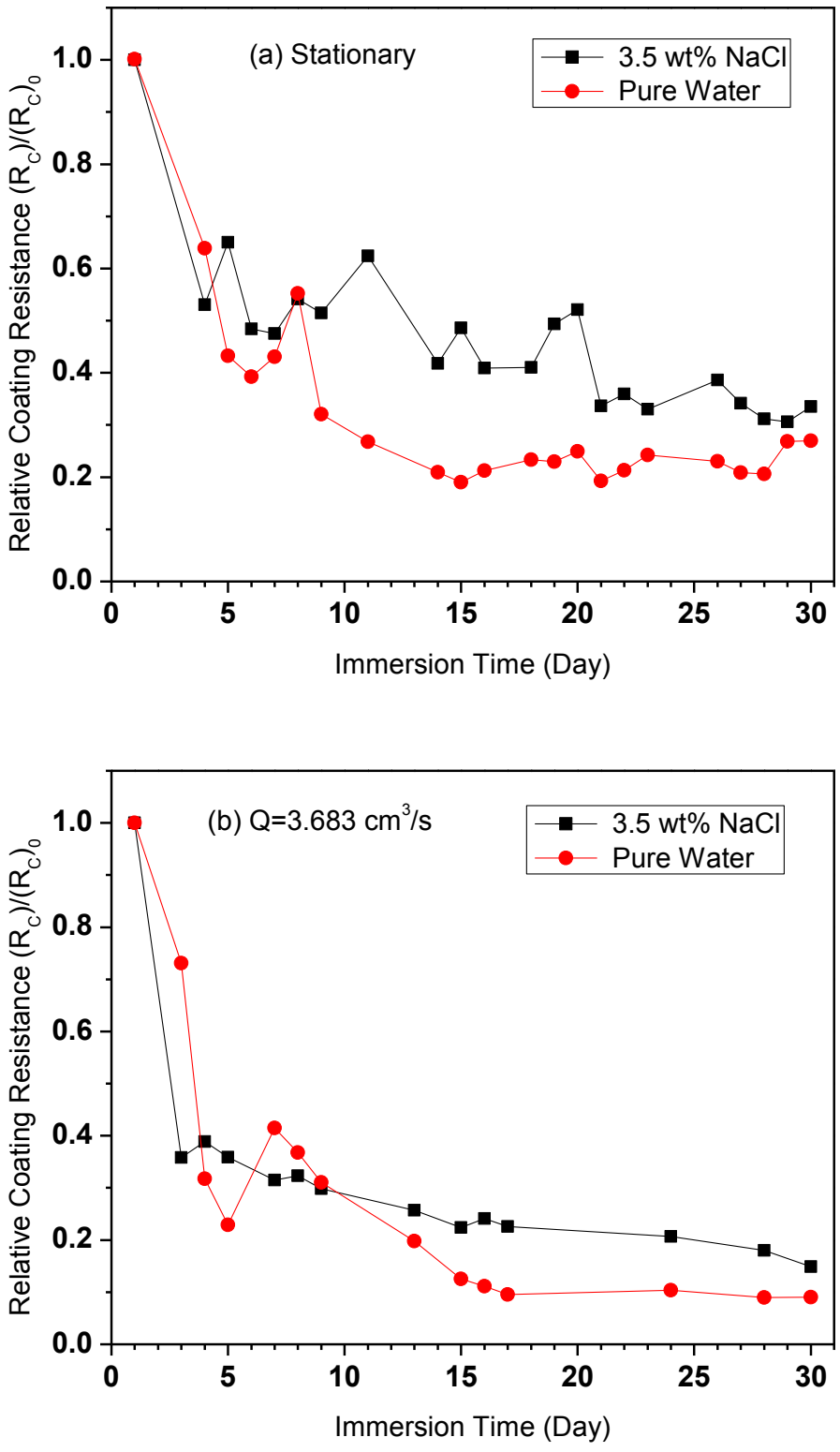

Figure 5.12. Relative coating resistance R_c as a function of immersion time for marine coating samples immersed in 3.5 wt% NaCl solution and pure water for flow rates (a) Q=0 (stationary), (b) Q=3.683, and (c) Q=5.233 cm^3/s.

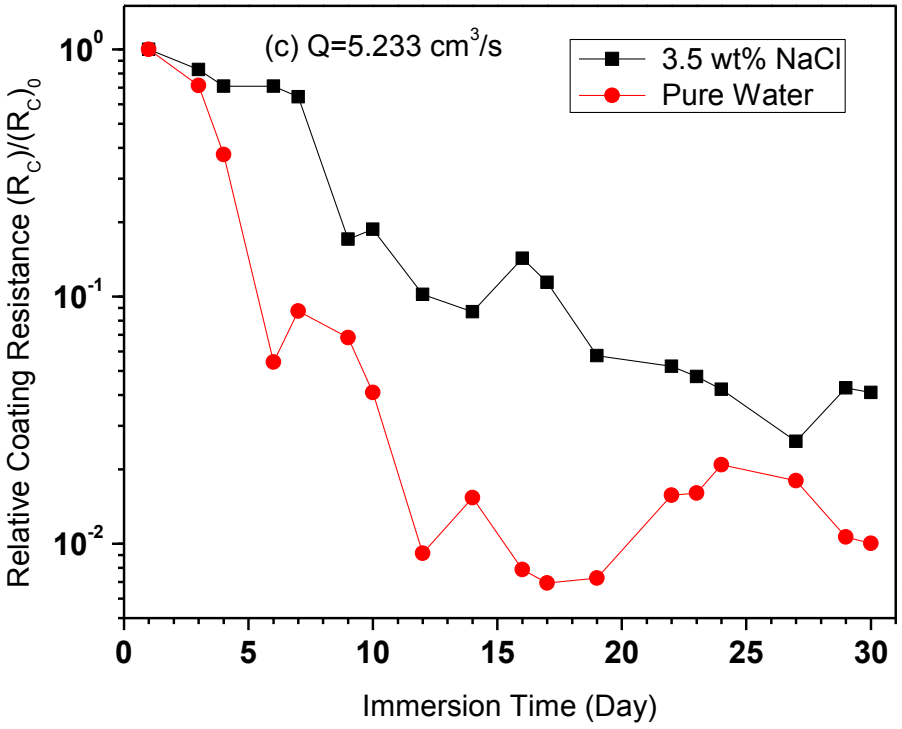

Figure 5.12. Relative coating resistance R_c as a function of immersion time for marine coating samples immersed in 3.5 wt% NaCl solution and pure water for flow rates (a) Q=0 (stationary), (b) Q=3.683, and (c) Q=5.233 cm^3/s, (continued).

5.4. Conclusions

The study in this chapter evaluated the degradation behavior of four clear coatings immersed in a stationary 3.5 wt% NaCl solution and pure water characterized by EIS method. Equivalent circuit models were employed to analyze EIS spectra and the models presented a good fitting agreement with the experimental data. The two working fluids percolating into the clear coatings caused the decrease in coating's resistance and increase in coating's capacitance, which eventually deteriorated the coating's barrier property. Water absorption process was observed which showed an initial fast increase in coating's capacitance followed by a saturation state. Comparing with the 3.5 wt% NaCl

solution, pure water incurred a more substantial decrease in coating's impedance modulus as well as pore resistance which implied faster ion diffusion in the coatings. In addition, pure water leaded to a faster increase in coating's capacitance as well as a greater saturated water volume fraction which indicated a more substantial water uptake. The more prominent coating degradation in pure water is due to the larger activity and diffusion coefficient of water at lower concentrations of ions. We conclude that the different properties of working fluids influence the water uptake and ion diffusion, and eventually affect the coating degradation. Pure water appeared to facilitate more efficiently the deterioration of the barrier property of organic coatings against corrosion.

This chapter also includes the comparison of marine coating degradation in flowing pure water and a 3.5 wt% NaCl solution. The decay of relative impedance modulus was larger for the marine coatings immersed in pure water, which demonstrated that the coating was more sensitive to the penetration of pure water than the 3.5 wt% NaCl solution. We also observed by comparing the values of physical elements in the equivalent circuit model that pure water deteriorated the barrier properties of organic coatings more aggressively. The differences in physical elements between the usages of these two working fluids were more substantial for higher flow rates. We conclude that the flowing fluid, especially pure water, over coating surface could be used as an effective acceleration method.

5.5. References

[1] M. Delucchi, G. Cerisola, Influence of organic coatings on the stability of macrodefect-free cements exposed to water, *Construction and Building Materials*, **15** (2001) 351-359.

[2] Y. Hamlaoui, L. Tifouti, F. Pedraza, On the corrosion resistance of porous electroplated zinc coatings in different corrosive media, *Corrosion Science*, **52** (2010) 1883-1888.

[3] W. Ji, J. Hu, L. Liu, J. Zhang, C. Cao, Water uptake of epoxy coatings modified with γ-APS silane monomer, *Progress in Organic Coatings*, **57** (2006) 439-443.

[4] T. Nguyen, E. Byrd, D. Bentz, C. Lint, In situ measurement of water at the organic coating/substrate interface, *Progress in Organic Coatings*, **27** (1996) 181-193.

[5] L.V.S. Philippe, S.B. Lyon, C. Sammon, J. Yarwood, Validation of electrochemical impedance measurements for water sorption into epoxy coatings using gravimetry and infra-red spectroscopy, *Corrosion Science*, **50** (2008) 887-896.

[6] Y. Wang, G.P. Bierwagen, A new acceleration factor for the testing of corrosion protective coating: flow-induced coating degradation, *Journal of Coatings Technology and Research*, **6** (2009) 429-436.

[7] T. Hodgkiess, D. Mantzavinos, Corrosion of copper-nickel alloys in pure water, *Desalination*, **126** (1999) 129-137.

[8] Z. Lu, T. Shoji, Y. Takeda, Y. Ito, A. Kai, S. Yamazaki, Transient and steady state crack growth kinetics for stress corrosion cracking of a cold worked 316L stainless steel in oxygenated pure water at different temperatures, *Corrosion Science*, **50** (2008) 561-575.

[9] D.A. Lytle, M.N. Nadagouda, A comprehensive investigation of copper pitting corrosion in a drinking water distribution system, *Corrosion Science*, **52** (2010) 1927-1938.

[10] M.C. Zhao, M. Liu, G.L. Song, A. Atrens, Influence of pH and chloride ion concentration on the corrosion of Mg alloy ZE41, *Corrosion Science*, **50** (2008) 3168-3178.

[11] V.N. Nguyen, F.X. Perrin, J.L. Vernet, Water permeability of organic/inorganic hybrid coatings prepared by sol–gel method: a comparison between gravimetric and capacitance measurements and evaluation of non-Fickian sorption models, *Corrosion Science*, **47** (2005) 397-412.

[12] S. Zhang, Y. Ding, S. Li, X. Luo, W. Zhou, Effect of polymeric structure on the corrosion protection of epoxy coatings, *Corrosion Science*, **44** (2002) 861-869.

[13] S. Zhang, S. Li, X. Luo, W. Zhou, Mechanism of the significant improvement in corrosion protection by lowering water sorption of the coating, *Corrosion Science*, **42** (2000) 2037-2041.

[14] S.R. Taylor, P. Moongkhamklang, The delineation of local water interaction with epoxy coatings using fluorescence microscopy, *Progress in Organic Coatings*, **54** (2005) 205-210.

[15] L. Philippe, C. Sammon, S.B. Lyon, J. Yarwood, An FTIR/ATR in situ study of sorption and transport in corrosion protective organic coatings: 1. Water sorption and the role of inhibitor anions, *Progress in Organic Coatings*, **49** (2004) 302-314.

[16] F. Deflorian, S. Rossi, An EIS study of ion diffusion through organic coatings, *Electrochimica Acta*, **51** (2006) 1736-1744.

[17] F. Wong, R.G. Buchheit, Utilizing the structural memory effect of layered double hydroxides for sensing water uptake in organic coatings, *Progress in Organic Coatings*, **51** (2004) 91-102.

[18] W. Ji, J. Hu, J. Zhang, C. Cao, Reducing the water absorption in epoxy coatings by silane monomer incorporation, *Corrosion Science*, **48** (2006) 3731-3739.

[19] J.H. Park, G.D. Lee, H. Ooshige, A. Nishikata, T. Tsuru, Monitoring of water uptake in organic coatings under cyclic wet–dry condition, *Corrosion Science*, **45** (2003) 1881-1894.

[20] M. Morcillo, F.J. Rodríguez, J.M. Bastidas, The influence of chlorides, sulphates and nitrates at the coating-steel interface on underfilm corrosion, *Progress in Organic Coatings*, **31** (1997) 245-253.

[21] F. Rezaei, F. Sharif, A.A. Sarabi, S.M. Kasiriha, M. Rahmaniam, E. Akbarinezhad, Evaluating water transport through high solid polyurethane coating using the EIS method, *Journal of Coatings Technology and Research*, **7** (2010) 209-217.

[22] T.E. ToolBox, www.engineeringtoolbox.com/oxygen-solubility-water-d_841.html.

[23] Q. Zhou, Y. Wang, G.P. Bierwagen, Influence of the composition of working fluids on flow-accelerated organic coating degradation: Deionized water versus electrolyte solution, *Corrosion Science*, **55** (2012) 97-106.

[24] N. Fredj, S. Cohendoz, X. Feaugas, S. Touzain, Some consequences of saline solution immersion on mechanical behavior of two marine epoxy-based coatings, *Progress in Organic Coatings*, **69** (2010) 82-91.

[25] J.R. Svendsen, G.M. Kontogeorgis, S. Kiil, C.E. Weinell, M. Grønlund, Adhesion between coating layers based on epoxy and silicone, *Journal of Colloid and Interface Science*, **316** (2007) 678-686.

[26] S.S. Pathak, A. Sharma, A.S. Khanna, Value addition to waterborne polyurethane resin by silicone modification for developing high performance coating on aluminum alloy, *Progress in Organic Coatings*, **65** (2009) 206-216.

[27] D.P. Schmidt, B.A. Shaw, E. Sikora, W.W. Shaw, L.H. Laliberte, Corrosion protection assessment of sacrificial coating systems as a function of exposure time in a marine environment, *Progress in Organic Coatings*, **57** (2006) 352-364.

[28] A. Husain, O. Al-Shamah, A. Abduljaleel, Investigation of marine environmental related deterioration of coal tar epoxy paint on tubular steel pilings, *Desalination*, **166** (2004) 295-304.

[29] C.R. Alentejano, I.V. Aoki, Localized corrosion inhibition of 304 stainless steel in pure water by oxyanions tungstate and molybdate, *Electrochimica Acta*, **49** (2004) 2779-2785.

[30] K. Saito, J. Kuniya, Mechanochemical model to predict stress corrosion crack growth of stainless steel in high temperature water, *Corrosion Science*, **43** (2001) 1751-1766.

[31] B.R. Hinderliter, K. Allahar, G.P. Bierwagen, D.E. Tallman, S.G. Croll, Water sorption and diffusional properties of a cured epoxy resin measured using alternating ionic liquids/aqueous electrolytes in electrochemical impedance spectroscopy, *Journal of Coatings Technology and Research*, **5** (2008) 431-438.

[32] G.P. Bierwagen, L. He, J. Li, L. Ellingson, D.E. Tallman, Studies of a new accelerated evaluation method for coating corrosion resistance - thermal cycling testing, *Progress in Organic Coatings*, **39** (2000) 67-78.

[33] V.F. Lvovich, Impedance spectroscopy application to electrochemical and dielectric phenomena, John Wiley & Sons, Hoboken, New Jersey, 2012.

[34] J. Zhang, J. Hu, J. Zhang, C. Cao, Studies of water transport behavior and impedance models of epoxy-coated metals in NaCl solution by EIS, *Progress in Organic Coatings*, **51** (2004) 145-151.

[35] P.L. Bonora, F. Deflorian, L. Fedrizzi, Electrochemical impedance spectroscopy as a tool for investigating underpaint corrosion, *Electrochimica Acta*, **41** (1996) 1073-1082.

[36] C. Corfias, N. Pebere, C. Lacabanne, Characterization of a thin protective coating on galvanized steel by electrochemical impedance spectroscopy and a thermostimulated current method, *Corrosion Science*, **41** (1999) 1539-1555.

[37] Y. González-García, S. González, R.M. Souto, Electrochemical and structural properties of a polyurethane coating on steel substrates for corrosion protection, *Corrosion Science*, **49** (2007) 3514-3526.

[38] M.E. Orazem, B. Tribollet, Electrochemical Impedance Spectroscopy, John Wiley & Sons, Inc., Hoboken, New Jersey, 2008.

[39] M. Del Grosso Destreri, J. Vogelsang, L. Fedrizzi, F. Deflorian, Water up-take evaluation of new waterborne and high solid epoxy coatings. Part II: electrochemical impedance spectroscopy, *Progress in Organic Coatings*, **37** (1999) 69-81.

[40] G.J. Brug, A.L.G. van den Eeden, M. Sluyters-Rehbach, J.H. Sluyters, The analysis of electrode impedances complicated by the presence of a constant phase element, *Journal of Electroanalytical Chemistry and Interfacial Electrochemistry*, **176** (1984) 275-295.

[41] N. Fredj, S. Cohendoz, X. Feaugas, S. Touzain, Ageing of marine coating in natural and artificial seawater under mechanical stresses, *Progress in Organic Coatings*, **74** (2012) 391-399.

[42] D.M. Brasher, A.H. Kingsbury, Electrical measurements in the study of immersed paint coatings on metal. I. Comparison between capacitance and gravimetric methods of estimating water-uptake, *Journal of Applied Chemistry*, **4** (1954) 62-72.

[43] A. Peyman, C. Gabriel, E.H. Grant, Complex permittivity of sodium chloride solutions at microwave frequencies, *Bioelectromagnetics*, **28** (2007) 264-274.

[44] J. Zhang, J. Hu, J. Zhang, C. Cao, Studies of impedance models and water transport behaviors of polypropylene coated metals in NaCl solution, *Progress in Organic Coatings*, **49** (2004) 293-301.

[45] J. Hu, J. Zhang, C. Cao, Determination of water uptake and diffusion of Cl^- ion in epoxy primer on aluminum alloys in NaCl solution by electrochemical impedance spectroscopy, *Progress in Organic Coatings*, **46** (2003) 273-279.

[46] M.M. Wind, H.J.W. Lenderink, A capacitance study of pseudo-fickian diffusion in glassy polymer coatings, *Progress in Organic Coatings*, **28** (1996) 239-250.

[47] F. Galliano, D. Landolt, Evaluation of corrosion protection properties of additives for waterborne epoxy coatings on steel, *Progress in Organic Coatings*, **44** (2002) 217-225.

[48] N. Fredj, S. Cohendoz, S. Mallarino, X. Feaugas, S. Touzain, Evidencing antagonist effects of water uptake and leaching processes in marine organic coatings by gravimetry and EIS, *Progress in Organic Coatings*, **67** (2010) 287-295.

[49] X. Yang, J. Li, S.G. Croll, D.E. Tallman, G.P. Bierwagen, Degradation of low gloss polyurethane aircraft coatings under UV and prohesion alternating exposures, *Polymer Degradation and Stability*, **80** (2003) 51-58.

[50] J. Hu, J. Zhang, C. Cao, Determination of water uptake and diffusion of Cl^- ion in epoxy primer on aluminum alloys in NaCl solution by electrochemical impedance spectroscopy, *Progress in Organic Coatings*, **46** (2003) 273-279.

[51] X. Yang, D.E. Tallman, S.G. Croll, G.P. Bierwagen, Morphological changes in polyurethane coatings on exposure to water, *Polymer Degradation and Stability*, **77** (2002) 391-396.

[52] A.S.L. Castela, A.M. Simões, M.G.S. Ferreira, E.I.S. evaluation of attached and free polymer films, *Progress in Organic Coatings*, **38** (2000) 1-7.

CHAPTER 6. OTHER INFLUENCING FACTORS FOR ORGANIC COATING DEGRADATION

6.1. Introduction

In stationary tests, the NaCl solution was normally kept in use for the entire duration of the immersion of samples. We are curious whether or not refreshing NaCl solution would give different degradation results. For flowing tests, since the working fluids were all recirculated back into the reservoir in previous flowing tests, we are curious whether or not the non-recirculated fresh fluid can bring more deterioration to the coatings. The ion concentration of the recirculated working fluids may be modified due to the ion diffusion process and leaching-out process of coating materials, while the non-recirculated fluid is fresh enough to maintain the material concentration. Section 6.2 and Section 6.3 present our results and comparison of stationary tests on clear coatings with non-refreshed and refreshed NaCl solution and those of flowing tests with non-recirculated and recirculated NaCl solution, respectively.

Different concentrations of NaCl solution may affect the diffusion or transport of ions, which, in turn, may contribute to the degradation of organic coatings. Reported studies on the metal or alloy corrosion demonstrated that increased concentration of NaCl solution could increase the corrosion rate of metal or alloy [1-5]. It is worthy to evaluate whether organic coatings present the same behavior as metal. Section 6.4 summarizes our tests for both clear and pigmented coatings using NaCl solution with different concentrations.

6.2. Non-refreshed and Refreshed Stationary NaCl Solution for Clear Coating Degradation

6.2.1. Materials and Methods

The commercially available polyurethane and epoxy based clear coatings were chosen for the evaluation [6-10]. The same clear coatings as mentioned in Chapter 5 were used. The sample preparation procedures were also the same as described in Chapter 5.

6.2.2. Experimental Setup and EIS Measurement

The traditional three-electrode Electrochemical Impedance Spectroscopy (EIS) setup was employed [11, 12], as shown in Figure 2.5 in Chapter 2. At least three samples of each coating system were measured under the same testing condition. For the non-refreshed tests, the 3.5 wt% NaCl solution was kept in the glass cell during the entire immersion process. For the refreshed tests, the 3.5 wt% NaCl solution immersing the coating samples was dumped and refilled every day during the test. The NaCl solution was prepared and stored in a large glass container for one set of tests in order to assure that the same NaCl solution was used for non-refreshed and refreshed tests.

The electrochemical cell, EIS measurement conditions, coating thickness and gloss measurement are the same as our previous tests as described in Chapter 2.

6.2.3. Results and Discussion

The impedance modulus of EIS spectra at low frequency serves as a strong indicator of the corrosion resistance of coating samples [13, 14]. The relative low-frequency (0.01 Hz) impedance modulus is obtained by normalizing the low-frequency impedance modulus with the modulus at the initial immersion. The low-frequency (0.01 Hz) values for representative samples of each type of coating system at the initial

immersion are listed in Table 6.1. The table shows that the initial impedance values are at the same order of magnitude of the same coating system for the evaluations.

In order to demonstrate the difference of the coating's barrier property immersed between non-refreshed and refreshed NaCl solution, a plot of the relative impedance modulus at low-frequency (0.01 Hz) as a function of time is shown in Figure 6.1. The solid black curves present the decrease of the relative impedance modulus of the coatings immersed in non-refreshed 3.5 wt% NaCl solution, while the hollow red curves present the refreshed cases. The universal trend among all coating samples is that the relative impedance modulus shows a faster decrease in the first few days, and then it maintains a relatively slow decrease rate during immersion. As for all the coatings, it is clear that the changes of the impedance modulus are almost overlapped under both non-refreshed and refreshed conditions, disregard of small difference among different coating samples. The refreshed NaCl solution shows no significant difference comparing with the non-refreshed one, based on the stationary immersion tests on the degradation of clear coatings. Therefore, we conclude that the coating degradation could not be much influenced by only refreshing the working fluid.

We also compare the change of coating thickness for samples immersed in stationary under non-refreshed and refreshed conditions, as shown in Figure 6.2. The overall thickness shows no significant change before and after the coating degradation for all types of coating samples, although the initial coating thickness varies among different types of coatings. The swelling effect is more obvious for coating E3 demonstrated by a larger increased thickness after the degradation.

We also conducted the gloss measurement of the coating's surface, as shown in Table 6.2. The gloss value shows a slight decrease after the immersion for all types of coating samples. This demonstrates that the roughness of the coating surface increased insignificantly. The difference between non-refreshed and refreshed immersion conditions is negligible based on the topographical results.

Table 6.1. Initial impedance at 0.01 Hz for coating samples immersed in 3.5 wt% NaCl solution.

Coating P (Ω)	**Coating E1 (Ω)**	**Coating E2 (Ω)**	**Coating E3 (Ω)**
3.60×10^8	5.24×10^6	1.63×10^{10}	1.31×10^6
5.05×10^8	1.22×10^6	2.44×10^{10}	1.33×10^6
4.43×10^8	4.37×10^6	8.16×10^9	2.17×10^6
5.23×10^8	1.62×10^6	1.26×10^{10}	2.56×10^6
5.72×10^8	5.27×10^6	2.15×10^{10}	6.19×10^6
5.41×10^8	4.81×10^6	2.24×10^{10}	2.03×10^6

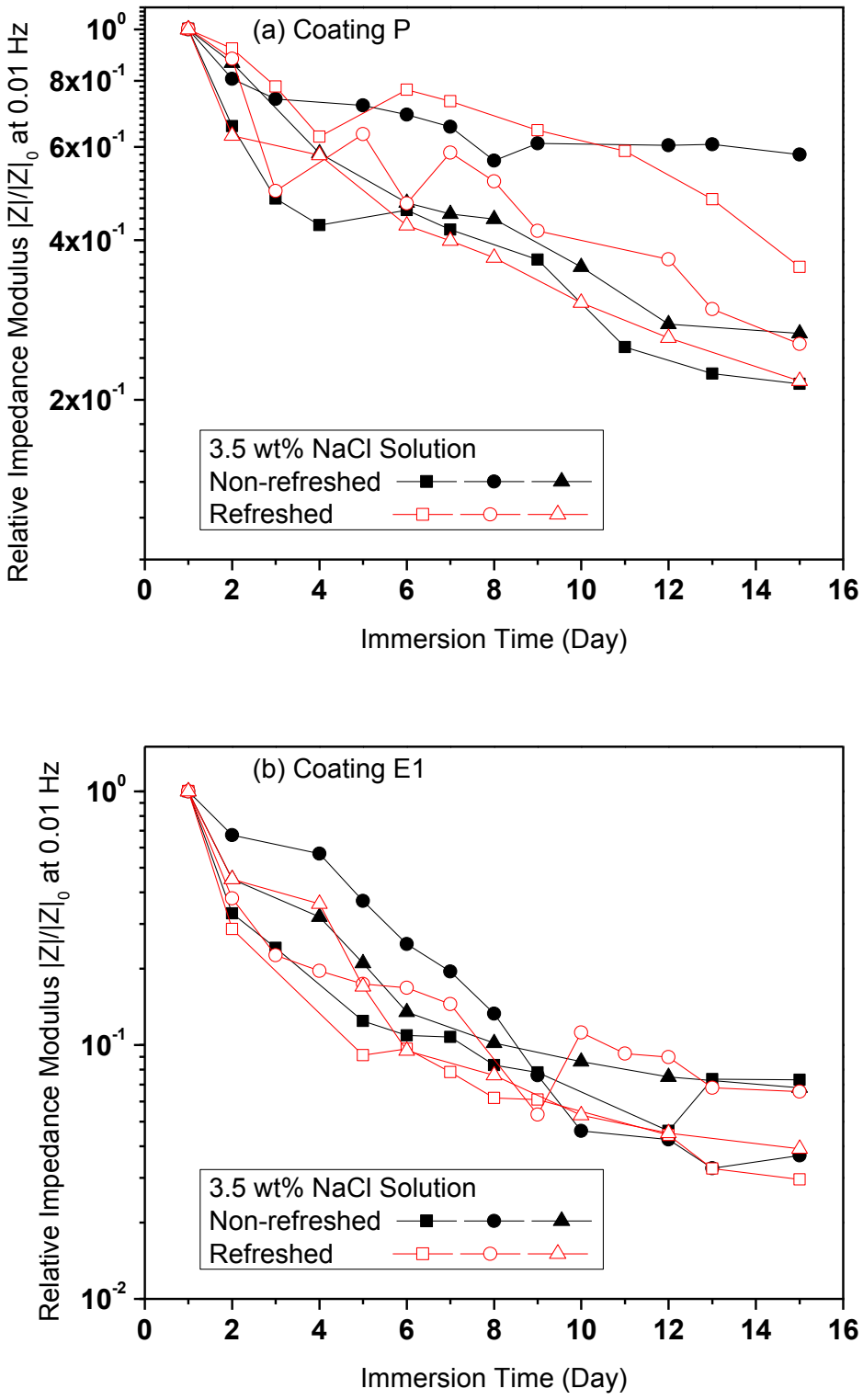

Figure 6.1. Relative impedance modulus as a function of immersion time for coating samples of (a) P, (b) E1, (c) E2, (d) E3 immersed in non-refreshed and refreshed 3.5 wt% NaCl solution.

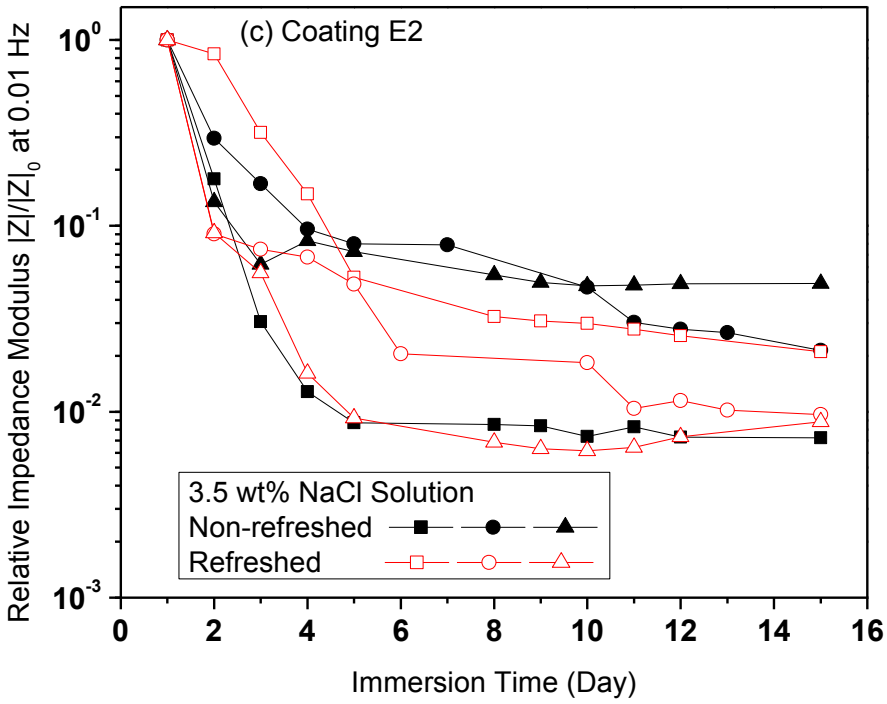

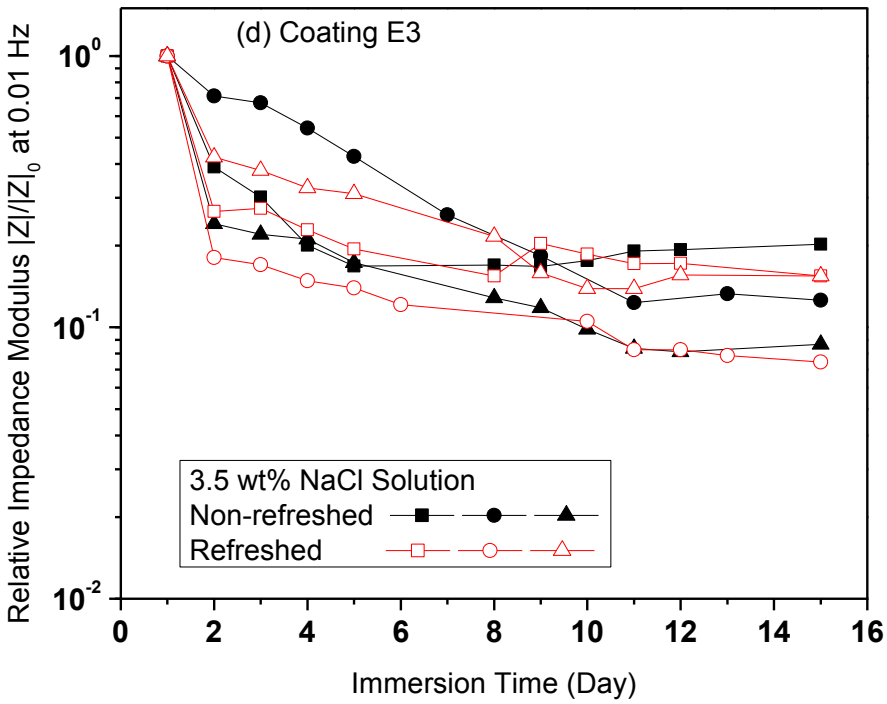

Figure 6.1. Relative impedance modulus as a function of immersion time for coating samples of (a) P, (b) E1, (c) E2, (d) E3 immersed in non-refreshed and refreshed 3.5 wt% NaCl solution, (continued).

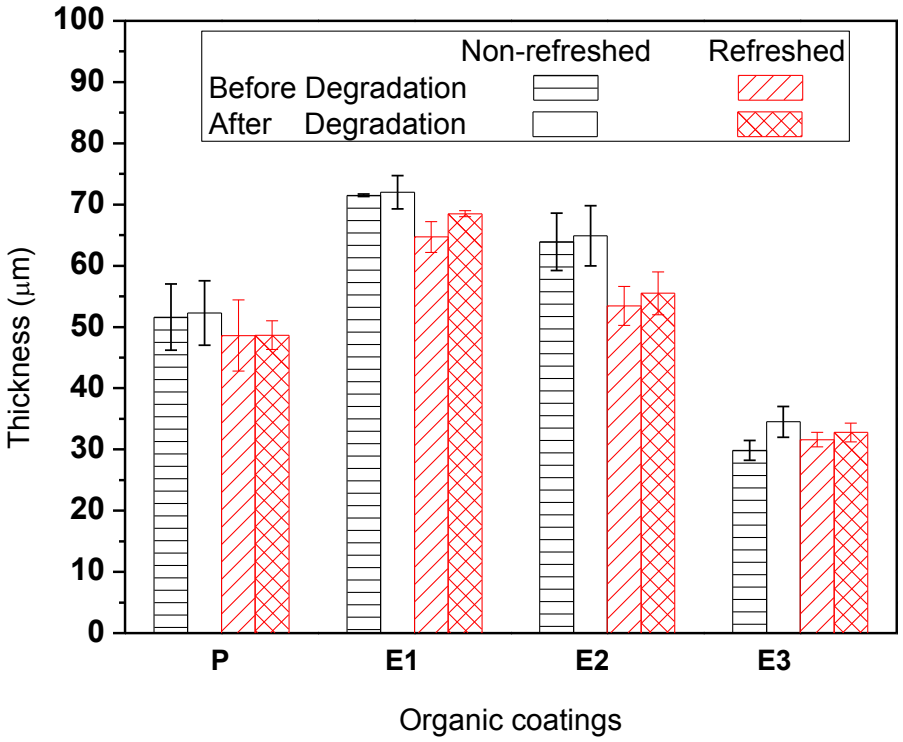

Figure 6.2. Thickness of coating samples immersed in non-refreshed and refreshed 3.5 wt% NaCl solution.

Table 6.2. Gloss measurement for coating samples immersed in non-refreshed and refreshed 3.5 wt% NaCl solution.

Organic Coat-ings	**3.5 wt% NaCl Solution: Non-refreshed**						**3.5 wt% NaCl Solution: Refreshed**					
	Before Immersion			**After Immersion**			**Before Immersion**			**After Immersion**		
	20˚	**60˚**	**85˚**	**20˚**	**60˚**	**85˚**	**20˚**	**60˚**	**85˚**	**20˚**	**60˚**	**85˚**
P	90.43 ±0.27	96.13 ±2.37	87.90 ±1.40	86.50 ±3.80	95.63 ±1.87	81.47 ±8.47	90.70 ±4.70	97.77 ±1.57	89.37 ±1.37	88.60 ±2.0	95.80 ±1.10	88.37 ±1.53
E1	103.25 ±0.75	106.15 ±0.45	86.00 ±1.20	99.00 ±0.70	105.90 ±0.50	81.45 ±5.65	99.20 ±3.60	103.80 ±1.40	91.15 ±1.05	97.30 ±0.80	102.25 ±1.15	85.55 ±2.25
E2	105.97 ±4.67	107.17 ±1.03	95.10 ±5.40	105.20 ±3.10	106.45 ±0.35	92.60 ±4.50	105.63 ±1.07	107.53 ±1.67	89.93 ±5.73	102.85 ±0.85	104.65 ±0.85	88.50 ±0.40
E3	92.73 ±2.37	102.13 ±1.23	97.77 ±7.13	75.70 ±7.10	89.30 ±2.90	91.70 ±8.90	89.67 ±4.83	101.73 ±0.17	92.57 ±9.13	83.25 ±1.95	95.25 ±0.45	85.90 ±9.30

6.3. Recirculated and Non-recirculated Flowing NaCl Solution for Clear Coating Degradation

6.3.1. Materials and Methods

Q-panel standard steel panels (S-36 from Q-Panel Lab Products) were cut into 51 × 51 mm and used as the metal substrate. The commercially available epoxy based clear coating was chosen for the evaluation. The epoxy coating is the same as what we used in Chapter 3. The sample preparation procedure is the same as described in Chapter 2.

6.3.2. Experimental Setup and EIS Measurement

We modified our previous flow channels (as shown in Chapter 2 and 3) and designed a miniaturized device which is more practical, portable, and efficient, to undertake the non-recirculated flow loop. The small flow channel was printed layer by layer using a 3D printer. Figure 6.3 (a) is the 3D image for the base of the flow channel; (b) show the front view and back view for the top layer of flow channel; the base (a) and the top (b) were glued together to complete the flow channel (c). The coating panel was attached to the inserting modulus (d) which can be inserted into the flow channel (c). The platinum meshes were attached on top channel wall (b) acting either as counter or reference electrode.

The schematic of the experimental setups is shown in Figure 6.4. The picture of the flow channel and EIS setups in the experiment is shown in Figure 6.5. The picture of the experimental setups for the flowing tests is shown in Figure 6.6. The working fluid, 3.5 wt% NaCl solution, was pumped from the fluid reservoir to the flow channel. The flow rate was maintained by a syringe pump at 20.66 cm^3/min. The temperature was maintained at 25 ˚C by a water bath and a temperature controlling system. The recirculated and non-recirculated flowing mode was conducted. The flowing NaCl solution was circulated back to the reservoir under the recirculated mode; while the flowing solution was dumped and new NaCl solution went through the testing channel and over the coating surface under the non-recirculated mode. EIS measurement conditions are the same as our previous tests described in Chapter 2.

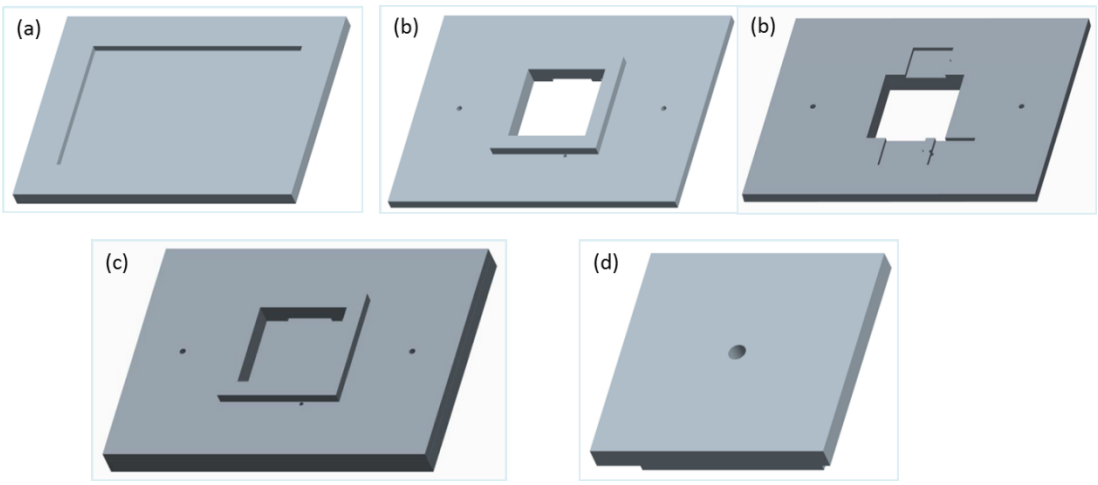

Figure 6.3. Schematic diagram of flow channel, (a) base, (b) top (front and back), (c) the whole channel, and (d) inserting modulus.

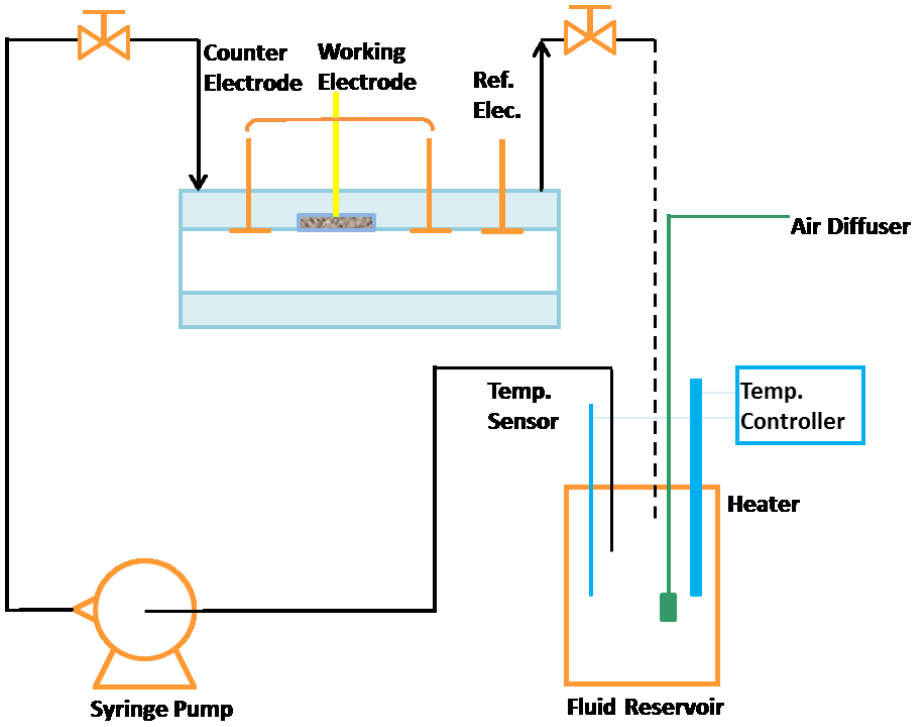

Figure 6.4. Schematic diagram of recirculated and non-recirculated flow loop. The dashed line means that the working fluid goes into the fluid reservoir in the recirculated mode while the working fluid goes towards waste reservoir in the non-recirculated mode.

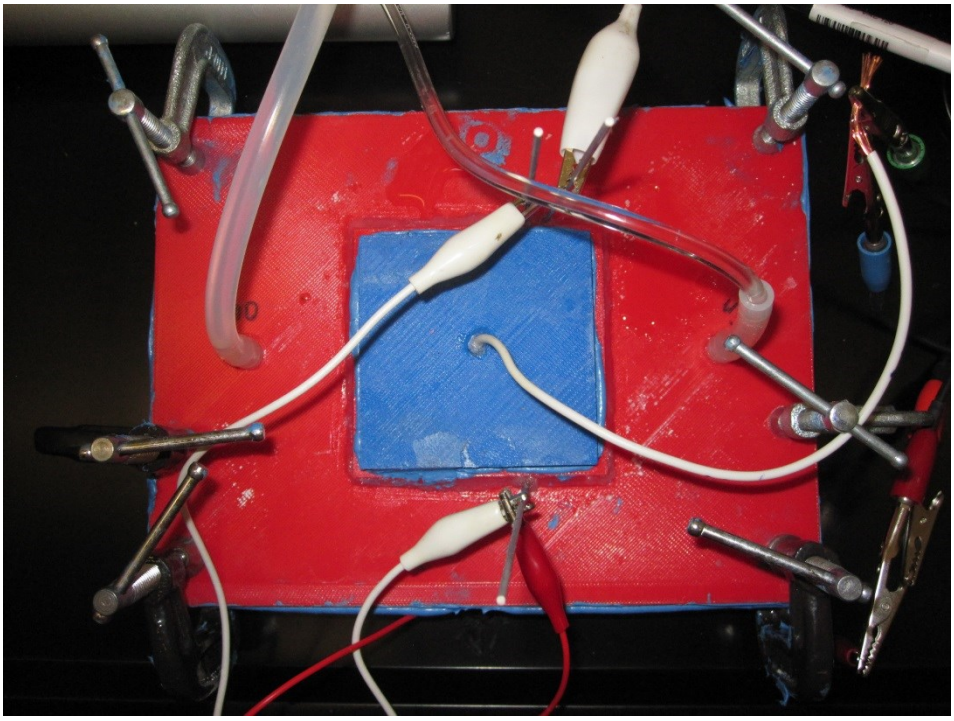

Figure 6.5. A picture of the small flow channel and EIS setups.

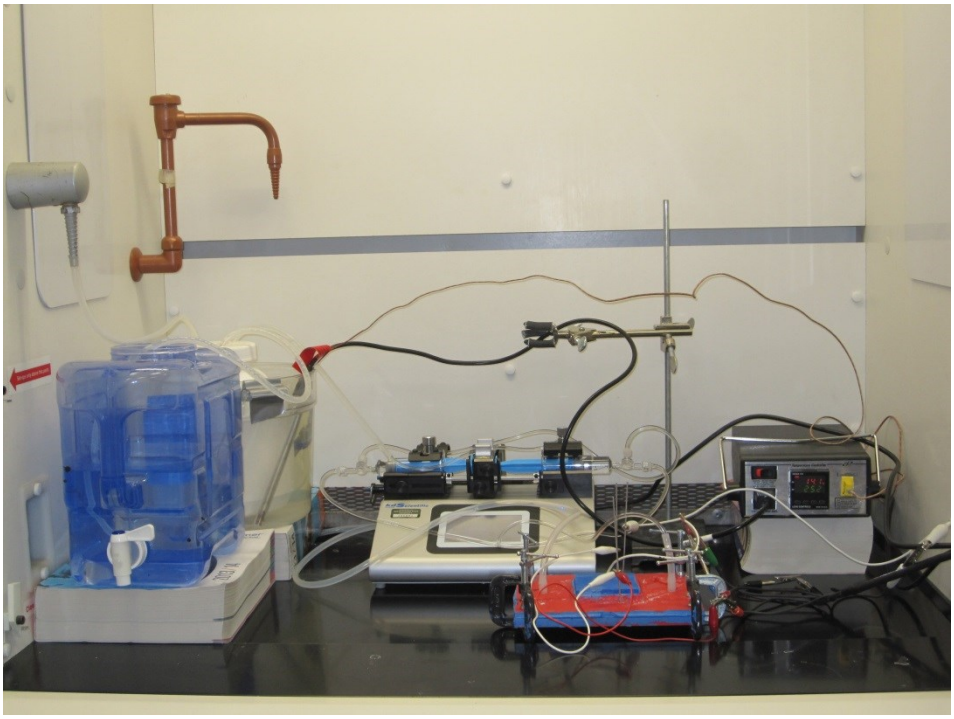

Figure 6.6. A picture of experimental setups for the flowing test: reservoir, syringe pump, flow channel, and temperature controlling system (from left to right).

6.3.3. Results and Discussion

In order to demonstrate the influence of different flowing modes on the coating degradation, we compare the relative impedance modulus at 0.01 Hz of different coating samples. The relative low-frequency (0.01 Hz) impedance modulus is obtained by normalizing the low-frequency impedance modulus with the modulus at the initial immersion. The low-frequency (0.01 Hz) values for representative samples at the initial immersion are 6.12×10^6, 7.96×10^6, and 4.41×10^6 $\Omega \cdot cm^2$ for the non-recirculated flowing mode with flow rate 20.66 cm^3/min, and 8.91×10^6 and 2.93×10^6 $\Omega \cdot cm^2$ for the recirculated flowing mode with flow rate 20.66 cm^3/min. So the initial impedance values are at the same order of magnitude of the coatings under the evaluation.

Figure 6.7 shows a plot of the relative impedance modulus at low-frequency (0.01 Hz) as a function of time for coating samples under the recirculated and the non-recirculated flowing mode with the flow rate 20.66 cm^3/min. The decrease of the impedance modulus is almost overlapped under the two flowing mode, although there exists a little difference among different coating samples. Therefore, the coating's barrier property could not be much influenced only by changing the circulating flowing mode, although it was first thought that the non-recirculated fluid is fresh and may not contain the unexpected materials leaching from the coating, while the leaching materials may accumulate in the recirculated fluid. Based on the experiments in this study, we conclude that the effect of the refreshed fluid on the coating degradation is negligible.

Topography characterizations were also measured on the coating's surface. The change of the coating's thickness is shown in Figure 6.8. The thickness group of the first three columns presents the three coating samples under the non-recirculated flowing

mode with the flow rate 20.66 cm^3/min, while those of the last two columns are the two coating samples under the recirculated flowing mode with the same flow rate. The coating thickness presents a slight increase after the degradation as a result of swelling, disregard of the little difference in the initial thickness. And the increased thickness varies among different samples.

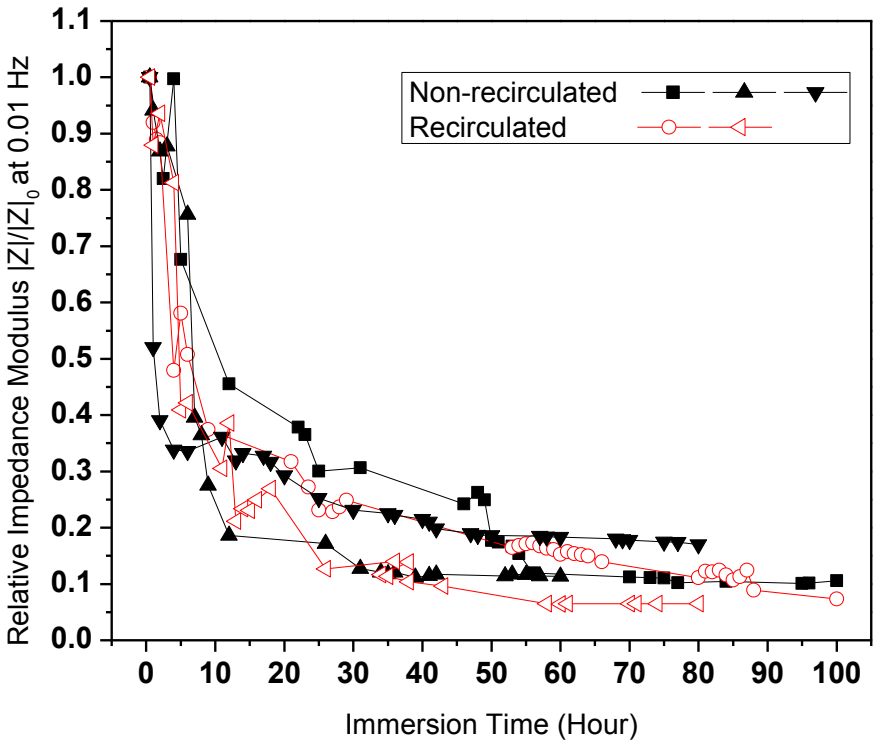

Figure 6.7. Relative impedance modulus as a function of immersion time for coating samples immersed in 3.5 wt% NaCl solution with flow rate Q=20.66 cm^3/min under non-recirculated (3 samples) and recirculated (2 samples) flowing mode.

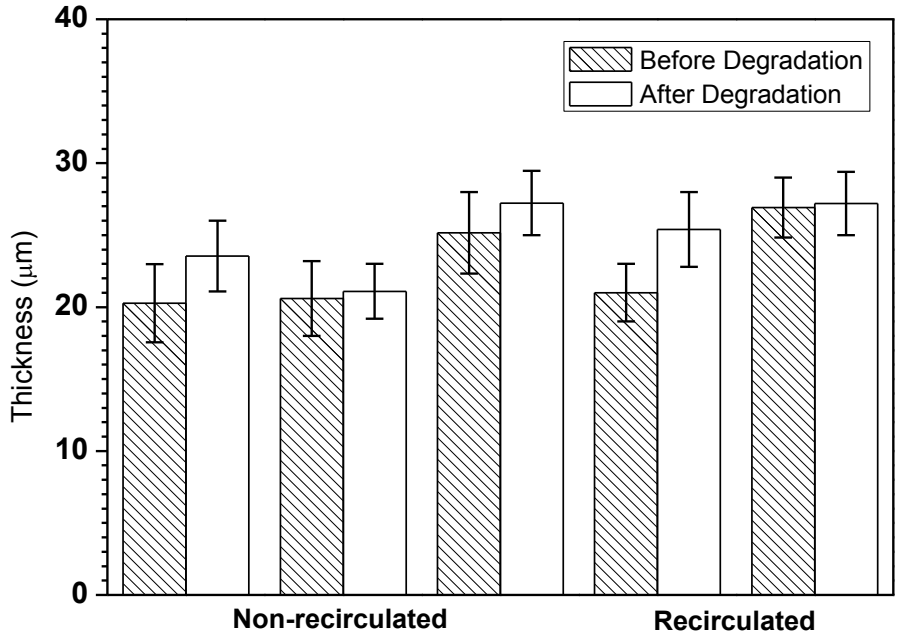

Figure 6.8. Thickness of coating samples immersed in 3.5 wt% NaCl solution with flow rate Q=20.66 cm^3/min under non-recirculated (3 samples) and recirculated (2 samples) flowing mode.

The results of the gloss measurements are shown in Table 6.3. By comparing the data before and after immersion, it is obvious that the gloss value decreases after the immersion, which demonstrates that the roughness of the coating sample is increased as a result of the flowing effect. However, both the thickness and gloss change present little difference between the recirculated and the non-recirculated flowing mode.

Table 6.3. Gloss measurements for coating samples immersed in 3.5 wt% NaCl solution with flow rate Q=20.66 cm^3/min under non-recirculated and recirculated flowing mode.

Immersion	**Before Immersion**			**After Immersion**		
Condition	**20°**	**60°**	**85°**	**20°**	**60°**	**85°**
Non-recirculated	71.04 ± 8.76	108.64 ± 8.36	70.82 ± 4.38	37.98 ± 4.92	79.06 ± 1.56	46.82 ± 7.78
Non-recirculated	78.48 ± 7.28	100.62 ± 6.68	78.72 ± 3.32	39.68 ± 2.92	68.96 ± 1.24	27.72 ± 1.18
Non-recirculated	79.23 ± 8.93	109.43 ± 4.63	75.42 ± 8.58	45.35 ± 7.85	89.65 ± 8.75	37.95 ± 4.95
Recirculated	74.58 ± 9.88	113.74 ± 9.04	75.32 ± 9.18	41.22 ± 9.02	94.18 ± 6.78	28.94 ± 9.84
Recirculated	73.68 ± 2.48	115.78 ± 9.68	73.56 ± 6.06	37.60 ± 2.90	72.54 ± 2.04	31.94 ± 1.96

6.4. NaCl Concentrations for Organic Coating Degradation

6.4.1. Materials and Methods

The commercially available pigmented marine coating and epoxy based clear coating were evaluated in this study. The marine coating is the same as what we used in Chapter 2 and the clear coating is the same as in Chapter 3. The sample preparation procedure is described in Chapter 2.

6.4.2. Experimental Setup and EIS Measurement

The traditional three-electrode EIS setup was employed for evaluating coating degradation as shown in Figure 2.5 in Chapter 2. The glass cell was filled in NaCl

solution with different concentrations: 1 wt%, 2 wt%, and 3.5 wt%, respectively. At least three samples of each coating system were measured under the immersion of the same concentration of NaCl solution. The electrochemical cell and the EIS testing conditions were the same as described in Chapter 2.

6.4.3. Results and Discussion

In order to present the effect of NaCl concentrations on the coating degradation, we compare the relative impedance modulus at 0.01 Hz of coating samples immersed in different NaCl solutions. The low-frequency (0.01 Hz) values are listed in Table 6.4 for representative samples of both marine coating and epoxy coating at the initial immersion under different concentrations of NaCl solutions. The table shows that the initial impedance values are at the same order of magnitude of the same coating system for the evaluations.

The relative impedance modulus at low-frequency (0.01 Hz) as a function of time for coating samples immersed in different concentrations of NaCl solution are shown in Figure 6.9 for marine coating degradation and Figure 6.10 for clear coating degradation, respectively. The solid black curves, half-hollow red curves, and hollow blue curves present the coating samples immersed in 1 wt%, 2 wt%, and 3.5 wt% NaCl solution, respectively. The decrease of the impedance modulus is nearly overlapped and no pronounced trend for different NaCl concentrations, both for marine and clear coating. Disregard the slight difference among different coating samples; the change of coatings' impedance modulus under different NaCl concentrations is not significant. So the coating's barrier property could not be much influenced by changing the concentration of

NaCl solution only. Based on the experiments in this study, we conclude that the effect of the NaCl concentration on the coating degradation is negligible.

We also compare the change of the coating thickness for samples immersed in different NaCl solutions, as shown in Figure 6.11 and Figure 6.12 for marine coating and epoxy coating, respectively. The overall thickness shows no significant change before and after the coating degradation under different concentrations of NaCl solutions. The epoxy coating shows a slight swelling effect by an increased coating thickness after the immersion, while marine coating presents a little reduced thickness after the immersion probably due to pigments effects.

The gloss change of the coating samples are also shown in Table 6.5 and Table 6.6 for marine coating and epoxy coating, respectively. It is hard to conclude the effect of NaCl concentrations on the reducing of coating's gloss because there is no pronounced difference of the changed gloss value among different NaCl solutions. Therefore, based on the thickness and gloss results, the influence of NaCl concentrations is insignificant in the change of coating's topography.

Table 6.4. Initial impedance at 0.01 Hz for marine coating and epoxy coating samples immersed in 1 wt%, 2 wt%, and 3.5 wt% stationary NaCl solution.

NaCl Concentration	**Marine Coating (Ω)**	**Epoxy Coating (Ω)**
1 wt%	4.98×10^9	1.59×10^6
	5.92×10^9	1.66×10^6
	2.79×10^9	1.79×10^6
2 wt%	2.71×10^9	1.55×10^6
	2.61×10^9	1.19×10^6
	4.08×10^9	3.27×10^6
3.5 wt%	4.47×10^9	1.15×10^6
	4.73×10^9	1.52×10^6
	4.16×10^9	2.04×10^6

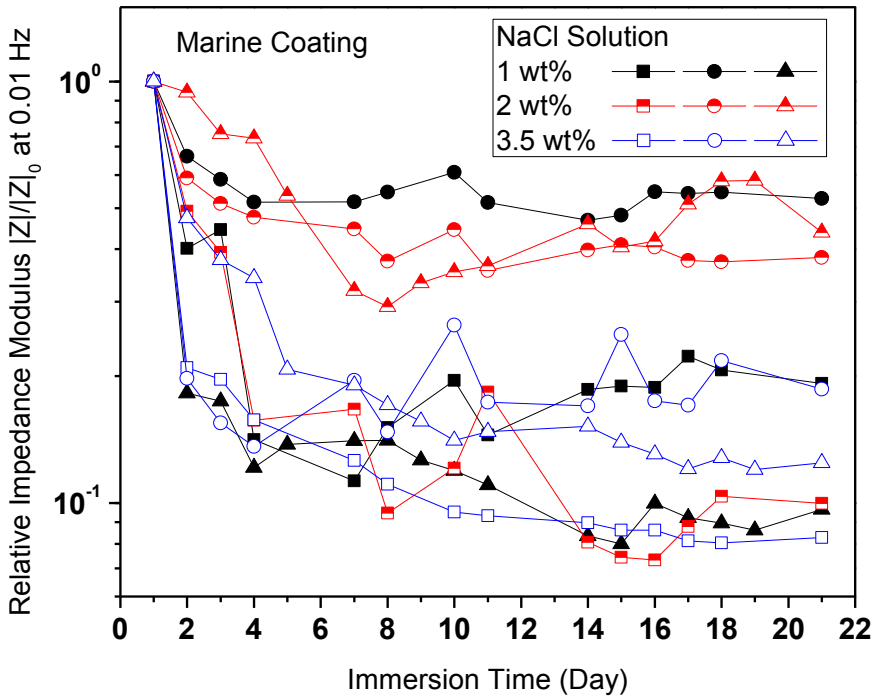

Figure 6.9. Relative impedance modulus as a function of immersion time for marine coating immersed in 1 wt%, 2 wt%, and 3.5 wt% stationary NaCl solution.

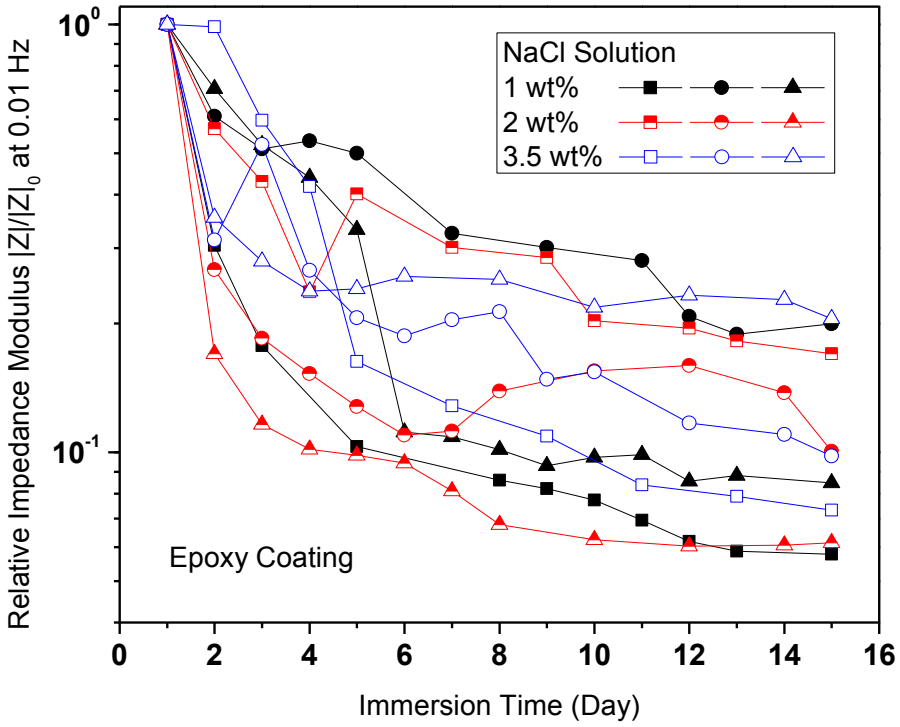

Figure 6.10. Relative impedance modulus as a function of immersion time for epoxy coating immersed in 1 wt%, 2 wt%, and 3.5 wt% stationary NaCl solution.

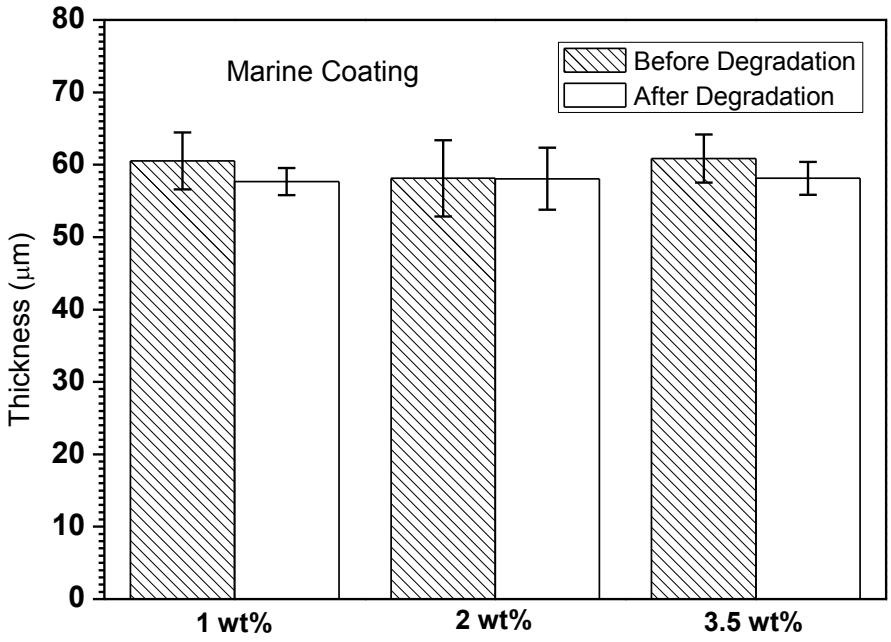

Figure 6.11. Thickness of marine coating samples immersed in 1 wt%, 2 wt%, and 3.5 wt% stationary NaCl solution.

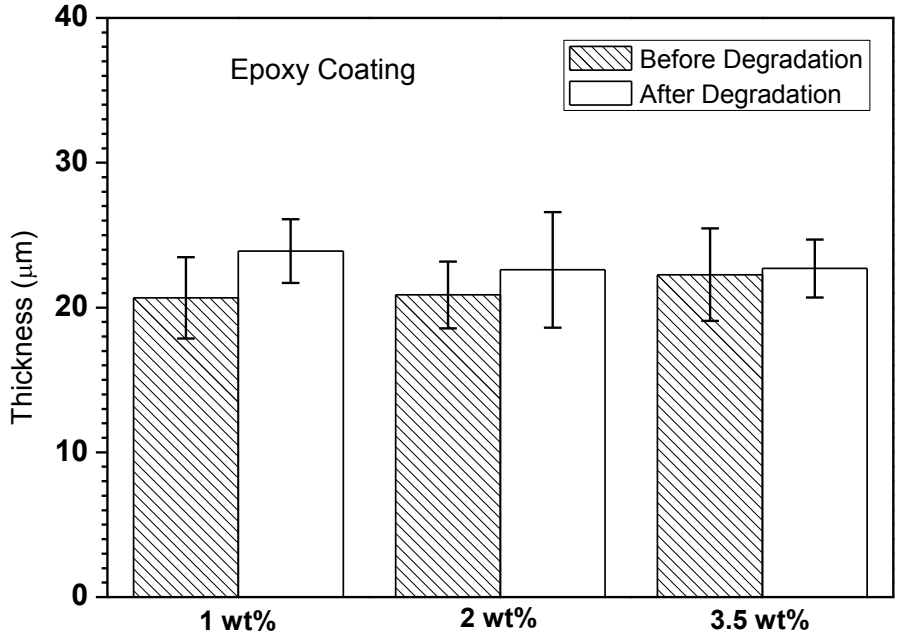

Figure 6.12. Thickness of clear coating samples immersed in 1 wt%, 2 wt%, and 3.5 wt% stationary NaCl solution.

Table 6.5. Gloss measurements for marine coating samples immersed in 1 wt%, 2 wt%, and 3.5 wt% stationary NaCl solution.

Immersion	**Before Immersion**			**After Immersion**		
Condition	**20˚**	**60˚**	**85˚**	**20˚**	**60˚**	**85˚**
1 wt%	23.50	61.10	60.60	17.43	45.67	47.36
	± 7.30	± 8.50	± 5.50	± 3.77	± 2.73	± 1.47
2 wt%	24.33	63.67	62.90	22.17	55.73	51.53
	± 0.87	± 1.73	± 3.50	± 1.23	± 3.87	± 2.67
3.5 wt%	22.13	59.80	59.53	19.13	50.63	45.10
	± 5.67	± 7.40	± 6.27	± 6.93	± 2.37	± 1.30

Table 6.6. Gloss measurements for epoxy coating samples immersed in 1 wt%, 2 wt%, and 3.5 wt% stationary NaCl solution.

Immersion	**Before Immersion**			**After Immersion**		
Condition	**20°**	**60°**	**85°**	**20°**	**60°**	**85°**
1 wt%	97.53	114.13	90.83	74.53	85.90	61.40
	± 9.17	± 8.47	± 6.93	± 7.63	± 9.03	± 9.97
2 wt%	94.33	112.70	87.77	72.30	88.68	62.90
	± 9.93	± 6.50	± 7.47	± 3.50	± 8.94	± 8.27
3.5 wt%	88.30	110.53	85.50	67.40	83.80	57.28
	± 9.60	± 6.17	± 9.50	± 8.53	± 9.19	± 7.19

6.5. Conclusions

The study in this chapter evaluated several influencing factors for organic coating degradation. Based on the experimental results on clear coating degradation under non-refreshed and refreshed stationary NaCl solution as well as non-recirculated and recirculated flowing NaCl solution, we conclude that the effect of refreshed NaCl solution is negligible and the coating degradation could not be influenced significantly by refreshing the working fluid only. The effect of different concentrations of NaCl solutions on organic coating degradation is not pronounced either. Although no clear trend is found in this study, these factors could somehow influence the coating degradation which still needs further investigations.

6.6. References

[1] H. Altun, S. Sen, Studies on the influence of chloride ion concentration and pH on the corrosion and electrochemical behaviour of AZ63 magnesium alloy, *Materials & Design*, **25** (2004) 637-643.

[2] A. Dhanapal, S. Rajendra Boopathy, V. Balasubramanian, Influence of pH value, chloride ion concentration and immersion time on corrosion rate of friction stir welded AZ61A magnesium alloy weldments, *Journal of Alloys and Compounds*, **523** (2012) 49-60.

[3] Y. Gu, X. Cai, Y. Guo, C. Ning, Effect of chloride ion level on the corrosion performance of MAO modified AZ31 alloy in NaCl solutions, *Materials & Design*, **43** (2013) 542-548.

[4] X. Jiang, Y.G. Zheng, D.R. Qu, W. Ke, Effect of calcium ions on pitting corrosion and inhibition performance in CO_2 corrosion of N80 steel, *Corrosion Science*, **48** (2006) 3091-3108.

[5] J. Liang, P.B. Srinivasan, C. Blawert, W. Dietzel, Influence of chloride ion concentration on the electrochemical corrosion behaviour of plasma electrolytic oxidation coated AM50 magnesium alloy, *Electrochimica Acta*, **55** (2010) 6802-6811.

[6] N. Fredj, S. Cohendoz, X. Feaugas, S. Touzain, Some consequences of saline solution immersion on mechanical behavior of two marine epoxy-based coatings, *Progress in Organic Coatings*, **69** (2010) 82-91.

[7] J.R. Svendsen, G.M. Kontogeorgis, S. Kiil, C.E. Weinell, M. Grønlund, Adhesion between coating layers based on epoxy and silicone, *Journal of Colloid and Interface Science*, **316** (2007) 678-686.

[8] S.S. Pathak, A. Sharma, A.S. Khanna, Value addition to waterborne polyurethane resin by silicone modification for developing high performance coating on aluminum alloy, *Progress in Organic Coatings*, **65** (2009) 206-216.

[9] D.P. Schmidt, B.A. Shaw, E. Sikora, W.W. Shaw, L.H. Laliberte, Corrosion protection assessment of sacrificial coating systems as a function of exposure time in a marine environment, *Progress in Organic Coatings*, **57** (2006) 352-364.

[10] A. Husain, O. Al-Shamah, A. Abduljaleel, Investigation of marine environmental related deterioration of coal tar epoxy paint on tubular steel pilings, *Desalination*, **166** (2004) 295-304.

[11] G.P. Bierwagen, Reflections on corrosion control by organic coatings, *Progress in Organic Coatings*, **28** (1996) 43-48.

[12] F. Rezaei, F. Sharif, A.A. Sarabi, S.M. Kasiriha, M. Rahmaniam, E. Akbarinezhad, Evaluating water transport through high solid polyurethane coating using the EIS method, *Journal of Coatings Technology and Research*, **7** (2010) 209-217.

[13] B.R. Hinderliter, K. Allahar, G.P. Bierwagen, D.E. Tallman, S.G. Croll, Water sorption and diffusional properties of a cured epoxy resin measured using alternating ionic liquids/aqueous electrolytes in electrochemical impedance spectroscopy, *Journal of Coatings Technology and Research*, **5** (2008) 431-438.

[14] G.P. Bierwagen, L. He, J. Li, L. Ellingson, D.E. Tallman, Studies of a new accelerated evaluation method for coating corrosion resistance - thermal cycling testing, *Progress in Organic Coatings*, **39** (2000) 67-78.

CHAPTER 7. SIMULATION OF SECM APPROACH CURVES FOR HETEROGENEOUS METAL SURFACES

7.1. Introduction

Scanning electrochemical microscopy (SECM) as pioneered by Engstrom and coworkers [1-3] and by Bard and coworkers [4-6] has found wide application in surface imaging and kinetic measurement [7]. One area of research where scanning probe techniques such as SECM have been particularly useful is the study of localized corrosion, and many applications have been described in the literature and recently reviewed [8, 9]. We have reported on the use of SECM to image the surface of the aluminum alloy AA 2024-T3 [10], to study corrosion protection of this alloy by active coatings [11-13], to probe Cu release from the alloy surface [9], and to study electron transfer rates at the heterogeneous surface of the alloy [10]. Our interest in electron transfer rate at this complex alloy surface stems not only from its importance to corrosion behavior of the alloy, but also from our desire to better understand mediated electrodeposition of conjugated polymers on the alloy surface, the first step of which is the oxidation of an electron transfer mediator [14-18].

One method for measuring local electron transfer rate at a substrate surface is to monitor the current at the SECM microelectrode probe (or tip) as it approaches the substrate surface in feedback mode [7], generating a probe approach curve of steady-state tip current (i_t) as a function of tip-substrate distance (L). In such an experiment, a mediator is oxidized (or reduced) at the tip at the diffusion limited rate. When the tip is near the substrate surface, the oxidized (or reduced) product generated at the tip diffuses to the substrate surface where it is reduced (or oxidized) back to the original form of the

mediator at a rate governed by the electron transfer rate. Therefore, the approach curve has a variety of shapes depending on the electron transfer rate at the substrate surface. At one extreme, the electron transfer rate is zero (i.e., no electron transfer at the substrate, an insulating surface) and the approach curve exhibits "pure negative feedback" where i_t is always less than the current measured when the tip is far from the surface ($i_{t,\infty}$) [7]. At the other extreme, the electron transfer rate is very large (essentially infinite, a conducting surface) and the approach curve exhibits "pure positive feedback" where i_t is always greater than $i_{t,\infty}$ [7]. For intermediate values of the electron transfer rate, a family of curves is obtained as a function of the potential-dependent electron transfer rate constants, k_{ox} and k_{red}.

The previous theories for steady-state approach curves are mostly based on simulations using some form of finite difference technique or analytical approximations based on numerical results. Diffusion-controlled and Nernstian steady-state approach curves have been simulated [6, 19, 20] and analytical approximations obtained [20, 21]. Similarly, the case of irreversible substrate kinetics (e.g., $k_{ox} > 0$, $k_{red} = 0$) has been simulated [22] and an analytical approximation obtained [23]. These simulations and analytical approximations assume a substrate of infinite extent. We have written a LabVIEW module that performs a least squares fit between approach curve data and these analytical approximations and have used it to obtain approximations of the electron transfer rate constants on various regions of AA 2024-T3. This alloy has Cu-rich intermetallic inclusions of a few microns dimension that exhibit the fastest electron transfer rate. The inclusions are surrounded by the alloy matrix that exhibits slower electron transfer rate [10]. The electron transfer rate depends on pH and for the mediator

hydroquinone sulfonate (HQS) under neutral pH, $k_{red} \approx 0.002$ cm/s and 0.0008 cm/s at the Cu sites and matrix, respectively. Under acidic conditions, the electron transfer rate increases with immersion time (rather slowly at the alloy matrix, stabilizing after ca. 1 h immersion [10]), at which time $k_{red} \approx 0.1$ cm/s and 0.007 cm/s at the Cu sites and matrix, respectively. The instability and increased electron transfer rate under acidic conditions is attributed to slow dissolution of oxide films on the Cu sites and matrix [10].

The Cu intermetallics of AA 2024-T3 are rather sparsely distributed on the alloy surface. For example, the Al_2CuMg (S-phase) particles are the most abundant, ca. 61% by number, occupying ca. 2.7% of the alloy surface [24]. The AlCuFeMn particles are the second most abundant, ca. 12% by number, occupying ca. 0.85% of the alloy surface [24]. Thus, the Al alloy may be characterized as isolated active Cu sites surrounded by less active matrix. Determining the electron transfer rate on the matrix is straightforward since the infinite substrate model may be used (the Cu sites are sufficiently distant so as to not influence the measurement). However, measurement at the Cu-rich intermetallic sites is problematic since these sites are small and are surrounded by matrix at which electron transfer also occurs, albeit at a smaller rate. A previous simulation considered a small conducting spot surrounded by insulator [22] and applied the results to the localized reactivity of a titanium alloy [25]. Another simulation considered a blocking film with microscopic disk-shaped defects [26]. Neither of the models used in these previous simulations is applicable to the Al alloy. Thus, we have not previously published the rate constants mentioned above since the infinite substrate model used for their determination was not appropriate for the Cu sites.

In this study, we use COMSOL Multiphysics software to simulate approach curves for an irreversible electron transfer reaction at a site of small dimension surrounded by a matrix that exhibits slower (or faster) electron transfer rate. Of particular interest are the influences of site size and the ratio of the rate constants (at the site and matrix) on the approach curves. Initial attempts at fitting experimental data with this model will be described.

7.2. Computational Details

7.2.1. Simulation Geometry and Definition of Parameters

The cylindrical SECM cell geometry for a substrate containing a circular active site of radius R_c surrounded by a less (or more) active matrix having radius $R_c + R_m$ is shown in Figure 7.1 (a circular active site is appropriate since the S-phase particles are often nearly circular in shape). The simulation is performed in a 2D axisymmetric geometry with the centerline of the probe (disk microelectrode) as the symmetry axis. The computational domain shown in Figure 7.1 is shaded in light blue. The remaining parameters are defined as follows: R and Z are the coordinates in the directions radial and normal to the electrode surface, respectively, with the tip surface located at Z=0 and the electrode centerline at R=0; *a* is the tip electrode radius; L is the distance between the tip surface and the substrate surface; L1 is the depth of tip immersion (i.e., required simulation space above the plane of the tip); R1 is the substrate (cell) radius; and RG is the outer radius of the tip-insulating material. All physical geometric parameters (Figure 7.1) are rendered dimensionless by dividing by *a*. The substrate is divided into a more active electron transfer site of radius R_c and a less active region (the surrounding alloy matrix) with radius R_m ($R_c + R_m$ = R1, the cell radius). Although the Al alloy matrix

always exhibits slower electron transfer rate than does a Cu site, for completeness we also simulate the situation where the matrix has higher electron transfer rate than does the active site. We consider only irreversible electron transfer at both the active site (with rate constants $k_{ox(c)}$ and $k_{red(c),}$ one of which is zero) and the matrix (with rate constants $k_{ox(m)}$ and $k_{red(m),}$ one of which is zero).

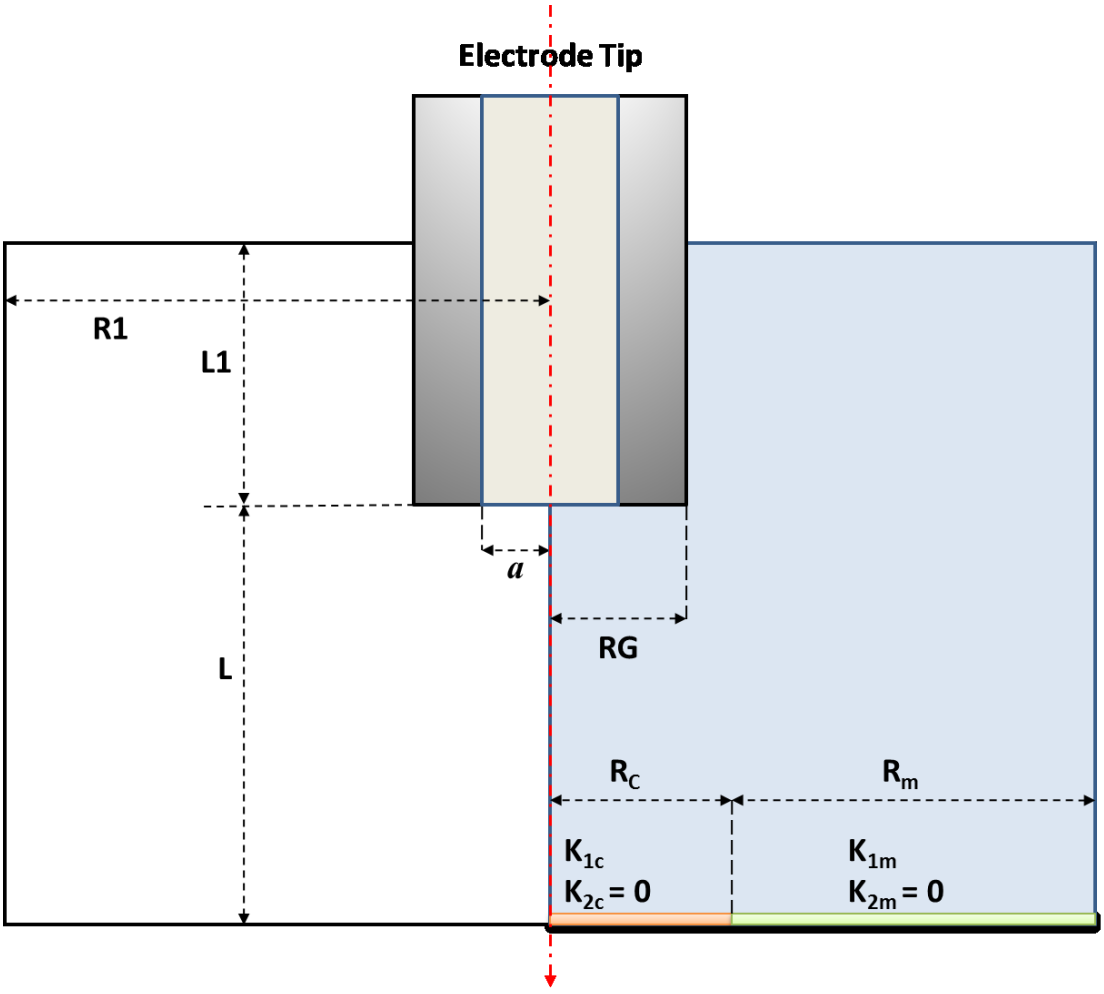

Figure 7.1. Two dimensional axisymmetric cylindrical geometry of the simulation domain (shaded in light blue) and the parameters defining the diffusion problem of SECM.

7.2.2. The Governing Equations and Boundary Conditions

The problem is formulated for a simple electron transfer reaction according to:

$$O + ne^- \underset{k_{ox}}{\overset{k_{red}}{\rightleftharpoons}} R$$

We assume equal diffusion coefficients ($D_O = D_R = D$) which permits the problem to be described in terms of a single species, simplifying the formulation. For the mediators we use to study the Al alloy, this is a reasonable assumption [8]. Furthermore, we study experimental approach curves under steady-state conditions and therefore simulate the approach curves using the steady state solver of COMSOL. In the equations that follow, all quantities are dimensionless, i.e., all geometric dimensions have been normalized by the tip electrode radius (a), the concentration of a species has been normalized with respect to the bulk concentration of mediator (C^*), the dimensionless tip current I_t is related to the physical current i_t by the equation

$$\mathrm{I_t} = \frac{\mathrm{i_t}}{\mathrm{nFD}C^* a} \tag{7-1}$$

and dimensionless time (T) is related to physical time (t) by the equation

$$\mathrm{T} = \frac{\mathrm{tD}}{a^2} \tag{7-2}$$

The steady-state diffusion equation for the cell geometry of Figure 7.1 in terms of the dimensionless concentration (C) of mediator is:

$$\frac{\partial^2 \mathrm{C}}{\partial \mathrm{Z}^2} + \frac{\partial^2 \mathrm{C}}{\partial \mathrm{R}^2} + \frac{1}{\mathrm{R}}\frac{\partial \mathrm{C}}{\partial \mathrm{R}} = 0 \qquad \mathrm{R} \geq 0, \mathrm{L1} \leq \mathrm{Z} < \mathrm{L} \tag{7-3}$$

The initial conditions (not required for the steady-state solver) are: C = 1 for T = 0 and R ≥ 0, 0 ≤ Z ≤ L or R ≥ RG, 0 ≤ Z ≤ L1. There are three sets of boundary conditions as follows [7]:

1) Boundary conditions at the SECM probe (tip):

Tip electrode:

$$C = 0 \qquad 0 \le R < 1, Z = 0 \qquad (7\text{-}4)$$

Zero flux normal to all insulating surfaces surrounding the tip electrode:

$$\frac{\partial C}{\partial n} = 0 \qquad \begin{matrix} 1 \le R < RG, Z = 0 \\ R = RG, L1 < Z < 0 \end{matrix} \qquad (7\text{-}5)$$

2) Boundary conditions on the substrate surface Z = L:

Active site:

$$\frac{\partial C}{\partial Z} = K_{1c}(1 - C) - K_{2c}C \qquad 0 < R \le R_c \qquad (7\text{-}6)$$

Matrix:

$$\frac{\partial C}{\partial Z} = K_{1m}(1 - C) - K_{2m}C \qquad R_c < R < R_1 \qquad (7\text{-}7)$$

For a mediator that is in its oxidized form (i.e., reduced at the SECM tip):

$$K_{1c} = \frac{k_{ox(c)}a}{D} \qquad K_{2c} = \frac{k_{red(c)}a}{D} \qquad K_{1m} = \frac{k_{ox(m)}a}{D} \qquad K_{2m} = \frac{k_{red(m)}a}{D}$$

with $k_{ox(c)}$, $k_{red(c)}$ and $k_{ox(m)}$, $k_{red(m)}$ being the potential-dependent rate constants for oxidation/ reduction on the active spot (*c*) and matrix (*m*), respectively. Conversely, for a mediator such as HQS that is in its reduced form (i.e., oxidized at the SECM tip):

$$K_{1c} = \frac{k_{red(c)}a}{D} \qquad K_{2c} = \frac{k_{ox(c)}a}{D} \qquad K_{1m} = \frac{k_{red(m)}a}{D} \qquad K_{2m} = \frac{k_{ox(m)}a}{D}$$

Ignoring signs usually associated with electrochemical currents, both forms of mediator yield identical approach curves (since $D_O = D_R$), the only difference being interpretation of the rate constants K_{1c} and K_{1m}. For the irreversible substrate kinetics considered here, $K_{2c} = 0, K_{2m} = 0$.

3) Boundary conditions at the simulation space limits:

$$C = 1 \qquad \begin{matrix} RG \le R < R1, Z = L1 \\ \text{or} \\ R = R1, L1 < Z < L \end{matrix} \qquad (7\text{-}8)$$

The dimensionless current I_t for any given L is given by

$$I_t = 2\pi \int_0^1 R \frac{\partial C}{\partial Z} dR \qquad (7\text{-}9)$$

This current is then normalized with respect to $I_{t,\infty}$, the current at large L (i.e., as $L \rightarrow \infty$), to give the normalized tip current i_T displayed in the figures. For $RG \geq 10$ we use $I_{t,\infty} = 4.00$ [7], whereas for $RG < 10$ we use the value of I_t at $L = 100$.

7.3. Computational Parameters and Validation of Simulation

The following COMSOL simulation parameters were chosen based on convergence tests: maximum mesh size = 1, minimum mesh size = 0.002, mesh growth rate = 1.05, resolution of curvature = 0.2 and resolution of narrow regions = 100. These parameters create an error of less than 1% with respect to the results obtained using the maximum number of nodes allowed by our computer configuration and represents the best compromise between computational accuracy and computation time. It has also been shown that the diffusion current obtained by COMSOL using integration of the local flux can be in error by as much as 2% [27]. This error should be reduced when ratios of diffusion currents are taken (as in the normalization to obtain i_T). From these considerations, we estimate the error in our computations to be no greater than 2%.

Although any RG value may be used in the simulation, an RG of 10 was chosen for most of our simulations since that most closely approximates the SECM probe used in our experiments. The optimum values for L1 and R1 were determined at various L for a uniform conducting substrate by increasing the values of L1 and R1 until any further

change in the normalized tip current (i_T) was less than 0.01%. From these studies, the optimum values were determined to be L1 = 15 and R1 = 100.

To confirm the accuracy of our simulations, we reproduced the results from equations 8 (conducting substrate) and 9 (insulating substrate) from reference [19] for RG values of 1.1, 2, and 10. The maximum observed difference is 1.3% for the conducting substrate and 1.5% for the insulating substrate, within the stated accuracy of the approximate equations. An example of the agreement for RG = 10 is shown in Figure 7.2. As a further check of our simulation, we verified our kinetic boundary conditions by simulating irreversible electron-transfer kinetics at a uniform substrate of infinite extent (i.e., R_c = R1), using K_{1c} values ranging from 0.01 to 1000 (K_{2c} = 0). The approach curves from our COMSOL simulations were within 1.0% of those generated based on approximate equations from previous work [22, 23]. Examples of the agreement for two values of K_{1c} are shown in Figure 7.2. Finally, we reproduced the results of Bard and coworkers for diffusion-controlled feedback at active sites of arbitrary size surrounded by insulator [22], using R_c values of 0.1, 0.3, 0.5, 0.7, 1.0, 40, and 99. Our results are in good agreement with Fig. 7 from reference [22]. An example of the simulation image for the concentration distribution at the electrode tip is shown in Figure 7.3.

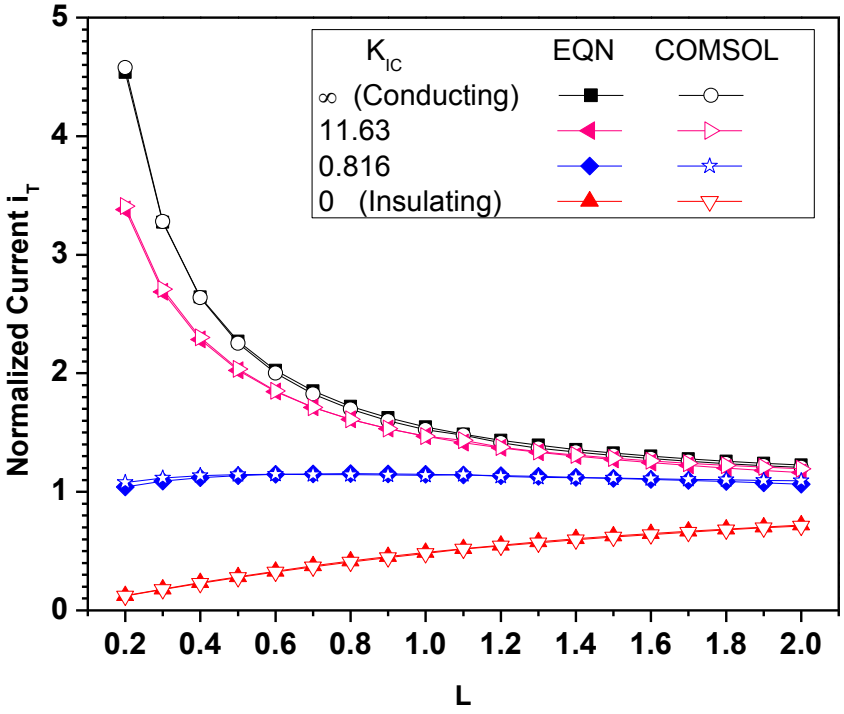

Figure 7.2. Approach curves from COMSOL (open symbols) for RG = 10 compared with the results from approximate equations (solid symbols) for conducting and insulating substrates [19] and for irreversible substrate kinetics [23]. The dimensionless rate constants (K_{1c}) of 11.63 and 0.816 correspond to the approximate values observed on a Cu site and the matrix, respectively, of the AA 2024-T3 alloy.

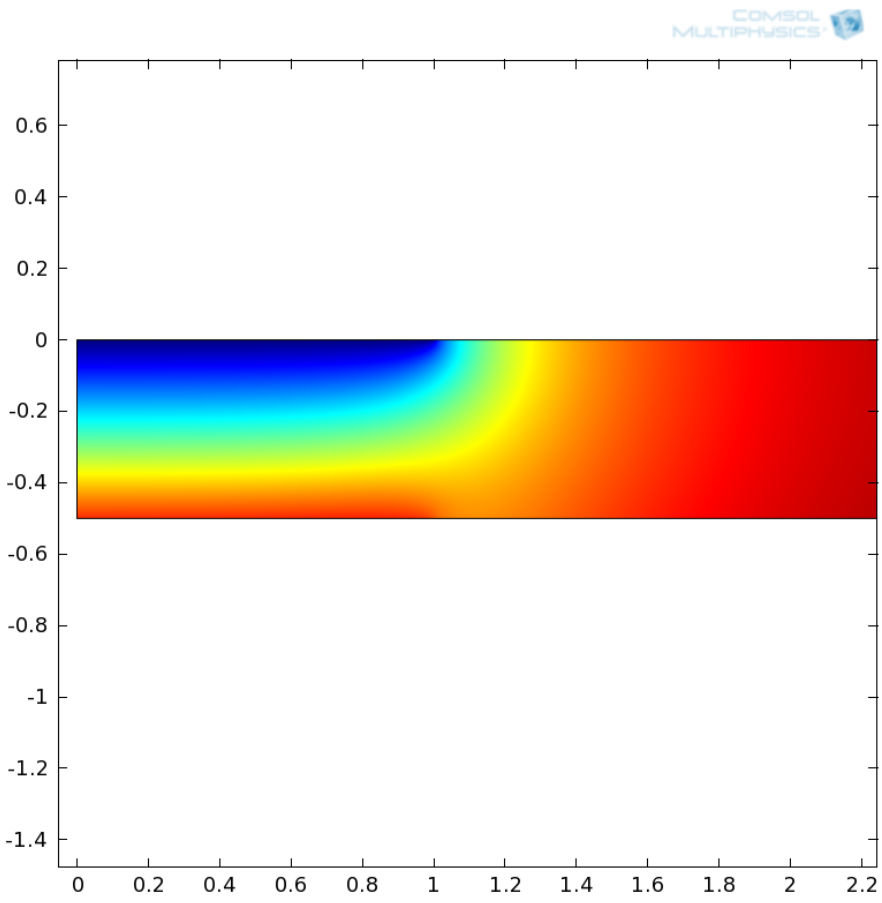

Figure 7.3. Image for concentration distribution at the SECM tip with computational parameters of L1 = 15, RG = 10, R1 = 100, L = 0.5, a = 1, R_c = 1.0, K_{1c} = 10, K_{2c} = 0, K_{1m} = 1.0, K_{2m} = 0.

7.4. Results and Discussion

7.4.1. Simulations for the Model Al Alloy

Figure 7.4 (a-e) displays the results of this computational study for various combinations of R_c, K_{1c}, and K_{1m}. In each of these five panels, K_{1c} = 0.1, 1.0, or 10, with K_{1m} chosen to give ratios K_{1c}/K_{1m} of 10, 5, 2, or 1. Thus, there are three sets of four curves each, with little overlap among the three sets. The top set of four curves in each panel corresponds to K_{1c} = 10, the middle set to K_{1c} = 1, and the bottom set to K_{1c} = 0.1. Within each set, the four curves correspond (from top to bottom) to ratios K_{1c}/K_{1m} of 1, 2,

5 and 10. Note that within each set, the ratio $K_{1c}/K_{1m} = 1$ corresponds to the infinite (uniform) substrate model for that particular value of K_{1c} and is the top curve within each set. The ranges of these various parameters were chosen to encompass the values typical of the alloy AA2024-T3.

It is not surprising that, as R_c increases, the matrix has less influence on the approach curve, but at what R_c is the influence of the matrix negligible? Figure 7.4 (e) shows that, for $R_c = 4$, the four curves within each set virtually overlap and, thus, the electron transfer rate on the matrix has negligible effect. Even for $R_c = 2$ and $K_{1c} = 10$ the curves overlap (Figure 7.4 d), although at lower K_{1c} there is increasing differentiation among the approach curves, particularly at larger L. Thus, for active spots with radii four times that of the SECM tip electrode, the infinite substrate model will suffice for any matrix activity that does not exceed that of the active spot. If $K_{1c} > 1$, the infinite substrate model will also provide reasonable results for R_c as small as 2.

At the other extreme, for very small R_c, the matrix dominates the behavior, especially for lower K_{1c} values. For example, at $R_c = 0.2$ (Figure 7.4 a), the approach curves for $K_{1c} = 0.1$, $K_{1m} = 0.1$ (i.e., the infinite homogeneous substrate model) and for $K_{1c} = 1$, $K_{1m} = 0.1$ are nearly superimposed. In other words, K_{1c} has little effect on the approach curve and a determination of K_{1c} from experimental data would not be feasible. For larger K_{1c}, some differentiation in the approach curves is observed, especially at small L. For example, the curves for $K_{1c} = 1$, $K_{1m} = 1$ and for $K_{1c} = 10$, $K_{1m} = 1$ show some separation at $L < 1$, but determination of K_{1c} from an experimental approach curve would be subject to considerable uncertainty. Thus, for active spots with radii less than or

equal to one-fifth the tip electrode radius, it would not be possible to extract reliable values of K_{1c}.

The heterogeneous model presented here appears most applicable to R_c values ranging from greater than one-fifth to less than four-times the tip electrode radius. For a 5-μm radius tip, this means active spot radii in the range > 1.0 μm to < 20 μm, the size range within which many Cu-rich intermetallic inclusions of AA 2024-T3 are found [24]. Of course, a smaller tip electrode radius (*a*) would permit smaller physical spot sizes to be probed. Figure 7.4 (f) shows a family of approach curves for differing R_c values for rate constants $K_{1c} = 10$ and $K_{1m} = 1$, typical of those estimated for the Al alloy under mildly acidic conditions. All exhibit positive feedback but with a shape greatly dependent on R_c for R_c values between 2 and 0.2. For $R_c \geq 2$, the approach curves are indistinguishable at these values of the rate constants and the infinite substrate model is applicable.

Figure 7.5 compares three models for the generation of approach curves for an alloy having a dimensionless active spot size R_c of 0.5 or 1.0 and an active spot rate constant K_{1c} of 10: 1) the infinite uniform substrate model ($K_{1m} = 10$); 2) the active spot surrounded by an insulating matrix model ($K_{1m} = 0$); and 3) the alloy model of this work (with $K_{1m} = 1$). It is clear from this figure that neither the infinite substrate model nor the insulating matrix model is applicable for these combinations of active spot size and rate constant, typical of those encountered with the AA 2024-T3 alloy. The insulating matrix model would lead to an overestimation of K_{1c} whereas the infinite substrate model would lead to an underestimation of K_{1c}. Thus, use of the model presented here should provide more reliable values of the rate constants on the Cu-rich inclusions of this alloy.

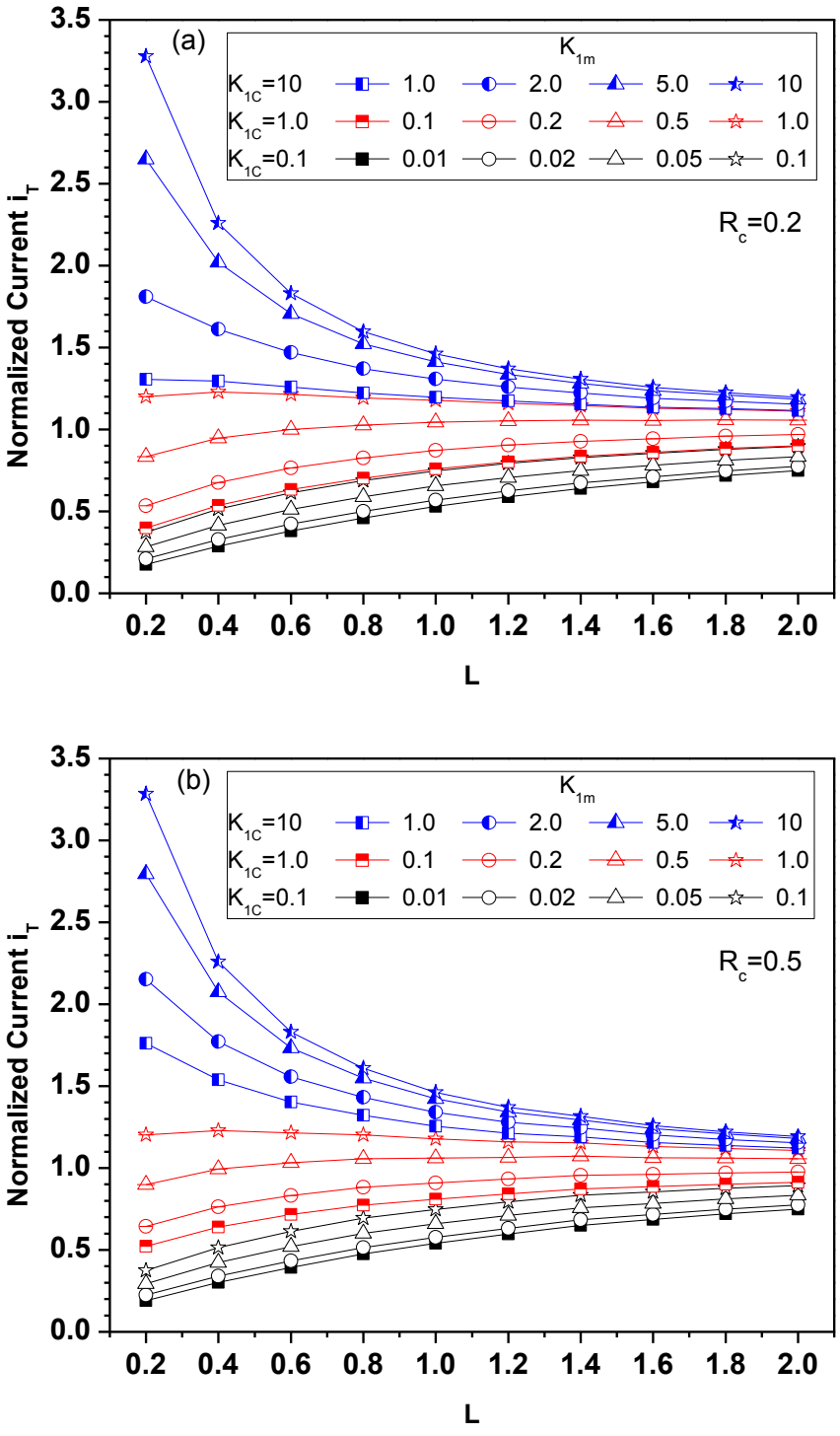

Figure 7.4. (a-e) Probe approach curves for various combinations of R_c, K_{1c}, and K_{1m}. In each case, K_{1c} = 0.1, 1.0, or 10 and K_{1m} is chosen to give ratios K_{1c}/K_{1m} of 10, 5, 2, and 1. Note that the ratio K_{1c}/K_{1m} = 1 corresponds to the infinite (uniform) substrate model. (a) R_c = 0.2, (b) R_c = 0.5, (c) R_c = 1.0, (d) R_c = 2.0, (e) R_c = 4.0, and (f) Probe approach curves for various R_c with K_{1c} = 10, K_{1m} = 1.

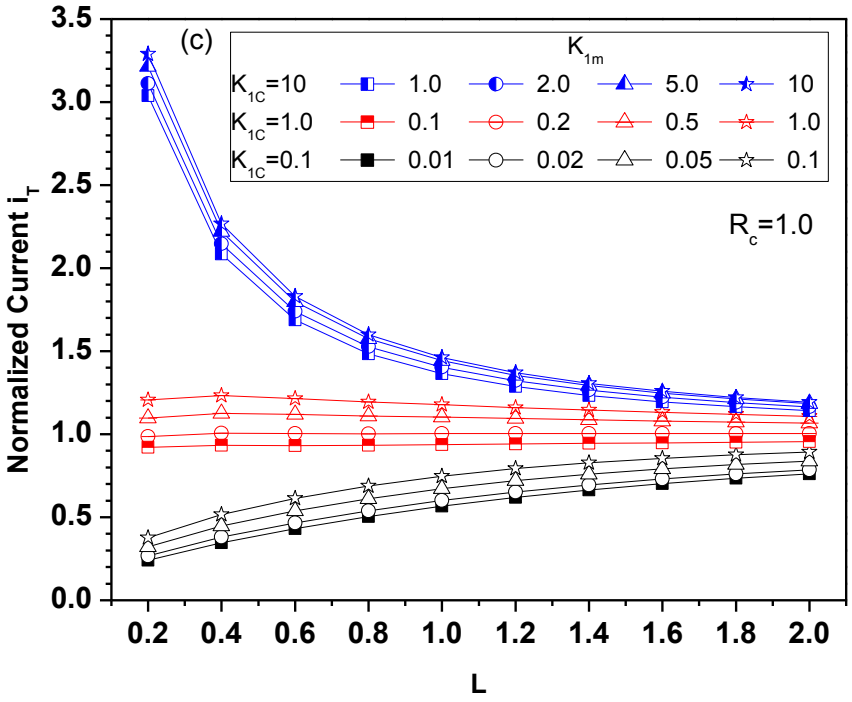

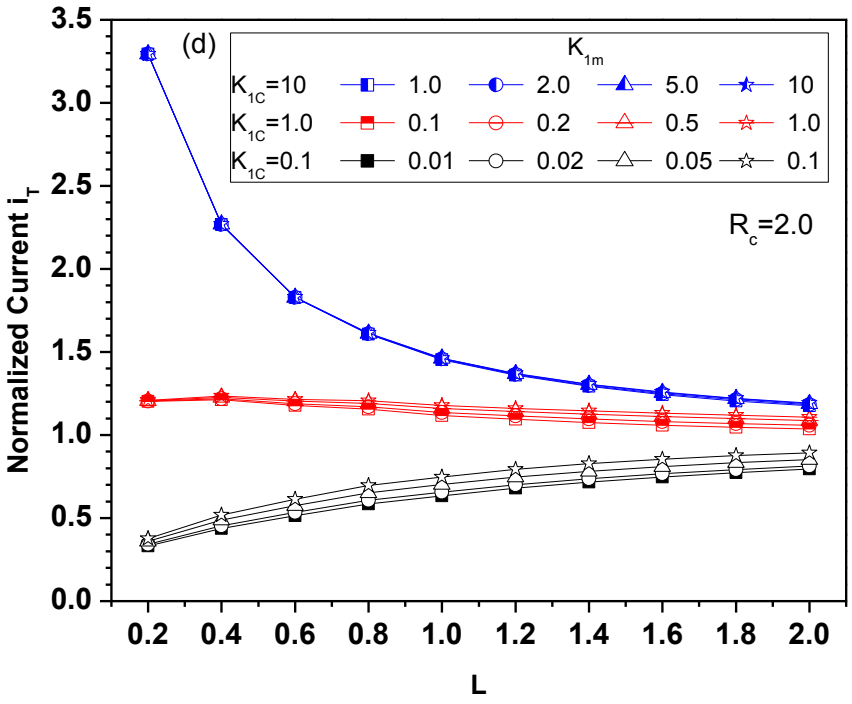

Figure 7.4. (a-e) Probe approach curves for various combinations of R_c, K_{1c}, and K_{1m}. In each case, K_{1c} = 0.1, 1.0, or 10 and K_{1m} is chosen to give ratios K_{1c}/K_{1m} of 10, 5, 2, and 1. Note that the ratio K_{1c}/K_{1m} = 1 corresponds to the infinite (uniform) substrate model. (a) R_c = 0.2, (b) R_c = 0.5, (c) R_c = 1.0, (d) R_c = 2.0, (e) R_c = 4.0, and (f) Probe approach curves for various R_c with K_{1c} = 10, K_{1m} = 1, (continued).

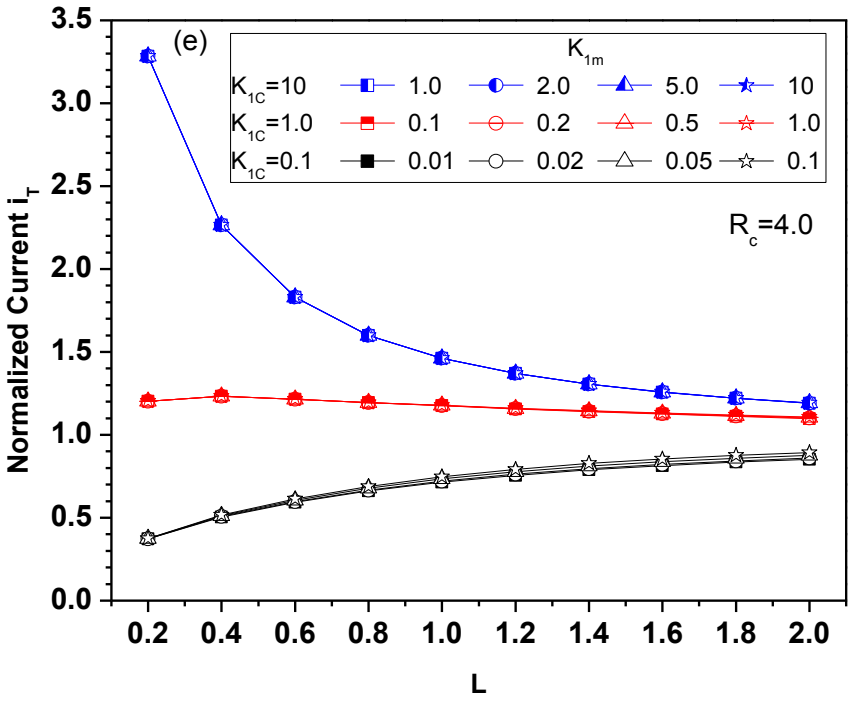

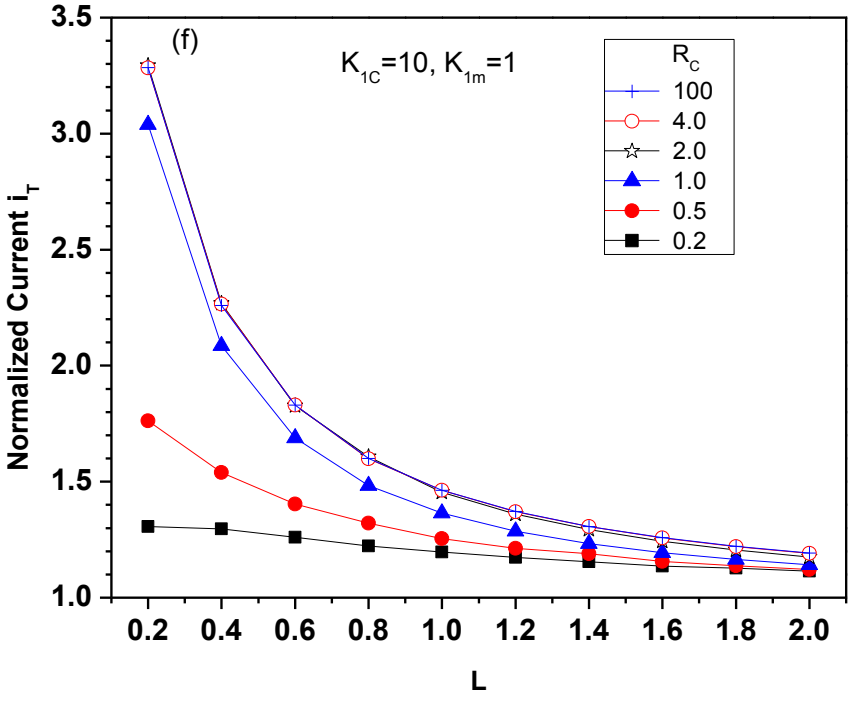

Figure 7.4. (a-e) Probe approach curves for various combinations of R_c, K_{1c}, and K_{1m}. In each case, K_{1c} = 0.1, 1.0, or 10 and K_{1m} is chosen to give ratios K_{1c}/K_{1m} of 10, 5, 2, and 1. Note that the ratio K_{1c}/K_{1m} = 1 corresponds to the infinite (uniform) substrate model. (a) R_c = 0.2, (b) R_c = 0.5, (c) R_c = 1.0, (d) R_c = 2.0, (e) R_c = 4.0, and (f) Probe approach curves for various R_c with K_{1c} = 10, K_{1m} = 1, (continued).

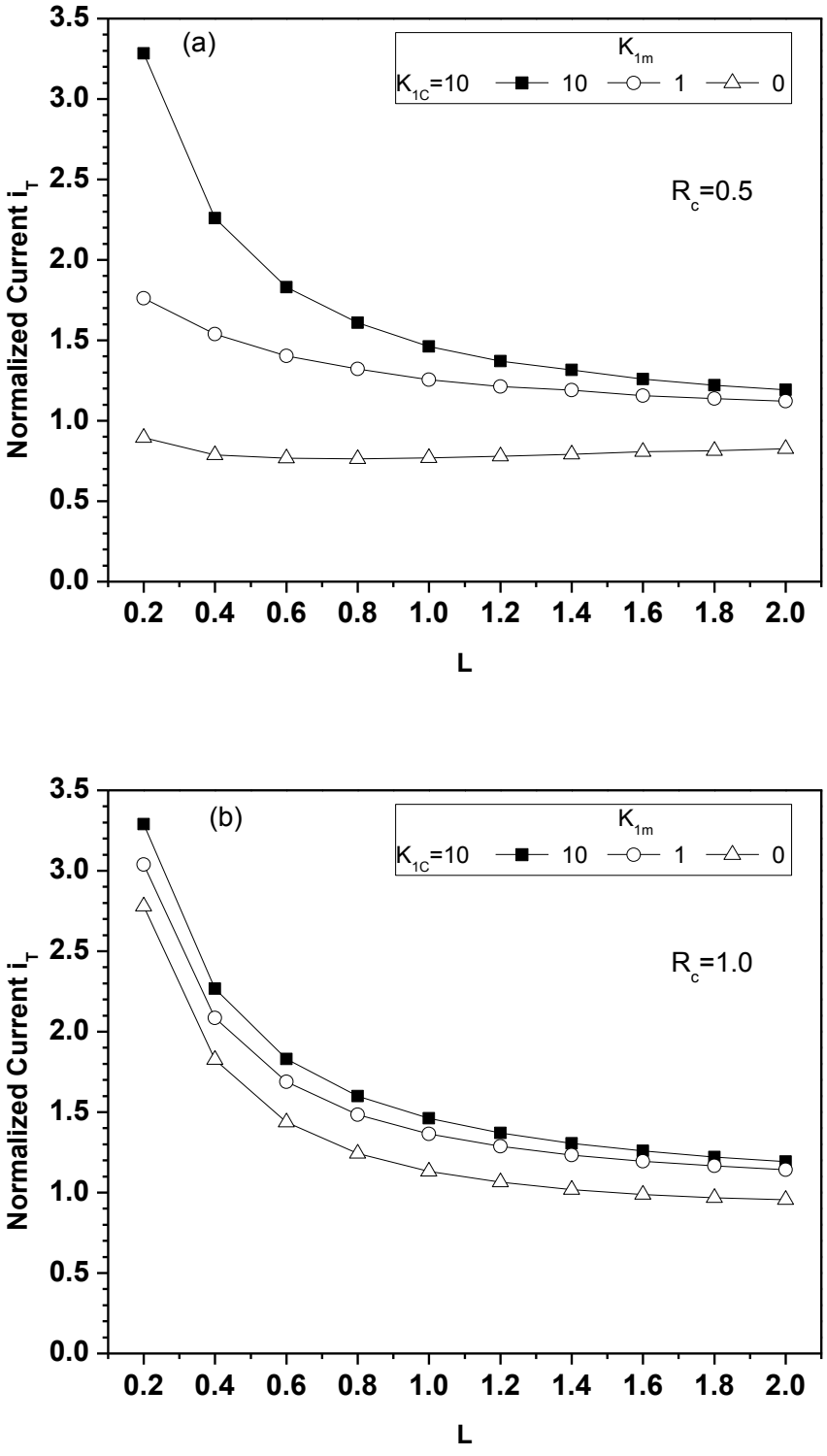

Figure 7.5. Probe approach curves for three models having (a) $R_c = 0.5$ and $K_{1c} = 10$, and (b) $R_c = 1.0$ and $K_{1c} = 10$. In each figure, the top curve is the infinite uniform substrate model ($K_{1m} = 10$), the middle curve is the alloy model of this work ($K_{1m} = 1$), and the bottom curve is the insulating matrix model ($K_{1m} = 0$).

Finally, although we always find the electron transfer rate to be higher on the Cu inclusions than on the matrix of AA 2024-T3, for completeness we consider one example where the matrix exhibits faster electron transfer rate than some small region it surrounds. Figure 7.6 shows such a case for $R_c = 1$ and for a range of K_{1c} and K_{1m} values. The middle curve in each set of three curves corresponds to the infinite substrate model (i.e., $K_{1c} = K_{1m}$). Of course, the approach curves tend to converge to the conducting ($K_{1c} = \infty$) limit for large K_{1c}, and the matrix then has little or no influence on the approach curve when $K_{1m} \geq K_{1c}$. Thus, the matrix has only small influence on the curves for $K_{1c} = 20$. For the smaller values of K_{1c}, the matrix has much more influence on the approach curve, increasing the current when $K_{1m} > K_{1c}$ and decreasing the current when $K_{1m} < K_{1c}$. Note that for $K_{1c} = 0.2$, the approach curve exhibits fully negative feedback for $K_{1m} = 0.02$ or 0.2, but exhibits positive feedback over most of the approach ($L \geq 0.4$) for $K_{1m} = 2.0$. Not surprisingly, the matrix has greater influence for smaller R_c (e.g., see Figure 7.4) and larger K_{1m}.

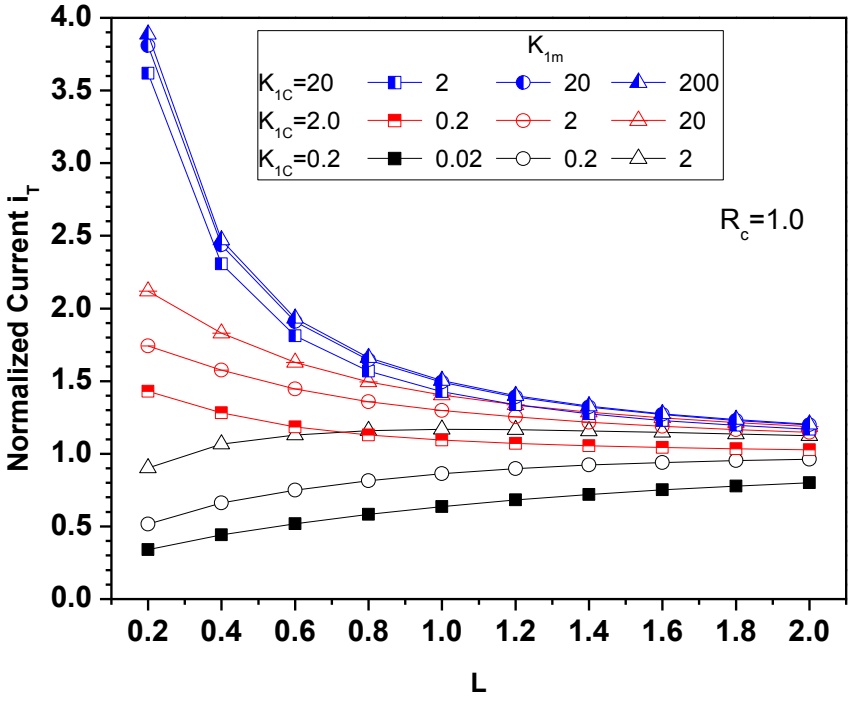

Figure 7.6. Probe approach curves for R_c = 1.0 and for K_{1c} = 0.2, 2.0, and 20, with K_{1m} chosen to given ratios K_{1c}/K_{1m} of 10, 1.0, and 0.1. Note that the ratio K_{1c}/K_{1m} = 1 corresponds to the infinite (uniform) substrate model whereas the ratio of 0.1 corresponds to a matrix more active that the "active spot".

7.4.2. Extracting Rate Constants from Experimental Data

We have previously demonstrated that every spot of high electron transfer activity (hotspot) on the AA 2024-T3 alloy is associated with a Cu-rich intermetallic inclusion [10]. Figure 7.7 shows a SECM map containing a nearly circular hotspot surrounded by less active matrix, obtained using the mediator HQS (10 mM, D = 4.4 × 10^{-6} cm^2/s) in an electrolyte of 1 M Na_2SO_4 and 1 mM H_2SO_4 [10]. The size of such hotspots can be estimated from both SEM and SECM, with some diffusional broadening expected in the SECM images. From measurements of the size of correlated SEM Cu sites and SECM hotspots [10], we find that the ratio of SECM dimension (defined at the boundary of

highest contrast) to SEM dimension is 1.07 ± 0.08 for the SECM tip and scan rate used in this work (a = 5 μm, RG = 10). The radius of the hotspot in Figure 7.7 is estimated to be 6.3 μm, corresponding to a R_c value of 1.26. As demonstrated in Figure 7.5 (for R_c = 1), the use of the insulating matrix model for an R_c of this magnitude can lead to substantial overestimation of the electron transfer rate constant at the hotspot (the additional flux at the SECM tip from the matrix would be interpreted as a larger rate constant at the hotspot). The infinite substrate model is a much better approximation, though some error (an underestimation of K_{1c}) would still be present.

The arrows in Figure 7.7 indicate locations where approach curve measurements were made, one on the matrix and one on the active spot. One difficulty we encounter is knowing with certainty the distance of closest approach between the SECM tip and the substrate surface, referred to here as the offset. Complicating this issue is the fact that these alloy surfaces are not particularly smooth, a result of the heterogeneous nature of the surface and differential polishing effects. Our alloy surfaces were prepared by cutting the alloy panel (from Q-Panel) into sizes appropriate for the SECM cell, sanding with 600-grit silicon carbide, rinsing with hexane, and air drying. The probe approach was conducted until the tip (electrode sheath) contacted the surface, signaled by the onset of constant tip current.

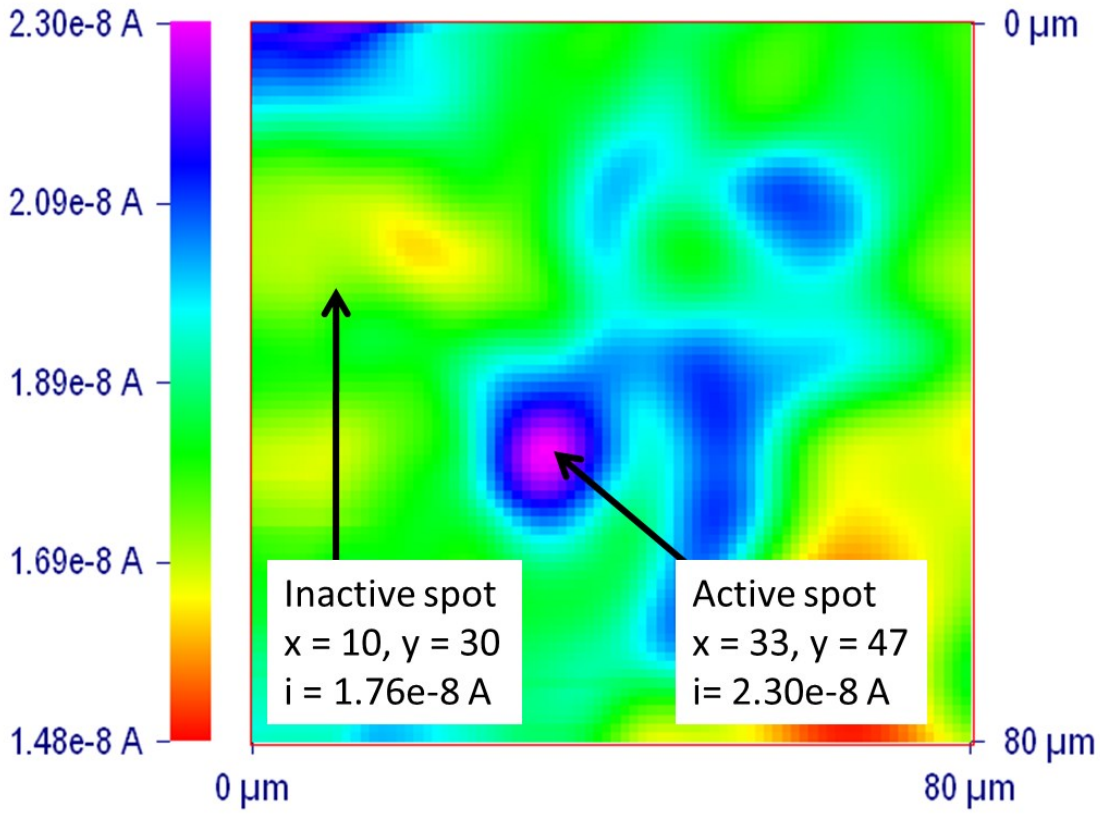

Figure 7.7. SECM image of AA 2024-T3 showing a circular active spot (Cu-rich inclusion) surrounded by less active matrix. Arrows show locations of the approach curve measurements. The mediator was 10 mM HQS in an electrolyte of 1 M Na_2SO_4 and 1 mM H_2SO_4. The SECM tip had an electrode radius *a* of 5 µm and a RG of 10, $i_{t,\infty} = 1.66 \times 10^{-8}$ A in the experiment.

For the approach curve on the matrix, the infinite uniform substrate model was used, as justified earlier. Using our LabVIEW program (which agrees with the COMSOL simulation for an infinite substrate as demonstrated earlier, but is only valid to L = 2), both the offset and the rate constant (K_{1m}) were systematically varied to give the best least-squares agreement between the experimental data and theory. The dimensionless values of offset and K_{1m} obtained from this optimization were 1.17 (or 5.8 µm) and 0.95 (or $k_{red,m} = 0.0084$ cm/s), respectively. This value of offset was then used in the COMSOL model for estimation of the rate constant K_{1m}, which was systematically varied

(using 0.95 as the starting value) to give the best least-squares agreement with the experimental data (i.e., the value of K_{1m} that minimized the sum of the squares of the deviations between experiment and theory). The result of this procedure is shown in Figure 7.8 for the optimum value $K_{1m} = 0.88$ (the average relative deviation of a point is 1.2%). This value of K_{1m} is in reasonable agreement with the LabVIEW result (0.95) which utilized far fewer data points ($L < 2$). For the experimental conditions used in this work, a K_{1m} of 0.88 corresponds to $k_{red(m)} = 0.0077$ cm/s. The rather constant current on the matrix surrounding the hotspot (Figure 7.7) suggest little variation in the value of K_{1m}. We have measured numerous approach curves to the alloy matrix and the one selected here is representative of the set.

For the approach curve on the active spot (having $R_c = 1.26$), the COMSOL alloy model was used with K_{1m} fixed at 0.88, using the offset determined above. K_{1c} was systematically varied to give the best least-squares agreement with the experimental data. The result is shown in Figure 7.8 for the optimum value $K_{1c} = 15$ (the average relative deviation of a point is 1.0%). As predicted from the discussion of Figure 7.5, this value is indeed larger than the value of 7.5 estimated from the LabVIEW program (i.e., the infinite substrate model). For the experimental conditions used in this work, a K_{1c} of 15 corresponds to $k_{red(c)} = 0.13$ cm/s.

We conclude with a comment on the uncertainty in the rate constants reported above. We estimate the uncertainty by noting the sensitivity of the fit to the corresponding rate constant. For $k_{red(m)} = 0.0077$ cm/s, the uncertainty is on the order of ±20%, determined as the range of $k_{red(m)}$ over which the sum-square increases by 50%. For $k_{red(c)} = 0.13$ cm/s, the uncertainty is larger and is not symmetrical, due to the

proximity of its corresponding approach curve to the conducting limit. The value may be significantly larger than 0.13 cm/s, and so it may be more appropriate to consider 0.13 cm/s to be a lower bound for the rate constant on the Cu site. In any event, it appears the electron transfer rate on the Cu site is at least 17 times faster than that on the matrix.

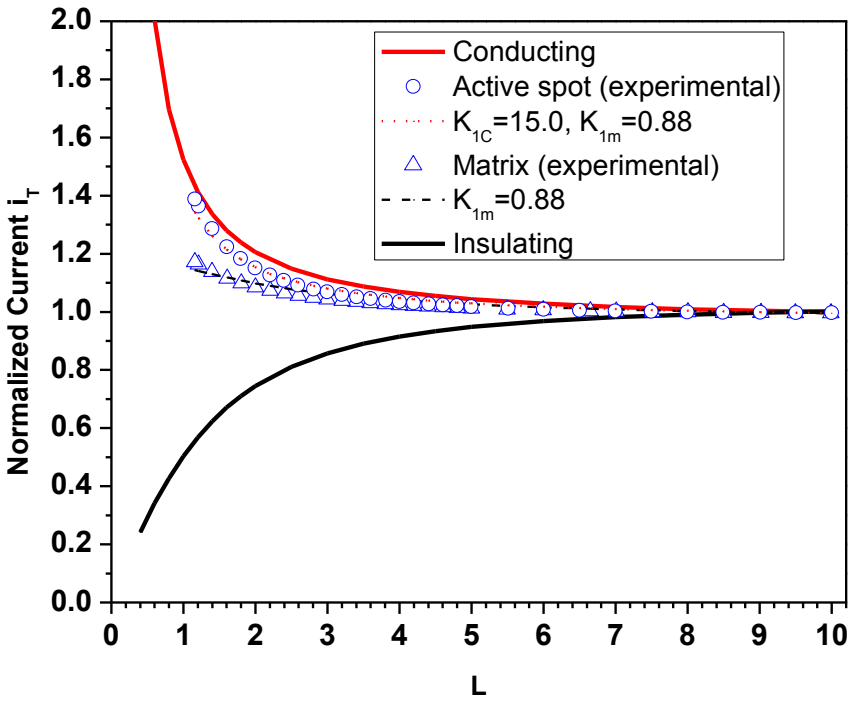

Figure 7.8. Probe approach curves from the COMSOL alloy model (lines) and from experiment (points). The conducting (K_{1c}, $K_{1m} = \infty$, top curve) and insulating (K_{1c}, K_{1m} = 0, bottom curve) limits are also shown. Probe approach rate was 0.25 μm/s. Matrix (Δ) using infinite substrate model with K_{1m} = 0.88; Active spot (○) using alloy model with K_{1c} = 15, K_{1m} = 0.88. For clarity, only selected experimental points are displayed.

7.5. Conclusions

The heterogeneous alloy model presented here provides insight into the influence of active spot size (R_c), matrix rate constant (K_{1m}), and active spot rate constant (K_{1c}) on probe approach curves obtained by SECM. The model can be used to obtain a more

accurate value of the rate constant on a small region (the active spot) surrounded by a large less (or more) active region (the matrix). Alternatively, the results presented here can be used to determine the SECM probe size (*a*) necessary to permit use of the infinite uniform substrate model for any alloy of interest having known (or estimated) R_c, K_{1m}, and K_{1c}. This alloy model will be useful in our future efforts to study electron transfer rate at AA 2024-T3 as function of Cu intermetallic inclusion composition, solution pH, nature of the mediator, and type of alloy surface preparation.

7.6. References

[1] R.C. Engstrom, M. Weber, D.J. Wunder, R. Burgess, S. Winquist, Measurements within the diffusion layer using a microelectrode probe, *Analytical Chemistry*, **58** (1986) 844-848.

[2] R.C. Engstrom, T. Meaney, R. Tople, R.M. Wightman, Spatiotemporal description of the diffusion layer with a microelectrode probe, *Analytical Chemistry*, **59** (1987) 2005-2010.

[3] R.C. Engstrom, R.M. Wightman, E.W. Kristensen, Diffusional distortion in the monitoring of dynamic events, *Analytical Chemistry*, **60** (1988) 652-656.

[4] A.J. Bard, F.R.F. Fan, J. Kwak, O. Lev, Scanning electrochemical microscopy. Introduction and principles, *Analytical Chemistry*, **61** (1989) 132-138.

[5] J. Kwak, A.J. Bard, Scanning electrochemical microscopy. Apparatus and two-dimensional scans of conductive and insulating substrates, *Analytical Chemistry*, **61** (1989) 1794-1799.

[6] J. Kwak, A.J. Bard, Scanning electrochemical microscopy. Theory of the feedback mode, *Analytical Chemistry*, **61** (1989) 1221-1227.

[7] M.V. Mirkin, Theory, in: A.J. Bard, M.V. Mirkin (Eds.) Scanning Electrochemical Microscopy, Marcell Dekker, Inc., New York, NY, 2001, pp. 145-199.

[8] M.B. Jensen, D.E. Tallman, Application of SECM to Corrosion Studies, in: A.J. Bard, C.G. Zoski (Eds.) Electroanalytical Chemistry: A Series of Advances, Taylor and Francis, Boca Raton, Fl, 2011, pp. 171-286.

[9] D.E. Tallman, M.B. Jensen, Applications of Scanning Electrochemical Microscopy in Corrosion Research, in: A.J. Bard, M.V. Mirkin (Eds.) Scanning Electrochemical Microscopy, Taylor and Francis, Boca Raton, Fl, 2012, pp. 447-484.

[10] M.B. Jensen, A. Guerard, D.E. Tallman, G.P. Bierwagen, Studies of Electron Transfer at Aluminum Alloy Surfaces by Scanning Electrochemical Microscopy, *Journal of Electrochemical Society*, **155** (2008) C324-C332.

[11] A.M. Simoes, D. Battocchi, D.E. Tallman, G.P. Bierwagen, Corrosion protection of aluminum substrates by a Mg-rich primer studied using electrochemical scanning techniques, *ICE 2007, Int. Coat. Expo Clean-Lean-Green Innovative Solutions Global Coat. Community*, (2007) 39/31-39/14.

[12] A.M. Simoes, D. Battocchi, D.E. Tallman, G.P. Bierwagen, SVET and SECM imaging of cathodic protection of aluminum by a Mg-rich coating, *Corrosion Science*, **49** (2007) 3838-3849.

[13] A. Simoes, D. Battocchi, D. Tallman, G. Bierwagen, Assessment of the corrosion protection of aluminium substrates by a Mg-rich primer: EIS, SVET and SECM study, *Progress in Organic Coating*, **63** (2008) 260-266.

[14] D.E. Tallman, C. Vang, G.G. Wallace, G.P. Bierwagen, Direct electrodeposition of polypyrrole on aluminum and aluminum alloy by electron transfer mediation, *Journal of Electrochemical Society*, **149** (2002) C173-C179.

[15] D.E. Tallman, C.K. Vang, M.P. Dewald, G.G. Wallace, G.P. Bierwagen, Electron transfer mediated deposition of conducting polymers on active metals, *Synthetic Metals*, **135-136** (2003) 33-34.

[16] K.L. Levine, D.E. Tallman, G.P. Bierwagen, The Mediated Electrodeposition of Polypyrrole on Aluminium Alloy, *Australian Journal of Chemistry*, **58** (2005) 294-301.

[17] K.L. Levine, D.E. Tallman, G.P. Bierwagen, Deposition of polypyrrole on porous aluminium oxide, *ECS Transactions*, **1** (2006) 81-91.

[18] J. Nie, D.E. Tallman, G.P. Bierwagen, The electrodeposition of polypyrrole on Al alloy from room temperature ionic liquids, *Journal of Coatings Technology and Research*, **5** (2008) 327-334.

[19] Y. Shao, M.V. Mirkin, Probing Ion Transfer at the Liquid/Liquid Interface by Scanning Electrochemical Microscopy (SECM), *Journal of Physical Chemistry B*, **102** (1998) 9915-9921.

[20] J.L. Amphlett, G. Denuault, Scanning Electrochemical Microscopy (SECM): An Investigation of the Effects of Tip Geometry on Amperometric Tip Response, *Journal of Physical Chemistry B*, **102** (1998) 9946-9951.

[21] M.V. Mirkin, F.R.F. Fan, A.J. Bard, Scanning electrochemical microscopy. Part 13. Evaluation of the tip shapes of nanometer size microelectrodes, *Journal of Electrochemical Society*, **328** (1992) 47-62.

[22] A.J. Bard, M.V. Mirkin, P.R. Unwin, D.O. Wipf, Scanning electrochemical microscopy. 12. Theory and experiment of the feedback mode with finite heterogeneous electron-transfer kinetics and arbitrary substrate size, *Journal of Physical Chemistry*, **96** (1992) 1861-1868.

[23] C. Wei, A.J. Bard, M.V. Mirkin, Scanning Electrochemical Microscopy. 31. Application of SECM to the Study of Charge Transfer Processes at the Liquid/Liquid Interface, *Journal of Physical Chemistry*, **99** (1995) 16033-16042.

[24] R.G. Buchheit, R.P. Grant, P.F. Hlava, B. McKenzie, G.L. Zender, Local dissolution phenomena associated with S phase (Al_2CuMg) particles in aluminum alloy 2024-T3, *Journal of Electrochemical Society*, **144** (1997) 2621-2628.

[25] R. Zhu, Z. Qin, J.J. Noeel, D.W. Shoesmith, Z. Ding, Analyzing the influence of alloying elements and impurities on the localized reactivity of titanium Grade-7 by scanning electrochemical microscopy, *Analytical Chemistry*, **80** (2008) 1437-1447.

[26] F. Forouzan, A.J. Bard, M.V. Mirkin, Voltammetric and scanning electrochemical microscopic studies of the adsorption kinetics and self-assembly of n-alkanethiol monolayers on gold, *Israel Journal of Chemistry*, **37** (1997) 155-163.

[27] I.J. Cutress, E.J.F. Dickinson, R.G. Compton, Analysis of commercial general engineering finite element software in electrochemical simulations, *Journal of Electrochemical Society*, **638** (2010) 76-83.

CHAPTER 8. SUMMARY

This study evaluated the flow accelerated organic coating degradation. The effect of flow rate, fluid shear, and fluid compositions on the degradation were investigated as well as other miscellaneous influencing factors. A finite difference simulation was carried out for the convective diffusion process of ions. A pigmented marine coating and commercially available clear coatings were adopted in the study. The coating degradation was monitored by Electrochemical Impedance Spectroscopy (EIS) measurement, analyzed by equivalent circuit modeling, and characterized by topography measurements.

For the influence of flow rate in the marine coating degradation, we conclude that higher flow rates bring more aggressive deterioration to the coatings than the stationary or lower flow rates. The decrease of impedance modulus was more substantial for flowing fluid at higher flow rates. The higher coating capacitance and lower coating resistance was shown under flowing immersion. The coating surface changed more pronouncedly for higher flow rates due to their enhancement of blister formation.

For the influence of fluid shear in the clear coating degradation, the organic coating materials released from the coating into surrounding fluid as a result of fluid shear, demonstrated by the Fourier Transform Infrared Spectrometer (FTIR) spectrum, the increased conductivity of the working fluid, and decreased coating thickness under higher flow rates. The increase in coating capacitance, decrease in coating resistance, and the evolution of coating's permittivity demonstrates that flowing fluid not only wears coating's surface by fluid shear, it also influences its internal property.

Four clear coatings were immersed in a stationary 3.5 wt% NaCl solution and pure water to study the influence of fluid composition on the coating degradation. Pure

water incurred a more substantial decrease in coating resistance, a faster increase in coating capacitance, and a greater saturated water volume fraction. Moreover, the marine coating was studied in flowing pure water and a 3.5 wt% NaCl solution. The decay of impedance modulus was larger for the marine coating immersed in pure water and it was more substantial for higher flow rates. Thus, the different properties of working fluids influence the water uptake and ion diffusion, and eventually affect the coating degradation. Pure water appeared to facilitate more efficiently the deterioration of the barrier property of organic coatings against corrosion.

Other effects such as the non-refreshed and refreshed stationary NaCl solution, non-recirculated and recirculated flowing NaCl solution, and different concentrations of NaCl solutions on organic coating degradation were also studied. These effects were not significant enough to make conclusions based the experimental results in this study.

The finite difference model successfully simulated the convective diffusion process of NaCl ions migrating into the epoxy coating. The concentration distribution and the average concentration in the coating domain were obtained. The simulation indicates that the convective diffusion of NaCl ions alone is not the dominant factor in affecting coating's electrochemical property.

Overall, we conclude that flowing fluid on the coating surface accelerates the transport of water, oxygen, and ions into the coating, as well as promotes the migration of coating materials from inside the coating into the working fluid, where coatings experience more severe deterioration in its barrier property under flowing conditions. The flowing fluid over the coating surface could be used as an effective acceleration method.

This dissertation also includes a separate research study on the simulation of Scanning Electrochemical Microscopy (SECM) approach curves for heterogeneous metal surfaces. The alloy model provides insight into the influence of active spot size, matrix rate constant, and active spot rate constant on probe approach curves obtained by SECM. The model could obtain a more accurate values of the rate constant on a small region (the active spot) surrounded by a large less (or more) active region (the matrix). The alloy model will be useful to study electron transfer rate on an alloy surface.

CHAPTER 9. FUTURE WORK

The research work in this study focuses on investigating the influence of a single phase flow on the organic coating degradation, while the effect of two phase flow is also interesting to be evaluated. The flow pattern could influence interactions between the fluid and the surface, since different flow patterns can generate different flow velocities, boundary layers, and mass and momentum transfer process. The intensity of the interaction between flowing media and solid walls depends on the number of fluid phases and the velocity in each phase.

Many studies investigated the corrosion behavior of bare metals under two phase flow immersions, especially the erosion corrosion study which can be found anywhere. Few studies have reported the corrosion resistance behavior of organic coatings under two phase flow, although some investigations were in the performance of corrosion inhibitors under slug flow conditions [1-3]. We will choose the slug flow to study the effect of flow pattern on organic coating degradation, since slug flow is known to enhance internal corrosion in multiphase pipelines [2]. The mixing vortex and the bubble impact in the mixing zone of slug can generate high rate of shear stress and turbulence, which can significantly increase the corrosion rate and reduce the performance of corrosion inhibitors [2, 4].

The existing experimental setups for slug flow are usually pipe flow or fluidized bed vertical flow [1-8], and these hydrodynamic circuits are designed to be similar to the industrial size, such as 40 m long, 5.08 cm inner diameter acrylic pipeline [6], 1.4 m^3 stainless steel tank [2], and 25 m long horizontal transparent test section [4]. We will conduct the laboratory scale flow loop as an initial attempt to study the effect of slug flow

on the degradation of organic coatings. We plan to design a flow circuit based on our existing flow channels. We choose the rectangular channel flow due to the easy preparation and assembly for coating panels. All components of the flow loop should be designed functionally: flow inlet and outlet, valves, temperature control systems, and flow control systems.

Besides, the second phase material should be chosen beyond sodium chloride solution as the continuous flowing phase. Carbon dioxide is often employed to generate the slug, while air could also be used due to its more availability. Oil is another option, since it will generate a liquid-liquid two phase flow, but an oil and water separation device should be considered. Fine particles or some surfactants creating bubbles could also be employed. We need to evaluate these materials' possibility, availability, and difficulty to be introduced into the channel flow. We also need to control the hydrodynamic parameters of both the continuous flowing phase and the slug either by gear pump, syringe pump or other devices.

The testing procedures could be much like what we usually adopt for single phase flow. EIS measurement and topography characterizations will be conducted to monitor the coating degradation. The composition of working fluid will also be measured to present the effect of the fluid shear. The influence of different velocities of the continuous flowing phase will be evaluated as well as different slug velocities.

9.1. References

[1] Y. Chen, T. Hong, M. Gopal, W.P. Jepson, EIS studies of a corrosion inhibitor behavior under multiphase flow conditions, *Corrosion Science*, **42** (2000) 979-990.

[2] Y. Chen, W.P. Jepson, EIS measurement for corrosion monitoring under multiphase flow conditions, *Electrochimica Acta*, **44** (1999) 4453-4464.

[3] T. Hong, Y.H. Sun, W.P. Jepson, Study on corrosion inhibitor in large pipelines under multiphase flow using EIS, *Corrosion Science*, **44** (2002) 101-112.

[4] J. Villarreal, D. Laverde, C. Fuentes, Carbon-steel corrosion in multiphase slug flow and CO_2, *Corrosion Science*, **48** (2006) 2363-2379.

[5] D. Zheng, D. Che, Y. Liu, Experimental investigation on gas-liquid two-phase slug flow enhanced carbon dioxide corrosion in vertical upward pipeline, *Corrosion Science*, **50** (2008) 3005-3020.

[6] M. Daas, D. Bleyle, Computational and experimental investigation of the drag reduction and the components of pressure drop in horizontal slug flow using liquids of different viscosities, *Experimental Thermal and Fluid Science*, **30** (2006) 307-317.

[7] Q.H. Mazumder, S.A. Shirazi, B.S. McLaury, J.R. Shadley, E.F. Rybicki, Development and validation of a mechanistic model to predict solid particle erosion in multiphase flow, *Wear*, **259** (2005) 203-207.

[8] R. Norling, A. Nafari, A. Nylund, Erosion–corrosion of Fe- and Ni-based tubes and coatings in a fluidized bed test rig during exposure to HCl^- and SO_2^- containing atmospheres, *Wear*, **258** (2005) 1379-1383.